

**Tunable Multifunctional Nanomaterial and Polymer Composites:
Nonwoven Applications**

BY

JOSEPH E. MATES
B.S., University of Florida, 2006

THESIS

Submitted in partial fulfillment of the requirements
for the degree of Doctor of Philosophy in Mechanical Engineering
in the Graduate College of the
University of Illinois at Chicago, 2015

Chicago, Illinois

Defense Committee:

Constantine M. Megaridis, Chair and Advisor
Stephen J. Guggenheim, Earth & Environmental Sciences
Amin Salehi-Khojin, Mechanical & Industrial Engineering
Tolou Shokuhfar, Michigan Technological University
Ilker S. Bayer, Istituto Italiano di Tecnologia

Copyright by
Joseph E. Mates
2015

To my mother, Sheila.

ACKNOWLEDGMENTS

In light of knowledge attained, the happy achievement seems almost a matter of course, and any intelligent student can grasp it without too much trouble. But the years of anxious searching in the dark, with their intense longing, their alterations of confidence and exhaustion and the final emergence into the light – only those who have experienced it can understand it. – Albert Einstein

There is simply no way to encapsulate in words either the uphill struggle that is a PhD thesis, or the exhilaration I feel as I finalize my work; all the moments of self-doubt, set-backs, and eventual triumphs are impossible to convey. Likewise, any attempt at honoring the help of all those who've made it possible can never come close to the immense gratitude that I feel. Whether it was something as simple as a few kind words of support from close friends to spur me on, a teacher's patient explanation with a difficult concept, or even a sandwich lovingly prepared by my wife before I left for a long day in the lab; these and countless other small acts served to buoy my soul during this transformative and edifying passage in my life. And so, this achievement, that could never have been accomplished on my own, this pride of attaining a goal—is a shared pride. The achievement set forth and any that come after, will always be, in some way, an effort on my part to fulfill a promise to all those who've helped me; whether they knew it or not. Truly, it is a debt which can never be repaid, but there is now a bright path in front of me *because of their help*—and there are many miles ahead for me in which *to try*.

ACKNOWLEDGMENTS (Continued)

There are only so many pages allotted for these acknowledgments, but there are an innumerable many more I could fill with thanks to all of those who have been instrumental to making me who I am, making possible all that I've done, and all that I will do. For the sake of brevity, I will limit these pages to those *closest to the fire*, so to speak.

My mother, Sheila, was a strong woman. It is for her that this thesis is dedicated. She raised me on her own, and taught me much about determination, respect, and compassion. Because she never gave up on me, I have never given up on trying to make her proud. Although she passed away many years ago, I would be nothing without her love. She is dearly missed, but her legacy lives on through her children, and I carry that responsibility with pride.

When I lost my mother to a car accident, Irwin and Karen Gilbert continued where my mother could not. They took me into their home and raised me as their own. I'm not sure what would have happened to me if they weren't there, and thankfully, I never had to find out. I don't think it's an exaggeration to say it was brave of them to bring a teenager into their home, and it was definitely not always easy. I'm thankful to them for what they've done for me, and also for all the guidance they've given since. But most importantly, just for being there. They have treated me like a son since day one, and I only hope they're as proud of me as I am of them. Their sons, Brett and Bryan, and their daughter, Samantha, are siblings to me in every sense of the word, and great friends as well.

Also, and while this may sound silly, I must thank my wonderful dog, Otter. She has been a bright nova in my skies, her faithful presence oftentimes being the only thing that kept me from falling apart. If it does sound silly, then I wish you to find a dog like her someday. She

ACKNOWLEDGMENTS (Continued)

has been with me from those first days on my own, a full 16 beautiful years I have been given with her by my side. She crossed the country with me many times, and was there through both my undergraduate degree and now my doctorate. Though she may not be long for this world (it seems to me so cruel that dogs do not have the same lifespan as Man), I've cherished every second. I honestly don't believe I could've done any of this without her.

My decision to enter graduate school, especially after working for several years in industry, was not made lightly. Even after starting, the decision *to remain* in graduate school was not always an easy, or straightforward choice. I think most people who have gone before me on this path will understand that there are almost certainly dark days, moments of self-doubt and introspection that will test even the most determined mind. It always seemed so easy to give up and acquiesce to gravity, I would be dishonest if I said I never wavered. But through it all, the self-doubt slowly gave way to a cautious self-confidence, not without the support of many amazing friends, family, and an incredible and gifted adviser, Professor Constantine Megaridis.

Prof. Megaridis took a chance on bringing me into a mechanical engineering lab. Firstly, my undergraduate work was in physics. The fundamental science is roughly the same but there are vast differences in application, as I spent my first couple of years learning *the hard way*. Secondly, I was half a decade out of practice. This may not seem like much, but when you're surrounded by fellow students who can recite solutions to third-order differential equations by rote, it can be extremely disheartening when you have to remind yourself of simple calculus rules. *It was incredibly humbling*. Yet, as the years wore on, and the mental rust gradually came loose, I felt I began to earn my place in the lab. Inexperience gave way to maturity. I

ACKNOWLEDGMENTS (Continued)

was happy to repay, through diligent research, the initial faith which Prof. Megaridis placed in me. His support and encouragement were the pillars for all my endeavors from then until now, leading to the completion of this thesis and beyond. I would be remiss if I didn't thank him as well for all of his life advice, which had nothing to do with engineering but more to do with everything else.

I would also like to thank Dr. Thomas Schutzius, a dear friend and model graduate student whom I wholeheartedly, and unabashedly, sought to emulate. He was my senior inside the lab, and a great friend outside of it. His knowledge was intimidating and seemingly without end, *a born scientist*. The trials and tribulations of graduate school were certainly softened by having him there to help, and I only hope my constant barrage of questions didn't distract him too much during the course of his work. I could not have accomplished even a small fraction of this work without him.

My predecessor in the lab, and research mentor, Dr. Ilker S. Bayer, also deserves special recognition. His innovative genius and chemical engineering knowledge paved the way for much of the novelty in my research. He is responsible for many of my *eureka* moments in the lab, and has been a great collaborator and friend along the way. If my work follows a clear path, it is because he laid down the bricks that line it. It was always a pleasure having him around, never failing to teach me something new. However, it was not just knowledge and guidance that accompanied his friendship, but also laughter. Always smiling and ready with a joke, he was incredibly fun to be around; constantly reminding me just why on Earth any sane person would choose to do this kind of work: simply, *because they love it*.

ACKNOWLEDGMENTS (Continued)

During my time at UIC, I've been blessed with a cavalcade of fellow engineering students, lab-mates, and scientists who've offered much-needed companionship, advice, and feedback. Dr. Arindam Das, Dominic Dannessa, Mohamed Elsharkawy, Aritra Ghosh, and Jinlong Song, were fellow friends and PhD students who've taught me as much about science as culture, understanding, and the beauty of different perspectives (not to mention food!). Shreyas Kapatral, Jared Morissette, Patrick Carrol, Ramsey Ibrahim, Alejandro Vera, and John Palumbo were excellent collaborators during my time in the Micro/Nanoscale Fluid Transport Lab. I can only hope that they learned from me some measure of all that I've learned from them. I must also thank Prof. Stephen Guggenheim for his invaluable advice and XRD training.

I also thank two separate funding institutions, and their advisers, whose consultation drove much of this work: Dr. Jian Qin from Kimberly-Clark Corp. (KCC), and Prof. Benham Pourdeyhimi from the Nonwovens Institute (NWI) at North Carolina State University (NCSCU), among a score of others directly involved in these projects. Their on-going support, feedback, and motivation propelled many of these ideas off the "drawing-room floor" and into real-world applications and devices.

My close friends and family, whom I'd like to thank for their unwavering support. Steven Duffie, David Duffie, Javier Hernandez, among a growing number of Chicago friends too long to name, have been great company during my time here. They have been there for me during those times when I just needed to get out of the lab and have some fun. Donny Melchior, Eli Pluzynski, and Heather Patrick, among many other hometown friends who've believed in me from early on, and have always been there to pick up the phone when I was homesick.

ACKNOWLEDGMENTS (Continued)

My sisters, Lisa, Carol, Nancy, Monica, Denise, and Morgan, all of whom I love dearly, have supported me through thick and thin. I also thank my brother Bryan, who I can only hope is as proud of me as I am of him.

Last, but far from least: I thank my gorgeous wife Erika, who has been as supportive and encouraging a partner as one could ever ask for. We met shortly after the start of my second semester, and surprisingly, *she has never known me as anything other than a graduate student*. I'm not sure what I ever did to deserve her, but I look forward to sharing our life together. A life that from here on, I hope, will reward her for her patience during this time. Not for anything as petty as monetary concerns, but for a life with a husband who has more *time*, something infinitely more precious.

Some of you may say, "But you will still be busy," and you'd be right. I even hope so, for I get bored very easily if there's not something to fix, or a problem to solve. *But I will have vacation time!* In closing, I leave you with an Irish blessing of good health, which may or may not be a drinking toast: *Sláinte!*

JEM

CONTRIBUTION

Chapter 2 and Appendix A were the result of collaboration between the University of Illinois at Chicago (UIC) and Kimberly-Clark Corp (KCC), made possible by funding from KCC. Joseph Mates conducted all experiments, data collection, and sample preparation, including construction of the hydrostatic pressure apparatus used for testing. Joseph Mates wrote the published manuscript and supplementary information, with input from Thomas Schutzius and Constantine Megaridis. Thomas Schutzius assisted with SEM imaging. The formulation used was developed by Thomas Schutzius and Ilker Bayer. Industrial advisers to the project were Jian Qin and Donald Waldroup. Constantine Megaridis was the primary research adviser to this work.

Chapter 3 and Appendix B were the result of a collaboration between UIC and KCC, made possible by funding from KCC. Joseph Mates conducted all experiments, data collection, and sample preparation, including construction of the hydrostatic pressure apparatus used for testing. Joseph Mates wrote the published manuscript and supplementary information, with input from Thomas Schutzius and Constantine Megaridis. The formulation used was developed by Thomas Schutzius and Ilker Bayer. Industrial advisers to the project were Jian Qin and Donald Waldroup. Constantine Megaridis was the primary research adviser to this work.

Chapter 4 and Appendix C were the result of a collaboration between UIC and KCC, made possible by funding from KCC. Joseph Mates developed the formulation used, conducted all experiments, data collection, and sample preparation, with assistance from Alejandro Vera and

CONTRIBUTION (Continued)

Ramsey Ibrahim. Joseph Mates wrote the manuscript and supplementary information, with input from Constantine Megaridis. Industrial advisers to the project were Jian Qin, Debbie Calewatts, and Donald Waldroup. Stephen Guggenheim assisted in XRD data collection. Constantine Megaridis was the primary research adviser to this work.

Chapter 5 and Appendix D were the result of a collaboration between UIC and the Italian Institute of Technology (IIT). Joseph Mates and Ilker Bayer developed the formulation used. Electronic Characterization, SEM imaging, profilometry, and sample preparation were performed by Joseph Mates, with assistance from Patrick Carroll. Durability testing and AFM/EFM/SKPM data collection were performed by Ilker Bayer and Marco Salerno at IIT. EMI shielding data collection was performed at Notre Dame University by Zhenguo Jiang and Lei Liu. Joseph Mates wrote the manuscript and supplementary information, with input from Ilker Bayer, Marco Salerno, Zhenguo Jiang, Lei Liu, and Constantine Megaridis. Constantine Megaridis was the primary research adviser to this work.

Chapter 6 and Appendix E were the result of a collaboration between UIC and IIT. Joseph Mates and Ilker Bayer developed the formulation used. Electronic Characterization, SEM imaging, and sample preparation were performed by Joseph Mates, including the construction of specialized stretching apparatus and SEM stubs for elastomeric characterization. Patrick Carroll and John Palumbo assisted in the data collection and sample preparation. Joseph Mates wrote the manuscript and supplementary information, with input from Ilker Bayer and Constantine Megaridis. Constantine Megaridis was the primary research adviser to this work.

CONTRIBUTION (Continued)

Chapter 7 was the result of a collaboration between UIC and North Carolina State University (NCSU), made possible by funding from the Industrial Advisory Board (IAB) and the Nonwovens Institute (NWI) at the College of Textiles at NCSU. The nonwoven materials used were fabricated at NCSU under the direction of Benham Pourdeyghi. Electronic Characterization, SEM imaging, and sample preparation were performed by Joseph Mates. Emulsion data collection was performed by Joseph Mates, with assistance from Jinlong Song. Joseph Mates wrote the manuscript, with input from Benham Pourdeyghi and Constantine Megaridis. Stephen Guggenheim assisted in XRD data collection. Constantine Megaridis was the primary research adviser to this work.

TABLE OF CONTENTS

<u>CHAPTER</u>	<u>PAGE</u>
1 INTRODUCTION	1
1.1 Nanomaterials	1
1.1.1 Graphene	5
1.1.2 Nano-clays and Metal Oxides	8
1.2 Polymers	9
1.2.1 Polymer Blends & Crystallinity	11
1.3 Functional Nanomaterial/Polymer Composites with Tunable Properties	12
1.3.1 Liquid Repellency	13
1.3.2 Conductivity	17
1.4 Nonwovens	19
1.4.1 Piezoelectricity	20
1.4.2 Oil-water Emulsion Separation & Self-defouling Filtration	24
1.5 Thesis Objective	25
1.5.1 Water-based Superhydrophobic Coatings	25
1.5.2 The Fluid Diode	26
1.5.3 Fluorine-free & Water-based Superhydrophobic Compositions	26
1.5.4 Graphene Composites for Conductive Paper Applications	26
1.5.5 Elastomeric & Conductive Superhydrophobic Composites	27
1.5.6 PVDF Nonwovens	27
1.6 Scope of the Work	28
 2 WATER-BASED SUPERHYDROPHOBIC COATINGS FOR NON-WOVEN AND CELLULOSIC SUBSTRATES	 31
2.1 Motivation	32
2.2 Experimental	35
2.2.1 Substrates	35
2.2.2 Materials	36
2.2.3 Procedure	37
2.2.4 Characterization	38
2.3 Results & Discussion	42
 3 THE FLUID DIODE: TUNABLE UNIDIRECTIONAL FLOW THROUGH POROUS SUBSTRATES	 52
3.1 Motivation	53
3.2 Experimental	55
3.2.1 Substrates	55

TABLE OF CONTENTS (Continued)

<u>CHAPTER</u>		<u>PAGE</u>
	3.2.2 Materials	56
	3.2.3 Characterization	57
	3.3 Results & Discussion	58
4	TRANSLUCENT-WHITE & FLUORINE-FREE WATER-BASED SUPERHYDROPHOBIC COMPOSITIONS	71
	4.1 Motivation	72
	4.2 Experimental	76
	4.2.1 Materials	76
	4.2.2 Procedure	77
	4.2.3 Characterization	78
	4.3 Results & Discussion	80
5	DURABLE & FLEXIBLE GRAPHENE COMPOSITES BASED ON ARTISTS' PAINT FOR CONDUCTIVE PAPER APPLICATIONS	93
	5.1 Motivation	94
	5.2 Experimental	99
	5.2.1 Materials	99
	5.2.2 Preparation & Application of Conductive Composite	100
	5.2.3 Characterization	102
	5.2.4 Morphological Characterization	102
	5.2.5 Electrical Characterization	102
	5.2.6 Thermal Measurements	104
	5.2.7 Durability Testing	104
	5.2.8 Raman Spectroscopy	106
	5.3 Results & Discussion	106
6	HIGHLY ELASTOMERIC & CONDUCTIVE SUPERHYDROPHIC COMPOSITES FOR SMART FABRIC APPLICATIONS	122
	6.1 Motivation	123
	6.2 Experimental	126
	6.2.1 Materials	126
	6.2.2 Preparation	126
	6.2.3 Characterization	127
	6.3 Results & Discussion	129
7	PVDF NONWOVENS: OIL-WATER EMULSION SEPARATION, ENERGY HARVESTING, AND SELF-DEFOULING FILTRATION MEDIA	142
	7.1 Introduction	143
	7.2 Experimental	147

TABLE OF CONTENTS (Continued)

<u>CHAPTER</u>		<u>PAGE</u>
	7.2.1 Morphological/Chemical Characterization of PVDF nonwovens	147
	7.3 Results & Discussion	148
8	CONCLUSIONS AND RESEARCH OUTLOOK	165
	8.1 Thesis Conclusion	165
	8.1.1 Environmentally-friendly Water-based Superhydrophobic Coat- ings	165
	8.1.2 The Fluid Diode	166
	8.1.3 Fluorine-free Water-based Superhydrophobic Compositions .	166
	8.2 Durable & Flexible Graphene Composites from Artists' Paint for Conductive Paper Applications	167
	8.2.1 Highly Elastomeric & Conductive Superhydrophobic Composites for Smart Fabric Applications	168
	8.3 PVDF Nonwovens	169
	8.4 Research contribution	170
	8.4.1 Water-based Superhydrophobic Coatings	170
	8.4.2 The Fluid Diode	170
	8.4.3 Fluorine-free & Water-based Superhydrophobic Compositions	171
	8.4.4 Graphene Composites for Conductive Paper Applications . . .	171
	8.4.5 Elastomeric & Conductive Superhydrophobic Composites . . .	172
	8.4.6 PVDF Nonwovens	173
	8.5 Recommendations for future research	173
	8.5.1 Water-based Superhydrophobic Coatings	173
	8.5.2 The Fluid Diode	174
	8.5.3 Fluorine-free & Water-based Superhydrophobic Compositions	174
	8.5.4 Graphene Composites for Conductive Paper Applications . . .	175
	8.5.5 Elastomeric & Conductive Superhydrophobic Composites . . .	175
	8.5.6 PVDF Nonwovens	175
	APPENDICES	177
	Appendix A	178
	Appendix B	183
	Appendix C	190
	Appendix D	192
	Appendix E	200
	Appendix F	204
	CITED LITERATURE	207
	VITA	227

LIST OF TABLES

<u>TABLE</u>		<u>PAGE</u>
I	SLIDING ANGLE MEASUREMENTS FOR THREE ADD-ON COATING LEVELS FOR EACH OF THE FOUR SUBSTRATES. IF DROPLETS WERE NOT OBSERVED TO ROLL, THE SUBSTRATES WERE DESIGNATED AS 'STICKY' (MARKED WITH AN 'S').	42
II	LAPLACE PRESSURE CALCULATIONS FOR ALL FOUR SUBSTRATES, AS BASED ON PORE SIZE RANGES ATTAINED FROM SEM IMAGE ANALYSIS FOR A 2.4 GSM COATING AND COMPARED WITH EXPERIMENTAL VALUES DERIVED FROM HYDROHEAD MEASUREMENTS. ALL COATING LEVELS LIE WITHIN THE SUPERHYDROPHOBIC RANGE WITH MINIMAL DEVIANCE.	46
III	SESSILE CONTACT ANGLE MEASUREMENTS ON GLASS SLIDES COATED WITH THE SAME ADD-ON LEVELS AS THE CELLULOSIC AND NONWOVEN SUBSTRATES	48
IV	ROLL-OFF ANGLE MEASUREMENTS FOR THE TiO_2 :PE COMPOSITES ON GLASS SLIDES. THE VALUES ARE IN TERMS OF TiO_2 FILLER CONTENT (<i>I.E.</i> , WT. %), NONE OF THE BELOW 50 WT. % SURFACES HAD MEASURABLE ROLL-OFF ANGLES.	89
V	CONDUCTIVITY VALUES (IN S/M) BASED ON 4-PROBE SHEET RESISTANCE VALUES (VOLUME DETERMINED BY 25 MM \times 25 MM SQUARES WITH AN AVERAGE COMPOSITE THICKNESS OF 30 μm) FROM THE PLOT IN FIGURE 24 FOR BOTH M- AND S-TYPES, AND FOR ALL MLG PARTICLE RADII AS MASS FRACTION OF MLG IN THE COMPOSITE IS INCREASED.	114
VI	INITIAL FLUX AND EFFICIENCY DATA (<i>I.E.</i> , PURITY) FOR WATER-IN-OIL EMULSION SEPARATION. INCLUDED IN THE BOTTOM TWO ROWS IS RELEVANT DENSITY AND SURFACE ENERGY INFORMATION FOR THE FLUIDS TESTED.	160

LIST OF TABLES (Continued)

<u>TABLE</u>		<u>PAGE</u>
VII	<p>TYPICAL IMAGES CAPTURED DURING CA MEASUREMENTS FOR ALL FOUR SAMPLES AT THREE COATING ADD-ON LEVELS. THE ROUGH NATURE OF THE SURFACE TOPOGRAPHY MAKES IT DIFFICULT TO OBTAIN ACCURATE AND CONSISTENT CA MEASUREMENTS. ALL MEASUREMENTS WERE TAKEN USING A HORIZONTAL SIDE VIEW AND THE CORRESPONDING CA ARE LISTED ABOVE LEFT OF EACH DROPLET MEASURED. ALL OF THE SHOWN COATING LEVELS ACHIEVE SUPERHYDROPHOBICITY ($CA > 150^\circ$) ON ALL SUBSTRATES. CA MEASUREMENTS FOR SIMILAR COATING LEVELS WERE OBTAINED ON GLASS SLIDES FOR COMPARISON WITH THESE ROUGH SAMPLES. THE NEEDLE DIAMETER IN ALL IMAGES IS 1 MM, IMPLYING AN AVERAGE DROPLET DIAMETER BETWEEN 3 AND 4 MM.</p>	181
VIII	<p>PORE SIZE AS A FUNCTION OF ADD-ON COATING LEVEL FOR TWO REPRESENTATIVE SUBSTRATES: HYDROPHILIC HDPT (TOP ROW), HYDROPHOBIC SMS (BOTTOM ROW). THE LEFT COLUMN DISPLAYS IMAGES OF UNCOATED PORES, THE MIDDLE COLUMN IS AT THE LIGHTEST COATING LEVEL OF 2.4 GSM, AND THE RIGHT COLUMN IS AT THE HEAVIEST COATING LEVEL OF 9.6 GSM. IT CAN BE CLEARLY SEEN FOR THE LARGER PORE SIZES ON HDPT, THE COATING HAS A NEGLIGIBLE EFFECT ON REDUCING PORE SIZE AS THE PORES ARE TOO LARGE FOR THE POLYMER TO BRIDGE AND SEAL. IN CONTRAST, THE MUCH SMALLER PORE SIZES OF SMS ARE GREATLY REDUCED BY THE COATING. THE SCALE BAR IN THE TOP LEFT SEM MICROGRAPH APPLIES TO ALL IMAGES.</p>	182

LIST OF TABLES (Continued)

<u>TABLE</u>		<u>PAGE</u>
IX	TYPICAL IMAGES CAPTURED DURING WATER CA MEASUREMENTS FOR HDPT AT THREE PMC/NANOCLAY COATING ADD-ON LEVELS, WITH ACCOMPANYING CA MEASUREMENTS ON COATED GLASS SLIDES LISTED FOR COMPARISON. THE ROUGH NATURE OF THE PAPER SURFACE TOPOGRAPHY POSED CHALLENGES IN OBTAINING ACCURATE AND CONSISTENT CA MEASUREMENTS. ALL MEASUREMENTS WERE TAKEN USING A HORIZONTAL SIDE VIEW AND THE CORRESPONDING CA FOR HDPT ARE LISTED WITHIN THE IMAGE OF EACH DROPLET MEASURED. ALL COATING LEVELS SHOWN ACHIEVED SUPERHYDROPHOBICITY ($CA > 150^\circ$) ON ALL SUBSTRATES. THE NEEDLE DIAMETER (TOP) IN ALL IMAGES IS 1 MM, IMPLYING AN AVERAGE DROPLET DIAMETER BETWEEN 3 AND 4 MM.	188
X	SUBSTRATE PORE SIZE AS A FUNCTION OF ADD-ON COATING LEVEL ON HDPT: THE LEFT IMAGE DISPLAYS THE UNCOATED PORE; THE MIDDLE IMAGE SHOWS THE SAME PORE WITH A LIGHT COATING LEVEL OF ~2.5 GSM; THE RIGHT IMAGE IS OF THE SAME PORE WITH A HEAVIER COATING LEVEL OF ~10 GSM. FOR THE LARGER PORE SIZES, THE COATING HAS A NEGLIGIBLE EFFECT ON REDUCING PORE SIZE, AS PORES ARE TOO LARGE FOR THE POLYMER TO BRIDGE AND SEAL. THE SCALE BAR IN THE LEFTMOST SEM MICROGRAPH APPLIES TO ALL IMAGES.	189
XI	ROUGHNESS AVERAGE (R_A , IN μM) VALUES FOR THE SMALLEST AND LARGEST MLG SIZES TESTED FOR BOTH THE M- AND S-TYPE (XG SCIENCES AND STREM, RESPECTIVELY).	192

LIST OF FIGURES

<u>FIGURE</u>		<u>PAGE</u>
1	The Lycurgus cup, made by the Romans in 4th century B.C. by dispersing gold and silver nanoparticles in glass. The behavior of incident light passing through the glass results in different colors when lit from different directions. This is one of the most well-preserved examples of nanoparticle composites from ancient times, and the only surviving example of a Roman <i>diatretum</i> , or “cage cup.” Image credit: <i>Nanotechnology in the Roman Empire</i> (http://newundersol.blogspot.com), 2013.	4
2	Research articles published in journals between 1985 and 2009, using the keywords: fullerenes, nanotubes, and graphene. Image credit: A. Plume, <i>Buckyballs, nanotubes and graphene: On the hunt for the next big thing</i> (http://www.researchtrends.com), 2010.	7
3	(a) The wetting behavior for a solid surface is determined by the energy balance at the triple interface, in this case for a droplet that is on the border between hydrophobic and hydrophilic - 90° . (b) The sliding angle α is the angle of tilt at which the droplet will be seen to roll, with the CA hysteresis ($\Delta\theta$) as the difference between the advancing (θ_{ADV}) and receding angles (θ_{REC}). (c) The behavior of a water droplet on a rough surface with low surface energy, hydrophobic. (d) The behavior of a water droplet on a rough surface with high surface energy, hydrophilic. Roughness will enhance the hydrophobicity or hydrophilicity of a solid surface.	15
4	(a) Cross-sectional SEM image displaying PVDF-PE fiber morphologies. (b) Close-up of fiber bundles showing the Islands-in-the-Sea pattern, with the islands (PVDF) surrounded by the sea (PE) in tight bundles with diameters ranging from 20-30 μm and individual fiber diameters approaching 1 micron.	21
5	Atomic representation (legend on bottom) of either (a) α -phase orientation of PVDF, or (b) PVDF in the β -phase. In the β -phase, hydrogen atoms are entirely oriented along one side of the carbon ‘back-bone,’ while fluorine atoms are entirely oriented along the opposite side, giving the polymer chain a polarized orientation with an electrically positive charge on the hydrogen side (top, green atoms) and an electrically negative charge on the fluorine side (bottom, blue atoms).	23

LIST OF FIGURES (Continued)

<u>FIGURE</u>		<u>PAGE</u>
6	Water droplet dispensed from a flat-tipped needle (top) on a glass slide coated with 4.8 gsm of PMC-nanoclay composite. The needle diameter is 1 mm.	40
7	(a) SEM image displaying porosity of HDPT coated with 4.8 gsm PMC-nanoclay. (b) Depiction of how effective pore size (orthogonal maximum, minimum diameters D_{\max} and D_{\min}) was determined to calculate the theoretical Laplace pressure needed to push the liquid through the pore.	44
8	Substrate landscape: SEM images of four uncoated substrates at the same magnification. The scale bar applies for all images. (a) SMS, hydrophobic substrate. The spunbond polypropylene fibers can be clearly discerned from the meltblown fibers beneath, which have much smaller diameters. (b) HDPT, hydrophilic substrate. The density of these fibers presents an advantage in water resistance after coating. (c) Tissue, hydrophilic substrate. Although very similar to HDPT, these fibers are slightly smaller and less dense but weaker in terms of mechanical strength. (d) Spunlace, hydrophobic substrate made of PET fibers. . .	45
9	Experimentally measured water penetration resistance (hydrohead) for each substrate at three coating levels: 2.4 ± 0.2 , 4.8 ± 0.2 , and 9.6 ± 0.2 gsm. The first two substrates, SMS and spunlace, are inherently hydrophobic and have a nonzero water resistance as received (uncoated). The other two substrates are hydrophilic, and thus have zero resistance in their uncoated state.	49
10	SEM images of SMS and HDPT substrates with 2.4 gsm (light) coating. (a) SMS fiber from the top, spunbond, layer displaying nonuniform coating; the raw fiber can be seen underneath the clay/polymer coating. (b) HDPT fibers are completely and uniformly covered with the light coating.	51

LIST OF FIGURES (Continued)

<u>FIGURE</u>		<u>PAGE</u>
11	<p>The Fluid Diode: Depending on the relative orientation of the liquid-repellent coating with respect to the porous wettable solid and the water column (blue) used to impose hydrostatic pressure, the transmission of water through the system will register as a 1 (fluid transmission, coating up, CU in green) or 0 (no fluid transmission, coating down, CD in red), similar to the function of an electronic diode. The CU schematic (top) displays a coated pore under pressure during the initial phase of fluid penetration and a sagging water interface movement (dashed black line in profile schematic). As pressure increases, the sagging water meniscus extends to the depth of the next uncoated fiber and once contact is made, fluid wicks through to the underside, imposing no further resistance to the water column above and forming a water film over the entire underside of the substrate <i>after the penetration pressure has been surpassed</i> (shown in the bottom view, right). For the CD case, the substrate is completely saturated with water before filling the coated pore; as the sagging water interface extends down under increased external forcing, the threshold pressure is generally much higher than that of CU due to the lack of any additional wettable material in the vicinity beyond the fluid barrier. Eventually, the emerging liquid forms a droplet once the Laplace pressure of the largest pore(s) is exceeded (droplet seen in bottom view, right).</p>	59
12	<p>Water pressure penetration resistance versus coating level in gsm for HDPT (left) and SPT (right): The blue downward pointing triangles denote tests conducted coating-side down (CD), while the red upward pointing triangles denote coating-side up (CU) orientation. The disparity in penetration pressures at the lower coating levels suggests fluid flow diodicity, allowing water to pass unimpeded when in the CU orientation, or forward flow, while resisting reverse flow in the CD orientation. The diodicity (<i>i.e.</i>, pressure differential) is greater for the HDPT over that of SPT due to a finer fiber structure in the substrate.</p>	61

LIST OF FIGURES (Continued)

<u>FIGURE</u>		<u>PAGE</u>
13	Center: SEM cross-sectional image of HDPT with a 2 gsm superhydrophobic coating on top. The conformal superhydrophobic coating is visible as a thin layer along the top of the cross-section, with the uncoated fibers seen below. The left inset is a close-up of a coated fiber and shows the polymer/clay nanostructure as a roughening of the plain ridged surface of the uncoated fiber (right inset). EDS spectra are included to distinguish the presence of the nanocomposite coating (left) with energy peaks for carbon, oxygen, fluorine, aluminum, and silicon, as compared to the uncoated cellulosic fibers (right) with peaks for carbon and oxygen only. Fluorine is due to the presence of the fluoropolymer matrix, while the nanoclay contains both aluminum and silicon.	62
14	False-color SEM micrographs of HDPT with a 2.5 gsm hydrophobic coating on one side; color has been added to the fluoropolymer coating for better visualization. Fiber spacing results in a disparity between threshold penetration pressures (hydrohead) depending on applied coating orientation, CU or CD. (a) Cross-sectional image (as in Profile Schematic of Figure 11) illustrates the average spacing (λ) between the coated top and the underlying wettable fibers; this spacing represents the maximum distance the liquid meniscus can sag into a coated pore before being wicked throughout the substrate, thus <i>designating the lower bound of threshold hydrohead in the CU orientation</i> . (b) Surface image (as in Bottom View of Figure 11) illustrates a typical pore that the liquid fills as it emerges from the uncoated side of the substrate and into the surrounding air. The orthogonal minimum and maximum pore dimensions <i>designate the Laplace pressure and upper bound for the maximum threshold hydrohead in the CD orientation</i> (in this case, ~38 cm head of water). Both spacing parameters are equally important for determining the upper and lower bounds in the operating range of the fluid diode. .	65
15	Using the fluid diode (HDPT with 1.5 gsm coating) to selectively separate water (left), or oil (right), from an oil-water mixture: (a) A dry sample is exposed coating-side up (CU) to an hexadecane oil (red)/water(blue) mixture; the oil readily penetrates the light superhydrophobic coating and leaves the water droplet behind on the surface. (b) An identical sample is first saturated with (undyed for visualization) water from the uncoated side. The sample is then exposed CU to the same oil/water mixture, but now resists the oil and allows for water absorption, leaving the oil droplet behind resting on the surface.	69

LIST OF FIGURES (Continued)

<u>FIGURE</u>		<u>PAGE</u>
16	Photograph of a water droplet (dyed blue) beading on a coated glass slide (75 wt. % TiO ₂). The tiled image in the background is the College of Engineering logo of the University of Illinois at Chicago, clearly visible through the translucent-white superhydrophobic surface treatment. . .	73
17	TEM images of 21 nm mixed phase TiO ₂ particles (left), and a > 50 nm anatase TiO ₂ particle (right). The smaller dimensions of the mixed-phase nanoTiO ₂ are evident, having a greater tendency towards aggregation over that of the anatase due to greater surface area and surface charging (<i>i.e.</i> , hydrogenation). The scale-bars in both images are 10 nm.	82
18	SEM images for the three variants of TiO ₂ composites tested, in a 75:25 ratio: anatase (left column), 21 nm mixed phase (middle column), and the 100 nm mixed-phase (right column); in low (top row, 50 μm scale-bar), and high magnification (bottom row, 5 μm scale-bar). The anatase composite forms the larger agglomerate particle sizes by far, with a much greater inhomogeneity in average agglomerate size as well. The 21 nm mixed-phase composite formed uniform small agglomerate sizes, while the 100 nm mixture formed slightly larger agglomerates. Of interest is the variation in visible smooth patches of exposed polymer in both the anatase and the 100 nm mixed-phase composites, yet the polymer appears to be entirely utilized in the higher surface area 21 nm mixed-phase composite.	84
19	XRD reflection peaks for an all-PE coating (bottom, black), and three variant nanoTiO ₂ composites (anatase in red, 2nd from bottom; 21 nm mixture in green, 2nd from top; 100 nm mixture in blue, top).	86
20	Dynamic wettability measurements for all three types of TiO ₂ tested for all nanoparticle mass fractions. For all three TiO ₂ samples, the increase in mass fraction above 50 wt. % boosts advancing contact angle (green) to above 150° while also increasing the receding contact angle (red). For select mass fractions, there exists a measurable roll-off angle (gray). . .	91
21	Application and setting of artists' acrylic emulsion paint (shown in blue) on a paper surface (gray). Circles represent the polymer emulsion, which upon drying cross-links to form hexagonal bonds, thus acting as a matrix for pigment nanoparticles (shown as green dots). Based on scheme reported in (128).	96

LIST OF FIGURES (Continued)

<u>FIGURE</u>		<u>PAGE</u>
22	SEM images of two composite coatings (50 wt. % filler particle loading) on paper, before and after polishing/compression. The left column shows images of unpolished S-5 (top) and S-25 μm (bottom) average particle radius; it is clear that there is a range of particle sizes up to twice the average radius. The right column is for the same MLG sizes and similar magnification (scale bar is 50 μm for all images), after polishing. It is clearly seen that the roughness is removed during the polishing and compression step, as particles become oriented parallel to the substrate surface, effectively smoothing the composite, creating a better percolation network for electron transport. The defects in the smooth composite, shown as cavities, are roughly of the same order of magnitude as the initial average particle radius.	108
23	SEM cross-sectional images of composites on printer paper for two representative M-type MLG: (a) 5 μm , and (b) 25 μm . These cross-sectional images are used to estimate coating thickness range, as well as display the brick-and-mortar assembly of the MLG composite. Raman spectroscopy data is also included (bottom) for the two MLG sizes shown, with visible peaks corresponding to n-type doping of both mono- and multi-layer graphene (as compared to the same MLG particles in a PMMA matrix).	110
24	(Left) Log plot of 4-probe sheet resistance as a function of the final mass fraction of MLG in the dried polymer composite for all samples and mass ratios; numerical conductivity values for these are listed in Table V. The resistances for lowest mass fraction (0.2 or 20 wt. %) with the exception of Strem 25 μm were in the $\text{k}\Omega/\square$ regime, the samples with lowest resistance were uniformly found to be in the 50 to 65 wt. % regime. Increased MLG content (above 65 wt. %), with the exception of the xGNP M-5 μm , resulted in insufficient polymer content to adhere the nanoparticles through the polishing process and caused resistance to increase. (Right) Representative I-V curves showing linear Ohmic resistance behavior for the S-5 samples; the slopes match very well with the 4-probe data which has been converted to conductivities (units of S/m , see Table V).	113

LIST OF FIGURES (Continued)

<u>FIGURE</u>		<u>PAGE</u>
25	(a) Effect of tape peel tests on the conductivity of the paper samples made with 65 wt. % (65:35) MLG coating loadings. (b) Effect of linear abrasion (at 20 kPa) on the conductivity of paper samples coated with 65 wt. % MLG loadings. (c) Effect of linear abrasion (at 70 kPa) on the conductivity of paper samples coated with 65 wt. % MLG loadings. The legends to the right of the plots refer to the type (M- or S-type) and the particle size (5, 15, or 25 μm) of the composite filler particles; for the abrasion tests (b,c), the type and size is accompanied by the pressure used (20 or 70 kPa).	116
26	(a) AFM surface topography of M-15 conductive paper sample with 35 wt. % (35:65) MLG loading. (b) Corresponding EFM map of the same conductive paper, and (c) SKPM surface potential map, which is more sensitive to the CuPc domains of the original artists' paint. (d) The amplitude (<i>i.e.</i> , deviations against the set-point in tapping mode) is an 'error' image which stresses the regions with flat topography, in which single MLG particle surfaces are observed (see dashed ellipses).	117
27	Quantitative results obtained from AFM (a) and SKPM (b) measurements, for M-15 and S-5 samples with different MLG:paint-solids loadings. Uniform work function (WF) indicates that the surfaces of the conductive papers have very uniform surface conductivity, resembling highly-ordered pyrolytic graphite.	118
28	Plot of wave attenuation as a function of frequency between 500 and 750 GHz (0.50–0.75 THz), universally showing a linear increase in attenuation at higher frequencies. The highest level of attenuation was found for the highest conductivity composites (Strem 5 and 25 μm , both 50 wt. % MLG composites) as expected, yet the larger 25 μm particle size showed increased attenuation over the 5 μm particle composite even though both have comparable sheet resistances (50 wt. % S-5 is 72 Ω/\square , 50 wt. % S-25 is 71 Ω/\square), suggesting that greater particle dimensions positively affect THz EMI attenuation. An all-paint composite (0 wt. % MLG) was also tested to determine effect of the CuPc pigment on the attenuation, having a negligible effect.	121
29	SEM images of a stretch sequence for a 50 wt. % composite on natural rubber substrates. (a) Before the stretch cycle, $\lambda = 1$. (b) $\lambda = 2$. (c) $\lambda = 6$. (d) After composite is allowed to relax to an unstretched state, $\lambda = 1$	130

LIST OF FIGURES (Continued)

<u>FIGURE</u>		<u>PAGE</u>
30	(Left) Sheet resistance values for all ratios of CNF to Parafilm tested (CNF:PF), through one full stretching cycle from $\lambda = 1$ to 6, then returned to a relaxed position ($\lambda = 1$). The 65 wt. % CNF composite has the greater recovery performance after the stretch cycle, and was thus chosen for further testing at lower strain. (Right) The 65 wt. % CNF composite was further tested at lower maximum stretch values ($\lambda = 4$, and 3) compared to the extreme $\lambda = 6$ stretch ratio. Stretched composites with λ -values of 4 and 3 have a much higher recovery performance suggesting $\lambda = 4$ may be the upper limit of sustainable strain with recoverable properties.	133
31	Cross-sectional profile SEM images of a stretch sequence for a 50 wt. % composite on natural rubber substrates. (a) Before the stretch cycle, $\lambda = 1$, average coating thickness $\sim 30 \mu\text{m}$. (b) $\lambda = 2$, average coating thickness $\sim 6\text{--}7 \mu\text{m}$. (c) $\lambda = 6$, average coating thickness $\sim 3\text{--}4 \mu\text{m}$. (d) After composite is allowed to relax to an unstretched state, $\lambda = 1$, average coating thickness $\sim 9 \mu\text{m}$	134
32	Average thickness (t) values of the composite (red squares) at stretch ratios $\lambda = 1, 2, 6$, and after relaxation to 1. Elongational thinning follows a power law curve, shown as a solid blue line. The power law equation derived from the experimental data points allows for an estimation of coating thickness, and therefore composite volume. For the elongation and relaxation cycles, there are two distinct power law curves as the properties of the composite have changed through deformation.	135
33	(Left) Conductivity values for all ratios of CNF to Parafilm tested (CNF:PF), through one full stretching cycle from $\lambda = 1$ to 6, then returned to a relaxed position ($\lambda = 1$). The 65 wt. % CNF composite has the greater recovery performance after the stretch cycle, and was thus chosen for further testing at lower strain. (Right) The 65 wt. % CNF composite was further tested at lower maximum stretch values ($\lambda = 4$, and 3) compared to the extreme $\lambda = 6$ stretch ratio. Stretched composites with λ -values of 4 and 3 have a much higher recovery performance suggesting $\lambda = 4$ may be the upper limit of sustainable strain with recoverable properties.	136

LIST OF FIGURES (Continued)

<u>FIGURE</u>		<u>PAGE</u>
34	(Left) Contact angle hysteresis measurements as a function of CNF mass fraction, through a full stretch cycle ($\lambda = 1 \rightarrow 6 \rightarrow 1$), advancing (solid line) and receding (dashed line) are both displayed with the difference referred to as CA hysteresis ($\Delta\theta = \theta_{\text{ADV}} - \theta_{\text{REC}}$). The superhydrophobic performance remains relatively unchanged through the extreme stretch conditions, suggesting an extremely robust fluid repellency. (Right) Sliding angle data for the same stretch cycle. With the exception of the 20 wt. % CNF composite (no sliding angles), all sliding angles are well below 10° , demonstrating high droplet mobility on the surfaces even under maximum strain. The 20:80 ratio was determined to be ‘sticky,’ attributed to the high CA hysteresis (low receding CA reflect high droplet adhesion to the surface).	139
35	The best-performing composite, 65 wt. % CNF, is tested under 50 cycles of stretching to determine durability after prolonged use. Contact angle hysteresis (Left) and electrical resistance measurements (Right) for a 65 wt. % CNF composite through 50 stretch cycles. Half cycles (<i>i.e.</i> , 5.5, 10.5, <i>etc.</i>) represent the coating returned to a relaxed state before the next high strain cycle.	140
36	A schematic illustration of an oil well, where billions of gallons of oil must be demulsified to remove contaminants such as water and solid impurities. Using novel filter systems such as PVDF nonwovens, purified oil can be processed at high flux rates.	144
37	(a) SEM image displaying PVDF fiber morphologies. (b) Close-up of fiber bundles remaining from the Islands-in-the-Sea fabrication; clearly the PVDF fibers remain grouped in 20–30 μm bundles. Another fibrillation step, such as hydroentanglement is necessary to realize the true 1 μm diameters of the PVDF fibers, and thus the finer porosity needed for more robust filtration.	149
38	(a) SEM image displaying PVDF-PE fiber cross-sectional profiles. (b) Close-up of fiber bundles displaying the Islands-in-the-Sea fabrication where PVDF ‘islands’ are observed within the surrounding PE ‘sea.’ . .	150
39	The evolution of the fabric morphology from (a) the original PVDF-PLA fabric, to (b) the fibers after the NaOH bath has removed the sacrificial PLA and exposed the PVDF 1 μm fibers embedded within, and (c) the fibers after a simple acetone dip resulting in a more fibrillated fabric by virtue of the fiber swelling in the acetone bath.	151

LIST OF FIGURES (Continued)

<u>FIGURE</u>		<u>PAGE</u>
40	XRD plot of the reflection peaks in the 2θ range between 10 and 36° . The blue line represents a purchased sample of β -phase PVDF film (Measurement Specialties: unmetallized all-PVDF piezo film, Part No. 3-1003352-0, 110 μm thick), which also displays clear peaks in the α -phase; this suggests it is not necessary to eliminate the α -phase from the sample to take advantage of the piezoelectric β -phase. Surprisingly, the as-received nonwovens produced similar reflection peaks for the β -phase, with a broadened peak for the α -phase, as opposed to the two distinct α -peaks in the purchased film. This result indicates that it may be possible to electrically pole the as-received nonwovens to realize some piezoelectric property.	154
41	XRD powder diffraction setup with new fiber mounting stage (Left). Crystallinity can now be measured along the length of individual fibers, and as the fibers are rotated. This will be a useful tool in determining the efficacy in fiber modification to bring about a majority β -phase for future electrical poling tests. (Right) Close-up of the fiber mounting apparatus, where the fiber can be mounted along the centerline of rotation to ensure accurate crystallinity data.	155
42	Cross-section SEM of a superhydrophobic conformal coating applied by dip-immersion of PVDF fabric in a 0.5 wt. % low surface energy polymer in toluene. The surface treatment is very uniform, leaving the as-received fiber morphology intact, yet lowering the surface energy of the fibers overall to a level that they become self-cleaning. These fabrics can be implemented for oil-water separation.	157
43	Visual comparison of a water-in-oil emulsion before (Left) and after (Right) separation; the micro-emulsion takes on a milk-white haze, while the separated hexadecane oil is completely clear.	158
44	Plot of flux and efficiency (<i>i.e.</i> , purity) data for water-in-oil emulsion separation.	161
45	SEM image of the PVDF fibers after dip-immersion in CNF and solution-processed Parafilm TM . Inset in top left is after post-processing with drop-cast fluoropolymer to impart oleophobicity (red-dyed hexadecane oil droplet, blue-dyed water droplet) by taking advantage of the reentrant morphology offered by the CNF-decorated PVDF fibers.	162

LIST OF FIGURES (Continued)

<u>FIGURE</u>		<u>PAGE</u>
46	(Left) SEM image of the PVDF fibers after dip-immersion in MLG and solution-processed Parafilm™. (Right) I-V curves for PVDF fabrics after dip-immersion in CNF/MLG and Parafilm bath (GNP in the plot refers to graphite nanoplatelets, or multilayer graphene, MLG).	163
47	Cross-section SEM image of the PVDF nonwoven with spray-cast electrodes on top and bottom. The top electrode is composed of 50 wt. % CNF to Parafilm®, while the bottom electrode is composed of 50 wt. % MLG and an adhesive acrylic polymer. Both electrodes are highly durable and flexible; the resulting fabric only requires the addition of an electrolyte to become a functional battery.	164
A1	Schematic of hydrohead apparatus consisting of pump reservoir, viewing mirror and column. The water column is filled slowly until breakthrough is seen (shown as a white spot in the inset).	180
C1	SEM images of uncoated HDPT and SPT for comparison of fiber spacing (effective pore radii) and fiber depth. Side-by-side comparison of substrates in profile show the fiber depths can be approximated to less than 10 μm, with clear evidence that it can be much smaller at intervals. Threshold pressures in the forward flow CU orientation will be limited by the fiber depth shown in profile, the weakest point will be the point where fiber depth is smallest. Further comparison of the two substrates in panoramic landscape “top-down” images reveals the much larger fiber spacing for SPT as opposed to HDPT, the Laplace pressure of the corresponding pores will determine the threshold pressure for the reverse-flow CD orientation. The weakest point in this orientation will be where the spacing is the largest.	187
B1	20 ml vials of sonicated TiO ₂ particles in water after one month. The left vial is the 21 nm mixed-phase nanoTiO ₂ , and maintained suspension in water indefinitely. A small amount of the larger particles or aggregates separated out, seen resting in the bottom of the vial. As compared to the anatase form on the right composed of much heavier particles which settled within the first hour.	191

LIST OF FIGURES (Continued)

<u>FIGURE</u>		<u>PAGE</u>
D1	Profilometry images of an unpolished 50 wt. % M-5 composite (a), as compared to the same composite after polishing (b). The deep valleys shown in blue are in stark contrast to the several peaks of deep red shown in (a). For the polished surface in (b), there are many more peaks of red, but these are much more common and not nearly as sharply angled as that observed in the unpolished surface. The unpolished surface has a roughness average, R_a , of $6.84 \pm 0.4 \mu\text{m}$ as compared to the polished R_a of $1.60 \pm 0.3 \mu\text{m}$	193
D2	SEM images of an all-paint coating in low-magnification (a), to high magnification (b) where individual CuPc aggregates can be discerned. A cross-sectional profile image (c) was also included to estimate coating thickness in the absence of any MLG filler particles.	194
D3	I-V plots for both types of MLG samples, Strem and xGNP, and all mass ratios tested. All 3 sizes (5, 15, and $25 \mu\text{m}$) were tested in all 5 mass fractions of particle filler content in the final composite (20, 35, 50, 65 and 80 wt. %). All samples, sizes, and ratios demonstrate linear (Ohmic) behavior, and decreasing electrical resistance with increased particle filler content, until the point where decreased polymer content provides inadequate adhesion to retain the MLG within the composite during the polishing step.	195
D4	DSC thermal characterization for the dried paint (green) as compared to a representative sample of S-25 in a 50 wt. % composite (black). The glass transition temperature (T_g) is found to be approximately around 190°C for both samples. The heat transfer of the composite is increased by the addition of MLG, as seen by the sharper transitions and less relative heat flow.	196
D5	(a) Morphological characteristics of the original artist paint containing CuPc particles in $5 \times 5 \mu\text{m}^2$ surface topography image obtained from drop-casting from a dilute acetone solution. (b) AFM phase contrast image. The particle-like features are likely chlorinated CuPc aggregates. The scale-bar is $1 \mu\text{m}$. (c) Roughness histogram of the measured film. .	198

LIST OF FIGURES (Continued)

<u>FIGURE</u>		<u>PAGE</u>
D6	A simple circuit was fabricated to display the collaboration between the Italian Institute of Technology (IIT) and the University of Illinois at Chicago (UIC). The circuit was designed such that the three LED lights would bridge the circuit forming a connection at the three i's in the logos. The LED's were affixed with adhesive copper tape, with a spot of silver paint to ensure good contact. The paper was sprayed with Strem 25 μm (S-25) MLG particles in a 50 wt. % blend with the CuPC paint solids. The electrical circuit is closed once the battery is placed upside down on the two conductive paper leads, and the i's are "dotted" with a bright white light.	199
E1	Images of the stretch apparatus used for deformation of the coated substrates through fixed stretch ratios. In the background on left, the 4-probe multimeter is included with two leads visible on the left with the other two resting on top of the machine. In the inset on left, a top-down view of the stretched composite with a beaded water droplet in center (dyed blue for visualization).	201
E2	Special SEM stubs were prepared to maintain the stretch ratios from the stretch apparatus in order to image the morphological deformation of the composites. On top of the image is a coated rubber strip along with a cm ruler in the bottom for size. The stub on the left is empty to display how the clamps swivel for inserting substrates <i>in situ</i> from the stretch apparatus. Once inserted, as shown in the stub on the left containing a coated substrate in a stretch ratio of $\lambda = 2$, a razor is used to sever any unnecessary material.	202
E3	Similar SEM stubs as those shown in Figure E2 were prepared in order to image cross-sectional profiles of the composites through various stretch ratios; useful for determining volume of the conductive composite. . . .	203
E1	Copy of the license allowing republication of copyright material for Chapter 2.	205
E2	Copy of the license allowing republication of copyright material for Chapter 3.	206

SUMMARY

Functional nanomaterial and polymer composites are present in nearly every facet of our daily lives. Many commercial products owe their beginnings to some nontrivial technological advance in this field of research; light-weight battery devices in smart phones, for instance, or filtration membranes for water purification. Oftentimes, this forward progression in fundamental materials science is accompanied by life-saving advancements in medicine as well; from fluid-resistant disposable clothing for surgeons, to advanced wound care that promotes healing, or even composite coatings for replacement joints to reduce friction. Not only do these materials impact our daily lives, they are paving the way for new research which will change the lives of generations to come. And so, the field of research to which this thesis makes a humble contribution is that of functional polymer composite materials. More specifically, it deals with the synthesis and application of these composites onto a family of substrates, namely, porous nonwovens. It is a rich field, and one that is presently growing. As new materials are synthesized, methods for their production are improved, and every year our understanding of fundamental chemical relationships deepens. Surface science is at the core of everything that is presented herein.

It is hoped that new developments in materials science will translate to an improvement in the quality of living world-wide. Many revolutionary polymer nanocomposites, comprising nanomaterials within a polymer matrix, have ushered in new areas of scientific research and innovation for their low-cost, light-weight, and high-efficiency potential as alternatives to existing

SUMMARY (Continued)

technologies in fast-growing areas of commercial development. However, many developments in this field are hindered by the inability to transition from the laboratory bench into large-scale industrial production. These developments should not be dismissed as they inevitably reveal new insight and contribute to our fundamental understanding as a whole. Yet, a primary goal of this thesis work was to enable many of the new composites and functional materials which we have developed *to be scalable*. It is with this stated goal in mind that much of the presented work was pursued.

One component which assists our pursuit of scalability, and therefore low-cost and high throughput, is our choice of substrates: nonwovens. *Nonwoven* is a broad term encompassing almost any fabric or textile which is made without weaving fibers together (*i.e.*, loom). These materials are valuable in that they can be made on very large scales, very quickly. Most importantly, they have a high degree of surface area which is directly proportional to their functionality. It is for this reason we have chosen to use them as substrates in nearly all of our applications, even though many of our methods are *substrate-independent*. To reiterate, this work's contribution relates to the science of modifying surfaces, and showing these modifications to be tunable. Thus, a material with a greater amount of surface area (*i.e.*, porosity) is ideal for these pursuits.

The initial focus of this work was in the arena of fluid management; more precisely, fluid repellency. Many of the prior advances in this field have relied on volatile organic compounds (VOC) and fluorine-based chemistry, which are known to have long-lasting impacts on the environment. Building on these pioneering examples from the literature, we have developed

SUMMARY (Continued)

environmentally-friendly water-based formulations to impart extreme water repellency, or *superhydrophobicity*, to a variety of surfaces. Using a novel water-based fluoropolymer system, we were able to achieve one of the first completely water-based superhydrophobic dispersions. After characterizing this system for the minimal mass deposition required, a novel fluid mechanism was subsequently discovered and characterized, termed the *fluid diode*; capable of fluid flow rectification in one direction. Although this mechanism is demonstrated using our first water-based formulation, the mechanism is independent of the formulation and substrate, requiring only a thin fluid barrier on one side of a porous medium. In an effort to generate an even more environmentally-benign formulation, the next task which was undertaken was to remove fluorine altogether, resulting in one of the first *water-based and fluorine-free superhydrophobic dispersions*. Additionally, the formulation has a translucent-white appearance and the constituent materials have prior FDA-approval; thus, overcoming a nontrivial hurdle in the transition from laboratory-scale development into viable commercial production.

The knowledge gained in materials systems from the previous work, specifically that of nanomaterial and polymer composites, has enabled the extension of this research into conductive composites. The motivation towards low-cost and large-scale solutions enabled the development of a unique conductive composite for paper-based electronics. By taking advantage of an ubiquitous material such as artists' acrylic paint and conductive graphite nanoparticles, a composite achieving quasi-metallic properties was achieved demonstrating extreme durability with competitive electronic performance; at a lower cost than current conductive inks and similar composite systems. This work was quickly followed by the development of another, extremely

SUMMARY (Continued)

elastomeric conductive and superhydrophobic composite; making use of carbon nanofibers and another commonplace material found in nearly all modern laboratories: ParafilmTM. It was found that by virtue of Parafilm's strong adherence to certain substrates, the material could be made to mimic reversible deformation, so-called *pseudo-reversible* elongation. The performance far exceeds previous benchmarks from the literature in both flexible conductivity and repellency metrics, even after multiple stretch cycles.

Unlike the previous examples, which were primarily substrate-independent and relied on novel composite systems, the final component to this work relies on a specific substrate, that of polyvinylidene fluoride (PVDF) nonwovens. Much of the characterization techniques and composites developed prior proved useful towards adding functionality to these unique nonwovens, which were made elsewhere by a unique method of manufacturing enabling repeatable fiber diameters of 1 μm . The attractive properties of the PVDF polymer enable exploration into the generation of piezoelectric fabrics for energy-harvesting and self-defouling filtration. To ascertain the viability of these materials for such applications, characterization of their crystallinity and the construction of an electrical poling apparatus was necessary. In addition to the piezoelectric component, these materials were also characterized for water-in-oil emulsion separation; achieving, and surpassing in some cases, performance benchmarks from industry and literature for similar applications. In almost all cases, previous examples were not able to achieve the high-throughput and therefore low cost of our substrate, thus making this work a significant advance in relevant textile industries.

LIST OF SYMBOLS AND ABBREVIATIONS

Acronyms

AFM	atomic force microscopy
ASTM	American Society for Testing and Materials
CA	contact angle
CCD	charge-coupled device
CD	coating down
CNF	carbon nanofiber
CNT	carbon nanotube
CU	coating up
CuPc	copper phthalocyanine
CVD	chemical vapor deposition
EA	ethyl acrylate
EDS	energy dispersive X-ray spectroscopy
EFM	electric force microscopy
EMI	electromagnetic interference
EPA	Environmental Protection Agency
FDA	Food & Drug Administration

LIST OF SYMBOLS AND ABBREVIATIONS (Continued)

GNP	graphite nano-platelet
gsm	grams per square meter, g/m^2
HDPT	high-density paper towel
HHT	high heat-treated
HOPG	highly-oriented pyrolytic graphite
IAB	Industrial Advisory Board
IIT	Italian Institute of Technology
KCC	Kimberly-Clark Corporation
LED	light-emitting diode
MMA	methyl methacrylate
MNFTL	Micro/Nanoscale Fluid Transport Lab
MWCNT	multi-wall carbon nanotube
NCSU	North Carolina State University
NWI	Nonwovens Institute
OCA	oil contact angle
PA	polyamide
PF	Parafilm TM
PFA	perfluorinated acid

LIST OF SYMBOLS AND ABBREVIATIONS (Continued)

PFOA	perfluorooctanoic acid
PMC	perfluoroalkyl methacrylate copolymers
PMMA	poly(methyl methacrylate)
ppm	parts per million
PTFE	poly(tetrafluoroethylene)
PVDF	poly(vinylidene fluoride)
RMS	root mean square
SEM	scanning electron microscope
SKPM	scanning Kelvin probe microscopy
SMS	spunbond-meltblown-spunbond
SPT	Scott [®] paper towel
SWCNT	single-walled carbon nanotube
TEM	transmission electron microscope
UIC	University of Illinois at Chicago
UV-Vis	ultraviolet-visible spectrometer
WF	work function
XRD	X-ray diffraction

LIST OF SYMBOLS AND ABBREVIATIONS (Continued)

Dimensionless Groups

$Bo = \frac{\rho g r^2}{\gamma_{LV}}$ Bond number

Subscript

o initial sheet resistance

a roughness average

ADV advancing contact angle

c critical probability for percolation pathway

f final length

$Forward$ forward intrusion pressure

g glass transition temperature, Chapter 1, 5, Appendix D

g ground, Chapter 5

$Hysteresis$ contact angle hysteresis

i initial length

L liquid

LV liquid-vapor

m melting point

max maximum pore diameter

LIST OF SYMBOLS AND ABBREVIATIONS (Continued)

min	minimum pore diameter
REC	receding contact angle
relax	elongational thickness after relaxation
Reverse	reverse intrusion pressure
s	sheet resistance
S	solid
SL	solid-liquid
stretch	elongational thickness under stretching
SV	solid-vapor

Greek Variables

α	sliding, or roll-off, angle ($^{\circ}$)
γ	surface energy (mN/m)
δ_{+}	positive charge (C)
δ_{-}	negative charge (C)
$\Delta\theta$	contact angle hysteresis ($^{\circ}$)
ΔP	Laplace pressure (cm head, kPa)
θ	contact angle ($^{\circ}$)
θ^{*}	apparent contact angle ($^{\circ}$)

LIST OF SYMBOLS AND ABBREVIATIONS (Continued)

λ	vertical fiber spacing, Chapter 3 (m)
λ	stretch ratio, Chapter 6
ρ	density (g/m^3)
σ	conductivity (S/m)
φ	solid to liquid interfacial contact area ratio

Variables

D	diameter, Chapter 2, 3 (m)
D	dispersive surface energy component, Appendix B (mN/m)
f	fractional surface area ratio
g	gravitational acceleration (m/s^2)
L	length (m)
p	probability of a percolation pathway, Chapter 1
P	pressure, Chapter 2, 3 (cm head, kPa)
P	polar surface energy component, Appendix B (mN/m)
R	roughness factor, Chapter 1, Appendix D
R	sheet resistance, Chapter 1, 5, 6 (Ω/\square)
R	pore radius, Chapter 3 (m)

LIST OF SYMBOLS AND ABBREVIATIONS (Continued)

t	thickness (m)
T	Temperature (°C)
V	volume (m ³)
W	width (m)

CHAPTER 1

INTRODUCTION

1.1 Nanomaterials

Nanomaterials, defined as having one or more dimensions on the nanometer scale (*i.e.*, nanoparticles, nanofibers, etc.), offer intrinsic functionality over their bulk form due to the increased surface area when the particles are discretized on such small scales. The large surface area to volume ratio of these materials gives rise to many interesting properties and forms the impetus for their extensive study in the field of materials science. Gold nanoparticles, for instance, when formed in a suspension actually take on a red appearance (1). This change in optical property, observed with many nanomaterials, results from the particles reduced to small enough scales that the wavelength of visible light is on the same order as the incident surface(s), and thus their reflection and absorption spectra change. The color of reflected light is only one property which can change when working with nanomaterials as compared to their bulk form; many other properties change because of the increased surface to volume ratio (*e.g.*, chemical reactivity, conductivity, magnetic properties, melting point, *etc.*). This high surface area enables nanomaterials to enhance surface functionality while minimizing volume in composites, readily translating to light-weight and high-efficiency substitutes for many industrial and commercial applications; commonly finding applications which would otherwise be impossible.

The use of nanomaterials for their unique properties is *not a new field*. There exist many examples in human history, from ancient to more modern times, where this science has been used to great effect. Gold and silver, historically two of the most coveted elements since the recorded advent of civilization, are perhaps the most significant examples of mastery over the nanometer realm in ancient history; with instances of their use in colloidal dispersions extending as far back as the 5th century B.C. The Lycurgus cup (shown in Figure 1), a 4th century B.C. Roman cup displaying an episode from the myth of Lycurgus, a king of the Thracians, is one of the most well-preserved examples of the craftsmanship attributed to first-hand knowledge of nanomaterials, and their inclusion in composite materials (2). The cup was made by dispersing gold and silver nanoparticles in glass, likely from a colloidal pre-suspension. The precise method of manufacture remains elusive to modern-day scientists, as attempts at reproduction have not met with complete success. Furthermore, the art of creating these colloidal nanoparticle suspensions was not isolated in specific regions. It is possible that the techniques were proliferated amongst trade routes, or even more remarkably, these processes could have been arrived at independently.

The ancient Egyptians were known to produce large quantities of what they referred to as “oil of gold,” having a reddish pink coloration, a well-known aforementioned attribute of colloidal nanogold suspensions (3). A property not confirmed for modern science until Faraday in 1857 (4). Several hundred years prior, in his book entitled, *The newe iewell of health* (5) from the 16th century A.D., the alchemist Paracelsus referred to his “*Elixir of Life*” as “*Aurum Potabile*,” or potable gold. At the time, this elixir, wherein sulfur was used to reduce a gold

chloride solution, was considered a curative treatment for many ailments, from heart problems to syphilis (6). It's conceivable that similar methods to produce colloidal gold may predate these examples from antique texts by several thousand years, evidenced by references in ancient Chinese and Egyptian literature.

Amazingly, it is clear from historical texts and archeological discoveries that what is commonly considered nascent *modern science*, is more precisely, the rebirth of a *lost art*. It is probable that future discoveries will push back the advent of nanomaterial engineering *even further* in human history.

Richard Feynman, one of the great physicists of the 20th century, played an instrumental role in the resurgence of nanomaterial research over the last 50 years. He famously gave a lecture entitled, "There's plenty of room at the bottom," in 1959 (7) at a meeting of the American Physical Society (APS). This talk is regarded as one of the more significant motivations for the growing field of nanomaterial research, to which this thesis makes it's humble contribution. For many decades since his lecture, and prior, advances in the precision of equipment used to detect and manipulate these minute particles has met with an increased understanding of both their properties and potential.

Many common materials, that have been essential for our emergence as a civilization into the technologically-connected global society we have become, are finding new, broader applications thanks to the increased understanding of their nanoscale attributes. Some recently discovered materials were even predicted in decades past; long before the methods, or knowledge, required for their synthesis were available. These new materials have only recently been made possible



Figure 1. The Lycurgus cup, made by the Romans in 4th century B.C. by dispersing gold and silver nanoparticles in glass. The behavior of incident light passing through the glass results in different colors when lit from different directions. This is one of the most well-preserved examples of nanoparticle composites from ancient times, and the only surviving example of a

Roman *diatretum*, or “cage cup.” Image credit: *Nanotechnology in the Roman Empire*

(<http://newundersol.blogspot.com>), 2013.

by innovations in production techniques coupled with a better understanding of nanomaterial systems. As is oftentimes the case with new materials and methods, costs remain relatively high; however, novel synthesis methods are constantly being pioneered and refined to reduce the production costs of these functional materials and resources.

1.1.1 Graphene

Graphene, a two-dimensional hexagonal mono-layer (one atom thick) lattice of carbon atoms, was one such material that was predicted long before it had been successfully isolated and observed. The use of graphite, essentially a disordered stacking of multilayer graphene, has a storied history in many cultures. Even the modern name of graphite, from the Greek *graphein*, meaning “to write,” reflects its history of use in pencils (8). The Boian culture in neolithic times (4th century B.C.) may be one of first documented cultures to make use of graphite in decorating ceramic pottery (9). Graphite was also used to line cannon-ball molds during the reign of Elizabeth I (1533 - 1603), producing cannonballs with a much greater degree of *smoothness*, thereby limiting their drag and allowing them to fly farther, and faster (10). As such, it was a closely-guarded military resource for the English navy.

This technological superiority in warfare, through mastery over graphitic materials and composites, is also exemplified in the Japanese art of sword-making; where the sharp edge of the *katana* could be strengthened by the addition of carbon. Early Japanese smiths found that by heating coal with what is referred to as “iron sand,” they could produce a steel called *tamahagane* (11). Not only does the addition of graphitic carbon promote the sword’s ability

to retain a sharp edge and resist breaking, but it also makes the sword considerably lighter; thus offering a distinct advantage in combat.

Evidently, much of the current interest in nanomaterial composites finds precedence throughout history, where innovation was often sought as a means to superior military strength. It is hoped that current advances in understanding of nanomaterial properties will yield a superior quality of living for generations to come, as we collectively benefit from the technological innovations of generations past. It is with this, perhaps idealistic, goal in mind that much of the presented work was pursued.

Monolayer graphene was predicted as early as 1947 by P.R. Wallace (12), although the lamellar structure of graphite was well-understood much earlier. Benjamin Collins Brodie studied graphite oxide and determined it to be the result of an ordered stacking of thin sheets into flake-like structures (13), although the true structure wasn't fully determined until more advanced observational methods became available. In 1918 (14), Kohlschütter and Haenni used powder diffraction to reveal the presence of ordered stacks of monolayer carbon lattices. This discovery served to fuel graphitic research, which blossomed over the next 50 years aided by the invention of the transmission electron microscope, greater precision in X-ray diffraction (XRD), and better theoretical models. These advances were quickly followed by the *re-discovery* of carbon nanotubes (CNT) in 1991 (15) and the Nobel Prize-winning discovery of the long-theorized single-layer graphite in 2004 (16), what is now commonly referred to as *graphene*. Research into graphene-related materials has grown exponentially since their respective discoveries as shown in Figure 2.

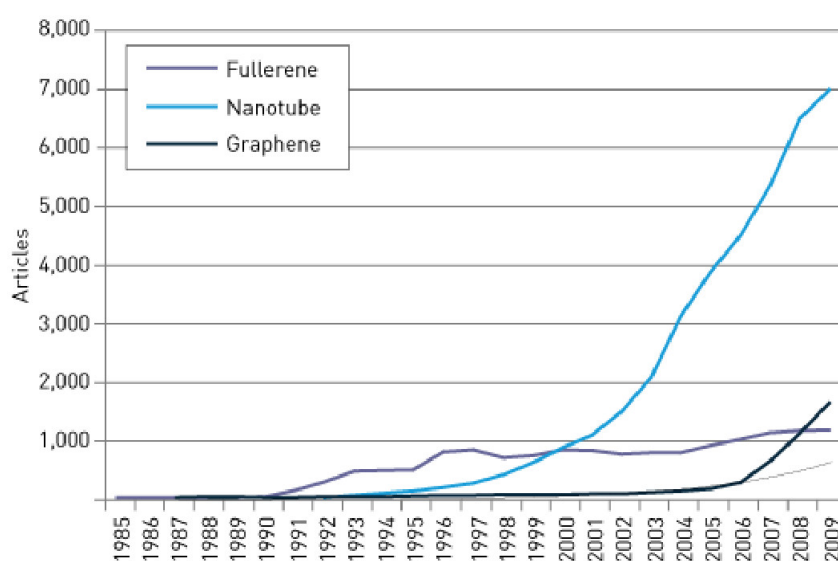


Figure 2. Research articles published in journals between 1985 and 2009, using the keywords: fullerenes, nanotubes, and graphene. Image credit: A. Plume, *Buckyballs, nanotubes and graphene: On the hunt for the next big thing* (<http://www.researchtrends.com>), 2010.

It is helpful to make the distinction between the various graphitic materials currently being studied, specifically that between graphene, carbon nanotubes (CNT), or carbon nanofibers (CNF). Graphene, as previously mentioned, is a 2-D hexagonal monolayer lattice of carbon atoms. These sheets of graphene can occur in a few layers (multilayer graphene) to many (graphite), it is currently much less expensive to produce multilayer graphene, in the form of high aspect ratio graphite nanoplatelets (GNP), than single sheets of graphene; although this may no longer be the case in the coming years as synthesis techniques improve.

If the single sheet of graphene is rolled into a cylinder, it forms what is known as a carbon nanotube (CNT). CNT can be produced in single-walled (SWCNT) or multi-walled (MWCNT) forms, where smaller concentric cylinders are nested within larger ones. In addition, nanomaterials known as carbon nanofibers (CNF) refer to cylindrical fibers made from nested bowl-, cup-, or plate-shaped lattices. The family of particles all derive from the intrinsic lattice structure of graphene, prized for high conductivities via ballistic electron transport, high thermal stability, and mechanical strength, to name just a few advantageous properties. In this work, GNP and CNF are used for their electro-conductive properties along with their high aspect ratios, which aid in the formation of charge percolation networks in polymer composites, as well as offering surface texture.

1.1.2 Nano-clays and Metal Oxides

In addition to the graphitic materials, there are several other nanoparticles of interest which are presented in this work. Nanoclays have proven extremely useful for their dispersability in water-based colloidal suspensions. Clays, typically comprising stacked layers of metallic

oxides and organic material, are a fine soil formed over relatively long geological time-scales from chemical weathering of silicate-bearing rocks. The distinction between silts and clays is not without some controversy, but depending on the academic source, the divide is generally considered to be somewhere between 1 and 4 μm , with clay being the finer of the two (17). In our work, we have strictly confined our studies to nanoclays where their platelet-type structure (*i.e.*, high-aspect ratio) are once again useful in generating nanoscale texture suitable for extreme water-repellency.

While nanoclays comprise metallic oxides, it is often useful to isolate these metallic oxides and work with them independently. Nanoclays such as smectite and vermiculite, upon wetting with water, will swell considerably which is undesirable in certain applications. Additionally, if specific metallic oxides are isolated and incorporated, greater functionality can be imparted to a composite. One such oxide nanoparticle is titanium dioxide (TiO_2), which has known photocatalytic properties (18) making it suitable for applications such as photovoltaics and tunable wettability. Other oxides which are used in similar composites herein, whether for comparison purposes or specific functionality, are silicon dioxide (SiO_2) and zinc oxide (ZnO).

1.2 Polymers

The field of polymer science has advanced by leaps and bounds since its beginnings in the late 1700's and early 1800's, when the macromolecules were erroneously believed to be a colloidal clustering of small molecules, lacking specific molecular weight (19). It wasn't until 1922 that Hermann Staudinger first suggested they were actually covalent macromolecules, bound together in long chains; a discovery for which he would go on to win the 1953 Nobel

Prize in chemistry. Since Staudinger's time, the commercial and academic base for polymer science has widened considerably; the understanding acquired in the last century for these macromolecules has launched entire industries and has even allowed mankind to *map the human genome* (20). It can be safely stated that there are very few facets of human life which have not been improved in some nontrivial manner by the introduction of a polymer, or polymer composite; furthermore, it can be safely assumed that this incorporation of polymers into our lives will only increase in the coming years. Polymeric composites have revolutionized materials science, dramatically reducing production costs to make functional composites economically feasible for introduction into modern consumer goods and providing solutions for industrial needs.

In general, polymers can be divided into two groups: thermoplastic and thermosetting. Thermoplastic refers to a group of polymers that do not actively cross-link across multiple layers or chains, remaining malleable both above the glass transition (T_g) and below the melting point (T_m) without undergoing a phase change. Thermosetting polymers on the other hand, will undergo an irreversible phase change upon curing due to the high level of cross-linking across polymer strands. Low T_m thermoplastic polymers are especially useful for forming and processing, and are used in a wide array of products from Nylon fabrics (polyamide, PA), to Plexiglas[®] (polymethyl methacrylate, PMMA), and non-stick coatings (Teflon[®]) (polytetrafluoroethylene, PTFE) for cookware.

1.2.1 Polymer Blends & Crystallinity

It is often useful to combine multiple polymers to take advantage of their individual properties in tandem, thus generating a composite material with unique properties. For example, adhesive polymers can be added to low surface energy polymers, which are notoriously difficult to bind to many surfaces. The blend can result in a new matrix capable of combining the low surface energies and adhesion properties, thereby forming an adhesive layer which resists dirt adhesion, exemplified in common household paints (21). This can be extended to incorporate not only two polymers of differing attributes, but several. Although with added complexity can come new and unforeseen attributes, as well as difficulties. It is often the case that polymer blends are limited to two or three distinct components, although this is more of a guideline for simplicity (*i.e.*, cost-point) rather than a strict rule of thumb.

Additionally, homopolymer (homogenous repeating units) blocks in a single chain can be modified and removed to constitute a new copolymer. A block copolymer consists of repeating units of ordered structure such that a polymeric backbone is broken up in distinct, repeating groups. If this ordering is random, it is referred to as a statistical polymer. Also, the addition of nanomaterials into a colloidal polymer suspension can graft them onto the chain itself via adsorption along the nanoparticle surface, thereby forming an ‘elemental block;’ or the addition of nanomaterials can form nucleation sites to enhance the ordering of the polymer structure, or crystallinity.

The ordering of a polymer into crystalline regions can result in dramatic changes to the material properties of a polymer group from that of their amorphous, or disordered form. Although

the usage of the term *crystalline* in polymers is somewhat ambiguous since it is generally defined more precisely as *atomic ordering*; however, the application of crystallographic techniques for assessing atomic ordering is entirely relevant to the study of ordered polymer groupings as well. Among some of the property changes as these macromolecular structures become more ordered are optical transparency (amorphous) and mechanical strength (crystalline). It can be advantageous to blend particle(s) into polymer composites to alter the degree of crystallinity, thereby tuning the resultant material properties.

1.3 Functional Nanomaterial/Polymer Composites with Tunable Properties

As has been discussed, there exists many advantages for incorporating nanomaterials in a composite. The composites of interest to the current work are all polymeric, consisting of one or more polymers forming a binder matrix. This matrix acts as scaffolding for the addition of nanomaterials, and/or determines the surface energy of the material formed from these composites. The composite materials are generally applied as a protective layer on a given substrate, in nearly all cases the substrate is a porous material of high surface area (*i.e.*, fibrous nonwoven). The change in material property of a composite with the addition of one or more nanomaterials for functionality is herein studied. It will also be shown that the surface area of the chosen substrate serves to enhance the properties of the conformal composite layer; thus, a substrate with high surface area is considered ideal for imparting greater surface functionality as they are directly proportional to one another.

1.3.1 Liquid Repellency

The wettability of a surface to liquid is determined by two factors: morphology and surface energy. For a smooth surface lacking rough texture, the behavior of a liquid contacting the surface will be determined solely by the surface tensions (γ) at each interface, not only for the liquid and solid surface but the surrounding vapor (See Figure 3a). If we solve the energy balance at the triple interface for the liquid/vapor (γ_{LV}), solid/vapor (γ_{SV}), and solid/liquid (γ_{SL}), we can obtain a definition for the contact angle (θ) of the droplet on the surface, called Youngs relation (22):

$$\gamma_{LV} \cos \theta = \gamma_{SV} - \gamma_{SL} \quad (1.1)$$

Extending this concept to a mildly textured surface, we can build from the simplified form delivered by Wenzel (23) for treating an apparent contact angle (θ^*). Wenzel made the assumption that for the textured case, the water will contact a greater portion of the solid, thus the apparent contact angle will differ from the original (equilibrium) contact angle by the relation,

$$\cos \theta^* = R \cos \theta, \quad (1.2)$$

called Wenzel's equation, where R is the roughness factor for the surface ($R > 1$). Of course, Wenzel's equation applies only for chemically homogenous surfaces as the surface tension values at the interface will change depending on the chemistry. However, Cassie and Baxter (24) later developed a theory for wetting of chemically heterogeneous surfaces where the apparent contact

angle can be considered to be the sum of the cosines for the equilibrium contact angles (θ_1 and θ_2) in a weighted form such that:

$$\cos \theta^* = f_1 \cos \theta_1 + f_2 \cos \theta_2, \quad (1.3)$$

called the Cassie-Baxter equation, where f_1 and f_2 represent fractional surface areas ($f_1 + f_2 = 1$).

For the case of a droplet resting on a surface with a very rough morphology, it is actually only partially in contact with the solid but will also entrain, and thus rest upon, pockets of vapor trapped within the surface roughness of the solid. The resultant equation is a modified form of the Cassie-Baxter equation such that,

$$\cos \theta^* = -1 + \varphi(\cos \theta + 1), \quad (1.4)$$

where φ represents the solid to liquid ratio for contact area. In general, for apparent contact angles above 150° , these surfaces are considered super*hydro*phobic; specifically, for water and oils, the terms super*hydro*phobic and super*oleo*phobic are used, respectively. In most cases, with rare exceptions (25), superoleophobic surfaces will be superhydrophobic as well but not *vice versa* due to the lower surface energies of oils. The unique cases where this *does not hold true* will be discussed later.

Another consideration in the theory of liquid repellency is that of droplet mobility. A surface is considered super-repellent, or self-cleaning (*i.e.*, lotus effect), if a droplet resting on the surface will roll off when the surface is tilted at an angle (Figure 3b, sliding angle α) less than

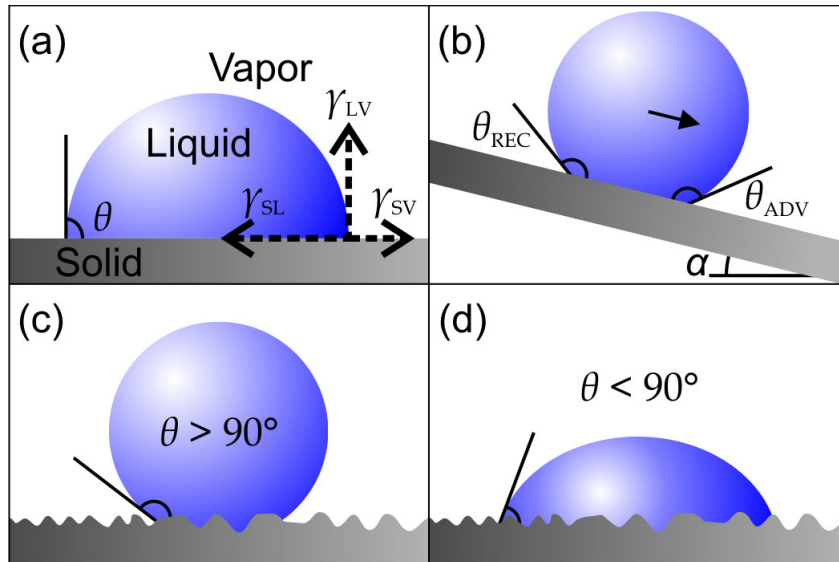


Figure 3. (a) The wetting behavior for a solid surface is determined by the energy balance at the triple interface, in this case for a droplet that is on the border between hydrophobic and hydrophilic - 90° . (b) The sliding angle α is the angle of tilt at which the droplet will be seen to roll, with the CA hysteresis ($\Delta\theta$) as the difference between the advancing (θ_{ADV}) and receding angles (θ_{REC}). (c) The behavior of a water droplet on a rough surface with low surface energy, hydrophobic. (d) The behavior of a water droplet on a rough surface with high surface energy, hydrophilic. Roughness will enhance the hydrophobicity or hydrophilicity of a solid surface.

10°. Many, but not all, superhydrophobic surfaces are super-repellent, or possess a high droplet mobility determined by low contact angle hysteresis ($\Delta\theta$), defined as the difference between advancing (θ_{ADV}) and receding contact angles (θ_{REC}). These angles refer to the angles formed at the leading and trailing edges of a droplet as it rolls off of a given surface (See Figure 3b), the closer the values are ($\Delta\theta \rightarrow 0$) implies a more mobile droplet.

Analyzing droplet sliding, or roll-off, the force of gravity must be brought to bear as it is the primary force which propels droplet motion when they are placed on a tilted surface; resulting in the important self-cleaning properties of these repellent surfaces. To quantify this behavior, the dimensionless Bond (Bo) number sheds insight, forming a ratio of gravitational body forces and surface tension forces:

$$\text{Bo} = \frac{\rho g r^2}{\gamma_{\text{LV}}}, \quad (1.5)$$

where ρ is the fluid density, g is gravitational acceleration, and r is the droplet radius. This implies that surface tension will be dominant when $\text{Bo} < 1$ for liquid droplets. The sliding angle α can be further quantified by the equation (26; 27),

$$\sin \alpha = \frac{2r\gamma_{\text{LV}}(\cos \theta_{\text{REC}} - \cos \theta_{\text{ADV}})}{\rho V g}, \quad (1.6)$$

where θ_{ADV} and θ_{REC} are the advancing and receding CA, respectively, and V is the liquid droplet volume. This equation demonstrates the critical factor in droplet mobility is not high CA, but rather low *CA hysteresis*.

In general, surface roughness will enhance the affinity, or aversion, of a surface to fluids (Figure 3c, d). For generating super-repellency to lower surface energy fluids, such as oils, the concept of surface roughness must be refined (28). A reentrant morphology is required such that the solid interface of the surface actually curves away from the advancing fluid/vapor interface. Reentrant is a term borrowed from mathematics, referring to a function that curves back in on itself; in our case, *reentrant* refers to surfaces with receding surface features. This type of morphology requires greater energies to fully wet the surface, and as such, wetting is thermodynamically unfavorable, resulting in a metastable equilibrium.

1.3.2 Conductivity

Of importance for a significant portion of this work is that of electrically conductive nanomaterials. As stated earlier, graphitic materials such as GNP and CNF are prized for their ballistic electron transport, made possible by a *quasi-metallic* carbon lattice conductivity (29). This unique property enables them to impart excellent electronic conductivities via their incorporation in polymer composites.

Percolation theory (30), a mathematical description for the behavior of connected clusters in a larger group, is helpful for explaining the imparted properties of graphitic materials embedded in an otherwise nonconducting medium. A conducting site can be considered to have a probability p that it will have another connecting site, there is a probability of $1 - p$ that it will not have a connecting site. Thus, there exists a critical probability, p_c , below which the percolation pathway through a lattice will be either closed (0 probability, $p < p_c$), or open (1)

if $p > p_c$. By varying the conductive filler content and analyzing their respective performances, ideal ratios can be arrived at, and p_c can be determined.

In an interconnected medium such as we find by dispersing conductive particles in polymer, each connection will increase resistance slightly. As such, the percolation pathways of electronic current will always be the path of least resistance (*i.e.*, energy minimization). The low resistances of graphene assists greatly in maintaining overall low electrical resistance in the composite.

The resistances presented herein are all in terms of *sheet resistance*, R_s . Made possible due to the electrically conducting composites having relatively uniform thickness. Resistance can be defined as:

$$R = \frac{\rho}{t} \frac{L}{W} = R_s \frac{L}{W}, \quad (1.7)$$

where ρ is the volumetric resistivity of the material, and t is the composite thickness ($\rho = R_s t$). L and W are the length and width of the composite, respectively. Sheet resistance can thus be determined using a 4-probe measurement of resistance if L and W are equal ($R_s = R$). Typical units for expressing R_s are Ohms per square, or Ω/\square , to distinguish them from units of bulk resistance (Ohms, Ω). The volumetric conductivity σ is simply the inverse of resistivity ($\sigma = \frac{1}{\rho}$) and has units of Siemens per meter, or S/m.

4-probe resistance measurements are used since they are more accurate and appropriate for low resistances, as the current carrying wires are separate from the voltage sensing wires in the impedance circuit. Current-voltage (I-V) curves are also employed to analyze linearity of the

Ohmic resistance in our composites, this is performed using the slightly less accurate 2-probe measurement since it is for determining linearity, and not resistance (slope).

1.4 Nonwovens

Nonwovens are generally fabrics/textiles bonded through any means (*e.g.*, mechanical, chemical, or heat treatment) other than weaving (31). Felt is one of the simplest and oldest of these, typically made from wool (synthetic wool is made from acrylic) fibers that are condensed and entangled together without the use of woven techniques (*e.g.*, looms). Felt is one example of a wide range of nonwovens with manufacturing techniques equally varied.

A more recently developed method of manufacture for polymeric nonwovens is that of *spun-laid* (32). This process requires the polymer to be melted, filtered, and then spun onto a belt by air deflectors. Multiple parameters, such as air speed, belt speed, temperature, and distance-to-belt, among many others, can be tuned to control fiber diameters and pore sizes of the resulting material in one continuous process. The belt then feeds onto a roll, with the polymer fibers rapidly cooling and bonding to one another to create a very repeatable and uniform fiber web. As stated, several factors go into the resultant properties (*e.g.*, fiber diameter, porosity) of the fiber web, but of critical importance is the choice of polymer(s), the material properties of which determine the subsequent ranges of variable parameters for spunlaid production. Depending on the application, it can be advantageous to use bicomponent polymer composite fibers which are made using a blend of two polymers to combine the properties of both into the fiber web for similar reasons to those discussed above.

One such bicomponent (*bico*) spunlaid process is that of spunbond (33), more specifically for this research, polyvinylidene fluoride (PVDF) “islands-in-the-sea” cross-sections (34). In this method, two polymers are extruded together through a conjugate spinneret distributor, with the center polymer forming filament structures embedded within a surrounding secondary polymer resembling islands in cross-section (See Figure 4). The spunbond process offers high throughput and uniformity as well as high fiber strength making it attractive for manufacturing over other nonwoven processes. The feasibility of using islands-in-the-sea fabrication to form high-strength fabrics after bonding has been studied extensively at NCSU, performing significantly better than the segmented-pie approach using either mechanical or thermal bonding methods (35). One key disadvantage of the segmented-pie cross-section over that of islands-in-the-sea is larger fiber diameters, along with inferior fiber properties in general. The challenge is to generate nonwovens with fiber diameters approaching 1 micron from PVDF for filtration applications, which at this point can only be met using the islands-in-the-sea approach. The subsequent choice and incorporation of a secondary polymer component representing the cross-sectional “sea” poses another challenge in designing and fabricating these unique nonwovens. Ideally, this bicomponent mixture should be separable once bonded to generate a pure PVDF nonwoven, although it may be of interest to separately investigate both PVDF-blend and all-PVDF nonwovens generated through the islands-in-the-sea spunbond process.

1.4.1 Piezoelectricity

The piezoelectricity of PVDF, studied as early as 1960 (36), is a by-product of the β -phase crystallinity. This change in crystallinity occurs from the linkages in the polymer which allow for

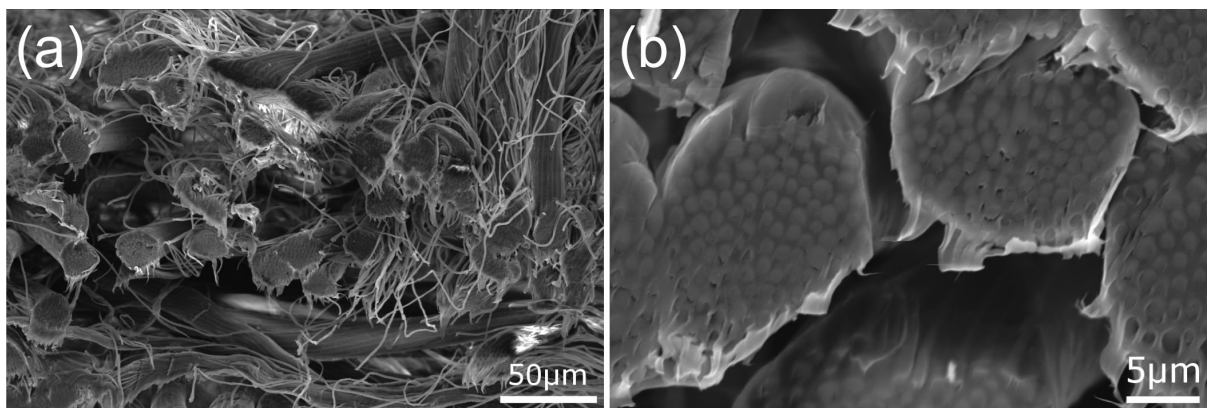


Figure 4. (a) Cross-sectional SEM image displaying PVDF-PE fiber morphologies. (b) Close-up of fiber bundles showing the Islands-in-the-Sea pattern, with the islands (PVDF) surrounded by the sea (PE) in tight bundles with diameters ranging from 20-30 μm and individual fiber diameters approaching 1 micron.

variant orientations. In the α -phase (Figure 5a), dipole moments arising from the arrangement of the atomic elements cancel. In the β -phase (Figure 5b), the entire polymer chain will have a positive (δ_+) and negative (δ_-) opposing charges giving rising to a net dipole moment; more specifically, the fluorine and hydrogen atoms group themselves on either side of the carbon back-bone in the polymer chain. This well-ordered polarity will cause the polymer chain to contract when a voltage is applied across it, or in the reverse, can actually generate a voltage if mechanically deformed. There exists great interest in utilizing this attractive attribute of PVDF for everything from energy harvesting to military drone surveillance equipment which can become airborne by mimicking insect wings (37).

One of the primary challenges associated with harnessing the piezoelectric properties of β -phase PVDF, especially in the case of a nonwoven fabric, is the high-voltage electrical poling required. Electric poling requires voltages on the order of MV/m to orient and organize the polarity in the structure of the fabric web. This is required to produce any piezoelectric response in the fabric via organizing the individual dipole moments *uni-directionally* within the polymer fiber; otherwise, when activated with a current, or attempting to generate a current from mechanical deformation of the fabric, disordered poles will cancel. The challenge of poling PVDF has been well-documented (38), but to-date has only been studied on polymer films or individual fibers (39; 40). Poling of PVDF nonwovens has not been previously reported, nor is there any certainty the nonwovens can withstand such high voltages without physical damage. The small diameters of the fibers ($\sim 1 \mu\text{m}$) may be exposed to temperatures during poling above the T_m of PVDF, and may result in melting or burning.

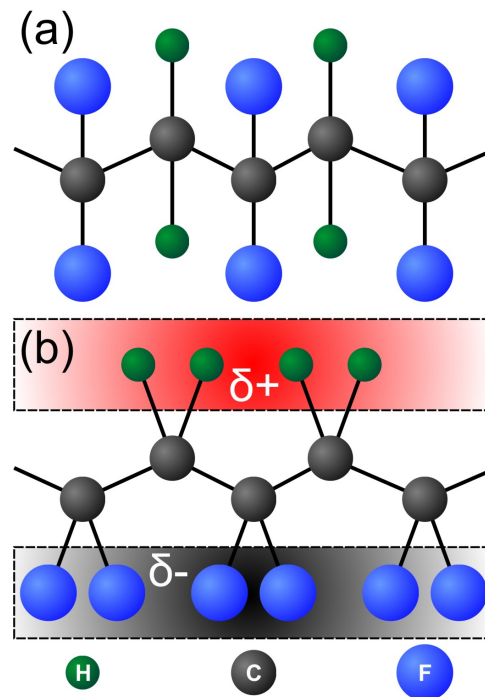


Figure 5. Atomic representation (legend on bottom) of either (a) α -phase orientation of PVDF, or (b) PVDF in the β -phase. In the β -phase, hydrogen atoms are entirely oriented along one side of the carbon ‘back-bone,’ while fluorine atoms are entirely oriented along the opposite side, giving the polymer chain a polarized orientation with an electrically positive charge on the hydrogen side (top, green atoms) and an electrically negative charge on the fluorine side (bottom, blue atoms).

1.4.2 Oil-water Emulsion Separation & Self-defouling Filtration

In regards to fluid repellency, the differences in surface energies between multiple fluids (*e.g.*, oils, water) make possible a selective separation of these fluids when a mixture is passed through an intelligently-designed porous medium. Polymeric nonwovens are used in a number of industries, such as liquid-solid, liquid-liquid, and air filtration applications. Combining the homogeneity and high-throughput of these materials with a tunable wettability has vast potential in liquid filtration; yet, a fibrous nonwoven with piezoelectric properties that could be actuated by an electric current has even greater potential to extend the life-span and efficiencies of these filters. Such a device could self-defoul when the pressure drop reaches a critical threshold, thus reinvigorating a high-performance without requiring filter replacement. Not only would this be applicable in liquid filtration applications, but also that of air filtration and aforementioned energy harvesting applications.

For selective multicomponent fluid separation, tuning the wettability to repel higher surface energy fluids while wetting to lower surface energies has been effectively demonstrated in the literature and in this thesis. Superhydrophobic surfaces, for instance, are often not able to repel lower surface energy fluids such as oils. These surfaces will resist wetting by water, but are easily wetted by oil, even when in a mixture or emulsion. Applying such a surface treatment conformally along the fibers of a nonwoven will enable this material to selectively deny transmission by water through the filter, yet oil will easily pass through. Emulsions contain fine suspended droplets of either water or oil dispersed in another fluid. Their small sizes (*e.g.*, 10–20 μm) make it very difficult to prevent passage of a droplet, even if the fibers themselves

are repellent to the emulsified liquid, since they can easily pass through open pores large enough to accomodate them. Tuning porosity such that passage can be limited to smaller and smaller emulsified droplets will necessarily negatively impact the flux rate, but also improve efficiency (*i.e.*, purity). Balancing these two factors with the design of nonwovens is of critical performance in today's economy, as water and oil shortages are only met with increasing demands world-wide.

1.5 Thesis Objective

The primary objective of this thesis is to explore the feasibility and applicability of large-area, technologically relevant nanomaterial and polymer composites with applications on porous nonwovens. With this objective, the following research topics were considered:

1.5.1 Water-based Superhydrophobic Coatings

- A *water-based* dispersion was formulated consisting of hydrophobic water-based fluoropolymer and nanoclay particles, thus eliminating the use of *volatile organic compounds*, to generate a spray-cast superhydrophobic fluid barrier treatment;
- Optimize the polymer and particle ratios such that they form a durable high-performance superhydrophobic coating;
- Demonstrate tunable properties on nonwoven media such as fiber diameter and porosity;
- Characterize the dependence of wettability on water intrusion pressures for relevant disposable nonwoven fabrics.

1.5.2 The Fluid Diode

- Characterize a fluid gating device analogous to the electronic diode, wherein fluid flow (*i.e.*, current) can be rectified in one direction;
- Optimize the coating weight (in gsm) to show the tunability of the operational ranges;
- Explore applications for the novel fluid device;
- Demonstrate selective separation of multi-component fluid mixtures (*e.g.*, oil-water) based upon surface energy differences.

1.5.3 Fluorine-free & Water-based Superhydrophobic Compositions

- Formulate a *water-based and fluorine-free* dispersion consisting of weakly hydrophobic water-based polyethylene co-polymers and titanium dioxide particles, thus eliminating the use of *volatile organic compounds and fluorinated compounds*, to generate a spray-cast superhydrophobic fluid barrier treatment;
- Optimize the polymer and particle ratios such that they form a durable high-performance superhydrophobic coating;
- Characterize the crystallinity of the polymer with the addition of particle filler content;
- Characterize particle aggregation and surface adsorption kinetics as determined by particle phase, dimensions, and dispersion pH.

1.5.4 Graphene Composites for Conductive Paper Applications

- Characterize a novel composite from combining multilayer graphene (MLG) nanoparticles in an artists' acrylic paint;

- Determine durability, conductivity, and flexibility of the composite for conductive paper applications;
- Assess the performance of the conductive composite for THz radiation absorption and attenuation;
- Design a simple circuit to assess efficacy in paper-based electronics.

1.5.5 Elastomeric & Conductive Superhydrophobic Composites

- Characterize a highly-elastic composite composed of carbon nanofibers in a paraffin wax and polyolefin polymer medium (ParafilmTM);
- Determine electronic performance and recovery of the composite through extreme strain cycles;
- Determine water repellency performance and recovery of the composite through extreme strain cycles;
- Analyze efficacy of material for smart fabric applications (*i.e.*, wearable electronics).

1.5.6 PVDF Nonwovens

- Characterize novel PVDF-blend nonwovens fabricated using bicomponent spunlaid processing, “islands-in-the-sea” cross-sections;
- Determine fiber fibrillation (1 μm fiber dia.) and nonwoven porosity for filtration applications;
- Determine fiber crystallinity, presence of β -phase PVDF;

- Electrically pole fabrics to determine piezo-responsiveness (energy-harvesting, self-defouling).
- Measure flux and filtrate purity to assess potential in emulsion separation of oils relevant to petrochemical industries.

1.6 Scope of the Work

Approaches to functionalizing nonwoven or porous media through the addition of a nanomaterial/polymer composite are investigated. Among the demonstrated functionalities are fluid repellency, electrical conductivity, and elasticity; in some cases, a combination of these properties are demonstrated. In certain instances, the composites are investigated independently, but with the end-goal of incorporation on nonwoven porous media. The composites investigated are all polymeric and universally substrate-independent, developed based on their surface energy, adhesion, and/or elasticity. The choice of nanomaterial used in composites is application-specific, and varies with each composite. In general, all of the nanomaterial composites were designed for the purpose of adding tunable surface functionality high surface area materials.

The work begins with tuning the intrinsic wettability of a set of ubiquitous nonwovens to improve resistance to water pressures in Chapter 2. The initial work involved characterization of one of the first-ever, completely water-based ($> 97\%$) dispersions for generating superhydrophobic surfaces. It was considered germane to test this novel composite on commercially available materials, while conducting an in-depth investigation into the correlation, if any, between water repellency and water resistance. The next step in the natural progression of these developments was to utilize such environmentally-benign coatings in a device platform, which is detailed in Chapter 3. The fluid diode is a liquid gating device made possible by a thin fluid

barrier applied onto one side of a porous media. As will be discussed in Chapter 3, the choice of both the fluid barrier and porous media is entirely arbitrary, as the mechanism is independent of these. A water-based superhydrophobic coating was used in this case to underscore the large-scale environmentally-benign feasibility of this method on industrial scales. The water-based work set the stage for a more challenging task, that of removing the fluorinated chemistry from super-hydrophobic dispersions, and creating an entirely water-based and fluorine-free formulation for generating robust fluid barriers, as detailed in Chapter 4. For this undertaking, polyethylene copolymers were combined with hydrophilic nanoparticles (TiO_2), representing the first-ever translucent-white nonfluorinated, water-based superhydrophobic coating.

From the knowledge gained through manipulation of filler particles and polymeric matrices, my work progressed into developing nanocomposites for conductive functionality, which can also double as radiation shielding devices and conductive paper-based electronics as described in Chapter 5. For this, exfoliated graphite nanoparticles (multilayer graphene, MLG) were dispersed in pthalo green acrylic artists' paint medium for high-adhesion and additional doping effects imparted by the pigment nanoparticles, copper phthalocyanine. The primary tenet of this work was to take a common material, such as artists' paint, and find novel uses in electronic device applications. Another example of incorporating common materials to achieve high performance and maintain low cost is included in Chapter 6, where ParafilmTM, a common vapor barrier film used in most modern research laboratories has been solution-processed with carbon nanofibers to form highly elastomeric and conductive superhydrophobic coatings. The performance of this particular composite far exceeds current benchmarks in industry and the

literature for similar devices. Thus, further strengthening the case for engineering nanomaterial composites using well-established materials to produce low-cost, large-area coatings and devices.

While much of the focus of the aforementioned works is in composite coatings, the substrates chosen for testing were all nonwovens, or similar porous media. Novel nonwovens are investigated independently in Chapter 7, fibers of which are polymer composites of PVDF and either polyethylene (PE) or polylactic acid (PLA). These fabrics were assessed in terms of their independent functionality, and a number of tunable properties added through the addition of conformal nanocomposites. Such properties include tunable wettability (oils, water, *etc.*), electro-conductivity, elasticity, and piezoelectricity, among others. Preliminary results for oil-water separation and fiber crystallinity/morphology are presented. As such, this chapter represents the most “in-progress” research of all the chapters, with much of the data scheduled for completion in the months following my final defense.

Finally, conclusions and research contributions from each of the chapters, as well as recommendations for future research, are given in Chapter 8.

CHAPTER 2

WATER-BASED SUPERHYDROPHOBIC COATINGS FOR NONWOVEN AND CELLULOSIC SUBSTRATES

This chapter and its associated appendix (Appendix A) are reprinted (adapted) with permission from Industrial & Engineering Chemistry Research, 53, Joseph E. Mates, Thomas M. Schutzius, Ilker S. Bayer, Jian Qin, Don E. Walldrop, and Constantine M. Megaridis, 222–227, Copyright 2014, American Chemical Society (41).

The intense commercial demand for efficient fluid management (*e.g.*, water barriers) has resulted in a recent proliferation of methods intended to impart liquid repellency to various substrates. Many such methods involve wet-based processing of hydrophobic polymers and thus rely heavily on organic solvents whose properties pose environmental challenges when scaled up from the laboratory bench. The current study presents a one-step, environmentally safe (> 97 wt % water), room-temperature, low-cost, polymer-based technique that imparts superhydrophobicity to commercially relevant porous substrates. The method features aqueous dispersions of a commercially available fluoroacrylic copolymer and hydrophilic bentonite nanoclay and uses spray casting to apply coatings which are subsequently dried in open air to form thin conformal films. Wettability measurements demonstrate that the coating formulation imparts considerable resistance to water penetration in polymeric nonwoven and cellulosic substrates. In addition to the benign environmental impact of the aqueous formulation, all

ingredients are commercially available, thus opening many technological opportunities in this area.

2.1 Motivation

The field of superhydrophobicity has garnered a great deal of interest in recent years with numerous scientific advances propelling its remarkable growth. The intense commercial demand for efficient fluid management (*e.g.*, water barriers) (42; 43; 44; 45) has resulted in the proliferation of methods that impart liquid repellency to various substrates. In some of these techniques, spray-coating has been demonstrated as a viable application tool due to its inherent large-area low-cost capabilities and its substrate independence (46; 47). Although many nonporous, untextured substrates may benefit from superhydrophobic coating treatments (*e.g.*, hulls, exterior walls, *etc.*), in general, many of the envisioned applications are in the textile and nonwovens industries.

Functional nanocomposite films synthesized by wet-processing of polymer-particle dispersions have been widely investigated. Applications of such surface treatments include, among many others, electromagnetic interference shielding (48) and liquid repellency (49; 50; 51; 52). In superhydrophobic coating applications, the dispersion of hydrophobic particles requires harsh organic solvents, such as ethanol and acetone. Despite their functional advantages, organic solvents are environmentally undesirable in large scale industrial processes. Water-based dispersions pose little environmental concern and are therefore of higher technological interest. However, water-based approaches are severely limited in the dispersion and delivery of low-surface energy (hydrophobic) particle fillers. Due to this difficulty, the development of water-based

coating formulations has been rare in the literature. Xu *et al.* (53) reported a one-step superhydrophobic coating method for cotton fabrics based on a modified silica hydrosol formed by cohydrolysis and co-condensation of methyl trimethoxy silane and hexadecyltrimethoxysilane (combined at ~5 wt. %). The size of the modified silica particles was adjusted by changing the ammonium hydroxide and sodium dodecyl benzenesulfonate surfactant concentrations (combined at ~2 wt. %). These researchers reported water contact angles of 151.9° and a water droplet shedding angle of 13° .

In polymer-particle composite coatings, the primary function of the polymer is to serve not only as a matrix for low-surface energy filler particles (51; 54; 55) but also as an adhesion promoter for the film on the underlying substrate. Fluoroacrylic polymer-based coatings have some very attractive properties, such as exceedingly low surface energy, low friction coefficients, repellency to both oil and water, and relatively low permeability to most gases (54). Among fluoroacrylic polymers, perfluoroalkyl methacrylate copolymers (PMC) have been characterized for water as well as oil repellency applications (56). Due to their environmental friendliness, water-dispersed PMC have been approved for industrial use. Although copolymers with a long perfluoroalkyl group demonstrate improved durability, they also raise environmental concerns due to adverse bioaccumulation rates (57) and breakdown into PFA (perfluorinated acids), which may pose toxicity threats. A recent study expressed concern that current maternal concentrations of perfluorooctanoic acid (PFOA) have the potential to cause adverse effects in human offspring (57). Thus, the US EPA invited fluoropolymer manufacturers to gradually eliminate precursor chemicals that can break down into PFOA. The PMC utilized in the present

study was created by industry in response to this EPA initiative and will not break down into PFOA in the environment. Although this copolymer has improved environmental properties due to its short perfluoroalkyl chain, its mechanical properties are compromised.

In general, liquid repellency (as demonstrated by high droplet mobility) is characterized by low-contact angle hysteresis, which is defined as the difference between the apparent advancing (θ_A^*) and receding (θ_R^*) contact angle values (58). Superhydrophobicity ($\theta_A^* \geq 150^\circ$) relies on low surface energy and micro-to-nanoscale hierarchical surface roughness. Most methods used to designate superhydrophobicity are based on nondynamic or quasi-dynamic (ratio of inertia to surface tension forces $\sim 10^{-5}$) contact angle measurements, which is hardly appropriate for designating liquid repellency under realistic situations. However, high θ_A^* values alone are not a reliable measure of liquid repellency (see SLIPS (59) surfaces, rose petal effect (60), *etc.*). In many applications, the coated substrate is expected to withstand more than just a thin film of fluid or a few distributed droplets, therefore a more robust approach and testing method is required to gauge a coating's liquid resistance. Liquid penetration resistance is a good metric for measuring repellency and depends upon substrate morphology and porosity.

This paper demonstrates a water-based superhydrophobic coating for use on, but not limited to, commercially relevant polymeric nonwoven and cellulosic porous substrates. The specific substrates were selected as being representative of a plethora of products in the market, ranging from consumer and industrial tissues and paper towels, to diapers and medical protective fabrics. The coating is a composite of a fluoroacrylic copolymer and hydrophilic bentonite nanoclay that is applied by spray. The use of the hydrophilic filler is counterintuitive but it facilitates the

water-based formulation pursued in this work. An apparatus has been constructed to challenge the substrates with liquid pressures that are slowly increased until reaching the upper limit of resistance to water penetration (*i.e.*, hydrohead). The water-repelling effectiveness of the dry coating is measured in terms of contact angles and hydrohead and is compared for a series of substrates. The study utilizes these water-based polymeric dispersions to reduce substrate effective pore size and solid wettability, with the ultimate goal of raising resistance to externally applied water pressure. In coupling the maximum water penetration data with the metrics of superhydrophobicity, the study sheds light on the connection between liquid repellency and liquid penetration resistance (61) for surfaces modified with successive surface treatments. The results demonstrate that it is possible to achieve a stable, water-based dispersion that achieves superhydrophobicity when applied and dried on commercially-relevant nonwoven and cellulosic substrates. It should be noted that the present composite coatings are not superoleophobic, although the presence of the fluoropolymer may impart some degree of oil repellency.

2.2 Experimental

2.2.1 Substrates

Spunbond/Meltblown/Spunbond (SMS) Nonwoven

SMS nonwovens combine two layers of spunbond with one layer meltblown into a layered fabric product. The SMS used in this study has a basis weight of ~24 g per square meter (gsm), 63% void fraction, and is made of polypropylene fiber.

High-Density Paper Towel (HDPT)

This is an absorbent cellulosic textile made from paper. Unlike cloth towels, paper towels are disposable and intended to be used only once. Paper towels soak up water because they are loosely woven, which enables water to wick between the fibers, even against gravity. The paper towel used herein (Kleenex hard roll towel 50606, Kimberly-Clark Corporation) has a basis weight of 38 gsm and 44% void fraction.

Tissue

This tissue substrate is made by a process named the uncreped through air-dried process (UCTAD). This process (62) eliminates the need for creping, and removes bulk-reducing steps. The tissue used in this article has a basis weight of around 30 gsm and 41% void fraction.

Spunlace Nonwoven

Spunlacing (*i.e.*, hydroentanglement) uses high-speed water jets to entangle fibers, thus promoting fabric integrity. Softness, drape, conformability, and relatively high strength are the major characteristics that make spunlaced products unique among all nonwovens. The spunlace material used in this study is comprised of polyethylene terephthalate (PET) fibers, has a basis weight of 50 gsm, and 58% void fraction.

2.2.2 Materials

Bentonite (hydrophilic) nanoclay particles were obtained from Sigma-Aldrich. The aqueous fluoroacrylic copolymer dispersion (PMC) was obtained from DuPont (20 wt. % dispersion in water; Capstone ST-100). Deionized water was used as a probe liquid for penetration pressure (hydrohead) tests, as well as the contact angle and roll-off angle measurements.

2.2.3 Procedure

To prepare 100 mL of sprayable dispersion, the following steps were followed. Initially, 1.25 g of nanoclay was added to 92.5 mL of deionized water and bath-sonicated for 15 min (Branson 8200, 20 kHz, 450 W). After sonication, a stir bar was added to the dispersion and 6.25 g of the PMC aqueous solution (20 wt. %) was added dropwise under mechanical mixing over the course of 1 min. The PMC was introduced slowly to ensure adequate mixing, as the solution became more viscous during this process. The final nanoclay/PMC dispersions (97.5 wt. % water, 1.25 wt. % PMC, 1.25 wt. % nanoclay) were applied by spray on each substrate. The 50:50 polymer-to-nanoclay solids ratio was chosen on the basis of preliminary qualitative results; increased polymer content significantly reduced surface roughness. Conversely, increased nanoclay content adversely impacted wettability as the clay is hydrophilic and requires a balanced fluoropolymer content to counteract its inherent tendency to absorb water. Likewise, increasing the overall solid content in the final dispersion increases viscosity, in turn, hindering the ability to spray; therefore, the solids wt. % in the dispersion was deliberately maintained below 3% to avoid complications during spraying. An airbrush atomizer (Paasche, VL siphon feed, 0.55 mm spray nozzle) was used to spray the samples from a distance of 15 cm. Water-based spray dispersions pose several challenges as the surface roughness imparted from the particle filler, and needed for repellency, is inhibited by the slow evaporation when the substrate is wetted during spraying. To this end, the spray nozzle was chosen because it offered the finest spray atomization achievable with the employed sprayer, in turn, enhancing water evaporation during spray application. The spray distance also greatly affects coating morphology and deposition

weight and, therefore, was chosen to avoid excessive substrate wetting during spraying, as would be the case if the spray distance were too small, and maximize coating deposition rate, which is reduced at greater spray distances. Care was taken to ensure spray uniformity and control over coating thickness. To determine coating weight and verify uniformity, glass slides were placed within the typical spray area normally occupied by the substrates during spraying. These slides were subsequently weighed on a per spray-pass basis to evaluate uniformity and determine amount of coating deposited in gsm. Each spray pass represented an average of ~ 0.6 gsm of coating applied onto glass slides; this base level was used as a gauge for determining approximate coating deposition onto the nonuniform porous substrates.

2.2.4 Characterization

Each of the samples, coated or uncoated, were characterized for hydrohead resistance and droplet contact/sliding angles. The difficulties in measuring contact angle hysteresis on substrates with roughness features of the same length scale as the test droplet sizes is addressed below as well as in the Appendix. In addition, Scanning Electron Microscopy (SEM) images were acquired to analyze coating levels, coating uniformity, and effective substrate pore size. It should be noted that these soft substrates (all disposable) are not intended for long-term or repeated use, thus attention was paid only to their single-use performance. Nonetheless, the applied coatings did not shed during normal handling.

The applied coating levels were quantified so as to ensure consistent coating properties over the entire sample area ($9.5 \times 7 \text{ cm}^2$). Four spray passes resulted in a uniformly distributed coating mass of 2.4 ± 0.2 gsm over that sample area. At coating add-on levels below 2.4 gsm,

individual droplets beaded upon contact but were absorbed into the underlying hydrophilic substrates after a few seconds. At or above 2.4 gsm, the water droplets remained beaded consistently for a prolonged period without absorption. The 2.4 gsm coating was then tested for all four substrates as the lowest coating level. Two other coating levels were also tested; 4.8 ± 0.2 gsm and 9.6 ± 0.2 gsm. These three coating levels represented light, medium, and heavy add-ons and were within the requirements of industrial applications (preferably below 10 gsm). At the light and medium add-on levels, the coatings were nearly imperceptible and did not change the as-received apparent feel and softness of the substrates. At the heaviest coating level, there is stiffening of the substrates from the increased polymer presence as well as perceptible roughening of the surface from the increased presence of clay particles.

For the hydrohead tests, a simple water column device was constructed; see Figure A1. The apparatus consisted of a 2.5 cm diameter graduated column placed over the 2.5 cm circular sample secured coating-side-up at the bottom of the column. A rubber gasket placed on top of the sample ensured that any liquid penetration would have to occur through the surface coating and then the porous sample itself. The column was slowly filled with water until the first breakthrough (water passed through sample) was visible, at which point, the height of the water column defined the maximum hydrohead (in centimeters head) endured by the sample. For the two hydrophilic samples (tissue, HDPT), water resistance for the uncoated case was naturally zero; water penetrated and absorbed into the sample immediately. The two inherently hydrophobic samples (SMS, spunlace) had nonzero hydrohead values before any coating was applied. Measurements were repeated at least five times (different sample cutouts) for a given

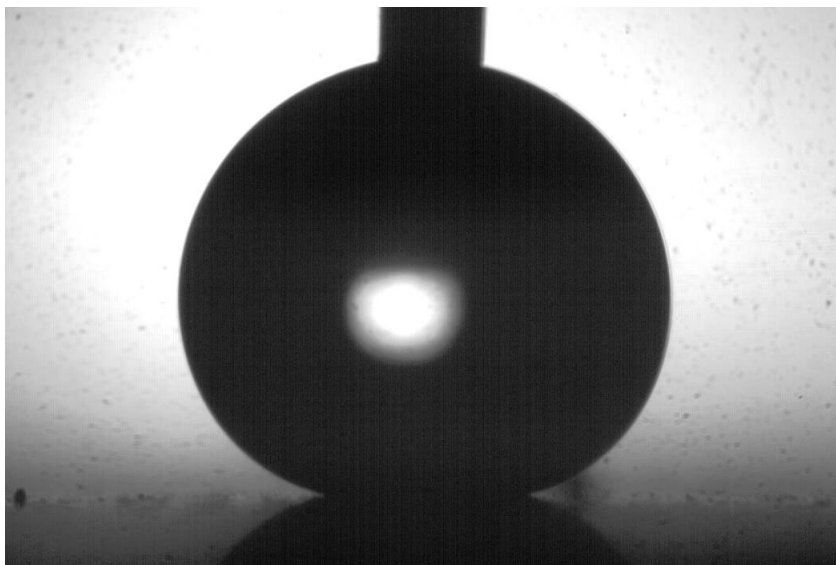


Figure 6. Water droplet dispensed from a flat-tipped needle (top) on a glass slide coated with 4.8 gsm of PMC-nanoclay composite. The needle diameter is 1 mm.

substrate and coating level. Extra care was taken to rule out the possibility of any time-dependence of water breakthrough at rising column pressures, as would have been the case if column pressure was maintained at a given level and the water had time to work its way into, and through, the sample. Thus, if a given substrate was introduced to column pressures below the breakthrough pressure, it could withstand those pressures for a prolonged period. Water column pressure was increased in increments of a few centimeter head at a time and was allowed to remain there for up to 5 min at a time before increasing it further and repeating this process until the limit was reached.

In the determinations of contact angles (CA), the irregularities in surface topography of the substrates made it difficult to obtain accurate and consistent measurements. This is due to the sample having surface features that were not much smaller than the test droplet size, as well as some of the substrates incorporating fibers that extended through the surface treatment, thus obscuring the contact line between droplet and substrate. Sample measurements and images (Table VII) demonstrate the uneven nature of these coated surfaces and demonstrate that even with the substrate texture, rough CA values visibly exceeded 150° (the accepted threshold for superhydrophobicity). To obtain these measurements, $3 \times 1 \text{ cm}^2$ coated sample strips were cut and attached to a glass slide using double-stick tape. To gauge the effectiveness of the coating at different add-on levels, smooth glass slides were sprayed in the exact same manner as the textured test substrates. The latter approach allowed for accurate measurement of the CA (see Figure 6) for a given coating add-on mass without being impeded by surface topography generated in the manufacturing processes of the individual rough substrates.

For sliding angles, the substrate strips affixed to glass slides were placed on a goniometer operated by a small DC servomotor, which allowed precise control as it stepped through small angle increments until the water droplets were seen to roll down the sample. If the droplets did not roll, the coated substrates were deemed “sticky” and were marked with “S” in Table I. The volume of droplets used in these tests was $\sim 10 \text{ }\mu\text{L}$. The dimples and other surface irregularities on a given substrate again interfered with the natural roll-off during these measurements, and caused the significant standard deviations listed in Table I. For SEM observations, a small

area (roughly 0.25 cm^2) was cut from each treated and untreated sample for comparison. The samples were then sputter-coated with a 4 nm Pt-Pd coating to facilitate SEM imaging.

TABLE I

SLIDING ANGLE MEASUREMENTS FOR THREE ADD-ON COATING LEVELS FOR EACH OF THE FOUR SUBSTRATES. IF DROPLETS WERE NOT OBSERVED TO ROLL, THE SUBSTRATES WERE DESIGNATED AS ‘STICKY’ (MARKED WITH AN ‘S’).

	SMS	HDPT	spunlace	tissue
$2.4 \pm 0.2 \text{ gsm}$	S	$28.3^\circ \pm 12.1^\circ$	$27.8^\circ \pm 4.3^\circ$	$30.5^\circ \pm 8.7^\circ$
$4.8 \pm 0.2 \text{ gsm}$	S	$26.6^\circ \pm 5.6^\circ$	S	$23.7^\circ \pm 4.7^\circ$
$9.6 \pm 0.2 \text{ gsm}$	S	$30.5^\circ \pm 10.6^\circ$	S	$25.4^\circ \pm 6.0^\circ$

2.3 Results & Discussion

The four types of substrates featured morphologies that varied according to their manufacture and intended use. SEM was employed to characterize samples before and after coating (Figure 7 and Figure 8). The cellulosic fibers had rough and irregular surfaces (see Figure 7

and Figure 8b,c). In contrast, the polymeric fibers had regular cylindrical geometries with smooth surface features (see Figure 8a,d). Using the SEM images, coating uniformity was verified and the effective pore size was estimated and averaged at several locations across each substrate. The estimates of the minimum and maximum pore diameters (D_{\min} , D_{\max}) were then employed to calculate an approximate theoretical Laplace pressure needed to penetrate the pore from $\Delta P = 2\gamma \cos \theta_A^* (1/D_{\min} + 1/D_{\max})$, where γ denotes the surface tension of water (72 mN/m at 20 °C). Because the exact values of the contact angle cannot be determined on each substrate, but are well within the superhydrophobic regime ($> 150^\circ$), we approximated $|\cos \theta_A^* \approx 1|$. The experimental determination of the Laplace pressure was made from the measured hydrohead (*i.e.*, minimum water column height at which water penetrated the substrate; see the Figure A1). The two values for each substrate are compared in Table II, which shows that the theoretical estimate exceeds the experimental value by an order of magnitude. This discrepancy is attributed to the underestimation of the maximum pore dimension from the SEM images; large pores critically influence the hydrohead, and due to their isolated presence could be difficult to detect by SEM when analyzing sample areas significantly smaller ($\sim 0.25 \text{ mm}^2$) than the surface area challenged during hydrohead pressure measurements (5.07 cm^2). Nonetheless, the data in Table II clearly indicate a correlation between pore size and penetration pressure; as the former grows, the latter is reduced. This supports the hypothesis that pore morphology is the primary factor in designating water barrier resistance. The effective pore size of each substrate was reduced by the coating addition, thus causing an increase in hydrohead resistance.

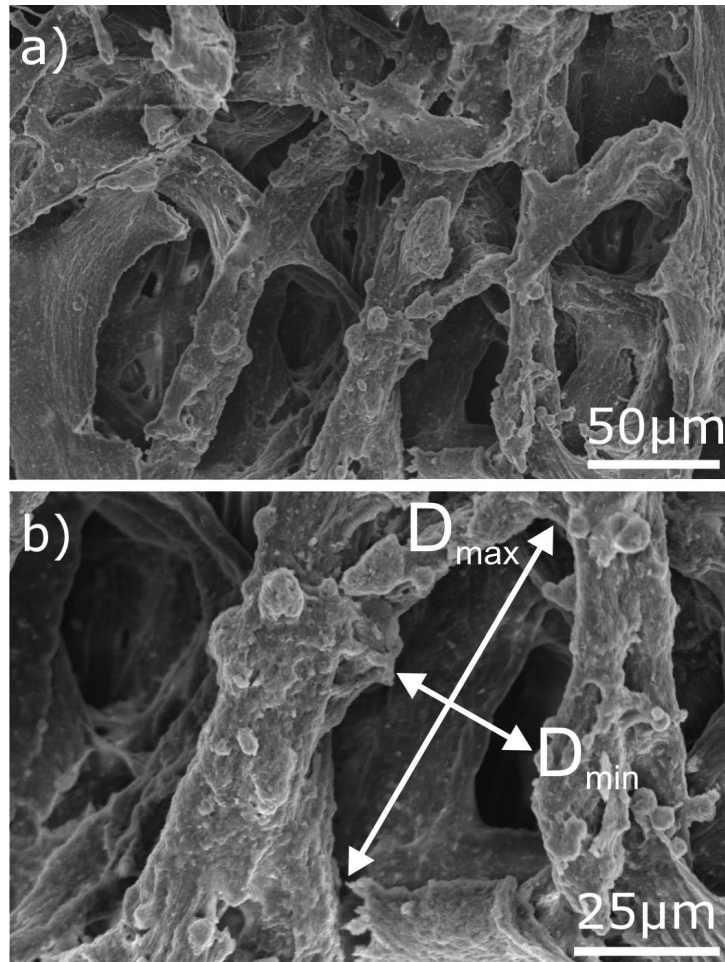


Figure 7. (a) SEM image displaying porosity of HDPT coated with 4.8 gsm PMC-nanoclay. (b) Depiction of how effective pore size (orthogonal maximum, minimum diameters D_{max} and D_{min}) was determined to calculate the theoretical Laplace pressure needed to push the liquid through the pore.

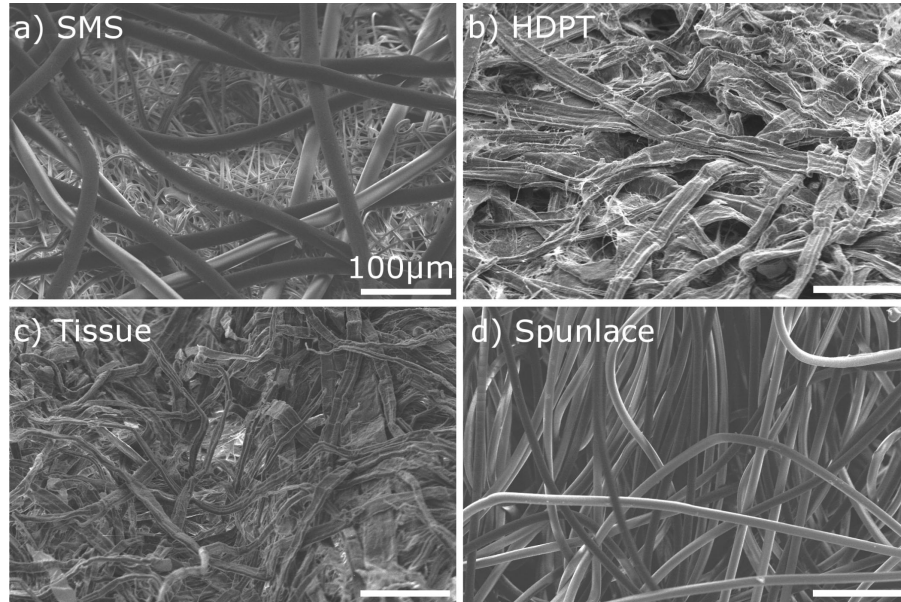


Figure 8. Substrate landscape: SEM images of four uncoated substrates at the same magnification. The scale bar applies for all images. (a) SMS, hydrophobic substrate. The spunbond polypropylene fibers can be clearly discerned from the meltblown fibers beneath, which have much smaller diameters. (b) HDPT, hydrophilic substrate. The density of these fibers presents an advantage in water resistance after coating. (c) Tissue, hydrophilic substrate. Although very similar to HDPT, these fibers are slightly smaller and less dense but weaker in terms of mechanical strength. (d) Spunlace, hydrophobic substrate made of PET fibers.

TABLE II

LAPLACE PRESSURE CALCULATIONS FOR ALL FOUR SUBSTRATES, AS BASED ON PORE SIZE RANGES ATTAINED FROM SEM IMAGE ANALYSIS FOR A 2.4 GSM COATING AND COMPARED WITH EXPERIMENTAL VALUES DERIVED FROM HYDROHEAD MEASUREMENTS. ALL COATING LEVELS LIE WITHIN THE SUPERHYDROPHOBIC RANGE WITH MINIMAL DEVIANCE.

Substrate	D _{min} range (μm)	D _{max} range (μm)	theoretical Laplace pressure (kPa)	experimental hydrohead (kPa)
SMS	5–10	20–25	20–36	3.4 ± 0.4
HDPT	10–25	40–80	8–18	1.7 ± 0.1
spunlace	15–25	40–65	8–13	1.3 ± 0.2
tissue	25–40	70–85	5–8	0.5 ± 0.2

Figure 9 presents the hydrohead data for each of the four substrates in their uncoated state as well as with light (2.4 gsm), medium (4.8 gsm), and heavy (9.6 gsm) coatings. The addition of the superhydrophobic coating consistently increased water resistance. However, when CA is compared against coating thicknesses (Table III), the trend is not clear. Even for the light coating (~ 2.4 gsm), very high contact angles were observed, and these increased only slightly for

the medium coating, while remaining approximately the same for the heavy coating. The first two substrates (SMS and spunlace) are inherently hydrophobic, with precoat water resistance values given by the black bar in Figure 9. The relatively slight increase in water resistance for each coating level on SMS is regulated by the smaller pore sizes of the middle, meltblown, layer. As shown in Figure 8a, the meltblown fibers and their spacing are much smaller with respect to the two outer, spunlaid layers and constitute the primary factor affecting the substrate's inherent water resistance (~ 32 cm). The coatings were applied only on the outer layer and reduction in that larger pore size due to coating did not impact, other than superficially, the inner layer's effective pore size. The tissue and HDPT substrates were wettable as-received and their initial water resistance was thus zero (Figure 9). An initial jump in water resistance was seen after a light coating (~ 2.4 gsm) on all substrates, and subsequent less pronounced increases were seen for spunlace and HDPT as the coating levels were doubled. The jump in water resistance for tissue from the low to the middle coating level (2.4 to 4.8 gsm) may be due to an initial mechanical weakness of this substrate. As pressure was increased, the induced curvature of the softer substrate could cause fibers to stretch and pores to widen. The added coating actually strengthened the robustness of the fibers, thus not permitting deformation of the intrinsic pores. Overall, the addition of increasing coating levels for a given substrate imparts optimal hydrohead performance before the coating begins to inhibit the properties of the material (*e.g.*, breathability). After a certain point, the addition of more coating material becomes counterproductive; the goal of applying such coatings is to create the best performance with the least expenditure of material and resources. Although the measurement of contact

and sliding angles are critical to assessing superhydrophobicity, imparting barrier resistance by spraying an aqueous dispersion was a focal point of this study. A secondary goal was to examine the relationship between increasing hydrophobicity and water barrier resistance. The data suggests that superhydrophobicity is entirely dependent upon surface energy and roughness, and can be achieved with a minimal coating add-on. On the other hand, water resistance is entirely dependent on substrate porosity and can be enhanced only through coating add-on insofar as the pore sizes are reduced (see Table VIII).

TABLE III

SESSILE CONTACT ANGLE MEASUREMENTS ON GLASS SLIDES COATED WITH THE SAME ADD-ON LEVELS AS THE CELLULOSIC AND NONWOVEN SUBSTRATES

coating weight	2.4 ± 0.2 gsm	4.8 ± 0.2 gsm	9.6 ± 0.2 gsm
CA on glass slide	$158.8^\circ \pm 4.5^\circ$	$166.2^\circ \pm 1.4^\circ$	$155.3^\circ \pm 7.5^\circ$

After analyzing the sliding angles for each substrate in Table I, it became evident that some of the substrates displayed poor sliding angle performance while possessing extremely high CA's and, more importantly, excellent resistance to water pressures. SMS maintained the highest

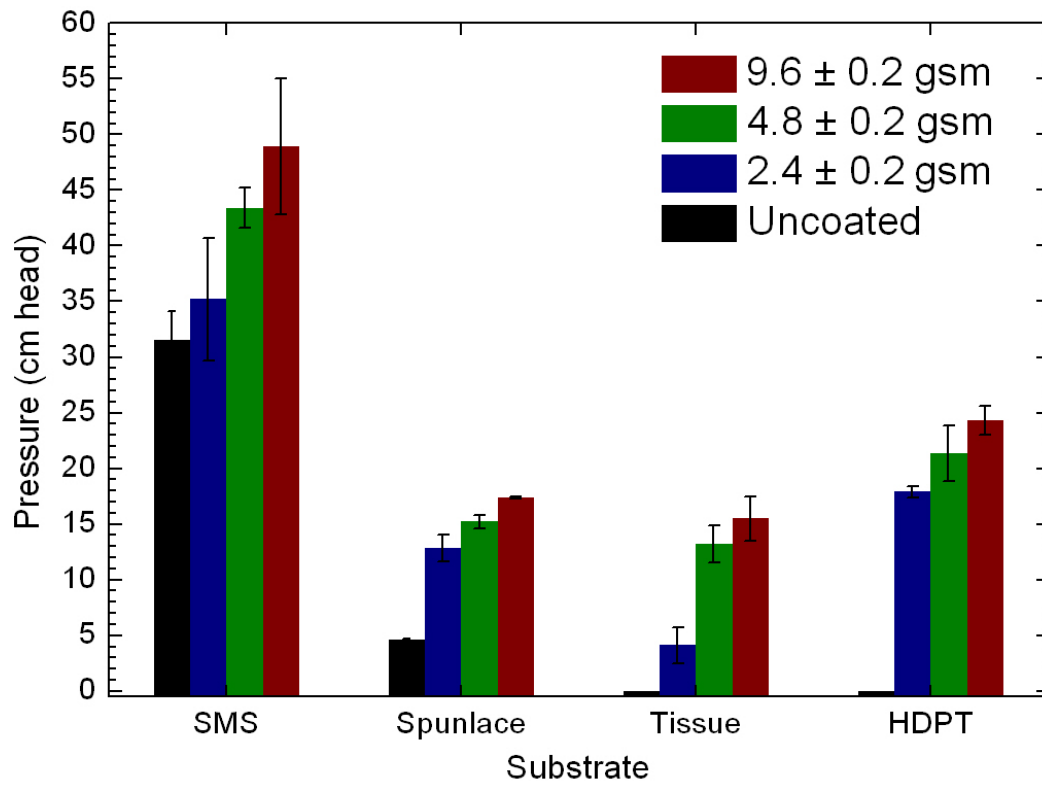


Figure 9. Experimentally measured water penetration resistance (hydrohead) for each substrate at three coating levels: 2.4 ± 0.2 , 4.8 ± 0.2 , and 9.6 ± 0.2 gsm. The first two substrates, SMS and spunlace, are inherently hydrophobic and have a nonzero water resistance as received (uncoated). The other two substrates are hydrophilic, and thus have zero resistance in their uncoated state.

water resistance from the outset, yet it was observed to be “sticky” by measure of droplet roll-off angles. Figure 10 shows the nonuniform coating of SMS compared to that of HDPT, a hydrophilic substrate. The water-based coating had difficulty spreading across the hydrophobic SMS fibers, thus leaving whole or partial fibers exposed during the curing process (Figure 10a). This causes water droplets to stick when moving over or resting across these features of varying surface energies, and does not allow for a consistent coating of the fibrous pore after successive coatings. This also accounts for the poor water droplet mobility, and the relatively minimal increase (when compared with the other three substrates) in hydrohead performance from light to heavy coatings (Figure 9). Although select materials may possess some aspects of both super-repellency and water resistance, these properties are mutually exclusive and one does not necessarily guarantee the other. The effective pore size of each substrate, determined by fiber spacing and diameter, is ultimately the limiting factor in designating water resistance.

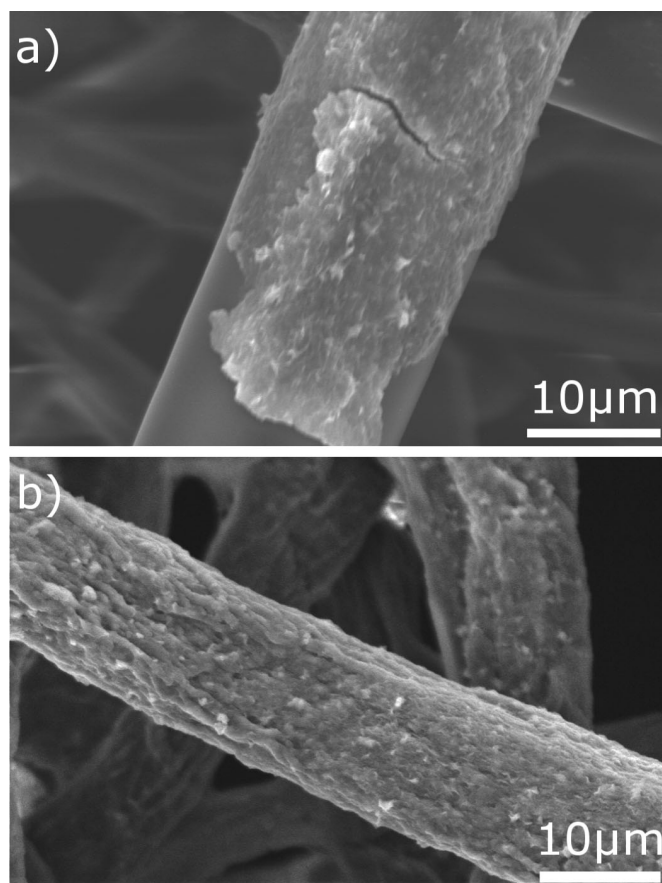


Figure 10. SEM images of SMS and HDPT substrates with 2.4 gsm (light) coating. (a) SMS fiber from the top, spunbond, layer displaying nonuniform coating; the raw fiber can be seen underneath the clay/polymer coating. (b) HDPT fibers are completely and uniformly covered with the light coating.

CHAPTER 3

THE FLUID DIODE: TUNABLE UNIDIRECTIONAL FLOW THROUGH POROUS SUBSTRATES

This chapter and its associated appendix (Appendix B) are reprinted (adapted) with permission from ACS Applied Materials & Interfaces, 6, Joseph E. Mates, Thomas M. Schutzius, Jian Qin, Don E. Waldrup, and Constantine M. Megaridis, 12837–12843, Copyright 2014, American Chemical Society (63).

Many important applications in fluid management could benefit from unidirectional transport through porous media via a simple, large-area, low-cost coating treatment; in essence, a fluid diode demonstrated herein for water using common cellulosic paper substrates. In electronics, the diode is an electrical component with asymmetric current transfer characteristics. A light ($< 2 \text{ g/m}^2$) superhydrophobic conformal coating applied onto *one side* of a porous substrate is shown to create a liquid transport function analogous to the electronic diode, facilitating fluid movement in one direction under negligible penetration pressures, but opposing it in reverse up to greater pressures. The phenomenon is driven by capillary action and can be observed using any similarly-thin fluid barrier applied on only one side (*i.e.*, wettability contrast) of an absorbent porous matrix. Diodic action and liquid transport rates are shown to be highly tunable, determined by fiber diameter and spacing, in combination with coating deposition amount. As an example, the device is used to separate an oil/water mixture, relying

upon the surface tension differences of the mixture constituents, and may be implemented in multicomponent fluid filtration/ separation technologies.

3.1 Motivation

The concept of the electronic diode has numerous analogues in fluid management, as the control and rectification of fluid flow is critical for commercial and industrial applications (*e.g.*, check valves) and necessary for life itself (*e.g.*, veins) (64). The diode is an electrical component with asymmetric current transfer characteristics: low resistance in one direction, ideally zero, and high resistance in the other, ideally infinite. Recent literature has extended this concept of diodicity into the realm of microfluidics: the thermal diode (65), relying on a pair of parallel/opposing super-hydrophobic/hydrophilic surfaces under an applied temperature gradient to induce heat transfer in one direction via jumping droplets; valve-less micropumps (66), utilizing flow rectifiers to generate a net flow in one direction; and superhydrophobic asymmetric ratchet structures (67), harnessing the Leidenfrost effect for unidirectional droplet transport via vapor flow rectification. A similarly titled paper (68) also exploited open-surface patterned hydrophilic channels on a hydrophobic background for fluidic logic circuits in single-use lab-on-a-chip applications. While these examples highlight analogous diodic behavior, the present device is novel. In addition, due to its inherent simplicity in terms of both fabrication and implementation, the present device is expected to be attractive for wide use in industrial and commercial applications. It is shown that the controlled application of a superhydrophobic treatment onto one side of an absorbent porous substrate imparts tunable fluid diodicity, made possible by competing capillary forces.

The fluid diode is demonstrated herein using a spray-based coating fabrication approach, yet the underlying mechanism requires only a thin, uniform fluid barrier applied onto *one side* of an absorbent (*i.e.*, wicking) porous substrate. The wettability contrast between the coated and uncoated sides of the substrate encountered by the fluid governs fluid flow, or lack thereof, through the material. The degree of repellency and thickness of the fluid barrier, as well as the structure of the porous solid, collectively determine performance (diodicity) of the fluid diode. A water-based superhydrophobic coating formulation (69) is used herein, solely to emphasize the low environmental impact and industry-ready nature of this approach, yet other liquid repellent coatings would behave similarly. Neither the barrier nor the substrate is unique to the operation of diodic fluid transport; greater pressure regimes can be achieved by choosing a substrate of finer pore dimensions than that of the present cellulosic substrates (41).

The development and application of functional superhydrophobic nanocomposite coatings applied by spray have been well investigated due to their low-cost, large-area capabilities (49; 70; 47; 71; 55; 72). There is great industrial interest to utilize such coatings in the areas of smart fabrics (73), filtration (74), pumpless transport (75), and enhanced heat transfer (76). In general, these surface treatments are deposited with the goal to impart water resistance and self-cleaning characteristics (apparent contact angle (CA) $\theta^* > 150^\circ$, droplet roll-off angle $< 10^\circ$) (77). It is reported that, at sufficiently low add-on levels, specifically those below 2 g/m² (gsm), of a superhydrophobic polymer-nanoparticle composite coating acting as a thin fluid barrier, fluid flow through the underlying porous hydrophilic substrate occurs under low hydrostatic pressures when the liquid encounters the nonwetable coating first, yet fluid flow

through the same system is opposed up to greater penetration pressures (*i.e.*, diodic function) if the liquid first encounters the substrate from the opposite (wetable) side. This disparity in the hydrostatic pressures necessary to force the liquid through the porous matrix is the foundation for fluid diode operation.

3.2 Experimental

3.2.1 Substrates

The porous solids used in this study are common paper towels. Paper towels are absorbent cellulosic textiles made from paper and, unlike cloth towels, are disposable; intended to be used only once. Paper towels soak up water because they are loosely woven, enabling water to wick between the fibers, even against gravity. The paper towels used in this study were Kleenex[®] hard roll towels (High-Density Paper Towels; HDPT) and Scott[®] Paper Towel (SPT) (Kimberly-Clark Corp, USA); these two materials were chosen for their low-cost and ubiquitous presence in the marketplace. However, the diode mechanism is substrate-independent and only requires the substrates to be absorbent; they must possess wettable fibers, pores, or channels that allow for fluid wicking by capillary action. If the diode action observed with water is to be repeated for oils, any substrate wettable by oil can be used in conjunction with a thin *superoleophobic* coating applied on one side; the mechanism will remain the same and is to be the subject of future work. For the purposes of this article, displaying functionality on disposable and ubiquitous materials with an environmentally benign coating underscores the inherent simplicity of the mechanism. The present technique can be implemented and further enhanced on more sophisticated substrates possessing specific characteristics, as will be discussed below.

Moreover, while oil-water separation has been demonstrated elsewhere using similar superhydrophobic treatments on porous media (78), it is also shown below that the present coating coupled with a cellulosic substrate can separate, not just oil from water, but also water from oil if the substrate is properly primed.

3.2.2 Materials

Bentonite (hydrophilic) nanoclay particles were obtained from Sigma-Aldrich (Product # 682659). The aqueous fluoroacrylic copolymer dispersion (PMC) was obtained from DuPont (20 wt. % dispersion in water; Capstone® ST-100). Deionized water was used as a probe liquid for characterization, and colored with blue food dye to visualize oil/water separation. Hexadecane dyed with Oil Red O, both obtained from Sigma-Aldrich, was used to demonstrate and visualize oil/water separation.

10 mL of sprayable dispersion was prepared as follows. Initially, 0.125 g of nanoclay was added to 9.25 mL of deionized water and bath-sonicated for 15 minutes (Branson 8200, 20 kHz, 450 W). After sonication, a stir-bar was added to the dispersion and 0.625 g of the PMC aqueous solution was added drop-wise under mechanical mixing over the course of 1 min. to ensure adequate mixing, as the solution became more viscous during this process. The final nanoclay/PMC dispersions (97.5 wt. % water, 1.25 wt. % PMC, 1.25 wt. % nanoclay) were applied by spray onto each substrate using an airbrush atomizer (Paasche, VL siphon feed, 0.55 mm spray nozzle) from a distance of 25 cm. Each spray-pass represented an average of ~0.5 gsm of conformal coating add-on applied in the typical spray area ($9.5 \times 7 \text{ cm}^2$). Add-on level was measured by placing glass slides within the spray area, which were then weighed after every

pass to determine average coating add-on weight and variance (See Appendix B); this base level was used as a gauge for determining approximate coating deposition onto the spatially non-uniform cellulosic substrates under similar conditions. After spraying, the samples were allowed to dry in open air overnight at room temperature.

An added benefit of the present superhydrophobic treatment (41) is that the sprayable dispersion is comprised of 97.5% water (See Figure 6, Table IX in Chapter 2, and Appendix B, respectively, for CA characterization), thereby reducing the adverse environmental impact intrinsic to the synthesis of harsh solvent-based superhydrophobic formulations, and is thus more attractive for industrial implementation. The fluoroacrylic copolymer (PMC) used in this study was created by industry in response to an initiative set forth by the EPA in 2006 to reduce the length of perfluoroalkyl groups in these copolymers, thus eliminating precursor chemicals that could break down into perfluorooctanoic acid (PFOA) (79).

3.2.3 Characterization

The paper towel samples were sprayed on one side only with increasing coating levels ranging from 0.5 gsm to 8 gsm. To demonstrate diodicity, hydrostatic pressure tests (hydrohead; see Appendix A, Figure A1) were performed for the same coating weights with the coating up (CU) or coating down (CD), representing forward or reverse flows, respectively (see Figure 11). Thus, diodicity is confirmed if there exist separate and distinct hydrohead thresholds determined by the orientation of the coated side (up or down) for the same coating add-on level. Without any surface treatment, the threshold pressure is naturally zero for both substrates, as water

immediately penetrates into and through the paper samples due to their as-received natural absorbency.

3.3 Results & Discussion

As can be seen in Figure 12 when testing CU, the coating add-on levels below 1 gsm for HDPT, and below 1.5 gsm for SPT, allow water penetration immediately through the samples under negligible applied pressures; the coating offers near zero penetration resistance. For these lower add-on levels, any water volume greater than a small droplet (10–30 μL) resting on the coated surface is instantaneously absorbed; this is due to insufficiently coated hydrophilic fibers creating an avenue for the wicking of water *through the coated layer*. Under the same add-on levels, Figure 12 shows that the CD orientation delivers non-zero resistance at even the lowest coating of 0.5 gsm for both HDPT and SPT. At this coating level and orientation, the hydrohead threshold is 13.9 ± 4.8 cm for HDPT and 3.9 ± 0.8 cm for SPT (the reduced resistance of SPT is due to its larger fiber spacing, see Figure C1). The maximum CD-CU pressure disparity was observed at 1 gsm for both substrates, with a difference of ~ 16 cm head for HDPT and ~ 6 cm head for SPT, both strongly favoring the CD orientation. These numbers are bounded by the intrinsic Laplace pressure of the effective pore radii (41), or fiber spacing, in the substrates. At heavier coating levels, the mm-thin substrates become almost entirely hydrophobic due to the absorption of the low surface energy polymer during spraying. Consequently, the threshold pressures for CD/CU converge in Figure 12 as substrate repellency becomes more uniform. Nonetheless, it is important to note that much higher pressure CD/CU differences could be attained by using other porous substrates that feature smaller fiber sizes and much tighter

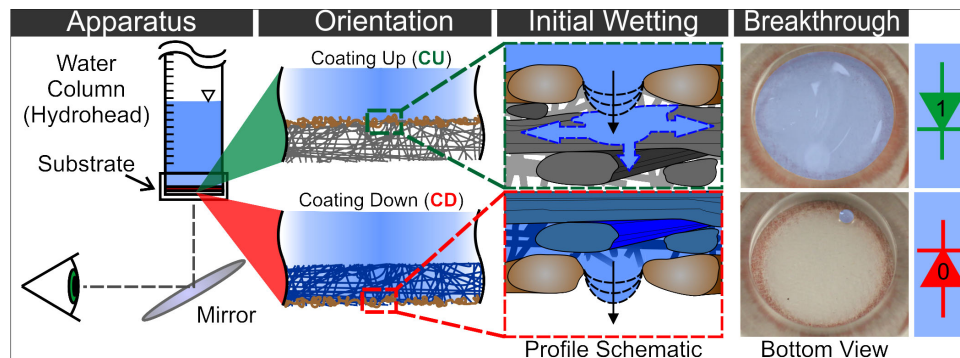


Figure 11. The Fluid Diode: Depending on the relative orientation of the liquid-repellent coating with respect to the porous wettable solid and the water column (blue) used to impose hydrostatic pressure, the transmission of water through the system will register as a 1 (fluid transmission, coating up, CU in green) or 0 (no fluid transmission, coating down, CD in red), similar to the function of an electronic diode. The CU schematic (top) displays a coated pore under pressure during the initial phase of fluid penetration and a sagging water interface movement (dashed black line in profile schematic). As pressure increases, the sagging water meniscus extends to the depth of the next uncoated fiber and once contact is made, fluid wicks through to the underside, imposing no further resistance to the water column above and forming a water film over the entire underside of the substrate *after the penetration pressure has been surpassed* (shown in the bottom view, right). For the CD case, the substrate is completely saturated with water before filling the coated pore; as the sagging water interface extends down under increased external forcing, the threshold pressure is generally much higher than that of CU due to the lack of any additional wettable material in the vicinity beyond the fluid barrier. Eventually, the emerging liquid forms a droplet once the Laplace pressure of the largest pore(s) is exceeded (droplet seen in bottom view, right).

fiber structures, both translating to higher Laplace penetration pressures, and thus improved diodicity.

Figure 13 shows an SEM cross-section of HDPT in the center, analogous to the simplified profile schematic in Figure 11. Visible along the upper fiber surfaces, the coating conforms to the fibers and effectively limits access to water except through the fiber spacing, or coated pores. The Figure 13 insets clearly show the difference in surface texture between a coated (left) and an uncoated (right) fiber surface along with accompanying EDS (energy dispersive X-ray spectroscopy) data verifying the presence of the fluoropolymer coating constituents on the top side. The polymer/clay nanocomposite coating is spread evenly over the top surface fibers; the fluoropolymer film greatly reduces the surface energy (~ 16.4 mN/m based on probe liquid CA measurements, see Appendix B for Owens/Wendt calculations (80)), while the nanoclay features along the intrinsic fiber morphology create a hierarchically-textured surface ideal for superhydrophobicity (See Figure C1 and Table X for additional SEM images of both substrates; Figure C1 offers a comparison of fiber size and spacing for both substrates, while Table X shows images of a single HDPT pore after successive coating applications).

Referring again to Figure 11, the water absorption mechanisms for CU and CD orientations are compared; as hydrohead pressure increases and water is forced into the nonwetable coated layer in both cases, the curvature (*i.e.*, sagging) of the water meniscus increases (see dashed black curves in Figure 11, profile schematic) between the fibers, or pore cross-section. Analogous to an electrical circuit, the “flow,” or current, will be in the direction in which the water is introduced over the substrate. The surface that the water encounters first, either the repellent

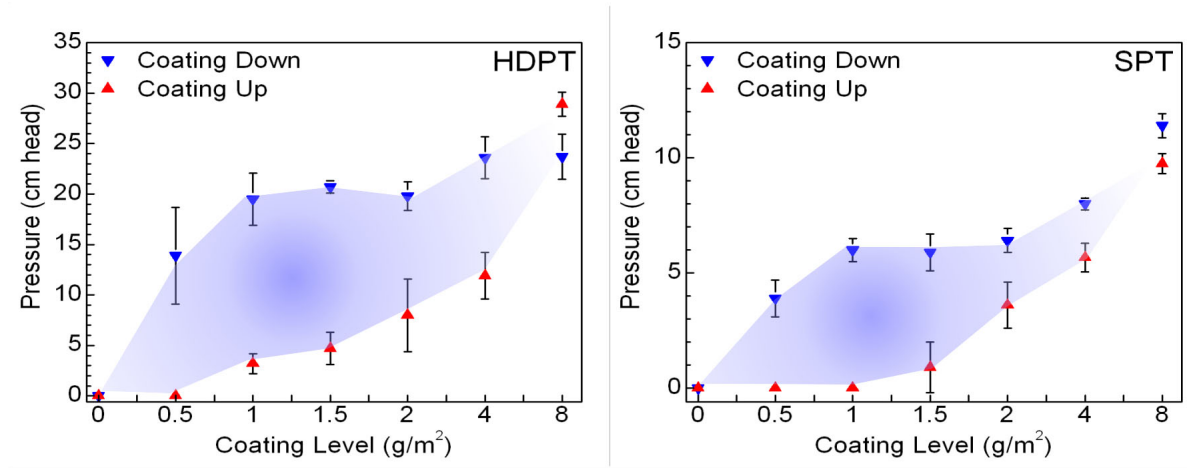


Figure 12. Water pressure penetration resistance versus coating level in gsm for HDPT (left) and SPT (right): The blue downward pointing triangles denote tests conducted coating-side down (CD), while the red upward pointing triangles denote coating-side up (CU) orientation. The disparity in penetration pressures at the lower coating levels suggests fluid flow diodicity, allowing water to pass unimpeded when in the CU orientation, or forward flow, while resisting reverse flow in the CD orientation. The diodicity (*i.e.*, pressure differential) is greater for the HDPT over that of SPT due to a finer fiber structure in the substrate.

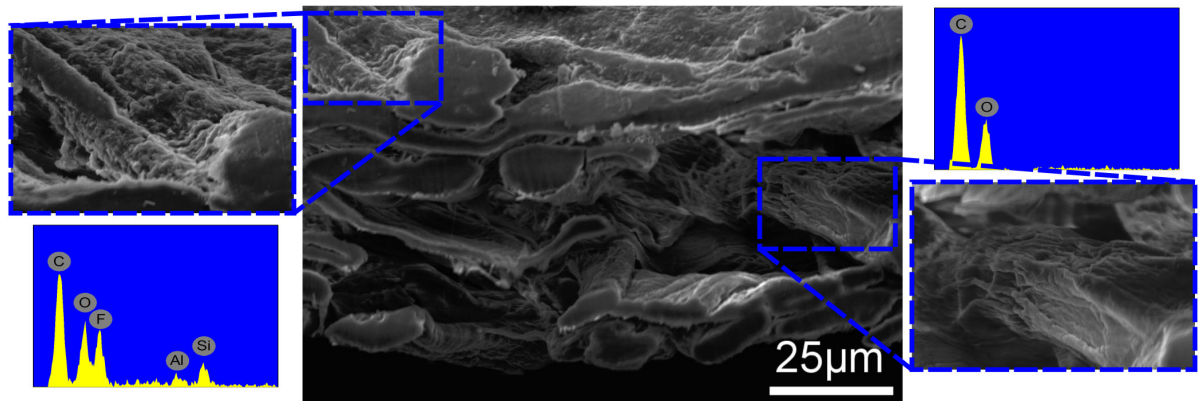


Figure 13. Center: SEM cross-sectional image of HDPT with a 2 gsm superhydrophobic coating on top. The conformal superhydrophobic coating is visible as a thin layer along the top of the cross-section, with the uncoated fibers seen below. The left inset is a close-up of a coated fiber and shows the polymer/clay nanostructure as a roughening of the plain ridged surface of the uncoated fiber (right inset). EDS spectra are included to distinguish the presence of the nanocomposite coating (left) with energy peaks for carbon, oxygen, fluorine, aluminum, and silicon, as compared to the uncoated cellulosic fibers (right) with peaks for carbon and oxygen only. Fluorine is due to the presence of the fluoropolymer matrix, while the nanoclay contains both aluminum and silicon.

nanocomposite coating (CU) or the absorbent fibers of the substrate (CD), determines the action of the fluid diode: allowing or denying transmission of the current, or fluid flow (in binary logic, a 1 or 0). As in electrical diodes, there is a maximum current regime (*i.e.*, imposed hydrostatic pressure in the present case) which, if exceeded, will result in device failure, or breakdown; in the case of the fluid diode, operating failure corresponds to leak-through. The threshold pressure is determined as the pressure under which water passes through the coating and substrate regardless of orientation (CU or CD).

For CU orientation, the pressurized water meniscus first encounters the superhydrophobic coating, and begins filling the coated hydrophobic pore(s) as the hydrostatic pressure is increased. The extent of the sagging interface, and thus the pressure threshold for fluid penetration into the underlying wettable matrix, is bounded by the depth of the next uncoated fiber(s) underneath. Once contact between the sagging water interface and the uncoated fiber(s) beneath the coated pore is made, wicking occurs immediately (blue arrows in Figure 11) and provides an avenue for saturation of the entire substrate and fluid transmission, thus designating the penetration pressure (as shown in the bottom view for CU). However, for the CD orientation, water saturates the hydrophilic fibers it encounters first before it reaches the non-wettable coating (bottom) and begins to emerge through the resistant hydrophobic porous layer separating the wetted fibers from the ambient air. Eventually, as the imposed hydrostatic pressure is increased, and the water meniscus sags further into the coated pores (and out of the bottom of the substrate), the threshold pressure is determined by the corresponding Laplace pressure of the spacing between the fibers, or pore radii. Once this limit is surpassed, the

system can no longer resist the imposed hydrohead above and water emerges in the form of distinct droplets from the pore (see Figure 11, CD bottom view—taken just after threshold pressure was exceeded).

Thus for CU orientation, or forward flow (Figure 11, green diode symbol), the hydrohead threshold is *primarily a function of fiber depth* (λ in Figure 14a) beneath the coated layer and corresponds to a diode logic value of 1 (pass mode), as this orientation (*counter-intuitively*, nonwetable coated-side towards the fluid) facilitates fluid transport at lower pressures. This is verified by calculating the forward threshold pressure (P_{Forward}) required for forcing the sagging meniscus (61) through the coated pore to the depth of the next, uncoated fiber, λ : $P_{\text{Forward}} \approx 2\lambda\gamma/R^2$, where γ is the surface energy of the liquid/vapor interface (~ 72 mN/m for water), and R is the radius of the pore (*i.e.*, lateral fiber spacing). If a λ -spacing of $10\text{ }\mu\text{m}$ is assumed (See Figure C1) for either of the two substrates tested herein, this delivers a negligible forward threshold pressure P_{Forward} below 2.3 cm head. Accounting for variations in the fiber spacing, which may give rise to values of λ well below the assumed $10\text{ }\mu\text{m}$ average depth, a near-zero pressure threshold in the CU orientation can be rationalized, and is directly observed (Figure C1, fluid penetration will occur at the most vulnerable point, *i.e.*, smallest λ). For thicker coatings, the spacing between fibers allows for excess coating material to penetrate the pores, thus forming a more torturous path for the water interface to penetrate, as seen by the converging pressure disparities at higher coating add-ons.

For the inverse CD orientation, or reverse flow (Figure 11, red diode symbol), the curved water interface also sags under increased pressure, but now advances into open air space beneath

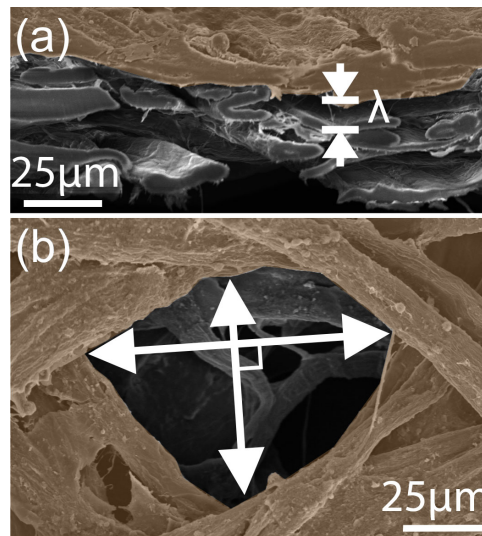


Figure 14. False-color SEM micrographs of HDPT with a 2.5 gsm hydrophobic coating on one side; color has been added to the fluoropolymer coating for better visualization. Fiber spacing results in a disparity between threshold penetration pressures (hydrohead) depending on applied coating orientation, CU or CD. (a) Cross-sectional image (as in Profile Schematic of Figure 11) illustrates the average spacing (λ) between the coated top and the underlying wettable fibers; this spacing represents the maximum distance the liquid meniscus can sag into a coated pore before being wicked throughout the substrate, thus *designating the lower bound of threshold hydrohead in the CU orientation*. (b) Surface image (as in Bottom View of Figure 11) illustrates a typical pore that the liquid fills as it emerges from the uncoated side of the substrate and into the surrounding air. The orthogonal minimum and maximum pore dimensions *designate the Laplace pressure and upper bound for the maximum threshold hydrohead in the CD orientation* (in this case, ~38 cm head of water). Both spacing parameters are equally important for determining the upper and lower bounds in the operating range of the fluid diode.

the wetted substrate. The CD threshold pressure is no longer dependent on adjacent fiber depth, but rather *only on effective pore size* within the coated layer itself (Figure 14b). This orientation corresponds to a diode logic value of 0 (no-pass mode), as fluid transport is impeded below a performance threshold determined by the fiber spacing and corresponding porosity. For the fiber spacing in Figure 14b, the reverse threshold pressure (P_{Reverse}) is given by the Laplace pressure $P_{\text{Reverse}} = \gamma(1/R_1 + 1/R_2)$, where $R_{1,2}$ are the orthogonal minimum and maximum pore radii. This delivers a value of ~ 38 cm head of water, higher than the observed ~ 21 cm head but not altogether unexpected. This discrepancy is explained by the existence of a range of fiber spacing in the coated layer, as reverse penetration pressures are determined by the weakest points (*i.e.*, largest pores) in the coated substrate. It is important to emphasize that fluid transport is qualified here in terms of liquid penetrating through the entire coated substrate from the water column side to the opposite (air) side, as shown in the bottom view of Figure 11 for both orientations.

As shown above, the two determining factors, pore size and fiber depth, are equally important and depend on the fiber orientation. The pore size determines the upper bound for the CD orientation and is the more critical factor in determining maximum pressure resistance in reverse flow; whereas, the fiber depth λ determines the lower bound in the CU orientation, or forward flow. Decreased fiber proximity in either orientation will deliver the best results: low resistance CU, and high resistance CD. This suggests a tunable design, where fiber size and packing density (porosity) can be selected for a desired fluid diode operation range. For more industrially-relevant pressure resistance regimes, the reduction of fiber size/spacing in the ab-

sorbent porous medium will increase the corresponding Laplace pressure. Thus, for low coating levels, it is possible to achieve a preferred directionality, or “diode window,” where a coated porous substrate will permit the flow of water in one direction, but oppose it in reverse for a tunable pressure range.

In general, the applications for controlled diodic fluid transport are abundant, such as any type of filtration where reverse-flow contamination is of concern. An example of practical application for fluid diode function would be that of a child’s diaper, where the area exposed to fluid saturation is much smaller than the absorbent volume capacity underlying the one-way fluid permeable barrier. Thus, enabling the diode barrier to operate under relatively large volumes of fluid before the hydrostatic threshold pressure is surpassed (*i.e.*, return of fluid in reverse flow, or leak-back) and will have the additional benefit that the surface in contact with a child’s skin remains dry. As fluid contacts the light coating (< 2 gsm) in CU orientation, it is absorbed through the insufficient barrier and wicks along the uncoated fibers beneath. Yet, when the flow is reversed in the CD orientation (*e.g.*, pressure increasing near the saturation point, child sitting, *etc.*), the same diodic substrate can withstand a much greater pressure without transmitting liquid (leaking) through. It is energetically more favorable for the water to saturate the remaining dry uncoated fibers “laterally” than to overcome the energy barrier created by the conformal coating and leak back through to the opposite (air/skin) side, not to mention more desirable for the parent.

When examining the potential of the fluid diode for multicomponent fluid (*i.e.*, oil-water) separation, it has been shown that many superhydrophobic surfaces remain oleophilic due to

the lower surface energy of oils and the lack of re-entrant surface features (81; 82; 83). This difference in surface tensions allows for simple oil-water separation and results in the wicking of oil out of an oil-water mixture and into the underlying substrate, as shown in Figure 15a with top-coated HDPT. In rare examples (84; 25), surfaces can be made both oleophobic and hydrophilic as shown in Figure 15b; A similar substrate to that shown in Figure 15a (fixed coating level of 1.5 gsm; CU orientation) is primed (pre-wetted) with water from the uncoated side before the oil-water droplet is placed on top. In this case, water (blue) separates from the mixture and leaves the oil (red) behind. Such oil-water separation examples have been shown in the literature for different coatings and/or substrate combinations, but not for environmentally friendly and biodegradable materials *in the exact same configuration*. Both images in Figure 15 were obtained for the same coating level (1.5 gsm), orientation (CU), and substrate (HDPT). The liquid separation in Figure 15b was achieved by first saturating the uncoated side with undyed water (undyed water was used to better visualize absorption from the coated side), whereas the substrate in Figure 15a was initially dry. This priming step gives the substrate an oleophobic character, as well as an increased hydrophilicity, due to the saturation of water beneath the thin conformal coating. The hexadecane treated with Oil Red dye had an oil contact angle (OCA) of 0° when tested on the unprimed substrate, and $\sim 90^\circ$ on the primed substrate (Figure 15b). The deionized water was treated with simple blue food dye and had a water contact angle on the superhydrophobic coating greater than 150° (see Appendix B) (41). It is interesting to note that in terms of sliding (roll-off) angles, the 1.5 gsm coating on dry HDPT had a water sliding angle of $15.2 \pm 6.2^\circ$; yet, after absorbing hexadecane oil (oil-wetted)

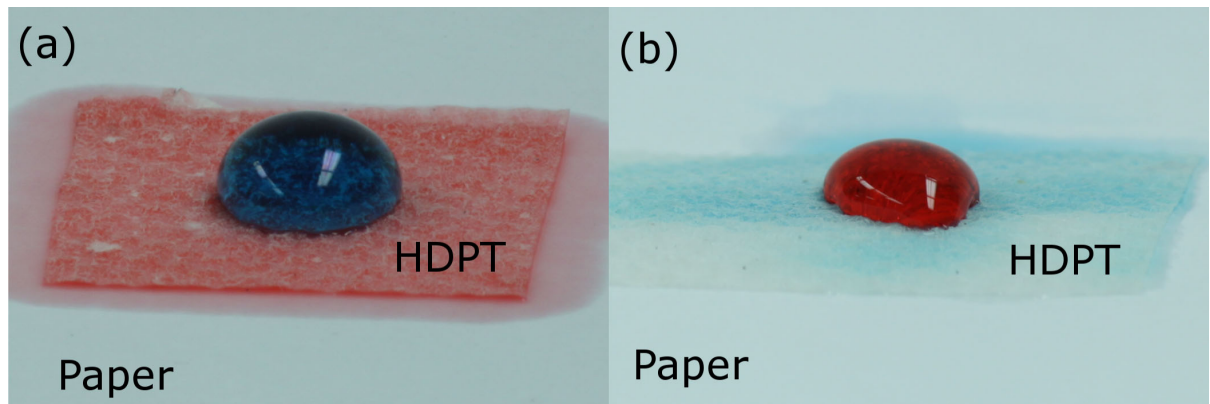


Figure 15. Using the fluid diode (HDPT with 1.5 gsm coating) to selectively separate water (left), or oil (right), from an oil-water mixture: (a) A dry sample is exposed coating-side up (CU) to an hexadecane oil (red)/water(blue) mixture; the oil readily penetrates the light superhydrophobic coating and leaves the water droplet behind on the surface. (b) An identical sample is first saturated with (undyed for visualization) water from the uncoated side. The sample is then exposed CU to the same oil/water mixture, but now resists the oil and allows for water absorption, leaving the oil droplet behind resting on the surface.

from a mixture, the sliding angle was nearly unchanged at $16.0 \pm 6.4^\circ$. For oil, in both scenarios for dry and water-wetted substrates, the surfaces were “sticky,” as oil droplet mobility was poor.

The demonstrated selective separation of an oil-water mixture suggests further avenues for research where the diode device can be tailored for fluid-specific separation/filtration applications. As mentioned earlier, to duplicate the diode function for oils, a polymeric substrate, such

as polypropylene nonwoven, can be used in conjunction with a light superoleophobic coating treatment, thus allowing for oil flow rectification. In this scenario, separation of multiple low surface energy fluids (preferably < 40 mN/m) could be achieved. This, however, is beyond the scope of the present work, which is intended to demonstrate the simplicity of enhanced device functionality with ubiquitous and environmentally benign materials.

CHAPTER 4

TRANSLUCENT-WHITE & FLUORINE-FREE WATER-BASED SUPERHYDROPHOBIC COMPOSITIONS

This chapter and its associated appendix (Appendix C) will be submitted for journal publication.

The bio-inspired field of superhydrophobicity has generally involved techniques for generating these surfaces which are environmentally detrimental, requiring harsh solvents and fluorinated compounds; thus, severely limiting their application on industrial scales. Previous approaches to reducing the use of volatile compounds have resulted in water-based dispersions which still require undesirable fluorinated chemistries to reduce surface energy, or if they do eliminate fluorine altogether, require charge-stabilization to suspend the nanoparticles required for roughness. An entirely water-based and fluorine-free superhydrophobic dispersion has been developed composed of hydrophilic titanium dioxide (TiO_2) nanoparticles suspended in a waterborne polyolefin copolymer blend that does not require additional surfactant or charge-stabilization. An added benefit of the composite coating is its translucent-white appearance and spray-cast application, making it readily applicable on an industrial scales in large-area fluid barrier surface treatments. Thus, the coating is not only environmentally benign befitting a bio-inspired design, the constituent elements are all FDA-approved and present in many con-

sumer products readily available on the market, eliminating a nontrivial hurdle in translating similar products into commercial application.

4.1 Motivation

The development and implementation of water-based and fluorine-free formulations for bio-inspired superhydrophobic surface treatments can greatly reduce the adverse environmental impact typically associated with their synthesis. Over the past several decades, many approaches to these highly liquid-repellent surfaces have been developed but commonly require harsh solvents (49; 85; 86), complex processing methods (74; 82), and/or undesirable fluorinated chemistries (41; 87). In addition, many of the demonstrated methods are not relevant in practice on large scales for commercial applications (88; 89), not only for their negative consequences to the environment, but also the inability to economically prepare large-area fluid barrier treatments at sufficiently low cost. Imparting liquid repellency via a large-area approach such as spray-casting has been shown to be viable for low-cost substrate-independent superhydrophobic coatings (87; 50; 47). Previously (70), a similarly water-based and nonfluorinated superhydrophobic formulation was presented achieving nanometer-scale roughness with the addition of exfoliated graphite nanoplatelets (GNP); unfortunately, this formulation had an opacity and dark color; thus, limiting its versatility in many commercial applications, as well as requiring pH adjustment to achieve suspension stability. Using a similar waterborne, wax-based (90) approach as the aforementioned work by Schutzius *et al.*, the need for fluorinated compounds is eliminated; alternately, incorporating titanium dioxide (TiO₂) nanoparticles to generate micro/nanoscale hierarchical surface roughness has made possible a translucent-white

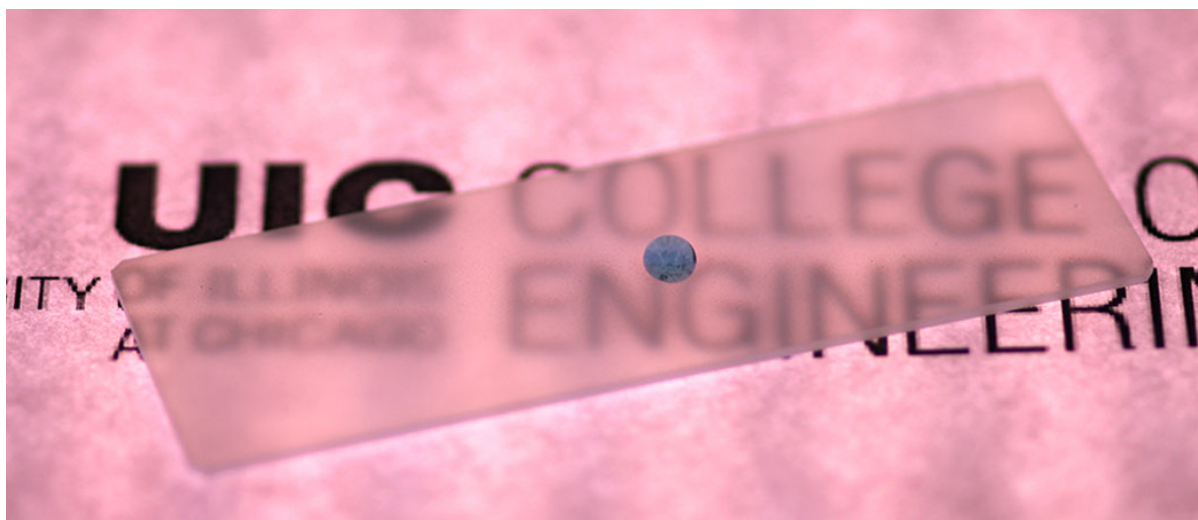


Figure 16. Photograph of a water droplet (dyed blue) beading on a coated glass slide (75 wt. % TiO_2). The tiled image in the background is the College of Engineering logo of the University of Illinois at Chicago, clearly visible through the translucent-white superhydrophobic surface treatment.

(See Figure 16) superhydrophobic composite. The composition does not require subsequent pH-modification and all constituent elements are FDA-approved (91; 92). This novel and environmentally-friendly formulation is characterized herein, having potential in numerous fluid management applications by virtue of its simplicity, efficiency, and versatility.

The study of functional nanoparticle-polymer composites has been aided in large part by the advancement in polymer synthesis methods, as well as greater control over nanoparticle

dimensions and purities. These composites have been used for a wide range of applications such as enhanced heat transfer (93; 94), low electrical resistance (95; 96), and radiation absorption (48; 97). For liquid repellent function, specifically to water, the surface requires relatively low surface energies, and a suitable degree of nanoscale roughness to reduce the liquid to solid interfacial contact area (98); thus, increasing the contact angle of water droplets which are used as a measure of surface wettability (99). The wettability (23) of a smooth un-textured surface in an air environment is determined by the free surface energies of the liquid and solid being introduced; whether the surface is hydrophobic or hydrophilic, the interaction with water is tunable via the surface roughness imparted by the addition of nanomaterials (24). A high-degree of surface roughness enhances the intrinsic wettability of the surface into two extreme cases (100), referred to as either superhydrophobic or superhydrophilic, having contact angles to water of greater than 150° or roughly 0° (101), respectively. In general, the polymer has the direct role in an applied composite of determining the affinity of liquid(s) to a given surface (*i.e.*, surface energy), as well as forming the adhesive matrix for any ensconced nanomaterials (*i.e.*, roughness) embedded within.

Until recently (69), the fabrication of super-repellent composites requiring polymers with sufficiently low surface energies (*i.e.*, for repelling water, $\gamma \ll 72$ mN/m) demanded the use of harsh solvents for wet-processing of the composite elements, thus hindering the development of entirely water-based systems. Fluorine-free, water-compatible polymer systems capable of delivering low surface energies have been the primary challenge for the development of truly environmentally-benign superhydrophobic coatings. In a previous formulation (41), a low sur-

face energy waterborne fluoropolymer dispersion was used in a water-based superhydrophobic spray where the correlation between contact angle and hydrostatic resistance was examined on nonwoven substrates, but again, the presence of fluorinated chemistry in the composite still posed environmental concerns (79). In 2006, the EPA initiated a reduction in the manufacture of many dangerous fluoropolymer compounds; such compounds have a high risk of breaking down into perfluorooctanoic acids (PFOA) and have extremely adverse environmental impacts (57). PFOA, a known cause of birth defects (102), can enter into ground water, polluting reservoirs and aquatic wild-life, eventually being ingested by humans where it can accumulate to hazardous levels. Although short-chain fluoropolymers made in response to the EPA initiative are available and pose less environmental risk, eliminating the necessity of fluorine altogether for super-repellency has been a primary goal of this work. It is hoped that, for fluid barrier applications, such fluorinated composites can become obsolete and be replaced by more environmentally-conscious, so-called “green,” alternatives.

The choice of particles having nano-scale dimensions allows for fine control over surface roughness and a greater reduction in the liquid to solid interfacial contact area; for hydrophobic, or low-surface energy surfaces, this translates into an increased resistance to fluid wetting by allowing the fluid surface to entrain pockets of vapor (103). Many superhydrophobic surfaces fabricated in the literature have utilized hydrophobic particle fillers (87; 72; 51), necessitating the use of non-aqueous suspensions or other additives. Although these hydrophobic particles aided in generating the repellent roughness, they are not viable in a water-based system without the use of charge-stabilization or surfactants. The hydrophilic nanoparticle TiO_2 is

demonstrated to supply an adequate amount of surface roughness, and is compatible with a waterborne polyolefin polymer wax blend; the polymer acts to conceal the hydrophilicity of suspended TiO_2 particles when dispersed, thus sheathing the nanoparticles in a weakly hydrophobic shell which is maintained once the final composite has been applied and residual water is removed. Using nanoparticles of extremely small dimensions (< 25 nm), a surface roughness is achieved thereby propelling the contact angles of the final composite upwards into the superhydrophobic regime. In addition, TiO_2 has been shown to be a non-toxic additive to food, skin lotions, and paint pigments (104), thereby further strengthening the claim of reduced impact, environmentally and otherwise, from the composite constituents.

The presence of a translucent-white, water-based, and entirely fluorine-free superhydrophobic formulation capable of large-area surface modification has been lacking in the literature, and for this reason has been developed and herein characterized.

4.2 Experimental

4.2.1 Materials

Titanium dioxide (TiO_2) nanoparticles (Titanium [IV] Oxide anatase nanopowders, < 25 nm particle size, 637254-100G) and two as-received mixtures of rutile and anatase (Titanium [IV] Oxide nanopowders; < 21 nm particle size, 718467-100G; Mixture of rutile and anatase, < 100 nm particle size, 634662-25G) were obtained from Sigma-Aldrich to better understand the roles of particle phase and dimension in the final composite. The polyolefin (PE) blend dispersion consisting of polyethylene-acrylic acid copolymer ($\sim 40\%$, stabilizing agent) and polyethylene-octene copolymer ($\sim 60\%$, adhesive elastomer), was obtained from DOW Chemical (~ 42 wt %

in water; HYPOD™ 8510). Deionized water was used as a probe liquid for contact and roll-off angle measurements.

4.2.2 Procedure

To prepare the sprayable dispersions, the following procedure was developed. Solids content in any sprayable dispersion is a critical component; too little requires unnecessary additional coatings and a wasteful expenditure of water; too much can cause high viscosities and/or clogging thus making spray atomization untenable. A solids content of 5 wt. % in water was selected as high enough for adequate coating deposition per spray pass, and well below the solids content where spray problems are encountered ($> 10\text{--}15$ wt. %). The solids content is then divided into a nanoparticle to polymer ratio to evaluate the effect of increased particle content. Composites tested, in ratios of nanoTiO₂:PE, were 0:100, 25:75, 50:50, 60:40, 75:25, 80:20, and 85:15. Ratios below, and including, the 50:50 particle to polymer composition did not possess adequate roughness to achieve a high degree of repellency due to the PE blend being only weakly hydrophobic, but are included and characterized to show the evolution in increased water contact angles as a function of nano-roughness as opposed to the smooth untextured all-polymer (0:100) coating. The limit of particle content was set at 85:15, above which the polymer content is reduced to such a low level that particle adhesion is severely compromised. To prepare a 20 g dispersion in a 50:50 ratio as an example, 0.5 g TiO₂ is initially weighed out into a 20 mL vial. Subsequently, 18.3 g of deionized water is then added to the dry particles and probe-sonicated for 1 minute (Sonics & Materials, Inc., 750 W, 13 mm probe dia., 20% amplitude, 20 kHz). The as-received PE polymer blend is 42 wt. % solids in water, the portion

of water from the polymer suspension is subtracted from the initial water balance added to the dry nano-powder; the water content in the final dispersion will be 95 wt. % after the next and final step. Immediately following the probe-sonication, 1.19 g of PE polymer (42 wt. % solids = 0.5 g PE, 50:50 blend of TiO₂:PE) suspension is added to the dispersion and then mechanically mixed for 5 minutes.

An airbrush atomizer (Paasche, VL siphon feed, 0.55 mm spray nozzle) was used to spray the prepared dispersions onto glass slides from a distance of ~20 cm. Water-based spray dispersions pose several challenges, as the formation of necessary roughness features in the composite is inhibited by the slow evaporation of the water. To this end, the smallest spray nozzle was selected for finer spray atomization to enhance water evaporation during application. Spray distance can affect morphology and deposition amount, the distance was thus selected to avoid excessive water accumulation during each spray pass at shorter distances, and to maximize coating deposition which can be reduced at greater distances. Between spray passes, a hand dryer was used to evaporate residual water in the composite. Care was taken to ensure spray uniformity and control over coating thickness. To determine coating weight and verify uniformity, glass slides were weighed before and after the coating process to determine coating weight in g/m² (gsm).

4.2.3 Characterization

Three glass slides were sprayed for each ratio tested, all of which were characterized for water droplet contact/roll-off angles to form a more accurate average incorporating any uncertainty in the spray parameters. In determining contact angle (CA) hysteresis, water droplets were

syringe-extruded, and similarly withdrawn, using a 1 mm needle-tip such that probe droplet diameters ranged from 1 mm to 4 mm size. This facilitated dynamic measurement of advancing and receding contact angles. For roll-off, or sliding angles, the glass slides were placed on an in-house goniometer operated by a small VXM motor allowing precise control through small angle increments until a 10 μ L water droplet was seen to roll from its initial position on the level glass slide. If the droplets did not roll, the composite surfaces were deemed “sticky” and marked with as “S” in Table IV.

NanoTiO₂ particles were imaged in a transmission electron microscope (TEM; JEOL JEM-3010, 300 keV) to verify dimensions, crystalline phase morphology, and aggregate size. For SEM observations, a small area (~ 0.25 cm²) was cut from coated aluminum foil. Aluminum foil substrates were coated in place of glass slides, prepared in the same manner, to prevent charging. The prepared samples were then sputter-coated with a 5 nm Pt-Pd coating to facilitate SEM imaging.

For X-ray diffraction (XRD) characterization (Siemens [Bruker] D5000 theta-theta powder X-ray diffractometer, 40 kV, 25 mA, Cu radiation, graphite monochromator). 2θ values were varied from 10° to 60° in 0.01° increments, with 1 s/increment. Quartz backgroundless slides were prepared with an all-PE sample, and compared with the three variants (anatase, 21 nm mixture, and 100 nm mixture) in a 20:80 ratio of TiO₂ to PE polymer. The all-PE slide was spray-cast with 5 wt. % PE in water (0.9 g solids). To obtain an accurate comparison of PE crystallinity with the nanoTiO₂ composites, the polymer content was fixed at 0.9 g such that the nanoTiO₂ addition of each of the three variants was 0.22 g (20:80, TiO₂:PE). The low filler

content was chosen to focus primarily on the PE crystallinity. A larger filler content would dilute the reflection peaks of the PE due to the sharper crystallinity observable in the TiO_2 .

4.3 Results & Discussion

The crystalline differences between anatase and rutile phases of TiO_2 are well understood (105); however, the adsorption mechanisms on the metal oxide surfaces, and their phase transitions have been the source of some controversy and lack of consensus in the literature (106). Aggregation of these nanoparticles into larger clusters is directly dependent on the phase, in turn sensitive to both particle dimensions, temperature, and pH (107; 108). In general, smaller nanoTiO_2 particles are more reactive based on the ratio of dissociative to molecular adsorption, but again, there are conflicting results in the literature on this point (109; 110; 111). Transmission electron microscopy (TEM) was employed to analyze nanoTiO_2 particles of each form; shown in Figure 17 are representative samples of both the anatase and 21 nm mixed-phase particles. Particles of the 21 nm TiO_2 blend were found to be ~ 21 nm in diameter as expected, yet readily tend toward agglomeration through surface charging mechanisms (*i.e.*, hydrogenation) (112). Even in vacuum, water adsorbate is likely retained on the surface of these particles (108), and may be contributing to the observed aggregation in the mixed-phase particles due to the presence of rutile. The anatase TiO_2 had a lower tendency for agglomeration explained by a lower surface energy over that of rutile (113). They were easily isolated in TEM vacuum for imaging, and observed to be ≤ 60 nm diameter in particle size; compared to their as-purchased size of < 25 nm, a common problem in large-scale batch-processing of nanoparticles.

The greater density of the anatase, attributed to the larger particle size, was evident by how quickly they settled when placed in an aqueous suspension, as shown in Figure B1. The photograph was taken one month after both types of TiO_2 were probe-sonicated in water at 5 wt. % concentration, and allowed to settle. The minute dimensions of the rutile allowed these particles to remain suspended indefinitely with some slight settling due to a statistical unavoidable presence of larger particles and agglomerates; whereas, the anatase phase was observed to be much more dense, occupying a smaller volume when measured into the vial as compared to the rutile and, not surprisingly, settling more rapidly.

After suspending the nanoparticles in water and fully dispersing through sonication, the PE polymer was added under mechanical mixing and the dispersion was then sprayed onto either foil for SEM imaging, or glass slide for CA measurements. Figure 18 shows SEM imaging of the three types of TiO_2 tested in a 75:25 dried-composite mass ratio of nanoparticle to polymer; anatase in the left column, the 21 nm blend in the middle column, and the 100 nm blend in the right column. The top (50 μm scale-bar) and bottom (5 μm scale-bar) rows of Figure 18 refer to lower and greater magnification, respectively. The anatase formed larger agglomerate features in the final composite as compared to the other two composite blends (mixed-phase 21 and 100 nm). This is notable because the anatase was easily isolated for TEM imaging in vacuum, as compared to the aggregate clustering observed for the 21 nm mixed-phase particles.

Surface adsorption of nano TiO_2 in water has been a well studied area in the literature (114), with the greater photoreactivity of anatase phase surfaces being of prime interest. Evidently, the addition of the aqueous polymer suspension allowed for greater aggregate clumping in the

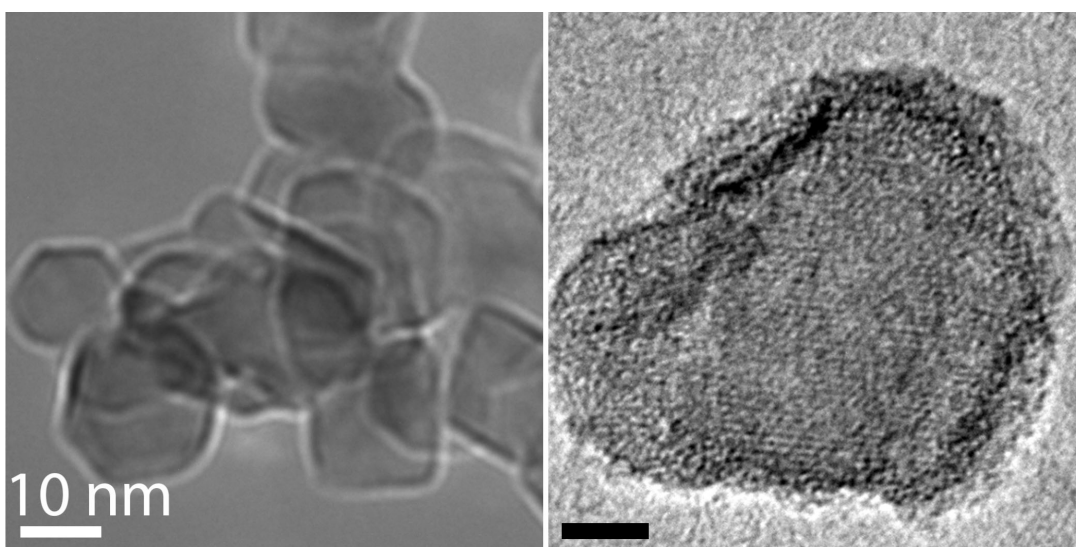


Figure 17. TEM images of 21 nm mixed phase TiO_2 particles (left), and a > 50 nm anatase TiO_2 particle (right). The smaller dimensions of the mixed-phase nano TiO_2 are evident, having a greater tendency towards aggregation over that of the anatase due to greater surface area and surface charging (*i.e.*, hydrogenation). The scale-bars in both images are 10 nm.

final composite as compared to the blended forms. The anatase was also seen to be unstable in the final dispersion, settling much faster likely due to an intrinsic higher density and greater agglomerate size. For the blended composites, the PE acted as a stabilizing agent preventing agglomeration. The higher surface charges held by the mixed-phase particles formed well insulated small clusters upon contact with the polymer. The final dispersion for the 21 nm mixed-phase was observed to separate slightly after one week when allowed to rest, forming a thin layer of water on the top of the vial but easily returning to a stable suspension when shaken; performance of the final composite after spraying was not noticeably affected. The 100 nm mixed-phase behaved similarly to the 21 nm, with slightly more settling from the larger particle dimensions but returning to suspension easily upon mild mechanical mixing.

To better understand the behavior of the variant nanoTiO₂ particles studied, the chemical kinetics of the surface interaction between the nanoparticles and the PE polymer chains must be understood. TiO₂ is known to induce nucleation of polyethylene co-polymer crystallinity (115), thereby increasing the hydrophobicity through a reduction in free surface energy. In general, polymers in ordered (*i.e.*, crystalline) groupings will have a lower surface energy than their amorphous form due to a more stable bonded state. The anatase nanoparticles are observed to induce larger aggregate groupings in the PE blend; whereas, the mixed-phase nanoTiO₂ particles induced smaller aggregate sizes, yet with far more numerous nucleation sites. This hierarchical surface texture from choice of filler particles, and lower surface energy of crystalline PE would thus be considered ideal for the purposes of generating liquid repellent surfaces.

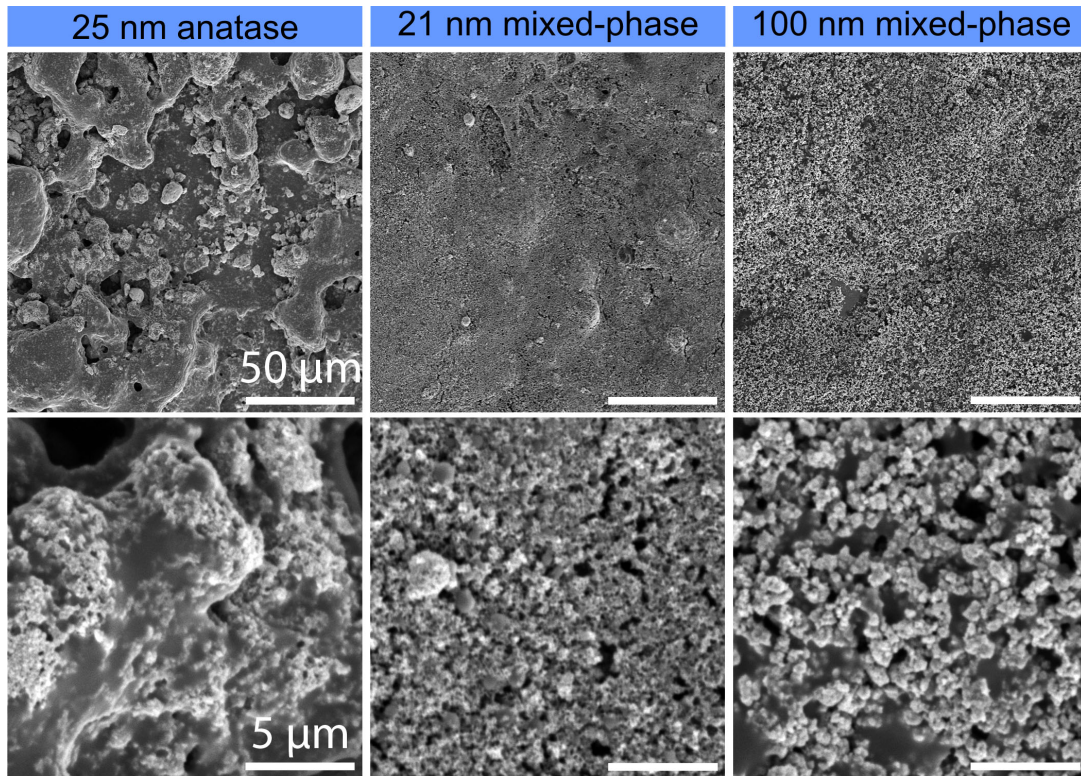


Figure 18. SEM images for the three variants of TiO_2 composites tested, in a 75:25 ratio: anatase (left column), 21 nm mixed phase (middle column), and the 100 nm mixed-phase (right column); in low (top row, 50 μm scale-bar), and high magnification (bottom row, 5 μm scale-bar). The anatase composite forms the larger agglomerate particle sizes by far, with a much greater inhomogeneity in average agglomerate size as well. The 21 nm mixed-phase composite formed uniform small agglomerate sizes, while the 100 nm mixture formed slightly larger agglomerates. Of interest is the variation in visible smooth patches of exposed polymer in both the anatase and the 100 nm mixed-phase composites, yet the polymer appears to be entirely utilized in the higher surface area 21 nm mixed-phase composite.

XRD measurements were performed on the three variant nanoTiO₂ composites and compared with an all-PE composite to determine if there is any crystallinity enhancement in the polymer. XRD measurements are sensitive to volume in the composite, and for this reason the polymer content (*i.e.*, volume) was fixed across all samples (0.9 g, see Figure 19); whereas, the filler particle content was held to a minimum of 20 wt. % (0.22 g) in the composite in order to better visualize PE crystallinity peaks. For the case of the all-PE sample, there are 2 θ peaks with values of ~ 19 and 22° , surrounding by an amorphous “halo” (115; 116). For the 20 wt. % anatase composite, the peaks from PE reduced slightly in intensity, with an additional slight narrowing of the peak width. The expected peaks from anatase were observed at 25° , 37° , 48° , 55° , and 56° , as well as being represented similarly in the two mixture samples as expected. The mixed-phase samples both had peaks indicative of the rutile phase at 27° and 45° , as expected. In regards to the broad peaks for PE, however, the degree of crystallinity contributed by the addition of nanoTiO₂ is inconclusive. There is a slight narrowing of the peak base for the anatase, but is accompanied by a diminished peak size, resulting in an ambiguous change in the area under the reflection-intensity curve. For the two mixed-phase samples, the peak base remains relatively unchanged and it is unclear from the background whether or not the reflection peaks have sharpened.

Additionally, the PE (HYPODTM 8510) has a high carboxyl content (117), which can become dissociated upon interaction with titanium nanoparticles (18). This reaction results in the formation of formic acid in the nanoTiO₂:PE dispersions, and thus formate is deposited along the grain boundaries of agglomerate nucleation sites in the dried composites. This is

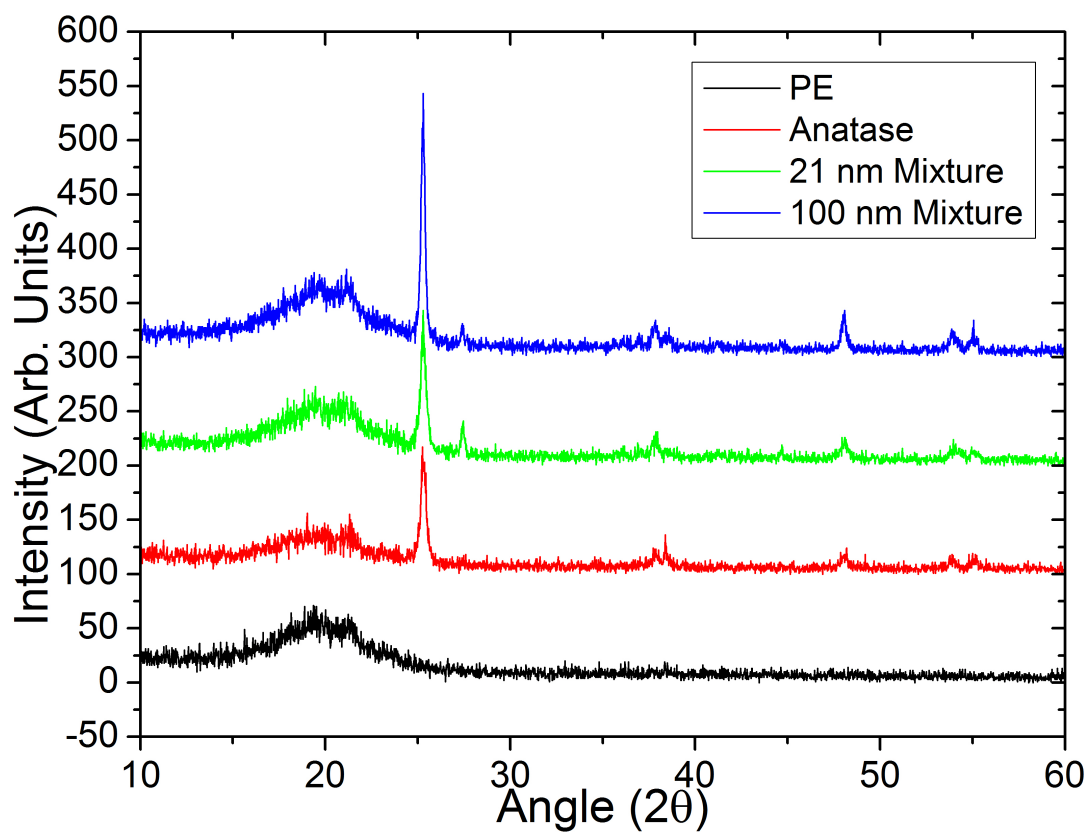


Figure 19. XRD reflection peaks for an all-PE coating (bottom, black), and three variant nanoTiO₂ composites (anatase in red, 2nd from bottom; 21 nm mixture in green, 2nd from top; 100 nm mixture in blue, top).

easily verified by comparing the pH of the prepared dispersions before spraying. The PE (42 wt. % in water) has an as-received alkalinity of pH 9. The nanoTiO₂ (all types) upon dispersing in deionized water retains a neutral pH (~7). Upon combining the filler and polymer, the pH is observed to reduce to 8 in all cases, suggesting a neutralizing effect brought on by the introduction of the reactive filler particles in the alkaline dispersion. The surface adsorption mechanisms of nanoTiO₂ are likely stripping the carboxyl groups from the polymer backbone, forming chemical bonds with PE and simultaneously neutralizing the dispersion. The mechanism partially explains the efficacy of the protective polymer “sheath,” or protective shell, surrounding the otherwise hydrophilic particle fillers.

The larger agglomerate sizes, or surface features of the composite, have a direct impact on droplet mobility in the final composite. The large clusters of anatase particles and exposed polymer can be observed in the left column of Figure 18. Referring to the bottom left column, the individual TiO₂ aggregates can be seen dotting the polymer surface. The unit size of these agglomerates matches well with the observed unit size in the other coatings and are all uniformly of submicron ($< 1\ \mu\text{m}$) dimensions; yet, for the anatase, these unit agglomerates further condense into much larger clumps, some approaching $50\ \mu\text{m}$ in size (Figure 18, upper left), during spray-casting. These hierarchical features are not entirely undesirable and can aid in generating super-repellency (81); unfortunately, the weakly hydrophobic *smooth* patches of exposed polymer can detract from droplet mobility, resulting in ‘sticky’ regions of the surface where droplets adhere, thereby pinning due to the roughness contrast (118). In contrast, the submicron agglomerates in the case of the 21 nm mixed-phase remain constant

during spray-casting, forming uniform nanometer-scale roughness along the surface. Regions of smooth exposed PE seem to be eliminated and well-absorbed by the nanoparticles, lacking the roughness contrast observed for the anatase composite. The 100 nm mixed-phase composite forms agglomerate sizes matching very well with the 21 nm composite despite the order of magnitude difference. The composite more closely resembles the 21 nm mixed-phase coating when compared to the anatase composite, likely due to a larger fraction of rutile over anatase in the as-received mixture. Yet, the 100 nm composite appears to inadequately allow the PE to cover the nanoparticle aggregates fully. Similar to the anatase composite, small regions of smooth exposed polymer are formed as seen under high-magnification (Figure 18, bottom right). The composite forms a unique blend of features observed in the composite images for anatase and the 21 nm mixed-phase, incorporating aspects of both with a larger range of aggregate sizes and intermittent small patches of smooth polymer.

Dynamic contact angles were measured for all coatings on glass slides in order to better understand the role of particle size, phase, and polymer coverage. For any superhydrophobic surface, the sessile contact angle is generally considered limited information for predicting dynamic droplet behavior when introduced to the surface. An advancing and receding contact angle is more appropriate when attempting to characterize a self-cleaning surface, wherein droplet mobility is important for transporting surface contaminants away. The difference in advancing and receding CA is known as CA hysteresis and is, ideally, as close to zero as possible for best performance in regards to self-cleaning, and therefore, super-repellency (99).

TABLE IV

ROLL-OFF ANGLE MEASUREMENTS FOR THE TiO_2 :PE COMPOSITES ON GLASS SLIDES. THE VALUES ARE IN TERMS OF TiO_2 FILLER CONTENT (*i.e.*, WT. %), NONE OF THE BELOW 50 WT. % SURFACES HAD MEASURABLE ROLL-OFF ANGLES.

	50	60	75	85
Anatase (25 nm)	S	38.7 ± 8.3	19.5 ± 6.3	13.6 ± 3.9
21 nm Mixture	S	38.7 ± 8.3	32.5 ± 2.6	34.7 ± 5.2
100 nm Mixture	S	24.2 ± 4.9	S	S

Figure 20 illustrates the behavior of water droplets introduced to the surfaces of the composites possessing a range of nanoparticle loadings for determining optimal ratios. The green line in each plot represents the advancing CA, as opposed to the red for receding CA. The CA hysteresis, the difference of the two, is shown as a blue dashed line, the closer to the x -axis being the more preferable for higher performance as advancing and receding CA become more aligned. The more closely matching the two CA become refers to a decrease in adhesion of the droplet to the surface which can likewise increase droplet mobility. The CA of $\sim 95^\circ$ for pure PE polymer (*i.e.*, 0:100 ratio, no roughness) is shown as the y -intercept for all three plots, of note is the zero

receding CA for the all-PE coating; the polymer itself is extremely sticky to water droplets and only weakly hydrophobic. As nanoparticle loading is increased, all three composites achieve higher advancing contact angles as well as a reduction in CA hysteresis (*i.e.*, the receding angle approached that of the advancing angle). CA hysteresis for the mixed-phase composites diminishes much more rapidly at increased particle loading, mainly due to the reduction of exposed polymer as discussed for Figure 18 and the greater prevalence of nanoscale roughness. The exposed patches of polymer in the anatase coating allow for regions on the surface for the droplet to anchor, thus pinning the receding contact line and preventing it from receding. The hybridized regions of nanotextured and smooth polymer in the 100 nm mixed-phase composite produces small variations in projected performance as the particle loading increases, compared to the steady and repeatable increase in performance for the 21 nm mixed-phase composites. This performance drops off dramatically above a 60–75 wt. % filler particle loading resulting in a wettable surface. Droplet roll-off angles were include in Table IV, reflecting the improved performance by the reduction in CA Hysteresis.

In terms of overall dispersion stability and performance, the 21 nm mixed-phase TiO₂ composites were the more uniform and repeatable superhydrophobic coatings. The suspension could be maintained indefinitely, making it ideal for large-area industrial-scale surface treatments, without fear of the formulation going out of suspension; thus, avoiding wasteful expenditures and poor efficiencies. Additionally, the anatase composites are much more photo-reactive, which can cause issues with repellency when exposed to UV radiation, dissociating the surrounding polymer and becoming increasingly hydrophilic due to an increase in free surface energy. All

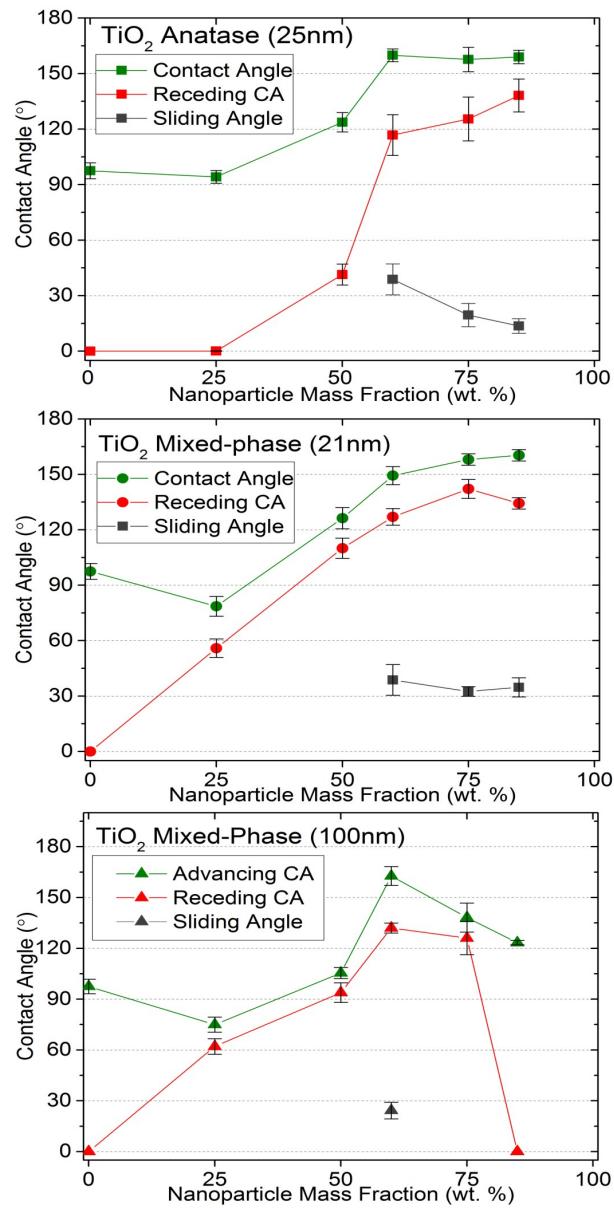


Figure 20. Dynamic wettability measurements for all three types of TiO₂ tested for all nanoparticle mass fractions. For all three TiO₂ samples, the increase in mass fraction above 50 wt. % boosts advancing contact angle (green) to above 150° while also increasing the receding contact angle (red). For select mass fractions, there exists a measurable roll-off angle (gray).

three variant nanoTiO₂'s were shown effective for achieving superhydrophobicity above a 60:40 ratio; however, reducing PE content severely inhibits nanoparticle adhesion above a 75:25 ratio. It is shown there is a desirable composite blend of nanoparticle to polymer ratio between 60 and 75 wt. % nanoparticles loading to achieve superhydrophobicity.

CHAPTER 5

DURABLE & FLEXIBLE GRAPHENE COMPOSITES BASED ON ARTISTS' PAINT FOR CONDUCTIVE PAPER APPLICATIONS

This chapter and its associated appendix (Appendix D) have been accepted to the journal Carbon, Joseph E. Mates, Ilker S. Bayer, Marco Salerno, Patrick J. Carroll, Zhenguo Jiang, Lei Liu, and Constantine M. Megaridis, November 2014, Elsevier.

An acrylic emulsion artists' paint containing chlorinated copper phthalocyanine pigment was modified with variable-size multilayer graphene (exfoliated graphite) to induce low electrical resistance; composites were spray-cast on common printing paper, and subsequently polished under mild compression, to produce highly conductive paper. The mechanically robust conductive paint showed excellent adhesion to the underlying paper, as determined by Taber abrasion and tape peel tests, which displayed no adhesive failure under the test conditions studied. The conductivity of the papers was tuned by changing the concentration and the size of the multilayer graphene particles. Detailed conductivity measurements showed stable Ohmic current-voltage behavior. The optimum graphene-in-paint formulations resulted in sheet resistances of the order of $10 \text{ } \Omega/\square$. Standard electrostatic force microscopy measurements showed uniform surface electric field gradient distribution strongly correlating with the topography. Similarly, scanning Kelvin probe microscope measurements indicated stable work functions close to 5 eV, comparable to highly-ordered pyrolytic graphite. Furthermore, Kelvin probe measurements

were more sensitive to surface charges related to copper phthalocyanine domains, which are known to have semiconducting properties. Finally, the conductive papers were also tested in the 0.50 to 0.75 terahertz (THz) frequency range for electromagnetic interference shielding (EMI) characterization and displayed quasi-metallic shielding performance.

5.1 Motivation

The demand for flexible and durable light-weight electronics has increased in recent decades due to the proliferation of new communications and sensor technologies, e-textiles, and the need for adaptable power storage. Conductive composites in paper-based and textile applications have been the subject of extensive research (119; 120; 121; 122; 123; 124) for their applicability towards addressing this demand in future electronics. A generic and ubiquitous substrate, such as paper, offers a unique platform for the testing and low-cost implementation of new composite technologies; easily translating across multiple substrate platforms and industrial applications, such as photodiodes, smart fabrics, and printable electronics, among many others. As technologies advance, obsolete electronic detritus from years past now present ethical and societal challenges for their environmentally-benign disposal. It is thus desirable that future technologies should be designed such that outdated equipment could easily break down under natural conditions with low environmental impact. Flexible paper and textile electronics represent solutions to these nontrivial challenges, with the added benefit of a reduced bulk which is present in much of the current and previous technology; eventually taking up space in a landfill or, even worse, increasing pollution in the natural landscape. A composite, comprised of multilayer graphene (MLG) in the form of exfoliated graphite in an acrylic artists' paint poly-

mer matrix, is presented herein for conductive paper applications requiring a light-weight and low-cost solution, with the added benefits of extreme durability, flexibility, and quasi-metallic electronic properties.

Acrylic emulsion artists' paints were introduced in the 1950's and 1960's. Compared to oil-based paints, acrylic emulsion paints are capable of high pigment loading, forming coatings that can dry quickly and be thinned with water; they also have good clarity, excellent elasticity and high resistance to ultraviolet degradation (125; 126). Earlier paint formulations used copolymers of methyl methacrylate (MMA) and ethyl acrylate (EA) (127). Today, the acrylic emulsion paints utilize poly (n-butyl acrylate/methyl methacrylate) copolymer dispersed in water. These films tend to be slightly tougher and more hydrophobic than the MMA/EA resins, making them more resistant to outdoor exposure. These emulsions offer advantages due to their unique interactions with paper surfaces after application, including efficient encapsulation of pigments to form a continuous film, absorption into the texture of the paper, and polymerization to form a robust film or painting, as schematically illustrated in Figure 21 (128).

There are many different types of pigments used in acrylic emulsion paints as color sources. Among them, phthalocyanine green (CuPc), a complex of copper (II) with chlorinated phthalocyanine, has been widely used as a filler (129). The chemical formula of this compound ranges from $C_{32}H_3Cl_{13}CuN_8$ to $C_{32}HCl_{15}CuN_8$, depending on the extent of chlorine substitution. Due to its stability, phthalo green is used in inks, coatings, and many plastics. The pigment is insoluble and has no tendency to migrate in the material. It is a standard pigment used in printing ink and in the packaging industry, as well as in many cosmetic products. Of interest, CuPc

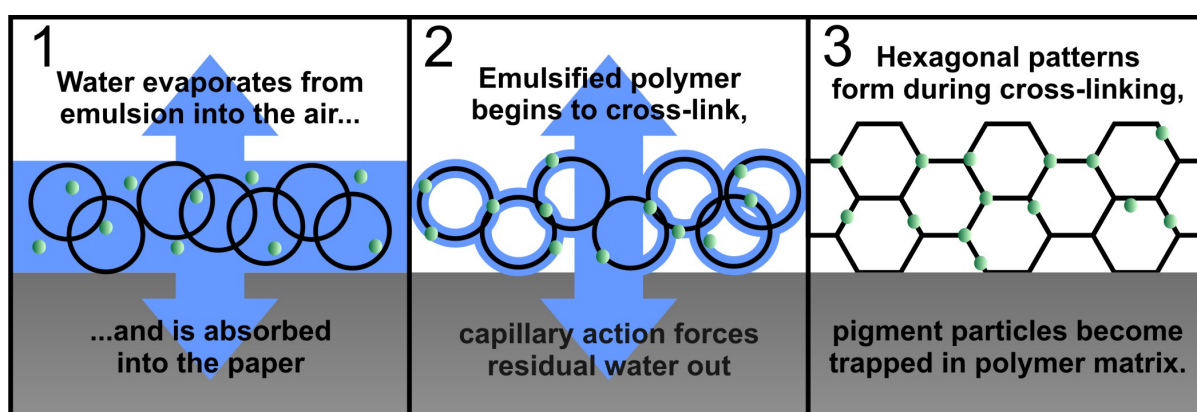


Figure 21. Application and setting of artists' acrylic emulsion paint (shown in blue) on a paper surface (gray). Circles represent the polymer emulsion, which upon drying cross-links to form hexagonal bonds, thus acting as a matrix for pigment nanoparticles (shown as green dots). Based on scheme reported in (128).

particles have recently been studied for use in quantum computing (130) and as a doping agent to enhance material properties in electrical and semiconductor systems (131), thus forming the rationale for choosing this specific pigment to create a novel conductive composite.

Long theorized (132), graphene has been a major focus of research efforts since its discovery in 2004 (16); however, processing large sheets for commercial and industrial applications still remains cost-prohibitive. A cheaper, albeit less conductive, alternative to monolayer sheets of graphene is the use of exfoliated graphite: an aggregate nanoparticle comprised of MLG with high aspect ratio that is relatively simple to manufacture in bulk for low cost. Monolayer graphene consists of a sheet of carbon atoms arranged in a hexagonal lattice, the structure of which gives rise to an inherent mechanical strength (133), as well as ballistic electron transport (29) along the many interlinked covalent bonds. The attractive properties of graphene are numerous, yet generating defect-free and large-area graphene lattices necessary for realizing many of the desired attributes remains a challenge, and reproducibility is a concern. A spray-cast MLG composite, in the form of exfoliated graphite dispersed in a pigmented acrylic artists' paint polymer matrix, possessing attributes approaching that of highly-ordered pyrolytic graphite is shown here to have potential for durable and flexible conductive paper applications, such as large-area flexible electronics and electromagnetic interference (EMI) shielding surface treatments without exorbitant monetary and environmental costs.

Approaches towards conductive papers and inks have been studied in the past (134; 135; 136; 137; 138), but many have required costly components, complicated fabrication procedures, or high energy expenditure to produce. As synthesis techniques improve, comparable inks and

conductive colloidal suspensions are becoming cheaper but often rely on ground-up development of compatible polymer binders. The novelty of this approach is in using an existing polymer emulsion technology found in acrylic artists' paint to reduce costs, which simultaneously takes advantage of the nano-pigment suspension to add additional doping properties. For similar reasons, composites containing precious metals, such as gold and silver, are only economically viable for small-scale specialized electronics. Chemical vapor deposited (CVD) graphene is viable on large-scales (assuming the fabrication chamber is made sufficiently large); however, this method is also costly and limited in continuous throughput. Spray-cast functional composites have been proven suitable and advantageous in low-cost and large-area application (41; 139), and are compatible with the delivery of MLG dispersed in a diluted polymer matrix (70). A desirable nanoparticle-polymer composite should be durable and flexible, as well as possessing a low electrical resistance by allowing the MLG flakes to communicate free electrons through a well-connected percolation network. Acrylic artists' paint meets these criteria, being a novel material in the pursuit of environmentally low-impact conductive binding agents and maintaining a low price-point for realistic application.

Currently, the development of light-weight, durable, and flexible electronics has become a focal point of research into next-generation battery and supercapacitor devices over the last decade, with graphene capturing the imagination of the research community as a wonder material towards this end. Carbonic electrodes are currently the predominant materials in power storage, with strong demand for cheaper production methods and innovative approaches for their incorporation in smaller, light-weight devices. A thin, foldable and substrate-independent

electrode has great potential in applications for energy storage and wearable electronics, as well as for reducing environmental concerns that arise from energy losses due to low efficiencies. Similarly, the EMI shielding potential for carbon-based composites has also been extensively studied (140; 141), both theoretically and experimentally, but only in the last few years have experimental analyses of the EMI shielding potential of graphene composites been realized (142; 143; 144; 145). In this work, a novel approach to low-cost, robust, and flexible conductive MLG composites adhered on paper substrates via a water-based acrylic artists' paint is investigated; experimental evidence shows these composites to possess the high-conductivities necessary for many conductive paper applications. Effectiveness for large-area terahertz (THz) EMI shielding is demonstrated in addendum to the characterization of these composites.

5.2 Experimental

5.2.1 Materials

Exfoliated graphite nanoparticles with typical thickness of 6–8 nm were obtained from XG Sciences (M-type xGNP) and Strem Chemicals (denoted as S-type for simplicity). MLG were supplied in three sizes from both suppliers with average radii of 5, 15, and 25 μm (referred to in the text as M-5, M-15, and M-25, or S-5, S-15, and S-25). The pthalo green acrylic paint, manufactured by M. Graham & Co., was obtained from Dick Blick Art Supplies (Catalogue #: 01601-7064). Polymethyl methacrylate (PMMA, Product # 182265) and acetone (ACS reagent, $\geq 99.5\%$ purity) were obtained from Sigma-Aldrich. Substrates for applying and testing the resultant conductive composites were standard 8.5 x 11" printer paper and microscope glass slides ($25 \times 75 \times 1$ mm). PuffsTM Basic 2-ply tissues were used for polishing after spray-casting.

5.2.2 Preparation & Application of Conductive Composite

To determine the solids content of the acrylic paint, test amounts were weighed before and after curing. This allowed for an average estimate of ~67 wt. % solids in the as-received acrylic paint. This solids content is the basis for all subsequent composite ratios, being a proprietary blend of copper phthalocyanine (CuPc) green pigment nanoparticles and acrylic polymer poly (n-butyl acrylate/methyl methacrylate) emulsion. A stock solution of 10 wt. % acrylic paint solids in acetone was prepared, and after bath-sonicating for 15 minutes (Branson 8200, 20 kHz, 450 W) was allowed to soak under mechanical mixing for at least 24 hours before preparation of spray dispersions.

The sprayable dispersions were prepared as follows. The total solids content of the sprayable dispersion was deliberately maintained at 3 wt. % in acetone to avoid complications during spraying; heavier solids content negatively impacted spray uniformity by causing clogging, while lower solids content unnecessarily decreased spray deposited mass and increased spraying time. The solids content for the final composite coatings were varied in ratios of MLG to paint solids: 20:80, 35:65, 50:50, 65:35, and 80:20. For example, to prepare 16 g of a dispersion at 3 wt. % solids (0.48 g) in a 50:50 ratio of MLG:Paint-solids, 0.24 g of MLG (50 wt. % solids) was carefully weighed out into a 20 ml glass vial, to which 13.36 g of acetone (this excludes the amount of acetone from the acrylic stock solution to be added later) was added. The MLG in acetone was then probe-sonicated (Sonics & Materials, Inc., 750 W, 13 mm probe dia., 20% amplitude, 20 kHz) for 1 min., to which the remaining 2.4 g of 10 wt. % acrylic-in-acetone stock solution (0.24 g acrylic paint solids) was added drop-wise under mechanical mixing. The

mixture was then bath-sonicated for an additional 5 min. to ensure adequate homogeneity in the final spray dispersion.

The dispersion was spray-deposited (Paasche, VL siphon feed, 0.73 mm nozzle) from a distance of 20 cm onto an area of $7.5 \times 9 \text{ cm}^2$ to form the composite coating; greater spray distances increased the spray cone, such that control of spray area was compromised, while shorter distances did not allow adequate time for acetone to evaporate during atomization, resulting in excessive wetting and dripping. The substrates placed in the spray area were either glass slides or cutouts of standard printer paper. For the given spray area, paper substrates were cut to match the $7 \times 9.5 \text{ cm}^2$ spray area, or when spraying on glass, 3 glass slides fit neatly in a vertical arrangement with 1 cm spacing between. The coating deposition mass (g/m^2) was determined by weighing the glass slides before and after spraying to ensure uniformity of coating.

After spraying, the coated substrates were placed in an oven to cure at 150°C for 1 hour. The heating promotes relaxation of surface MLG into the polymer as the glass transition ($\sim 190^\circ\text{C}$, see *Thermal Measurements*) is approached. After heating, the surfaces were polished manually in a circular motion under compression (44–66 N) using untreated soft tissues to orient the surface MLG parallel to the substrate. Loose surface MLG is removed in this step; the amount removed is increased at greater graphene loadings in the composite, as the reduced polymer content results in insufficiently adhered MLG. The surface takes on a reflective silver sheen after polishing; light refraction is increased as the graphene becomes homogeneously oriented. After polishing, the substrates are replaced in the oven at 150°C for another hour to allow any

residual loose surface MLG to relax into and recombine with the composite. The surface is once again briefly polished for approximately 1–2 min. and prepared for characterization after the final heating.

5.2.3 Characterization

5.2.4 Morphological Characterization

Scanning electron microscopy (SEM, Hitachi S-3000N) was employed to visualize surface morphology and estimate coating thickness using cross-sectional profiles. Profilometry (Zygo NewView™ 6300) results were used to compare smoothness of final composite to the roughness before polishing. Atomic force microscopy (AFM, Asylum Research MFP-3D) was used to analyze the roughness features at the micro-scale. The scan size was set to 40 μm with 5122 pixels, and the line frequency to 0.4 Hz. These settings, operated in two pass mode due to the simultaneous performance of surface electrical measurement, required an acquisition time of approximately 50 min. per image. The all-paint coatings (containing no MLG particles) were spray-cast on glass slides to gauge their surface morphology for comparison. However, the spray-cast films were too rough for accurate AFM measurements. The MLG:Paint-solids composites were polished under mild compression, and as such, they were rendered smooth enough for AFM measurements. However, smoother all-paint films were formed by drop-casting and AFM morphology measurements for these surfaces are included in Appendix D.

5.2.5 Electrical Characterization

For conductivity measurements, the composite coatings of all MLG types and ratios were applied onto glass slides. Silver paint was applied across the shorter dimension of the glass

slide in two thin strips (~ 3 mm wide) to form 25×25 mm² composite squares of coating in the center. Current-voltage (I-V) curves were obtained to verify linear Ohmic resistance of the composites, with input voltage varied from -1.0 to 1.0 V, in 0.1 V increments. The slopes (inverse of resistance) obtained through I-V characterization were then compared to the more accurate 4-probe sheet resistance values.

Electric Force Microscopy (EFM) was carried out to determine uniformity of the conductive coatings and map the surface electrical properties. Scanning Kelvin Probe Microscopy (SKPM) was also carried out to quantify the electrical surface potential at the micro-scale. For both EFM and SKPM modes, Electrilever probes (Olympus, Japan) were used, consisting of rectangular silicon cantilevers with tip apex diameter of ~ 60 nm and ~ 25 nm Ti-Ir coating on the tip side (resonance frequency ~ 300 kHz). The tip was biased at +3 V with respect to the sample surface, set to ground ($V_g = 0$ V) at the silver strips by adhesive copper tape. The second pass scan was taken at an elevation height of 70 nm, with mechanical and electrical excitation resulting in approximately one fourth or one tenth of the first (tapping mode) pass amplitude, in EFM and SKPM mode, respectively. From the SKPM measurements of surface potential voltage, V_{SP} , the maps of local work function WF of the sample surfaces were calculated, as the difference $WF = WF_{tip} - eV_{SP}$, where e is the electron charge and WF_{tip} is the WF of the probe tip used (~ 5.3 eV), previously calculated by calibration of the setup on a reference sample with known work function (highly-ordered pyrolytic graphite, ~ 4.65 eV (146)). Comparison SKPM measurements on all-paint coatings were not possible due to insulating polymer encapsulation of the chlorinated copper phthalocyanine pigment. However, SKPM measurements on vapor-

deposited pure ultra-thin copper phthalocyanine films have been reported in literature with relevance to charge transport in organic devices (147), where it has been found that pure copper phthalocyanine films have an exponential density of states with a characteristic value of 0.11 eV, which is known as a good hole transport material.

THz EMI shielding measurements were performed using an Agilent N5245A PNA-X system with full two-port WR-1.5 (0.50–0.75 THz) extenders (Virginia Diodes, Inc.) to evaluate the potential of these composites in a real-world application (148).

5.2.6 Thermal Measurements

A differential scanning calorimeter (DSC-Q200, TA Instruments) was used to measure the thermal properties of the acrylic paint on a stand-alone basis and compared to the thermal properties of the Strem 25 μm (S-25) 50 wt. % composite. The temperature was stabilized at 100 °C, and increased to 400 °C in increments of 10 °C/min for both samples. The glass transition temperature (T_g) was determined by analyzing the hysteresis of a heat flow plot vs. temperature, as the latter rose well above T_g , and slowly returned back through the temperature region of interest.

5.2.7 Durability Testing

Conductive coating durability was tested by two different approaches: standard peel tests using adhesive tape and abrasion testing. The peel tests were conducted using a POLKEN 203 tape having 9.4 N/cm adhesion force to steel in air. A loop tack method was used for peel tests. In this method, the adhesive side of a loop of the tape was lowered onto a substrate and pressed to cause adhesion. The other end of the loop was attached using a grip to an

Instron tensile tester, which then pulled the tape and recorded the force as a function of time and distance until lift off. The setup was used to execute several peel lift-off events (1 mm/s) to gauge whether the conductivity of the nanocomposite coating is affected as a function of repeated tape peels. At the end of each tape lift-off, the electrical resistance on the surface was measured and compared with the original value.

The abrasion durability of the surfaces was measured with the TABER Reciprocating Abraser (Abrader) - Model 5900 according to test method ISO 1518. The tester can be configured with optional attachments to evaluate the relative resistance or susceptibility of a material surface to physical damage, such as wear and abrasion, rub, scratch, mar, gouge and scrape. The tester incorporates a horizontal arm that reciprocates in a linear motion. The arm can be fitted with different weight disks in order to adjust the severity of the abrasion; in addition, speed and abrasion length can also be adjusted. The abrader was fitted with plastic replacement accessories including a rod to further decrease the load suitable for acrylic coatings. The device can be fitted with various abrasion materials, from soft cloths to hard aluminum oxide sand papers. For abrasion tests, we used a solid smooth plastic disk (2 cm in diameter) with Rockwell hardness of M70 (R-scale; ISO 2039-2), similar to polycarbonate. The linear abraser was applied with a single stroke at a time, separately, for two varying weights corresponding to 20 and 70 kPa abrasion pressure. After each stroke, the electrical resistance was measured on the ~8 cm-wide abraded region. Up to 100 abrasion cycles were applied on conductive paper samples to monitor changes in the surface resistance as a function of abrasion handling.

5.2.8 Raman Spectroscopy

Raman spectroscopy (Renishaw 2000, 514 nm Argon ion laser with 1800 l/mm grating) was used to determine the nature of the graphene present in the MLG of the final composites. The same process as given in the *Preparation & Application of Conductive Composite* section was used to create MLG:PMMA composites for Raman spectroscopy comparison, where the mass fraction of paint solids is replaced with PMMA to analyze the effect of the CuPc pigment particles on the final composite. Peaks from Raman data were used to analyze the presence of single layer, or stacked graphene, as well as to determine any n- or p-doping (negative or positive) in the final composites by comparison with known Raman peaks (149).

5.3 Results & Discussion

As shown in Figure 22, the SEM images from before (left column) and after polishing/compression (right column) show the reduction in surface roughness for a 50 wt. % filler particle composite coating on printer paper. The amount of graphitic coating which is lost during the polishing process depends on the nanoparticle-to-polymer ratio in the final composite; less particle fillers means more adherent polymer to retain filler mass in the composite. The reverse is true, as increased particle filler content in the composite (*i.e.*, reduced polymer content) causes inadequate adhesion for much of the filler mass. For all composites tested, before and after mass measurements of the coated glass slides yielded a repeatable 16.5 ± 2.9 g/m² of composite coating, with an average of 3.25 ± 2.19 g/m² removed during the polishing step for the 50 wt. % S-15 MLG composite. For the coatings of higher and lower MLG loading, the amount lost during polishing can significantly increase and decrease, respectively. For the more evenly

balanced MLG:Paint mass fraction ratios (35:65 – 65:35), the polishing step serves to reorient much of the MLG and align them parallel to the substrate surface. This alignment serves to enhance the charge percolation network, and, in turn, increase electrical conductivity. When the particles are oriented randomly, the interconnections between the conductive particles will be less organized, allowing regions of high resistance to form.

The top row in Figure 22 shows a 5 μm MLG (Strem, S-5) composite coating, where the particle sizes are seen to vary up to roughly twice the average radius with some particles being as large as $\sim 10\ \mu\text{m}$. This trend is repeated for the 25 μm average particle radius (S-25) samples in the bottom row of Figure 22, where particles approaching 50 μm are observed in the coating. Similar size variations were observed in the xGNP M-type (M-5, -15, -25) samples, where the as-received particle radius is a statistically accurate average with a wide distribution. After polishing, defects were greatly reduced and the composites took on a smooth silver sheen. The remaining defects, however, appear to be of the same magnitude as the original particle sizes and decrease in regularity with increased particle radius. The right column of Figure 22 shows the polished composites of both the S-5 (top) and S-25 samples (bottom); the smaller 5 μm particles of S-5 create regular pitting of roughly 5 μm gaps in the otherwise smooth surface, similar to the S-25 sample, where the pitting is larger but farther apart for comparable test areas. This sparsity of surface pitting in the 25 μm MLG composites naturally tends to decrease sheet resistance.

Profilometry results (Figure D1 and Table XI) were used to ascertain the reduction in roughness brought about during the polishing process. Before polishing, the smaller MLG radii

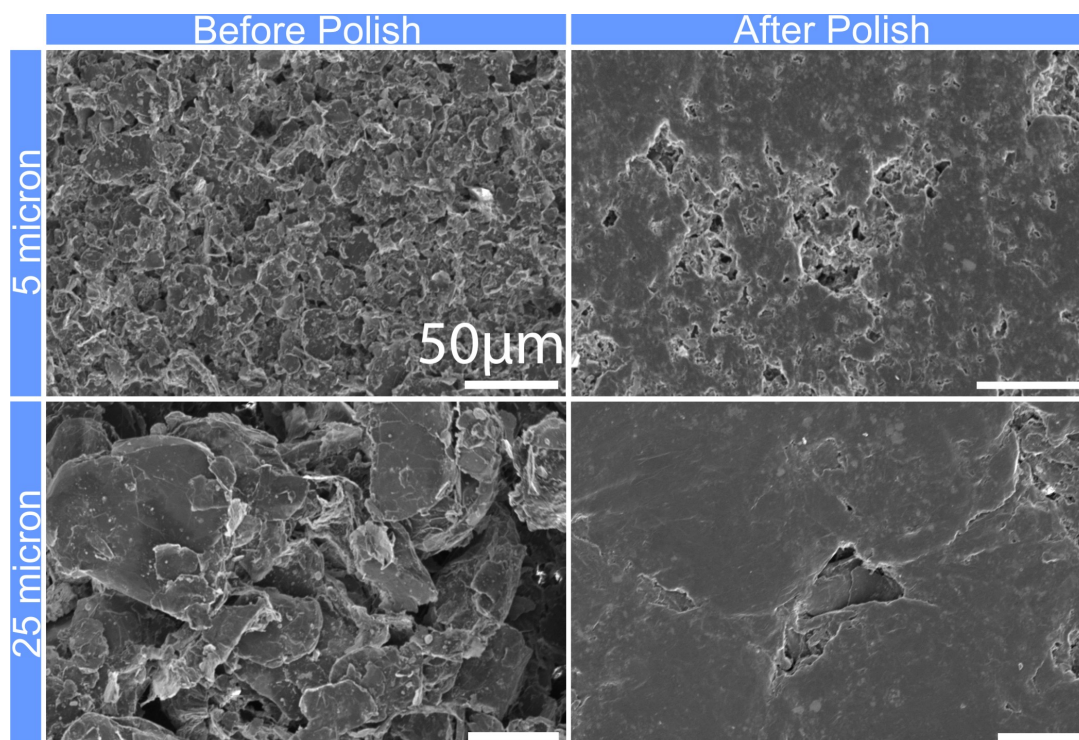


Figure 22. SEM images of two composite coatings (50 wt. % filler particle loading) on paper, before and after polishing/compression. The left column shows images of unpolished S-5 (top) and S-25 μm (bottom) average particle radius; it is clear that there is a range of particle sizes up to twice the average radius. The right column is for the same MLG sizes and similar magnification (scale bar is 50 μm for all images), after polishing. It is clearly seen that the roughness is removed during the polishing and compression step, as particles become oriented parallel to the substrate surface, effectively smoothing the composite, creating a better percolation network for electron transport. The defects in the smooth composite, shown as cavities, are roughly of the same order of magnitude as the initial average particle radius.

tested (5 μm) for both the M- and S-types had roughness average (R_a) values of 6.84 ± 0.4 and 11.11 ± 2.1 μm , respectively. After polishing, the roughness of the samples declined significantly to 2.15 ± 0.1 μm for the M-5 samples, and 1.60 ± 0.3 μm for S-5. Similar results were obtained for the largest MLG radii (25 μm) to compare the opposite end of the particle size spectrum. For the M-25 and S-25 samples, the R_a values before polishing were 33.24 ± 4.1 and 43.4 ± 9.0 μm , respectively. After polishing, they were reduced to 3.88 ± 1.2 μm (M-25) and 3.16 ± 0.6 μm (S-25). The final polishing step dramatically reduces the average roughness to within the same order of magnitude regardless of original particle size, thus suggesting the MLG were oriented parallel to the substrate during polishing and compression, giving rise to the observed smoothness.

Cross-sectional SEM was employed to visualize the “brick-and-mortar” structure formed from the horizontally-aligned MLG “bricks” embedded in the CuPc acrylic polymer “mortar” matrix, as shown in Figure 23. From these coating profile images, the average coating thickness (~ 30 μm) is useful for calculating the total volume of the coating, which is needed for converting surface sheet resistance measurements into volumetric resistivity and conductivity values, as discussed below. The thickness value is only an approximation, and is used only for rough calculations; as can be seen in Figure 23a and Figure 23b, the surface thickness can vary and is also dependent upon the nanoparticle-to-paint solids ratio (For SEM images of the all-paint coating, or 0:100 composite ratio, see Appendix D, Figure D2).

Raman spectroscopy was used to examine the nature of the graphene in the final MLG composites (Figure 23, bottom). The blue shift observed in the G-peak, and the red shift

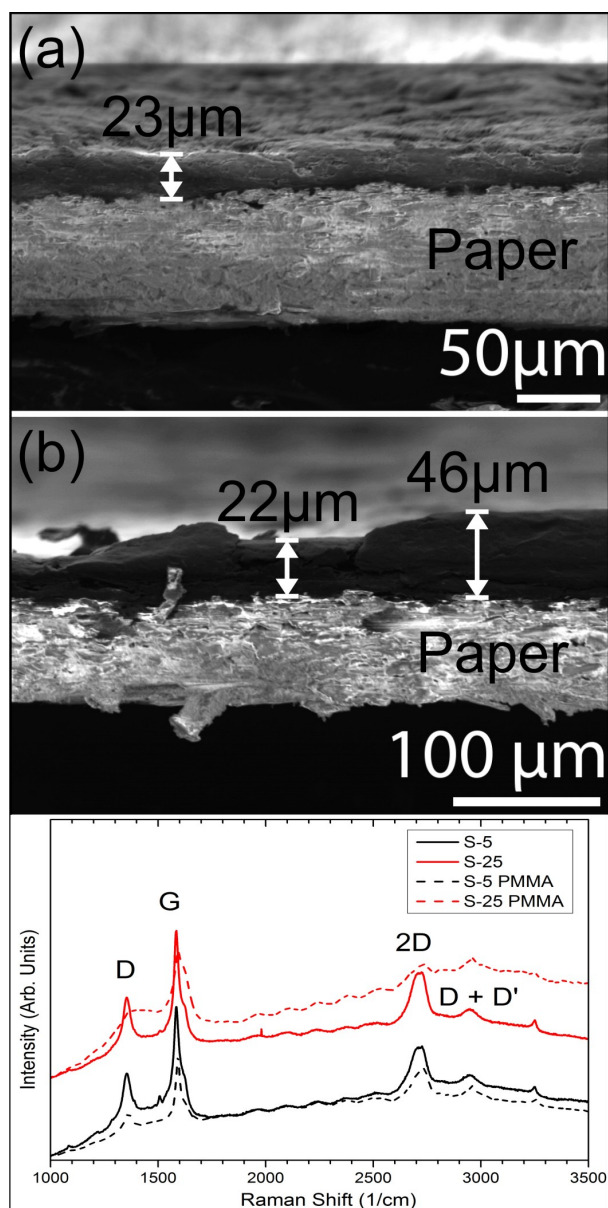


Figure 23. SEM cross-sectional images of composites on printer paper for two representative M-type MLG: (a) 5 μm , and (b) 25 μm . These cross-sectional images are used to estimate coating thickness range, as well as display the brick-and-mortar assembly of the MLG composite. Raman spectroscopy data is also included (bottom) for the two MLG sizes shown, with visible peaks corresponding to n-type doping of both mono- and multi-layer graphene (as compared to the same MLG particles in a PMMA matrix).

observed in the 2D peak, are indicative of n-type doping in multilayer graphene attributed to the presence of CuPc in the composite (149). Comparison measurements were performed by replacing the paint solids matrix with PMMA (See dashed lines in Figure 23, bottom) delivering noticeable relative peak diminishment in both cases; thus, further strengthening the case for addition of doping properties via the CuPC pigment in the final MLG composites. Along with peaks indicative of n-type doping, the Raman data reveals a mixed state of graphene in the composite. The G peak is roughly twice that of 2D, suggesting a majority presence of multilayer graphene, while the D peak suggests the presence of lattice defects (150). However, the aligned MLG stacks after polishing appear to overcome these defects to form a well-connected charge percolation network with low sheet resistance.

Sheet resistance measurements were made for all mass ratios, and compared in terms of particle radii and filler content, as shown in Figure 24 and converted to conductivity values (σ , S/m) in Table V (accompanying I-V curves for all mass fractions for both types of MLG tested are plotted in Figure D3). For comparison, an all-paint coating was measured for resistance to isolate addition of conductivity by the CuPc particles; the paint coating had a negligible conductivity (< 0 S/m). The lowest mass fraction of 20 wt. % MLG (*i.e.*, 20:80) for all types tested fell in the $k\Omega/\square$ resistance regime, with the exception of S-25 ($267 \Omega/\square$). At larger particle radii, resistance is seen to decrease due to the larger average radii of the stacked graphene layers; larger particle radius equates to fewer contact points throughout the percolation network and thus higher conductivity, as each connection made when conducting electrons through the graphene layers would increase contact resistance. In addition, the resistance decreases as

MLG content is increased as expected, until the polymer content is reduced (< 35 wt. % in the final composite) to an insufficient level for adequately adhering the MLG to the substrate during the polishing process. Sufficient polymer content is required to maintain conductivity and durability; as the polymer fraction became a minority in the final composite, more MLG was thus removed during polishing, resulting in increased resistance.

DSC measurements verified the glass transition temperature (T_g) of the dried phthalo green artists paint (151), and compared it to a representative 50 wt. % composite from the S-25 MLG. As shown in Figure D4, the T_g was found to be $\sim 190^\circ\text{C}$ for both samples. The MLG composite (Figure D4, black line) is shown to have sharper transitions as temperature is ramped compared to the dried paint (Figure D4, green line); this corresponds to a more efficient heat flow per gram, due to a greater heat transfer coefficient. With the exception of the increased heat transfer coefficient, the addition of MLG does not significantly alter the thermal stability of the phthalo green paint; making these coatings suitable for applications requiring thermal stability up to 190°C , but not above.

Tape peel and abrasion tests, as conducted on several representative composites, reveal (Figure 25) the extremely durable property of these coatings. Beginning with the peel tests shown in Figure 25a, the resistance was measured as a function of number of tape peels in a given region. The resistance rises almost linearly, but is only slightly higher than the original resistances after 15 peels for all composites tested. This linear trend in conductivity loss, when averaged across all substrates is a measured increase in resistance of only $\sim 1.75 \Omega/\square$ per tape peel, is surprisingly robust and suggests that very little of the charge percolation network is

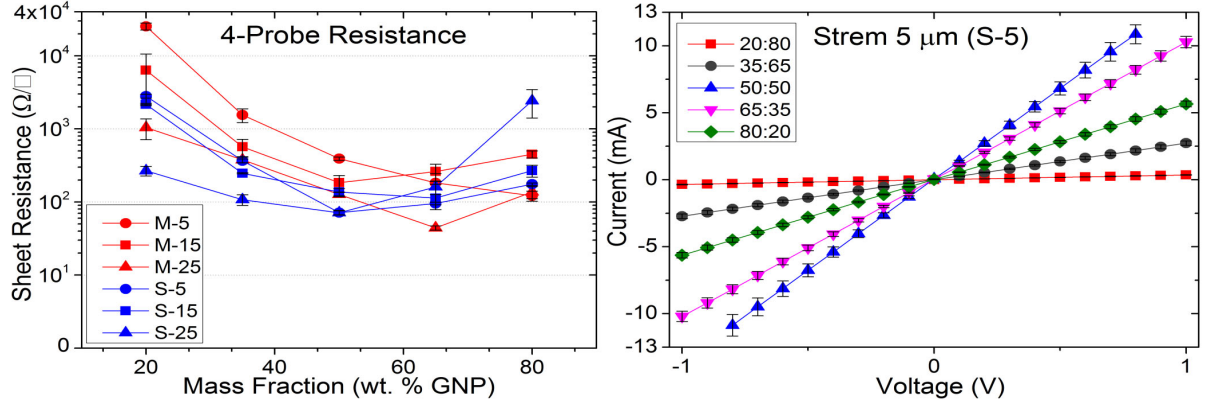


Figure 24. (Left) Log plot of 4-probe sheet resistance as a function of the final mass fraction of MLG in the dried polymer composite for all samples and mass ratios; numerical conductivity values for these are listed in Table V. The resistances for lowest mass fraction (0.2 or 20 wt. %) with the exception of Strem 25 μm were in the $\text{k}\Omega/\square$ regime, the samples with lowest resistance were uniformly found to be in the 50 to 65 wt. % regime. Increased MLG content (above 65 wt. %), with the exception of the xGNP M-5 μm , resulted in insufficient polymer content to adhere the nanoparticles through the polishing process and caused resistance to increase. (Right) Representative I-V curves showing linear Ohmic resistance behavior for the S-5 samples; the slopes match very well with the 4-probe data which has been converted to conductivities (units of S/m, see Table V).

TABLE V

CONDUCTIVITY VALUES (IN S/M) BASED ON 4-PROBE SHEET RESISTANCE
VALUES (VOLUME DETERMINED BY 25 MM \times 25 MM SQUARES WITH AN
AVERAGE COMPOSITE THICKNESS OF 30 μ M) FROM THE PLOT IN FIGURE 24
FOR BOTH M- AND S-TYPES, AND FOR ALL MLG PARTICLE RADII AS MASS
FRACTION OF MLG IN THE COMPOSITE IS INCREASED.

MLG Mass Fraction (wt.%)	20	35	50	65	80
xGNP					
5 μ m	1.3 ± 0.1	21.5 ± 4.6	85.0 ± 4.5	182.1 ± 8.9	274.7 ± 45.13
15 μ m	5.2 ± 9.8	58.5 ± 14.2	181.4 ± 41.8	127.6 ± 29.9	74.1 ± 8.2
25 μ m	32.0 ± 9.2	88.3 ± 7.3	262.8 ± 18.1	755.3 ± 53.4	243.0 ± 52.8
Strem					
5 μ m	11.9 ± 0.7	91.1 ± 5.6	465.3 ± 34.4	348.8 ± 15.0	190.2 ± 7.4
15 μ m	15.4 ± 0.5	134.9 ± 2.2	243.0 ± 27.3	295.2 ± 34.7	124.0 ± 23.0
25 μ m	124.8 ± 17.8	310.1 ± 48.2	468.2 ± 29.7	207.1 ± 200.2	13.7 ± 5.7

damaged by the adhesive tape peel. In addition to tape peel tests, abrasion tests were also carried out for 100 cycles using a plastic disk under two different weights (20 and 70 kPa, Figure 25b and Figure 25c, respectively). The robustness of the coating is once again reflected in the shallow linear behavior of conductivity loss as a function of abrasion cycles. For the 20 kPa weighted abrasion, the increase in resistance is $\sim 0.4 \, \Omega/\square$ per cycle. The 70 kPa abrasion tests displayed an average increase of $\sim 0.55 \, \Omega/\square$ per cycle, as expected due to the increased abrasion weight.

From the AFM/EFM/SKPM images (Figure 26, Figure 27), qualitatively, the pattern of the sample topography (*i.e.*, relative step-height of the coating, Figure 26a), is reproduced closely in the EFM image (Figure 26b). This is not an artifact due to interference of the electrical force image (during the second pass) with the topography, but is ascribed to a simple additive effect of the nanocomposite, locally containing more MLG where it appears to be thicker. However, the surface potential, as measured in the SKPM image (Figure 26c) reveals finer details not observed in the topographical data (Figure 26a); these are ascribed to CuPc domains from the original artists' paint. Figure 26d is an "error" image formed from amplitude deviations against the set-point in tapping mode, thus the image enhances regions with flat topography, in which single MLG particle surfaces are observed (see dashed ellipses). In Figure 27, quantitative results obtained from the AFM/SKPM measurements are shown. From the AFM topographical images (Figure 27a), the root mean square roughness of the surfaces has been extracted (pass number $N = 6$), whereas from the SKPM images (Figure 27b), the average work function (WF) of the effective resulting coating material was calculated, on the imaged areas ($N = 3$).

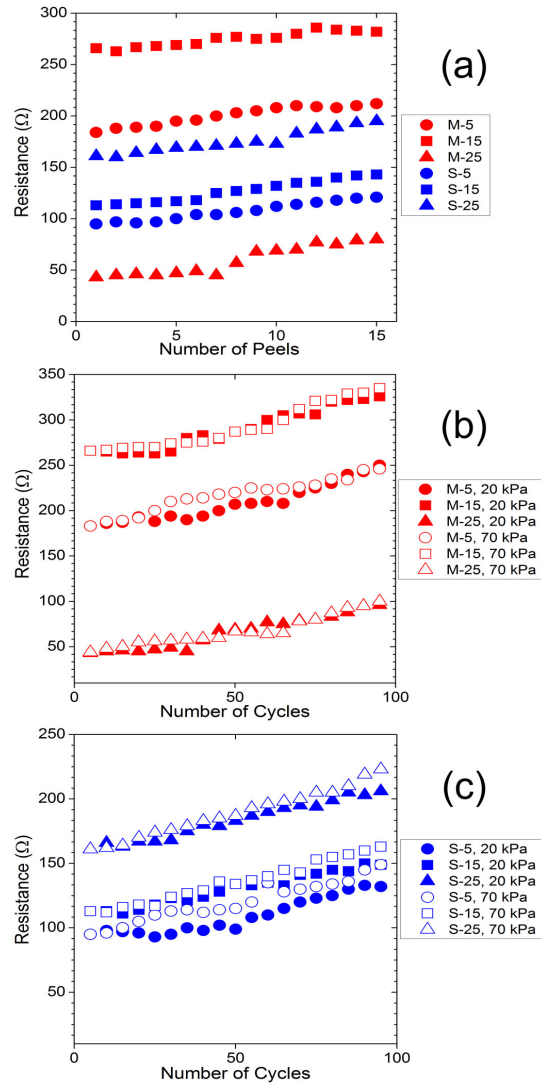


Figure 25. (a) Effect of tape peel tests on the conductivity of the paper samples made with 65 wt. % (65:35) MLG coating loadings. (b) Effect of linear abrasion (at 20 kPa) on the conductivity of paper samples coated with 65 wt. % MLG loadings. (c) Effect of linear abrasion (at 70 kPa) on the conductivity of paper samples coated with 65 wt. % MLG loadings. The legends to the right of the plots refer to the type (M- or S-type) and the particle size (5, 15, or 25 μm) of the composite filler particles; for the abrasion tests (b,c), the type and size is accompanied by the pressure used (20 or 70 kPa).

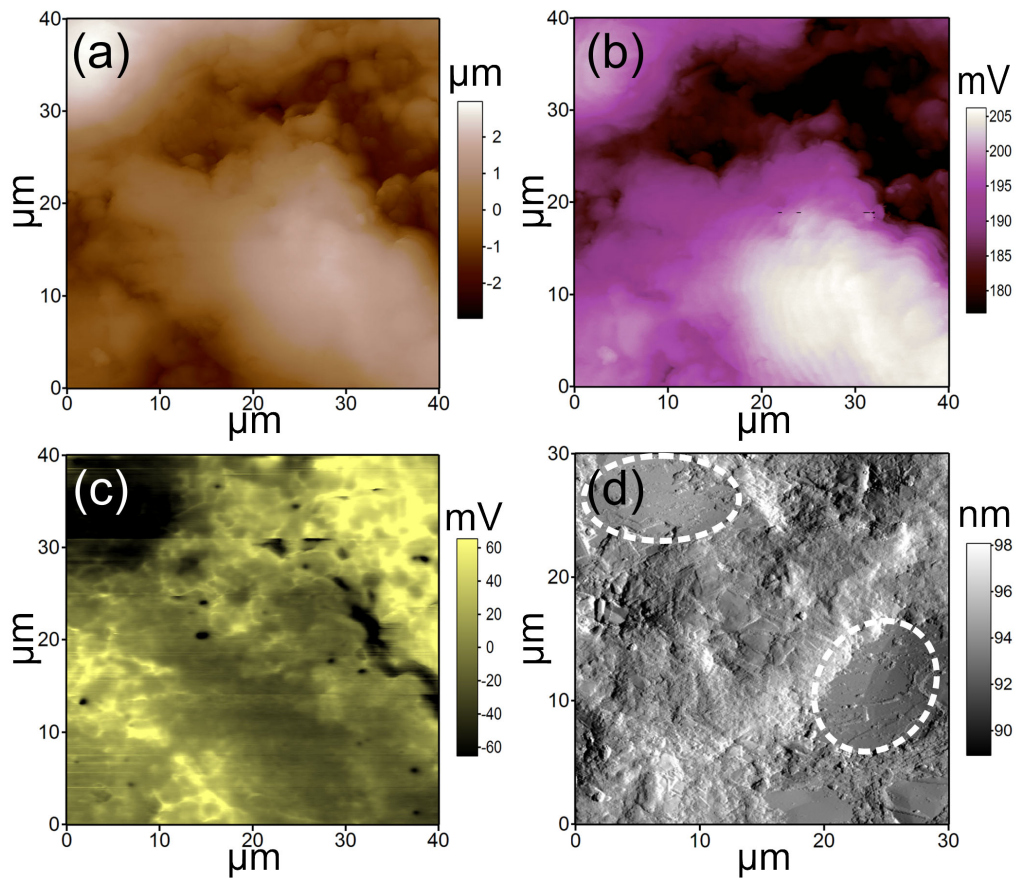


Figure 26. (a) AFM surface topography of M-15 conductive paper sample with 35 wt. % (35:65) MLG loading. (b) Corresponding EFM map of the same conductive paper, and (c) SKPM surface potential map, which is more sensitive to the CuPc domains of the original artists' paint. (d) The amplitude (*i.e.*, deviations against the set-point in tapping mode) is an 'error' image which stresses the regions with flat topography, in which single MLG particle surfaces are observed (see dashed ellipses).

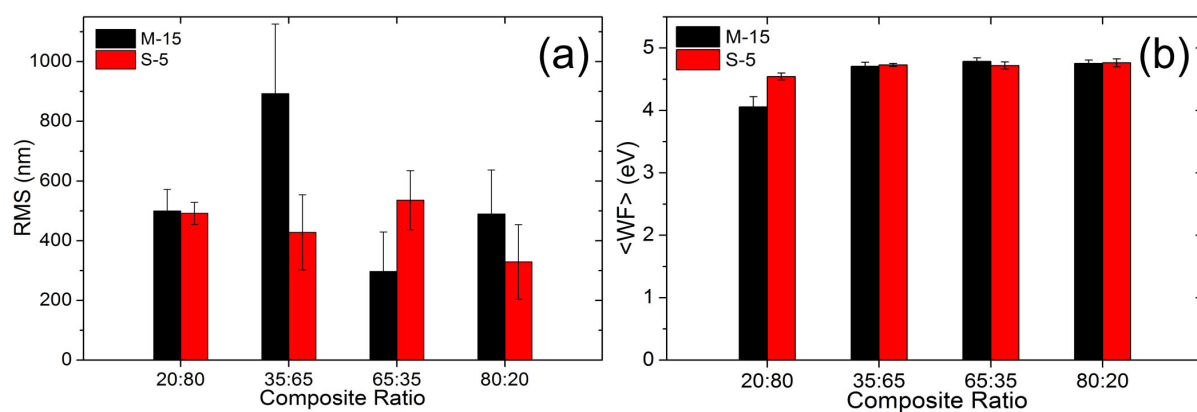


Figure 27. Quantitative results obtained from AFM (a) and SKPM (b) measurements, for M-15 and S-5 samples with different MLG:paint-solids loadings. Uniform work function (WF) indicates that the surfaces of the conductive papers have very uniform surface conductivity, resembling highly-ordered pyrolytic graphite.

The RMS roughness plots (Figure 27a) show that for the M-15 series, the 35:65 values are very different from (*i.e.*, higher than) all others ($p \sim 0.002$ for 20:80, $p \sim 0.0001$ for 65:35, and $p \sim 0.001$ for 80:20). For the S-5 series, the only significant difference occurs instead between 65:35 and 80:20, but to a lower degree (only 5 % significance, as $p \sim 0.014$). Obviously, the larger graphene flakes have a greater impact on the resulting roughness of the composite film. In particular, the intermediate concentration of M-15 at 35:65 provided the highest roughness. Higher MLG loadings most likely result in flakes overlaying one another, having an opposite (*i.e.*, flattening) effect. The smaller flakes of the S-5 series instead show maximum roughness for the 65:35 MLG:paint-solids ratio, thus partly compensating the flake size.

The WF plots (Figure 27b) show that the mean WF values for all samples fall in the 4.0–4.8 eV range. For the sake of WF comparison for carbon-based materials, according to the available literature, in decreasing order one can find ~ 5.2 eV for C_{60} fullerenes, ~ 5.05 for SWCNT, ~ 4.95 for MWCNT, and ~ 4.65 eV of HOPG (152; 153; 154; 155). In fact, the highest values for the current composite are close, and even slightly higher than those for HOPG, whereas much lower values also appear, associated with composite formulations of low MLG content, as observed in the 20:80 sample for example.

For THz EMI testing to demonstrate real-world applicability of the MLG composite, samples were chosen for relative high, medium, and low conductivities to verify the correlation of conductivity and THz radiation absorption/reflection. Namely, two samples with roughly 2-3 $k\Omega/\square$ resistance (S-5 20 wt. % and S-15 20 wt. %, 2.8 and 2.2 $k\Omega/\square$, respectively), two samples between 100-400 Ω/\square resistance (S-5 35 wt. % and S-25 35 wt. %, 366 and 108 Ω/\square ,

respectively), and two samples below $100 \Omega/\square$ resistance (S-5 50 wt. % and S-25 50 wt. %, 72 and $71 \Omega/\square$, respectively). In addition, an all-paint coating was also tested as a control sample (0 wt. % MLG) to verify a negligible influence on attenuation (~ 0 dB). Figure 28 plots the EMI attenuation data (s_{21}) for the frequency range between 0.50 and 0.75 THz. For all samples tested, the figure shows a linear increase in attenuation at higher frequencies, following the well-known Drude model (141). The greatest attenuation occurs for the highest conductivity samples, as expected, namely 50 wt. % S-5 and 35 wt. % S-25; with the greatest attenuation observed (an average of ~ 36 dB over the entire frequency range) for the larger $25 \mu\text{m}$ particle radius MLG. In a similar study (156), composites with carbon nanofibers as particle filler achieved -32 dB attenuation for even higher reported conductivities, suggesting that MLG morphology assists in increased radiation absorption and is competitive as compared to similar materials in the nascent field of THz shielding research.

A simple electrical circuit (See Figure D6) was made from a 50 wt. % S-25 MLG composite sprayed on paper to demonstrate the composite's applicability in real-world conductive paper applications. The sprayed composite reduces the sheet resistance to below $100 \Omega/\square$ and forms an extremely adherent coating. The circuit incorporates the logos from the Italian Institute of Technology (IIT) and the University of Illinois at Chicago (UIC) to demonstrate the joint collaboration which facilitated this research. The three i's in the logos were bridged by LED lights to such that when a 9 V battery is placed upside down on the conductive paper leads, thereby closing the circuit, the i's are "dotted" with a bright white light.

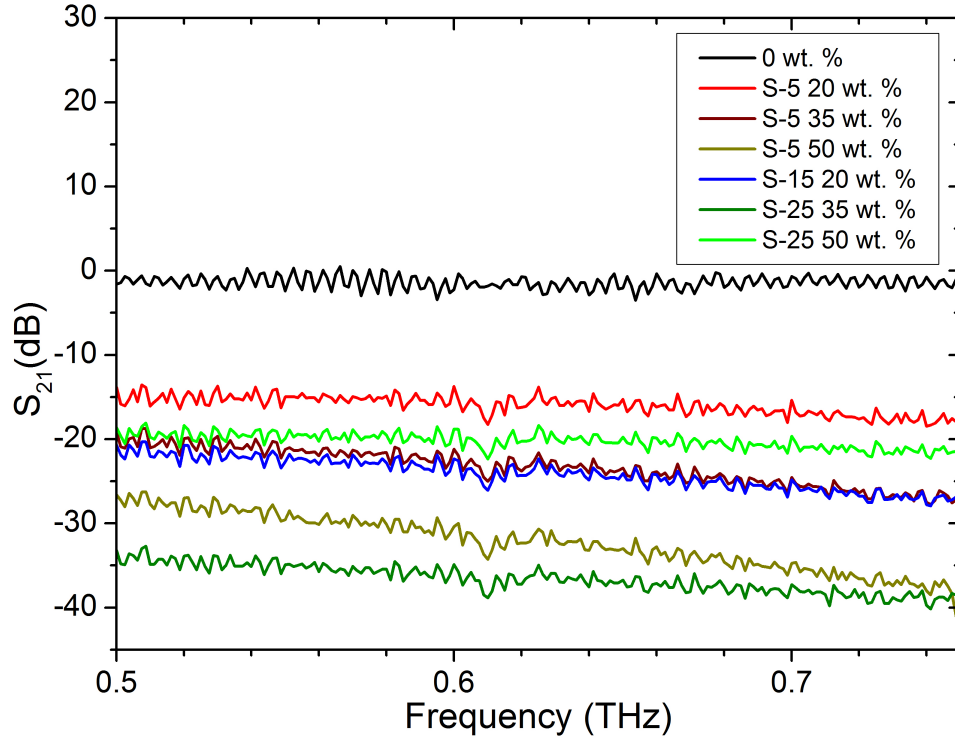


Figure 28. Plot of wave attenuation as a function of frequency between 500 and 750 GHz (0.50–0.75 THz), universally showing a linear increase in attenuation at higher frequencies. The highest level of attenuation was found for the highest conductivity composites (Strem 5 and 25 μm , both 50 wt. % MLG composites) as expected, yet the larger 25 μm particle size showed increased attenuation over the 5 μm particle composite even though both have comparable sheet resistances (50 wt. % S-5 is $72 \Omega/\square$, 50 wt. % S-25 is $71 \Omega/\square$), suggesting that greater particle dimensions positively affect THz EMI attenuation. An all-paint composite (0 wt. % MLG) was also tested to determine effect of the CuPc pigment on the attenuation, having a negligible effect.

CHAPTER 6

HIGHLY ELASTOMERIC & CONDUCTIVE SUPERHYDROPHIC COMPOSITES FOR SMART FABRIC APPLICATIONS

This chapter and its associated appendix (Appendix E) will be submitted for journal publication.

As electronic technology evolves, becoming simultaneously more complex and enmeshed in our daily lives, novel solutions are required to keep pace with the increasing demand. Often, advances in this arena are found in creative uses of common materials. ParafilmTM is one such useful material common in nearly all modern research labs, whose properties have been well-studied for decades. By combining a solution-processed blend of ParafilmTM and carbon nanofibers, an adherent composite can be formed capable of sustaining high strains with recoverable conductivities. In addition to the conductive element in the presented work, the composites are also extremely water-repellent, maintaining high performance through the maximum stretch ratios tested (> 600 % elongation). Such materials would be invaluable in corrosion-resistant wearable electronics and flexible power storage devices. The use of these common materials necessarily maintains a low cost for production, and combined with a large-area spray-cast approach, these composites can be easily transitioned into any number of specific applications in booming fields of research and commercial products. A novel flexible composite is herein pre-

sented capable of high conductivities and superhydrophobicity, which can be further modified with the addition of doping or catalyst nanoparticles for tunable electrode applications.

6.1 Motivation

The greater complexity of circuitry and power storage needs in modern electronics underscores the demand for simultaneously *more durable and versatile* functional components. Elastomeric conductive composites have shown promise for their ability to withstand high strain with recoverable conductivities (157; 158; 159; 160; 161; 162), much of the current interest involves battery applications (163; 164; 165). In addition, super-repellent conductive composites have been heavily investigated for their resistance to failure under wet or corrosive conditions (166; 167; 168; 95; 169). Combining stretchable and superhydrophobic functionalities is advantageous for a large variety of electronics applications, namely flexible, foldable, and wearable electronics, as well as printable circuitry. While there exist many examples (170; 171; 172) of such multifunctional conductive materials in the literature, their performance and recovery is not addressed under extreme high strain conditions ($> 300\%$, or $\lambda > 3$, where $\lambda = L_f/L_i$). An extremely robust conductive and superhydrophobic nanomaterial composite is presented, capable of withstanding stretching up to 600% ($\lambda = 6$) original size with high recovery rates of both the conductive and superhydrophobic properties. The spray-cast composite is formed from solution-processed ParafilmTM (PF) and a carbon nanofiber (CNF) ink dispersion, delivering a substrate-independent, low-cost, and large-area flexible conductive platform. The performance far exceeds previous performance benchmarks (160; 173; 164; 174) for elastomeric and flexible composites of either conductive or superhydrophobic property, yet possessing both.

CNF have been used extensively in composite materials since their re-discovery in 1991 (175). They have been shown to be effective in composite applications for high-conductivities (176; 177; 178; 179), enhanced heat transfer (180; 181; 182; 183; 184; 185), electromagnetic shielding (48; 186), and fluid repellency (71; 187; 188), among many others. The rationale for choosing CNF in the present application is their unique ability for forming excellent electronic charge percolation networks, even under high mechanical strain by virtue of their high aspect ratio (*i.e.*, high surface area to volume) (189; 190; 191). In addition to their ballistic electron transport capabilities, CNF offers unique reentrant surface texture which is ideal for robust superhydrophobic surfaces (61). Similar carbonaceous materials have been used in the past to dope paraffinic media for increasing heat transfer (192; 193), but an in-depth characterization of these composites for elastomeric conductive potential is lacking in the literature.

PF is an ubiquitous material used in almost all modern laboratories as a vapor barrier for sealing containers to prevent solvent evaporation; although, PF has also found use as grafting scaffolds in botanical applications (194; 195), gas chromatography (196), as well as medical testing (197; 198; 199). To the best of our knowledge, there have been no published attempts at either solution-processing PF for use in a composite, or embedding nanomaterials in PF to generate added functionality. The proprietary blend of paraffin waxes and polyolefins used in the manufacture of PF produces a slightly hydrophobic and self-adherent substrate; specifically made to have an irreversible elongation and thinning as the material is stretched. The adhesion of the PF polymer matrix to a given substrate, in our case high-strain sustaining natural rubber strips, is what enables the elongation of the PF composite to become pseudo-reversible.

Upon relaxation from a high-strain state, the adherent properties of the composite allow for an accordion-like collapse while still retaining the charge percolation network of the CNF, and also maintaining the hierarchical micro/nanoscale surface roughness required for robust fluid repellency.

Spray-cast functional composites have been proven viable in large-scale and substrate-independent applications (41; 63; 55; 200; 47). In this work, the multi-functional nanomaterial/polymer composite is spray-cast onto natural rubber substrates and characterized for high-strain elastomeric, superhydrophobic, and electro-conductive properties. The choice of natural rubber as a substrate was made solely for testing the properties before and after extreme stretching cycles, of which the natural rubber was observed to mechanically fail after stretching to $\lambda = 7$, or 7 times the original size; therefore, a maximum λ -value of 6 was determined to be the upper bound in our testing and, as stated prior, far exceeds previous performance benchmarks for similar materials.

The performance of the presented composite is exceptional in both electro-conductive or water-repellent applications, and the composite can be utilized in a wide variety of corrosion-resistant electronic devices in wet, dry, and high-strain situations. The composites form a base for electrical design and future characterization, with potential for the addition of doping or catalyst nanoparticles for refined functionality and specific application (*e.g.*, cathode, anode, *etc.*).

6.2 Experimental

6.2.1 Materials

High heat-treated carbon nanofibers (CNF) were purchased from Applied Sciences (Pyrograf III, PR-24-XT-HHT CNF, 40-100 nm dia., < 30 μ m length after sonication). Parafilm™ (PF) was purchased from Cole-Parmer (Parafilm Wrap PM992, 2" Wide; 250 Ft/Roll). Toluene was purchased from Sigma-Aldrich (244511; anhydrous, 99.8%). Sheets of rubber were purchased from McMaster-Carr (86085K101; Abrasion-Resistant Natural Latex Rubber Sheet 1/16" Thick, 12" \times 12"). Silver paint (Ted Pella, Inc., Prod. # 16034, 15 g Pelco® Colloidal Silver) was used to form contacts on the composite for 4-probe sheet resistance measurements. Deionized water was used as the probe liquid for dynamic and static water droplet contact angle and roll-off angle measurements.

6.2.2 Preparation

Sprayable CNF/PF dispersion preparation: A 10 wt. % stock solution of PF in toluene was prepared initially by cutting the required mass amount of PF from the roll and placing the solid film in suspension with the toluene. The sealed suspension was heated at 75 °C under mechanical mixing for ~1 hour, or until the Parafilm is observed to be completely dissolved; forming a light-gray viscous suspension. The total solids content of the final dispersion was maintained at 5 wt. % to avoid high viscosities and clogging during spray. As an example, to prepare 18 g of a 50 wt. % CNF composite (50:50, CNF:PF), 0.45 g of CNF are weighed out in a 20 mL glass vial. 15.05 g of toluene is then added and the mixture is probe-sonicated (Sonics & Materials, Inc., 750 W, 13 mm probe dia., 20% amplitude, 20 kHz) for 1.5 min (the

remainder of the toluene in the final dispersion will come from the 10% PF stock solution). 4.5 g of the 10 wt. % PF in toluene is added to the sonicated mixture drop-wise under mechanical mixing, and subsequently bath-sonicated (Branson 8200, 20 kHz, 450 W) for 5 min. to ensure adequate mixing and a homogenous final dispersion.

CNF/PF composite application onto rubber strips: Strips ($1.3 \times 7.5 \text{ cm}^2$) of natural rubber were cut from the sheet and affixed to a cardboard backing for spraying; strips were mounted in a $7.5 \times 9 \text{ cm}^2$ spray area. The as-received rubber strips had both a rough and smooth side, where the smooth side was always the side to which the composite was applied to avoid the addition of any roughness into the composite from the substrate itself. The CNF/PF dispersion was spray-cast (Blick Art Supplies 25010-0300; VL-3 siphon-feed airbrush) onto the rubber strips from a distance of $\sim 25 \text{ cm}$ to allow adequate spray atomization. The samples were then allowed to dry in open air for 24 hours after spraying before testing to ensure adequate removal of any residual solvent, although the toluene typically evaporates from the composite on the order of minutes.

6.2.3 Characterization

The coated natural rubber strips are clamp-mounted on a motorized slide (Vexta stepping motor, model PX245, see Figure E1) with an initial 2.5 cm gap. One clamped end is held stationary, while the other is withdrawn in increments of 2.5 cm ($\lambda = 2, 3, \text{ etc.}$). The stretch ratio λ can easily be converted to engineering strain, e , by the equality: $e = \lambda - 1$. Stretch speeds were also varied within the capabilities of the motor ($\sim 0.5 \text{ m/s}$) and found to have a negligible impact on performance, and were thus held constant at $\sim 1 \text{ mm/s}$. At each interval of

elongation, or stretch ratio, 4-probe resistance (HP 34401A Multimeter) and dynamic contact angles measurements were performed. To attain composite sheet resistance (R_s , units of Ω/\square , see Equation 1.7), two thin strips (~ 0.25 cm) of silver paint were applied across the width of the rubber strips perpendicular to the direction of stretch as contact points for the 4-probe measurements, forming a uniform square of conductive composite between. Three separate sheet resistance measurements were collected at each λ -value and averaged individually for all composites.

CA measurements were performed *in situ* on the motorized slide; water droplets were syringe-extruded on the composites, and similarly withdrawn, using a 1 mm needle-tip such that probe droplet diameters ranged from 1 mm to 4 mm size. For droplet roll-off angle measurements, the entire motorized slide was mounted on a tilting stage with 10 μL droplets placed on the level composites; the entire slide was tilted until the droplets were observed to roll off, thus determining the sliding, or roll-off angle.

Scanning electron microscopy (SEM, Hitachi S3000N VPSEM) was used to examine the morphology of the composites from an unstretched state ($\lambda = 1$), two strain ratios ($\lambda = 2, 6$), and after returning to an unstretched state from max deformation ($\lambda = 6 \rightarrow 1$). Special SEM stubs were machined in-house to maintain stretch ratios (See Figure E2) after removal from the stretch apparatus for imaging. SEM images were also employed to examine cross-sectional profiles of the composites in the aforementioned stretch ratios to determine the extent of elongational thinning that the composite experienced during strain cycles. Similar specialized SEM stubs as those shown in Figure E2 were also designed to facilitate these profile images

(See Figure E3). The composite thickness during elongation and after is helpful for determining the volume of the composite, when coupled with R_s values, composite conductivities (σ , units of S/m) can then be estimated.

6.3 Results & Discussion

SEM imaging (Figure 29) was employed to visualize a 50 wt. % CNF composite surface on rubber through a full stretch cycle ($\lambda \rightarrow 6 \rightarrow 1$): before stretching (Figure 29a), at two points of sustained strain ($\lambda = 2$, and 6, Figure 29b and Figure 29c, respectively), and an after image (Figure 29d) where the stretched composite relaxes to its original state ($\lambda = 1$) to assess morphological recovery of the surface. From the before image in Figure 29a, the high level of reentrant nanostructure roughness in the composite from the cylindrical CNF is clear, as well as some hierarchical micro-structures formed from larger agglomerates of CNF and PF. The roughness generated from the randomly-oriented and PF-clad CNF results in a highly-effective charge percolation network. Thus, any current traveling through the composite would experience low resistance due to the large number of charge-conducting pathways; nominally seeking the path of least resistance.

In Figure 29b and Figure 29c, the direction of stretch becomes evident in the composite as fissures begin to form, and greater CNF alignment appears; this is much more evident in the extreme case of $\lambda = 6$, but it will be shown that the charge percolation network remains intact, albeit damaged to some extent. Figure 29d shows the composite surface after returning to a relaxed state ($\lambda = 1$) resembling an accordion-like compression; this is primarily a result of the irreversible nature of PF elongation. The *irreversible* elongation of PF is overcome in

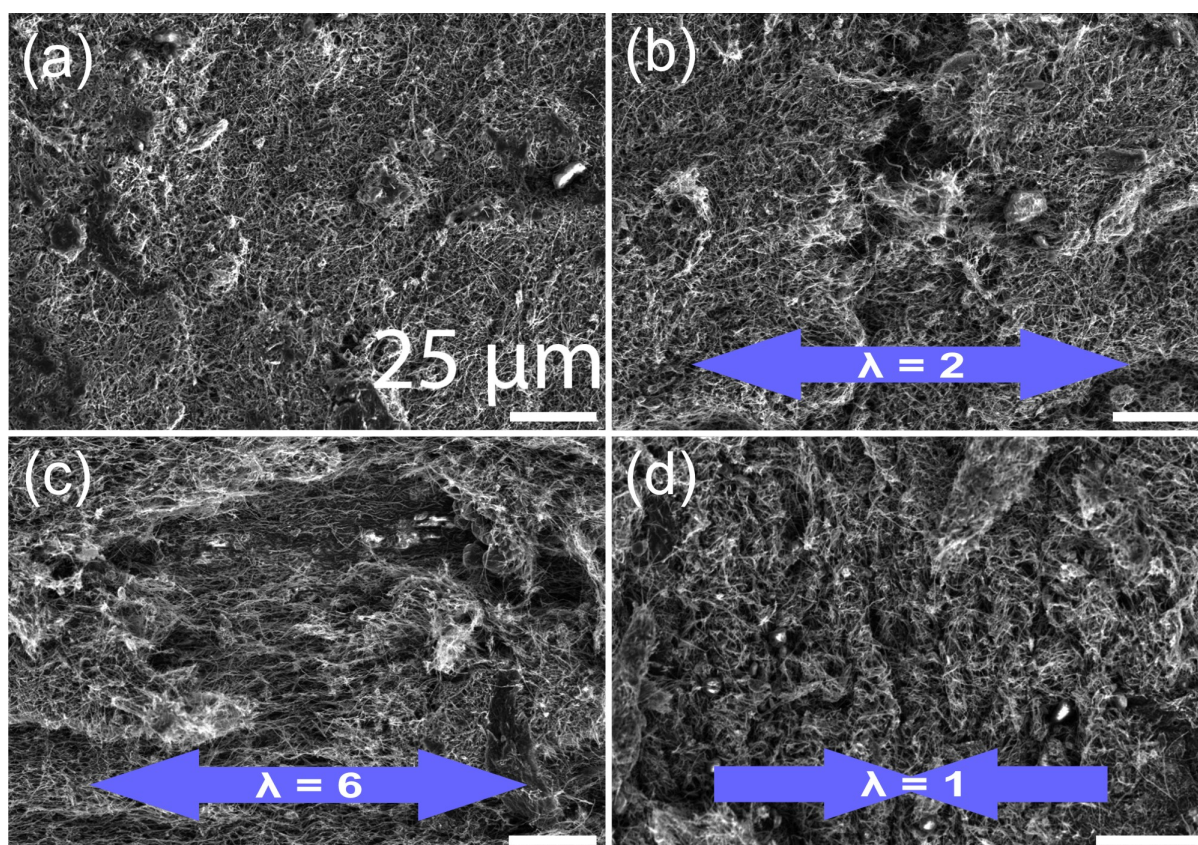


Figure 29. SEM images of a stretch sequence for a 50 wt. % composite on natural rubber substrates. (a) Before the stretch cycle, $\lambda = 1$. (b) $\lambda = 2$. (c) $\lambda = 6$. (d) After composite is allowed to relax to an unstretched state, $\lambda = 1$.

part by the excellent adhesion of the composite to itself and the rubber, aided by the *reversible* elastomeric properties of the natural rubber substrate. Figure 29d remains remarkably similar in morphology to the original composite surface, yet with clear fold lines formed perpendicular to direction of stretch, and similarly, the fissure lines. It will be shown that, while the current transfer network becomes more torturous as a result of the extreme stretch, the network remains intact, possessing some self-healing attributes in the form of repaired pathways across folds in the relaxed composite.

The ratio of CNF to PF in the composites was varied from low to high CNF filler content (20, 35, 50, 65, and 80 wt. % CNF) relative to PF; the electrical resistance of each ratio was measured as a function of deformation (*i.e.*, stretch ratio λ) from original size ($\lambda = 1$), through the maximum case of $\lambda = 6$, and allowed to relax again to $\lambda = 1$. From the left plot in Figure 30, the sheet resistance increases fairly linearly with stretch for all composites until $\lambda = 4$, where it then increases more rapidly for 3 of the composite ratios (35, 50, and 80 wt. %) until the maximum λ value, 6. When initially relaxing from $\lambda = 6$ down to 5, the resistance drops dramatically for all the composite ratios, suggesting a re-invigoration of the conductive CNF percolation network which was previously stretched to nearly linear orientations (Figure 29c) along the stretch axis, severely limiting the charge-conducting pathways. From this point of stretch at $\lambda = 5$, continuing to a relaxed state at $\lambda = 1$, the resistance is seen to increase once again in a nearly linear fashion (with the exception of the 20 wt. % CNF composite which is considered to be anomalous, containing the lowest mass fraction of conductive filler) and returning to the poor resistance observed in the maximum stretch. This is clearly indicative of

irreversible damage done by stretching to such high levels of strain, suggesting a lower maximum stretch is needed to attain a higher degree of reversibility for the composite's conductivity.

Figure 31 displays profile SEM images which were captured at similar stretch ratios as those shown in Figure 29. This enables an approximation of composite thickness due to elongational thinning under strain deformation as shown in Figure 32. Surprisingly, the measured thickness of the relaxed composite decreases from the initial dimensions. This is likely due to irreversible elongation in the substrate, and possibly compression effects of the high strain increasing the density of the composite. The coated substrates were observed during elongation to thin in two dimensions as length was increased; both thickness and width. To ensure accurate R_s measurements, the distance between the two strips of silver paint used for 4-probe contact points were equivalent to the reduced width at various elongations. To convert these values to conductivities, a more accurate representation of the composite robustness, the volume of the composite was calculated using the power law curves shown in Figure 32; elongation thickness $t_{\text{stretch}} = 22.7\lambda^{-1.14}$, relaxation thickness $t_{\text{relax}} = 10\lambda^{-0.59}$. The curve-fitted thickness values were coupled with obtained R_s values to derive composite conductivities (σ), as shown in Figure 33.

In any real-world application for a flexible and elastomeric electronic components, such high deformation ($\lambda = 6$) is well beyond most current robustness requirements; this high stretch ratio was chosen to gauge the robustness of the composites and to determine an ideal ratio of filler particle to polymer for further testing. From the left plot in Figure 30 and Figure 33, it is clear the 65 wt. % CNF composite forms the most ideal ratio of CNF to PF of those tested. This

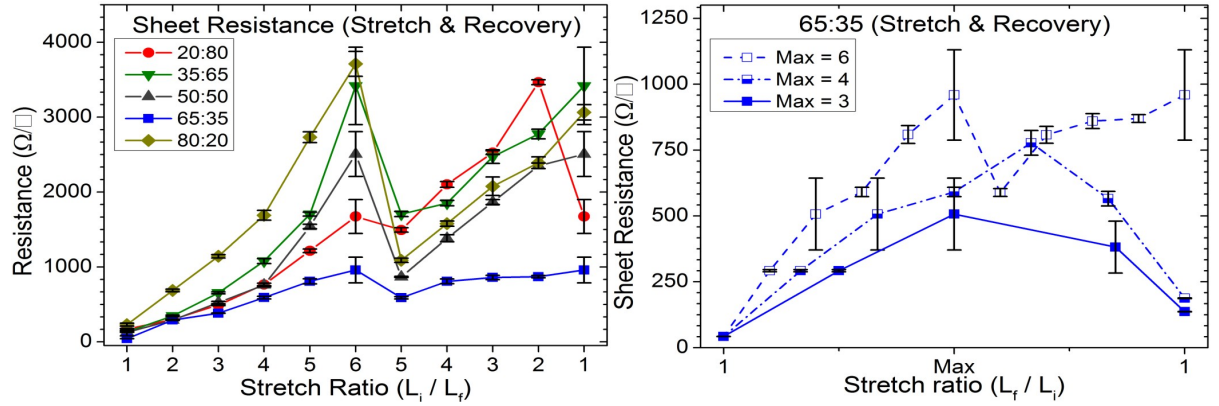


Figure 30. (Left) Sheet resistance values for all ratios of CNF to Parafilm tested (CNF:PF), through one full stretching cycle from $\lambda = 1$ to 6, then returned to a relaxed position ($\lambda = 1$).

The 65 wt. % CNF composite has the greater recovery performance after the stretch cycle, and was thus chosen for further testing at lower strain. (Right) The 65 wt. % CNF composite was further tested at lower maximum stretch values ($\lambda = 4$, and 3) compared to the extreme $\lambda = 6$ stretch ratio. Stretched composites with λ -values of 4 and 3 have a much higher recovery performance suggesting $\lambda = 4$ may be the upper limit of sustainable strain with recoverable properties.

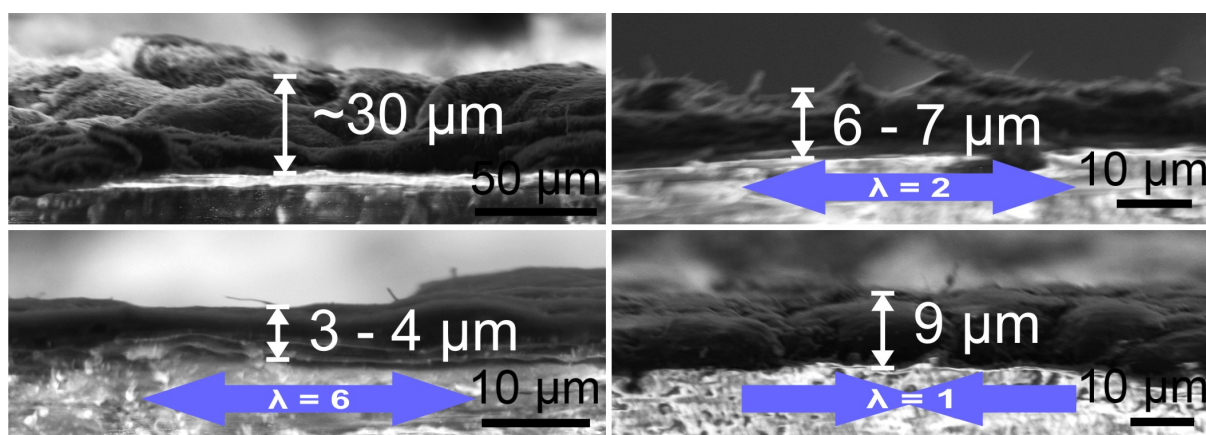


Figure 31. Cross-sectional profile SEM images of a stretch sequence for a 50 wt. % composite on natural rubber substrates. (a) Before the stretch cycle, $\lambda = 1$, average coating thickness $\sim 30 \mu\text{m}$. (b) $\lambda = 2$, average coating thickness $\sim 6\text{--}7 \mu\text{m}$. (c) $\lambda = 6$, average coating thickness $\sim 3\text{--}4 \mu\text{m}$. (d) After composite is allowed to relax to an unstretched state, $\lambda = 1$, average coating thickness $\sim 9 \mu\text{m}$.

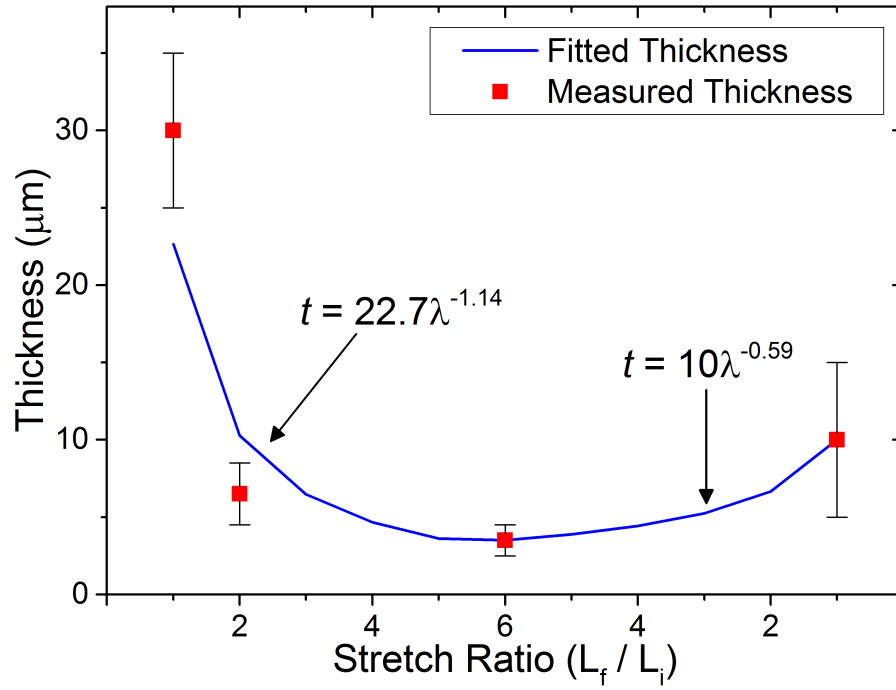


Figure 32. Average thickness (t) values of the composite (red squares) at stretch ratios $\lambda = 1$, 2, 6, and after relaxation to 1. Elongational thinning follows a power law curve, shown as a solid blue line. The power law equation derived from the experimental data points allows for an estimation of coating thickness, and therefore composite volume. For the elongation and relaxation cycles, there are two distinct power law curves as the properties of the composite have changed through deformation.

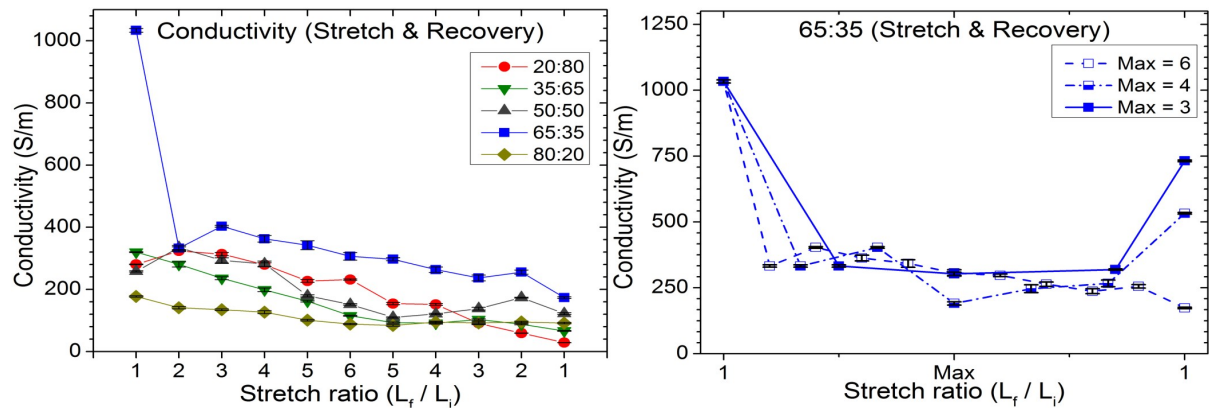


Figure 33. (Left) Conductivity values for all ratios of CNF to Parafilm tested (CNF:PF), through one full stretching cycle from $\lambda = 1$ to 6, then returned to a relaxed position ($\lambda = 1$).

The 65 wt. % CNF composite has the greater recovery performance after the stretch cycle, and was thus chosen for further testing at lower strain. (Right) The 65 wt. % CNF composite was further tested at lower maximum stretch values ($\lambda = 4$, and 3) compared to the extreme $\lambda = 6$ stretch ratio. Stretched composites with λ -values of 4 and 3 have a much higher recovery performance suggesting $\lambda = 4$ may be the upper limit of sustainable strain with recoverable properties.

filler particle ratio was chosen for further characterization at two lower max stretch ratios, $\lambda = 4$ and 3. The samples show a much greater degree of performance recovery when λ is confined to less than or equal to 4. Stretched composites with λ -values of 4 and 3 recover to 1.83 and 2.63 R/R_o (where R_o is the original sheet resistance value), respectively.

Dynamic repellency to water was characterized in Figure 34, with contact angle (CA) hysteresis (advancing, receding CA, Figure 34, left) and sliding angles (Figure 34, right) as a function of CNF filler mass for the unstretched ($\lambda = 1$), max stretch ($\lambda = 6$), and relaxed ($\lambda = 6 \rightarrow 1$) deformations. The 0 wt. % (0:100 ratio) represents an all-PF coating on natural rubber, also characterized for CA hysteresis to better visualize the evolution of the enhancement to water repellency imparted by the CNF filler particles. For all CNF filler ratios, the advancing angles are all well above the superhydrophobic regime ($> 150^\circ$). The receding CA (for all but the 20 wt. % CNF composite), also approach 140° delivering low hysteresis values below 20° . This indicates extremely low adhesion of the water to the composite surface made possible by the nanoscale roughness of CNF combined with the lower surface energy of the PF; this is verified by extremely low droplet roll-off angles ($< 7^\circ$) for all but the 20 wt. % composite. Hysteresis and roll-off angle plots indicate that the repellency is negligibly affected by the extreme stretch of the composite, retaining robust superhydrophobic performance through even the max stretch ratio ($\lambda = 6$). This retention of the superhydrophobic property after such severe mechanical deformation has never been reported for any other composite material, suggesting a novel advance in flexible repellent composites. Uniquely, the 20:80 ratio is extremely ‘sticky,’ 0° receding CA with no sliding angle. This anomalous behavior is likely due to the low CNF

concentrations resulting in inadequate roughness of the surface; the limited roughness appears to provide just enough surface asperities for the droplet interface to gain purchase and adhere (*i.e.*, pinning) as compared to the relatively smooth all-PF surface. At higher filler ratios, the roughness is sufficient to reduce the liquid to solid interface to negligible levels, thus allowing the droplet to rest on pockets of entrained air and therefore glide across the surface under low tilt angles.

Figure 35 demonstrates the durability for the best-performing 65 wt. % CNF composites through multiple strain cycles. The composite was cycled through 50 stretch routines from $\lambda = 1$ to 6, and back to 1 for each full cycle. The CA (Figure 35, Left) hysteresis and electrical resistance (Figure 35, Right) were recorded as a function of stretch cycle to determine robustness of the composite under excessive deformation. At discrete intervals of stretch cycling, namely 5, 10, 25, and 50, the performance was characterized for both sheet resistance and repellency. The half-cycles, when the composite was returned to an unstretched state before another full stretch are referred to as 5.5, 10.5, *etc.*. For CA hysteresis measurements, the performance is relatively unchanged, further strengthening the claim for a novel super-repellent composite capable of out-performing any preexisting coating currently on the market, or reported on in the literature. Unfortunately, the sheet resistance values are not quite so robust, and as such, the max stretch ratio was reduced to ascertain performance recovery at lower λ -values. The recovery performance improves considerably when the max λ -value is reduced to 4 for the 50 cycles; and even more so at $\lambda = 3$ (Figure 35, Left). The $\lambda = 3$ variation in sheet resistance

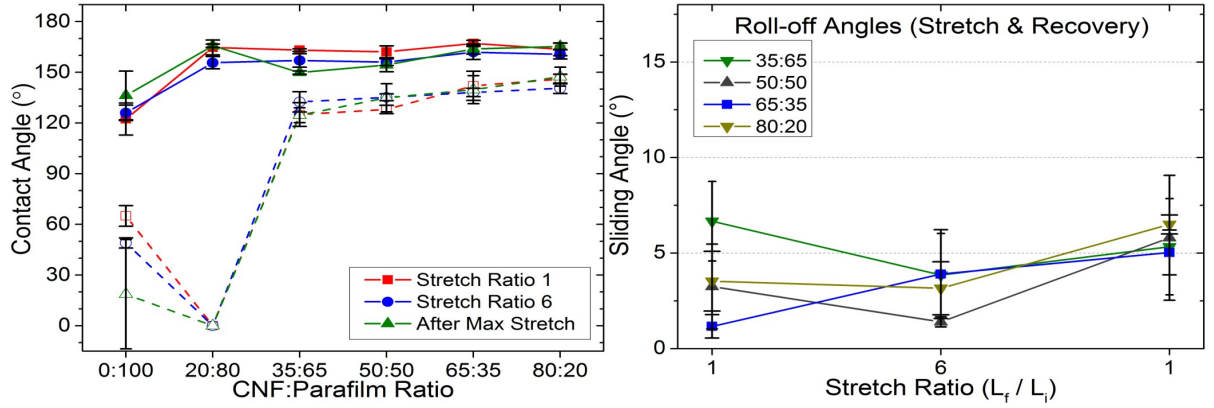


Figure 34. (Left) Contact angle hysteresis measurements as a function of CNF mass fraction, through a full stretch cycle ($\lambda = 1 \rightarrow 6 \rightarrow 1$), advancing (solid line) and receding (dashed line) are both displayed with the difference referred to as CA hysteresis ($\Delta\theta = \theta_{\text{ADV}} - \theta_{\text{REC}}$). The superhydrophobic performance remains relatively unchanged through the extreme stretch conditions, suggesting an extremely robust fluid repellency. (Right) Sliding angle data for the same stretch cycle. With the exception of the 20 wt. % CNF composite (no sliding angles), all sliding angles are well below 10° , demonstrating high droplet mobility on the surfaces even under maximum strain. The 20:80 ratio was determined to be ‘sticky,’ attributed to the high CA hysteresis (low receding CA reflect high droplet adhesion to the surface).

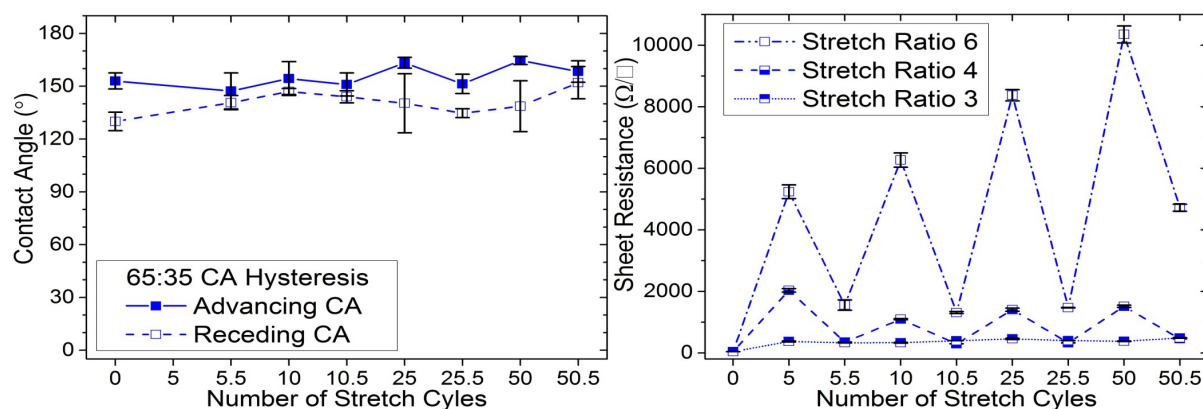


Figure 35. The best-performing composite, 65 wt. % CNF, is tested under 50 cycles of stretching to determine durability after prolonged use. Contact angle hysteresis (Left) and electrical resistance measurements (Right) for a 65 wt. % CNF composite through 50 stretch cycles. Half cycles (*i.e.*, 5.5, 10.5, *etc.*) represent the coating returned to a relaxed state before the next high strain cycle.

through 50 cycles is almost negligible, resulting in one of the most robust electrically conductive composites heretofore reported.

The novel conductive composite that is both superhydrophobic and highly elastomeric demonstrates extremely high performance and recovery under severe conditions. Such materials have potential in flexible fabric electronics where deformation-resistance is an intrinsic requirement. Future modifications to such composites could easily incorporate any number of doping or catalyst nanoparticles for added functionality by incorporating them with the CNF

during preparation. There also exists potential for utilizing the present method for solution-processing of PF with polymer blends such that the elastic PF matrix could be made more conductive. These blends may possibly detract from the elastic property but could yield a significant boost in electronic performance.

CHAPTER 7

PVDF NONWOVENS: OIL-WATER EMULSION SEPARATION, ENERGY HARVESTING, AND SELF-DEFOULING FILTRATION MEDIA

As current resources dwindle and purified filtrate oil becomes more difficult to attain, there exists a growing industrial demand for efficient separation of oil-water emulsions. Oil-water emulsions are of special interest to a diverse array of industries, such as aluminum, steel, food, textile, and petrochemical. Hydraulic fracturing (*i.e.*, fracking) is only one example of the current crisis caused by oil and water shortages world-wide, requiring *vast amounts* of purified water to extract the natural gas, and producing *billions of gallons of waste-water* in the process (See Figure 36). Such contaminated oil-water mixtures, if left untreated, can prove detrimental to the environment, resident populations, and infrastructures. Most conventional techniques for separating immiscible oil/water mixtures are not effective for emulsions, and traditional membrane-based separation is energy-intensive with fouling issues and limited flux. Large-area, low-cost nonwoven filter media with fine fiber diameters (*i.e.*, high surface to volume ratio) and tunable wettability can address these demands, for nearly all relevant demulsification applications, by virtue of their tunable functionality. Polyvinylidene fluoride (PVDF), a semi-crystalline polymer, has been extensively studied due to its low cost, high melting point (170°C), continuous service temperature up to 150°C, non-reactive properties, exceptional

chemical resistance, thermal and weathering stability, and outstanding dielectric and piezoelectric properties. Such a degradation-resistant material is ideal for filters undergoing exposure to a wide range of acids, bases, and harsh solvents, even UV/gamma radiation. Novel PVDF nonwoven fabrics with $\sim 1\ \mu\text{m}$ fiber diameters are presented for the efficient separation of oil/water micro- and nano-emulsions. The work makes use of state-of-the-art technology developed at N.C. State University (NCSU) in collaboration with the University of Illinois at Chicago (UIC) to produce the first of these nonwovens; previously impossible by other means due to PVDF's low melt strength, forcing ultra-low processing speeds. In addition, PVDF's piezoelectric functionality, up to 10 times that of any other fluoropolymer, if harnessed, could yield large-scale fabrics for energy harvesting applications and self-defouling filtration.

7.1 Introduction

Polyvinylidene Fluoride (PVDF) nonwoven properties were evaluated based on fiber dimensions and added functionalities (*e.g.*, liquid repellency, electro-conductivity, piezoelectric function). PVDF fabrics were produced at North Carolina State University and supplied to the University of Illinois at Chicago (UIC) for characterization and additional functionalization through the application of fiber-conforming dip-immersed, or spray-cast, nanocomposite coatings; other avenues of fiber modification (thermal-, solvent-induced, *etc.*) are also considered. Of primary interest were any treatments to enhance the antifouling properties of the PVDF nonwovens, primarily through tunable adhesion of any conformal treatments, modification of wettability, and self-cleaning ability via hierarchical surface texture imparted through the addition of low surface energy fillers; any added functionality, which could be tuned through the

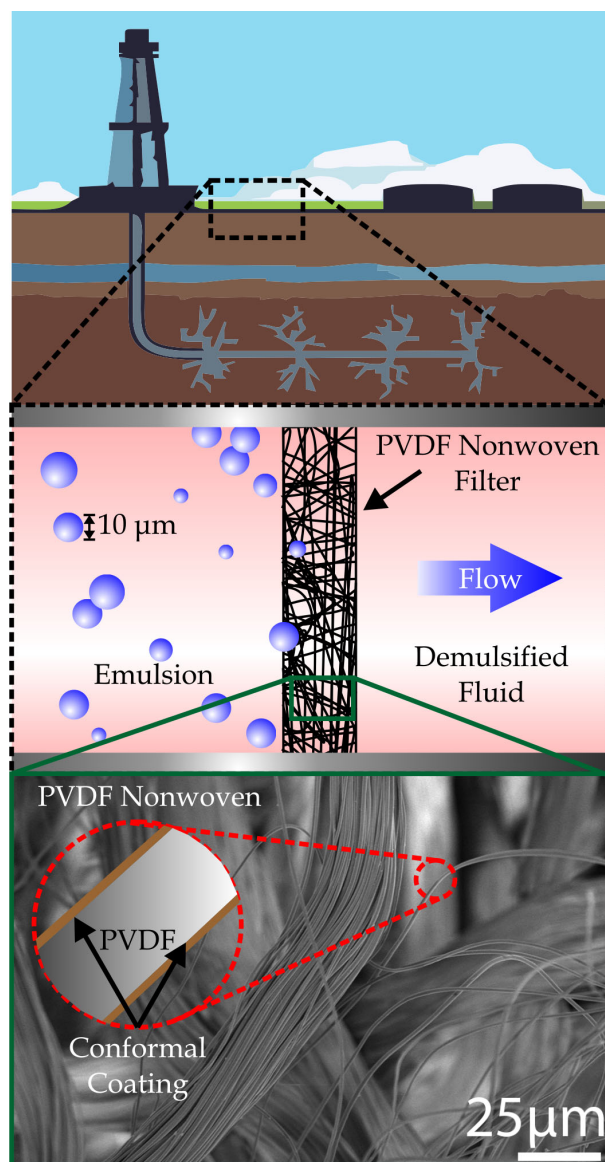


Figure 36. A schematic illustration of an oil well, where billions of gallons of oil must be demulsified to remove contaminants such as water and solid impurities. Using novel filter systems such as PVDF nonwovens, purified oil can be processed at high flux rates.

choice of filler particles or polymer matrix, were also of interest. The polymorph attributes of PVDF along with the intrinsic difficulties of achieving the most interesting of the various crystalline phases, namely β -phase, have been the primary hindrance in incorporating piezoelectric properties into cost-effective commercial production. Developing a low-cost, efficient process of generating β -phase PVDF using known nonwoven techniques is of great interest to the scientific community, having vast potential for energy storage, energy harvesting, and self-defouling applications.

Pure PVDF nonwovens with $\sim 1\text{ }\mu\text{m}$ fiber diameters have not been possible to manufacture in the past due to the low melt strength of PVDF, which requires spinning at ultra-low speeds ($< 1000\text{ m/min}$). Recently, the synthesis of such PVDF nonwovens has been achieved at NCSU in collaboration with the original manufacturer of PVDF, Arkema, Inc. These fabrics were produced using a spunlaid method of bicomponent fiber cross-sections known as ‘Islands-in-the-Sea,’ which can deliver sub-micron islands, thereby increasing the surface area considerably as compared to other fibers, while maintaining a high throughput.

Our investigations and characterization since the generation of these novel nonwovens have focused on both PVDF-polyethylene (-PE) and PVDF-polylactic acid (-PLA) fabrics; the functionalization of the nonwovens remains an ongoing pursuit at UIC. To date, the goals of tunable adhesion and repellency have been met with advances in tailoring these fabrics towards specific filtration applications, as well as gaining a better understanding of the intrinsic material properties and their relationship to the nonwoven structures. The goal of greater surface areas ($15\text{ m}^2/\text{g}$), enhanced filtration efficiencies, and antifouling properties, have been demonstrated.

The initial focus of this work revolved around approaches using polymer/nanocomposite formulations with the end-goal of generating multifunctional conformal coatings on PVDF-blend nonwovens. Desired properties, such as piezoelectric functionality, tunable fluid repellency, and electrical conductivity were analyzed for their utility in enhanced filtration and antifouling. Tailoring these nonwovens for specific applications by imparting added functionalities is of critical importance, as new coating synthesis methods are implemented and characterized. In addition to functionality, a better understanding of the material properties in a unique fabric form is necessary to fully characterize their potential. The research has two parallel paths:

- Building from existing coating formulations developed at UIC, new and modified formulations were transitioned for application onto the PVDF nonwovens and characterized. Previously, added functionalities were imparted by spray, but dip-immersion coating has proven to be a more effective route to generating conformal coatings.;
- Determining the presence and fraction of β -phase PVDF in the nonwoven is currently underway as compared to that of the more common, α -phase crystallinity. Baseline measurements of the PVDF fibers have been made, with reference data for the two phases of interest for PVDF, α - and β -phase. A new, single-fiber apparatus has been fabricated for characterizing the phases of individual PVDF filaments. Electrical poling will be performed to align the net dipole moments in the fabric for piezoelectric function, useful for energy harvesting or self-defouling applications. Fiber modification through other means, such as thermal- and solvent-induced phase change will be pursued for exploring their potential in antifouling filtration applications.

7.2 Experimental

7.2.1 Morphological/Chemical Characterization of PVDF nonwovens

The PVDF nonwovens produced at NCSU were delivered to UIC for characterization and functionalization in two forms: with either PLA or PE as the secondary component in the bicomponent fibers. SEM imaging was performed on all samples before and after treatment (See Figure 37 displaying SEM images of typical fiber morphologies of the PVDF fabrics after PLA has been removed), enabling a better understanding of intrinsic fiber morphology, as well as the effectiveness and uniformity of any subsequent modifications. Additional characterization was performed using X-ray diffraction (XRD) to determine crystallinity of the fibers for piezoelectric function.

The first samples produced via this method were supplied to UIC for characterization and further functionalization; these initial samples consisted of a blend of PVDF (60%) and PE (40%) in both 100 and 150 g/m² (gsm) basis weights. The nonwoven fabrics were hydroentangled after fabrication to release the PVDF fibers from the PE “sea” in the hope of also removing much of the PE from the fabric; residual PVDF-PE bundles (~30 μm) remained in the nonwovens (See Figure 38), hindering the realization of finer fiber diameter fabrics and the full investigation into their potential. The primary focus of the original investigations revolved around outlining approaches for surface functionalization of the nonwoven fibers to achieve conformal coatings having tunable wettability and adhesion for antifouling filter applications. Some of the demonstrated properties are fluid repellency, electro-conductivity, and elastomeric functionalization achieved through similar processes.

An alternate PVDF blended nonwoven was also characterized with polylactic acid (PLA) in place of PE in the fabrication of bicomponent PVDF-PLA nonwovens at NCSU. The sacrificial PLA was removed in a NaOH bath from the nonwoven, leaving only pure PVDF fibers behind with a very uniform 1 μm diameter. As will be discussed, PVDF has known compatibility issues with strong bases ($\text{pH} > 13$) which may be inadvertently changing the material properties.

7.3 Results & Discussion

As seen in Figure 37, the individual fibers remained bundled in undesirable 20–30 μm dia. groupings. Although an all-PVDF fabric has been achieved by removal of the sacrificial PLA, the nonwovens require subsequent steps to release the fiber bundles to fully realize the 1 μm fiber diameters (hydroentanglement is a viable route). New samples have been provided by NCSU, which have been hydroentangled in multiple stages to ascertain the effectiveness of this route for fibrillation of the bundled fibers.

In addition to previous difficulties associated with incomplete fibrillation of the fiber bundles, problems arose with the caustic NaOH bath needed for removal of the PLA in the samples. PVDF has known compatibility issues (201) with strong bases ($\text{pH} > 13$), resulting in defluorination of the fiber surfaces; visible as a brown discoloring of the normally white fabric. This can cause variations in the surface energy of the fibers and loss of overall homogeneity of the material, both of which were considered necessary to achieve high flux and efficiency for liquid filtration applications. However, defluorination of the fibers may actually assist in hydrophilicity and fouling resistant properties (202). For certain applications, this may be advantageous to some extent. SEM images displaying the evolution of these fibers through the NaOH rinse to

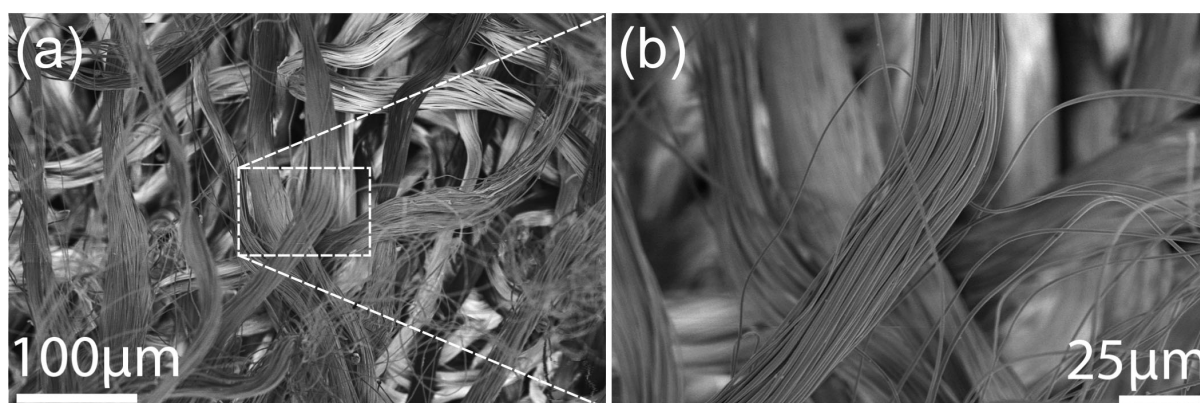


Figure 37. (a) SEM image displaying PVDF fiber morphologies. (b) Close-up of fiber bundles remaining from the Islands-in-the-Sea fabrication; clearly the PVDF fibers remain grouped in 20–30 μm bundles. Another fibrillation step, such as hydroentanglement is necessary to realize the true 1 μm diameters of the PVDF fibers, and thus the finer porosity needed for more robust filtration.

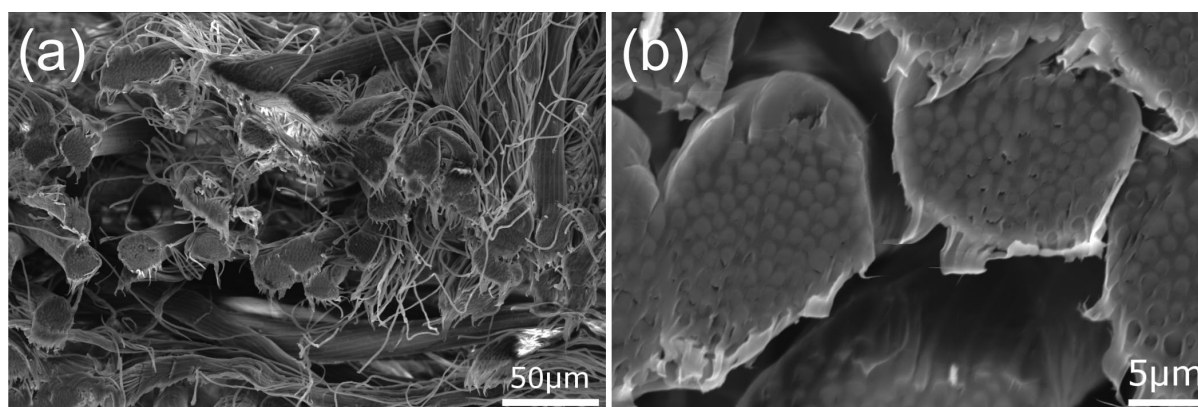


Figure 38. (a) SEM image displaying PVDF-PE fiber cross-sectional profiles. (b) Close-up of fiber bundles displaying the Islands-in-the-Sea fabrication where PVDF ‘islands’ are observed within the surrounding PE ‘sea.’

remove the PLA, and a subsequent acetone dip for further fibrillation of the fibers is included in Figure 39.

Potential solutions may involve the use of a less caustic base for PLA removal, or shorter rinse times and lower bath temperatures. Previous methods employed rinsing for 20–30 minutes at 90 °C, it may be possible to adjust these parameters to limit the extent of defluorination in the PVDF polymer. An extreme approach would be to pursue other bicomponent composite fibers such that an alternative sacrificial polymer could be used in the fabrication process. This route is not feasible at present, but may be worth pursuing if current methods prove insufficient for generating the required filter performance.

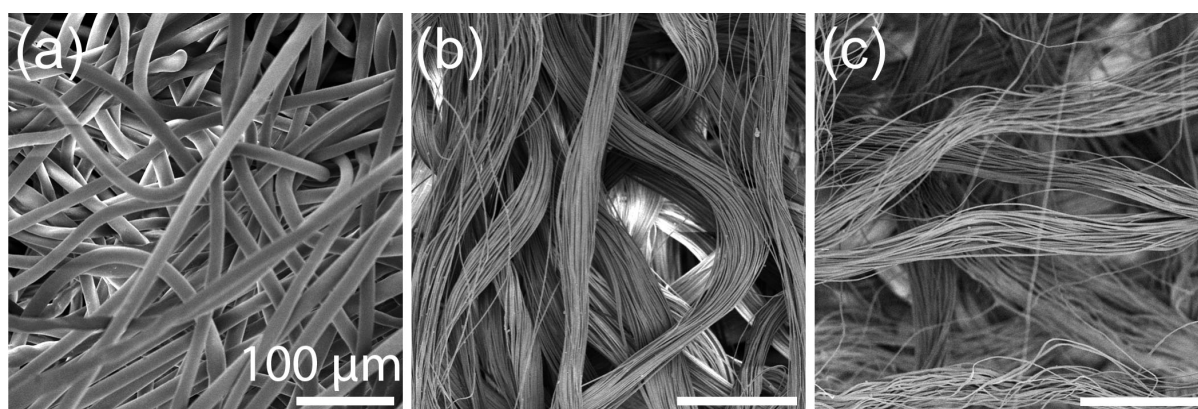


Figure 39. The evolution of the fabric morphology from (a) the original PVDF-PLA fabric, to (b) the fibers after the NaOH bath has removed the sacrificial PLA and exposed the PVDF 1 μm fibers embedded within, and (c) the fibers after a simple acetone dip resulting in a more fibrillated fabric by virtue of the fiber swelling in the acetone bath.

The β -phase of PVDF has been one of the most highly studied crystalline phases of any polymer. Studies have shown that using filler particles or other copolymers along with PVDF can induce the polymer to crystallize in the desired phase. Initial work in this area focused on duplicating standalone β -films PVDF films using these techniques and additives to formulate an approach for translating these films onto nonwovens; thereby gaining a better understanding of methods for generating the desired phase *in situ* during fabrication. Fortunately, while creating films of β -phase PVDF has been demonstrated in the literature, and applying a conformal coating onto existing nonwovens may prove to be relatively simple, it may be unnecessary if a sufficient portion of the fiber crystallinity is already in the required β -phase. If a majority β -phase is extant in the fibers inherently, likely through constraints placed upon the cooling polymer fibers during fabrication, it should be possible to detect piezo-responsiveness through a series of simple electrical poling experiments.

As noted, the nonwovens provided by NC State were either all, or majority-PVDF in their composition. Determining the crystalline phase of the PVDF in the fibers is of critical importance for realizing several potential applications. XRD measurements were performed (Figure 40) to determine the crystalline structure of the as-received nonwovens; and likewise going forward, XRD will be the primary tool for determining feasibility of the piezoelectric property. It is shown that the fibers, by virtue of their synthesis at NC State, possess some β -phase crystallinity to begin with. If this is not in sufficient fraction, there may be certain avenues through heating in solvent(s) accompanied by rapid cooling that can induce or enhance the desired phase in the nonwovens without any additional treatment. Whether this is an effective

method has yet to be seen, the challenge remains as to how effective electrical poling will be on the as-received nonwovens. A poling apparatus has been assembled at UIC to determine the feasibility of this task on a large scale. Poling experiments are to begin in November 2014 with the hope that confirmation of a successful alignment of fiber dipole moments will follow.

In addition to the previous XRD measurements of the bulk fabric, a new apparatus has been constructed to determine crystallinity on an individual fiber basis. These measurements will refine the accuracy of the previous results shown in Figure 40 to better ascertain the crystalline composition of the fibers themselves (Figure 41).

Additional functionalities are an ongoing pursuit with moderate successes already achieved in accordance with tunable wettability goals; in addition, these coatings serve a parallel goal of better understanding and enhancing the piezo-responsiveness of the PVDF nonwovens. These functionalities began primarily with spray-coatings developed at UIC, as based on prior work. The work transitioned into dip-immersion processes based on better conformality. As stated, these unique nonwovens have envisioned applications in filtration and subsequent functionalities geared towards this end. Demonstrated functionalities (*i.e.*, refined data collection) are presented below.

Super-repellent surfaces are characterized by high CA ($> 150^\circ$) to either water or oils, with high droplet mobility (sliding angle $< 10^\circ$) (98). Generating super-repellent surfaces has been a well-investigated area at UIC (48; 55; 41) with many possible avenues towards this end. Of key importance is the reduction of surface energy (relative to the fluid) and the addition of

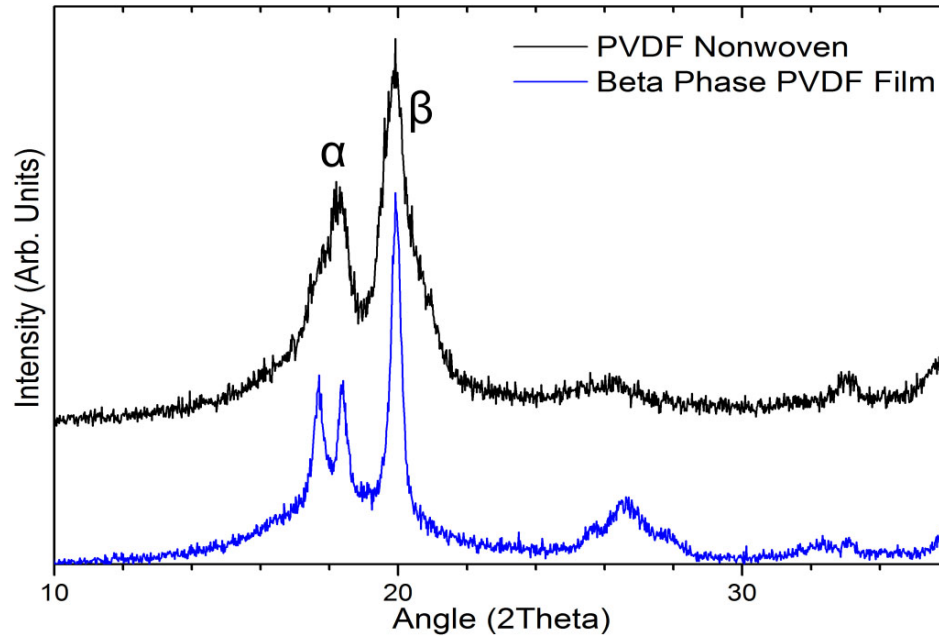


Figure 40. XRD plot of the reflection peaks in the 2θ range between 10 and 36° . The blue line represents a purchased sample of β -phase PVDF film (Measurement Specialties: unmetallized all-PVDF piezo film, Part No. 3-1003352-0, 110 μm thick), which also displays clear peaks in the α -phase; this suggests it is not necessary to eliminate the α -phase from the sample to take advantage of the piezoelectric β -phase. Surprisingly, the as-received nonwovens produced similar reflection peaks for the β -phase, with a broadened peak for the α -phase, as opposed to the two distinct α -peaks in the purchased film. This result indicates that it may be possible to electrically pole the as-received nonwovens to realize some piezoelectric property.

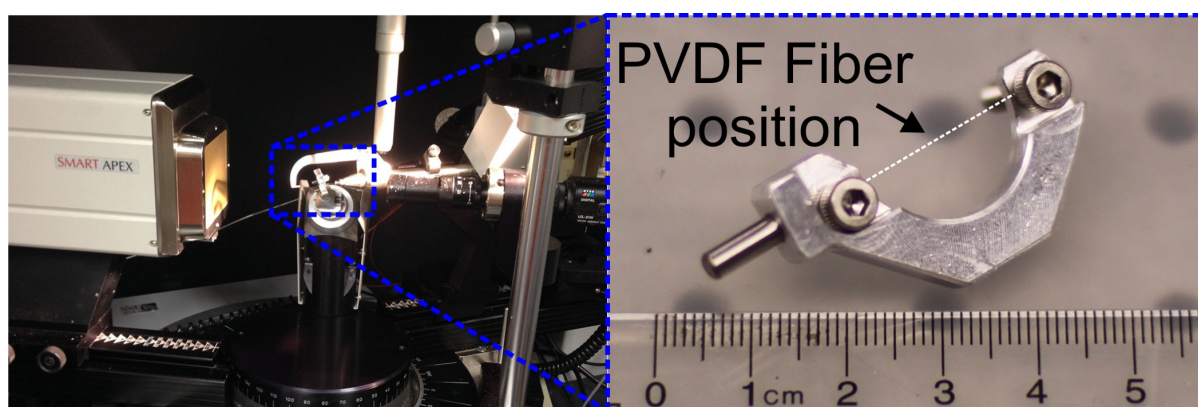


Figure 41. XRD powder diffraction setup with new fiber mounting stage (Left). Crystallinity can now be measured along the length of individual fibers, and as the fibers are rotated. This will be a useful tool in determining the efficacy in fiber modification to bring about a majority β -phase for future electrical poling tests. (Right) Close-up of the fiber mounting apparatus, where the fiber can be mounted along the centerline of rotation to ensure accurate crystallinity data.

hierarchical micro/nanoscale roughness to the fibers for reducing the liquid-to-surface ratio, and in turn preventing wetting by a desired fluid.

The presented work has been geared towards efficiency; a simple formulation with effective results for easy translation into large-scale applications. PVDF has CA to water that is slightly above 90° , making it weakly hydrophobic by virtue of the fluorine content, but not enough to prevent water droplets from sticking to, and/or penetrating the fabric. Using a solution-processed blend of low surface energy polymers in varying dilutions (0.25–3 wt. %), into which the fabrics were dip-coated, is shown to generate a tunable conformal coating along the fibers (Figure 42), thus lowering their overall surface energy. The fiber morphology of the nonwovens now act as re-entrant surface features, thus allowing fluid droplets (both oil and water) to bead; self-cleaning fabrics can be formed via a simple one-step process. Fiber spacing, and thus porosity, are highly tunable based on the polymer dilution in the dip-coating process.

In the previous example, a simple method for imparting a self-cleaning conformal layer of low surface energy polymer was examined; using this process, it is possible to separate multi-component fluid mixtures based upon surface energy differences. The PVDF surfaces naturally lend themselves towards separation and filtration applications (203), where the resistance of the surface to water allows oil to absorb. Not only are we able to perform simple oil and water separation, but we are also able to separate submicron, and possibly even nano-emulsions (Figure 43).

Currently, we are investigating water-in-oil emulsions (10 v/v % water in oil). Oils of interest for the current study are hexadecane, hexane, isooctane, petroleum ether, and mineral oil.

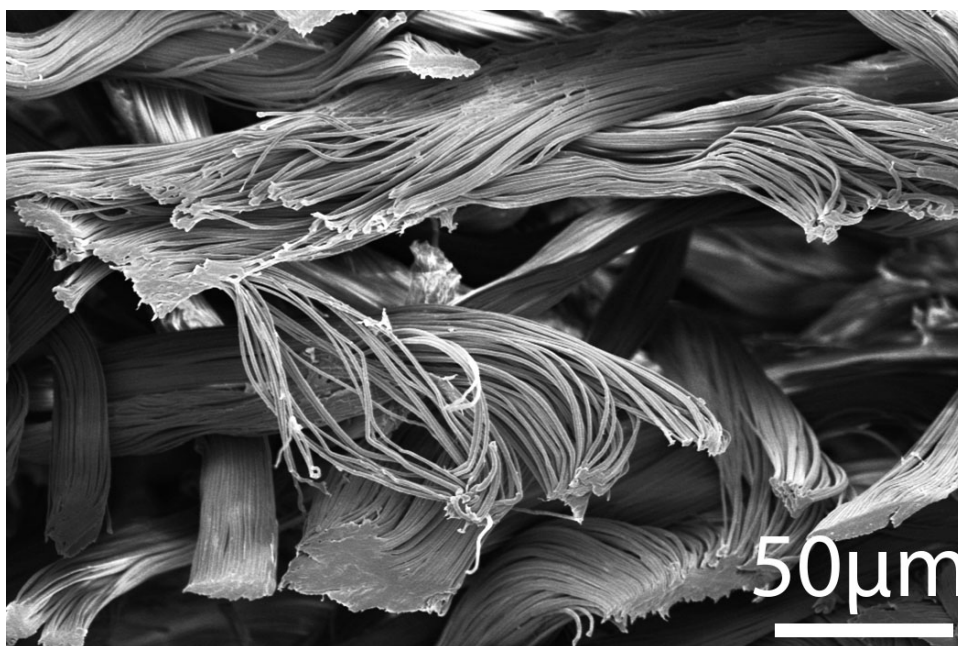


Figure 42. Cross-section SEM of a superhydrophobic conformal coating applied by dip-immersion of PVDF fabric in a 0.5 wt. % low surface energy polymer in toluene. The surface treatment is very uniform, leaving the as-received fiber morphology intact, yet lowering the surface energy of the fibers overall to a level that they become self-cleaning.

These fabrics can be implemented for oil-water separation.

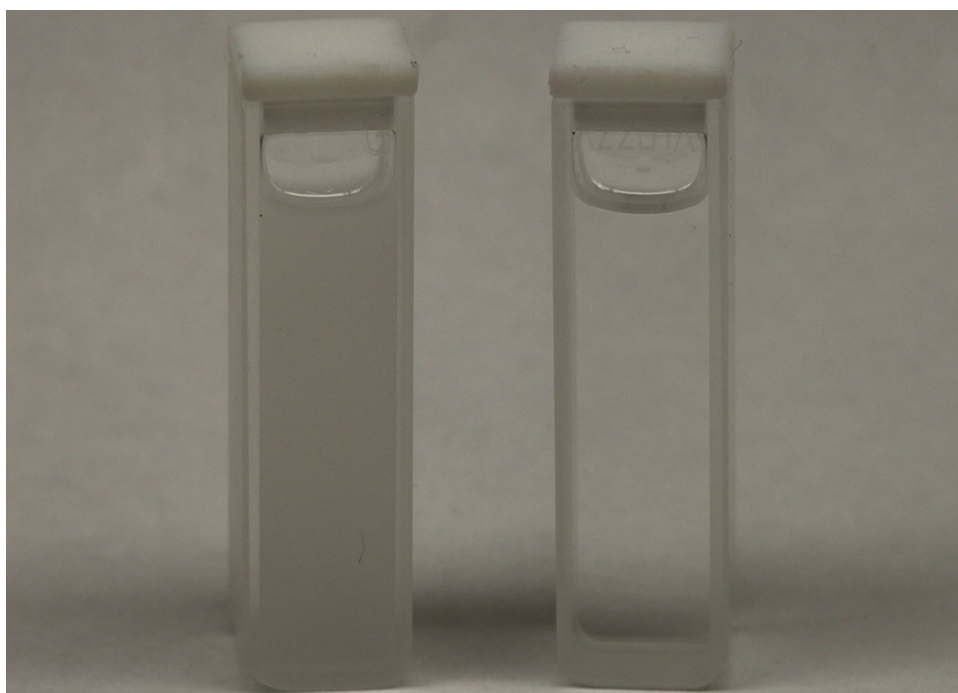


Figure 43. Visual comparison of a water-in-oil emulsion before (Left) and after (Right) separation; the micro-emulsion takes on a milk-white haze, while the separated hexadecane oil is completely clear.

Future work will attempt to demonstrate the reverse, oil-in-water. For the reverse separation, the surface will need to be both hydrophilic and oleophobic—a rare accomplishment in the literature (204), but still possible depending on the choice of conformal treatment.

It may not be entirely necessary to modify the fibers beyond a simple acetone dip to achieve efficient emulsion separation. Figure 39 demonstrates the evolution of the fabric morphology from the original PVDF-PLA fabric (Figure 39a), to the fibers after the NaOH bath has removed the sacrificial PLA (Figure 39b), and the resultant fibers after a simple acetone dip (Figure 39c). It is evident from the post-acetone dip that the fibers were fibrillated via the polymer swelling achieved during the acetone bath. This creates a more torturous path for emulsion droplets, making it increasingly unlikely they'll be transmitted through the material, thus generating higher separation efficiencies.

Initial results of oil filtrate after separation confirms the ultra-low presence of water, where ultraviolet-visible (UV-Vis) spectrometry is employed to ascertain the purity, as it is on the order of parts per million (ppm). Initial flux results for water-in-hexadecane emulsion is presented in Table VI and Figure 44. Flux rates are impressive for these filters with feasible improvement in efficiency as ppm content can be improved (*i.e.*, lowered). Possible solutions may be to run the emulsions through a filter more than once to observe if there is any noticeable improvement.

By adding conductive fillers to the dip-immersion process, such as carbon nanofibers (See Figure 45) and multilayer graphene (See Figure 46), conductive coatings are achieved with potential in smart fabric (*i.e.*, filters, wearable electronics, *etc.*), EMI shielding, and energy storage applications. Characterization of these coatings involves I-V curves to determine linear Ohmic

TABLE VI

INITIAL FLUX AND EFFICIENCY DATA (*i.e.*, PURITY) FOR WATER-IN-OIL EMULSION SEPARATION. INCLUDED IN THE BOTTOM TWO ROWS IS RELEVANT DENSITY AND SURFACE ENERGY INFORMATION FOR THE FLUIDS TESTED.

	Hexadecane	Hexane	Petroleum Ether	Isooctane	Mineral Oil
Flux (L/m ² s)	0.80	8.16	7.81	3.82	Unknown
Purity (ppm)	916	253	6906	3871	46
Density (g/cm ³)	0.77	0.65	0.64	0.69	0.80
Surface Energy (mN/m)	27.47	17.91	17.45	18.77	28.21

resistance, along with testing for electromagnetic wave attenuation at various frequencies (extending into the THz regime). Conductive coatings have great potential for energy storage applications where the PVDF nonwovens can be used as separators.

Combining many of the techniques employed previously for different functionalities into a cohesive application, we will investigate the effectiveness of these nonwovens towards energy storage in the areas of fuel cell, battery, and supercapacitor technology. PVDF has been investigated to act as a separator in the past (205), however the fiber diameters were much larger

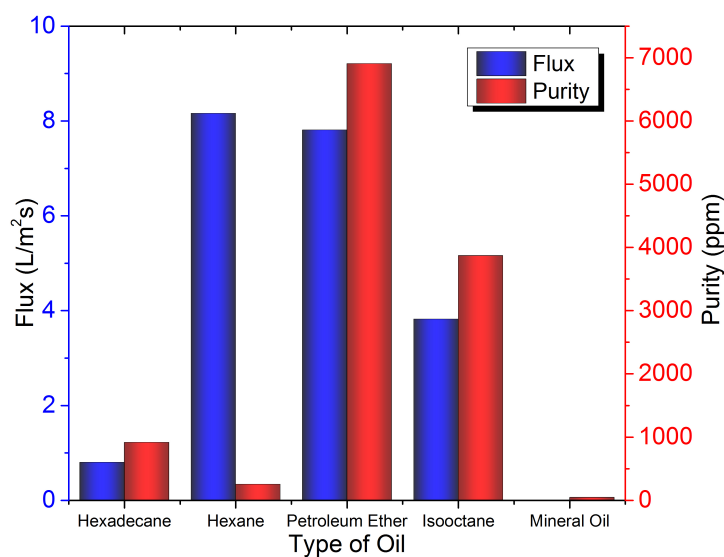


Figure 44. Plot of flux and efficiency (*i.e.*, purity) data for water-in-oil emulsion separation.

and therefore possessed a greatly reduced surface area. With the 10–15 m²/g all-PVDF nonwovens studied herein, a more-effective separator could be utilized for similar goals (Figure 47). Using a dip-coating treatment to functionalize individual fiber surfaces, and combining these with conductive spray-cast coatings, it is possible to generate large-area flexible electrodes on either side of a functionalized PVDF fabric. Future work will examine the best electrolyte (water-based electrolytes pose difficulties due to the hydrophobicity of PVDF) for studying the energy storage (*i.e.*, increased energy density) potential of these nonwovens.

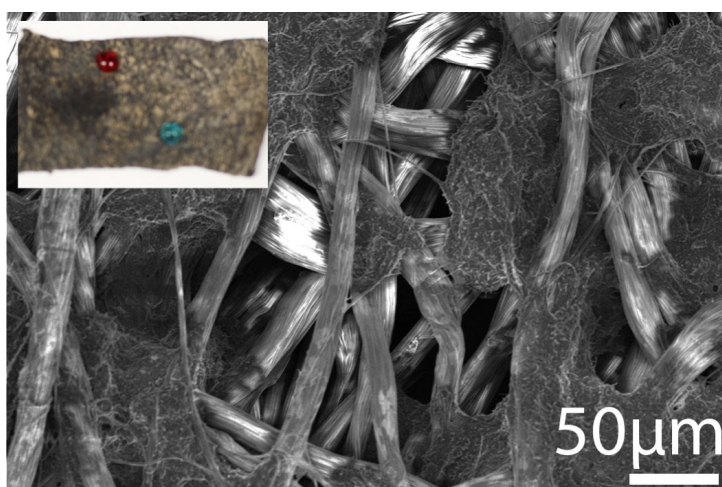


Figure 45. SEM image of the PVDF fibers after dip-immersion in CNF and solution-processed Parafilm™. Inset in top left is after post-processing with drop-cast fluoropolymer to impart oleophobicity (red-dyed hexadecane oil droplet, blue-dyed water droplet) by taking advantage of the reentrant morphology offered by the CNF-decorated PVDF fibers.

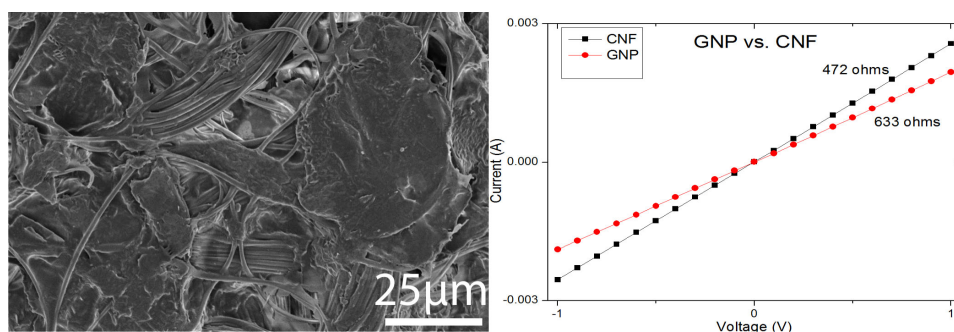


Figure 46. (Left) SEM image of the PVDF fibers after dip-immersion in MLG and solution-processed Parafilm™. (Right) I-V curves for PVDF fabrics after dip-immersion in CNF/MLG and Parafilm bath (GNP in the plot refers to graphite nanoplatelets, or multilayer graphene, MLG).

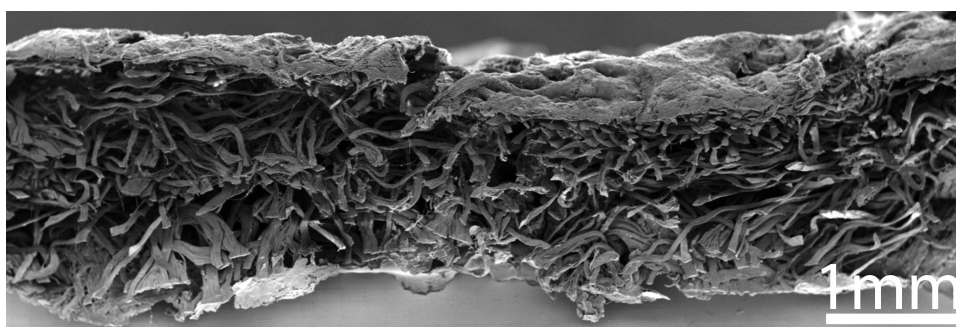


Figure 47. Cross-section SEM image of the PVDF nonwoven with spray-cast electrodes on top and bottom. The top electrode is composed of 50 wt. % CNF to Parafilm[®], while the bottom electrode is composed of 50 wt. % MLG and an adhesive acrylic polymer. Both electrodes are highly durable and flexible; the resulting fabric only requires the addition of an electrolyte to become a functional battery.

CHAPTER 8

CONCLUSIONS AND RESEARCH OUTLOOK

This thesis has involved the synthesis and characterization of multifunctional nanomaterial and polymer composites with tunable properties; all of which are designed for, or involve the novel production of, nonwoven porous media. The conclusions from each of the previous research topics is presented:

8.1 Thesis Conclusion

8.1.1 Environmentally-friendly Water-based Superhydrophobic Coatings

This study reported a water-repellent coating formulation based on an aqueous spray comprising 97.5% water and commercially available materials: a fluoroacrylic copolymer and hydrophilic bentonite nanoclay. The wet processing relied on spray application and drying, both performed at room temperature. The dried coating imparts superhydrophobicity (contact angles over 150°) at minimum add-on levels of 2.4 gsm. The results indicate the lack of a correlation between water droplet beading (repellency) and water barrier resistance (hydrohead). A naturally hydrophobic substrate showed high water barrier resistance despite having poor water mobility after coating application. It was shown that resistance to water penetration pressure is derived primarily from substrate porosity (fiber spacing and diameter). Although the coating formulation shows increased water resistance with coating deposition mass, especially in the

case of inherently hydrophilic substrates, this increased resistance is bounded by the Laplace pressure associated with the effective pore size.

8.1.2 The Fluid Diode

In summary, an effective fluid barrier coating treatment applied on common cellulosic paper substrates has been demonstrated to facilitate fluid diodicity: distinct pressure thresholds depending on the orientation of the substrate coating with respect to the adjacent fluid. The preferred flow directionality resulting from differences in penetration pressure resistance arises due to capillary action, facilitated by the fluid wicking into the absorbent fibers. This technology could be effective in filtration/separation with a wide range of applications, from personal hygiene products to water purification or oil removal. The threshold pressure difference, or “diode window,” is highly tunable for application- and fluid-specific designs determined by the choice of substrate, fiber size/spacing, and precision/morphology of the coating. The multi-component fluid separation method is of practical use to industry for its ability to preselect which liquid is retrieved from a given mixture, as based upon surface energy and priming of the porous solid.

8.1.3 Fluorine-free Water-based Superhydrophobic Compositions

A stable, entirely water-based and nonfluorinated spray dispersion has been shown to achieve a translucent-white superhydrophobic composite coating applicable for large-area surface treatments. Comprised of TiO_2 and a water-borne wax polyolefin polymer, the ideal ratios of the formulation moieties were determined by dynamic contact angle measurements, emphasizing the reduction in contact angle hysteresis to target droplet mobility as a critical performance

requirement. Analysis of SEM and TEM images allowed for a better understanding of the hydrophilic TiO_2 nanoparticle variants and the impact of particle size and phase on coating performance. XRD measurements were made to determine the role of nano TiO_2 on polymer crystallinity, with pH sampling of the final dispersions to better understand chemical kinetics of the nanoparticle and polymer interactions. The 25 nm anatase TiO_2 was observed to resist the formation of aggregates when suspended in water, whereas the 21 nm mixed phase TiO_2 quickly formed particle groupings most likely due to the presence of surface charges on the rutile particles. This surface charging explains the uniformity of the spray-cast 21 nm mixed-phase composites when combined with the alkaline polymer blend, such polar interactions serve to more completely sheath the hydrophilic particles in a hydrophobic polymer shell. Alternately, the anatase particles, being more intrinsically inert, will form greater agglomerate sizes due to the slightly charged free polymer strands seeking equilibrium by decreasing the volume to surface area ratio in the composite. Thus, the incorporation of a unique waterborne polymer blend is shown to be effective in low environmental-impact superhydrophobic composites achieved through tuning of nanoscale roughness of hydrophilic titanium dioxide.

8.2 Durable & Flexible Graphene Composites from Artists' Paint for Conductive Paper Applications

A low-cost and durable conductive composite coating comprised of graphene nanoparticles and phthalocyanine green artists' paint is presented for conductive paper applications, including EMI shielding and flexible electronics. Exfoliated graphite nanoparticles, otherwise referred to as multilayer graphene (MLG), are used as an alternative to costly pristine monolayer graphene,

yet the composite approximates many similar material properties approaching the quasi-metallic low electronic resistance regime. Conductivity measurements were made to determine ideal mass loading of MLG and analyze the electronic potential on the micro-scale. Representative resistances were then selected for THz EMI attenuation in the 0.50–0.75 THz frequency range yielding excellent results (~ 36 dB attenuation) for the larger particle sizes and higher conductivities, suggesting the graphitic material aids in radiation absorption at higher frequencies. Raman spectroscopy revealed the presence of majority multilayer graphene, as well as verified a negative doping effect from the pigment copper phthalocyanine nanoparticles found in green acrylic artists' paint. These nanocomposites were shown to be highly durable during fold and abrasion tests, representing a viable option for conductive paper applications, such as large-area EMI shielding and flexible electrodes in energy storage.

8.2.1 Highly Elastomeric & Conductive Superhydrophobic Composites for Smart Fabric Applications

A novel conductive composite has been presented capable of super-repellency to water and recovery of conductive property even under extreme strain. Innovative advances in high-conductivity materials research can respond to the ever-increasing demand for more robust and versatile electronic components; light-weight, foldable, all-weather electronics are a reality that can improve existing technology considerably towards reduced cost and bulk, with added functionality. The current trend in electronics for reduced dimensions and scaled-up production will only increase in the foreseeable future. Therefore, a durable, and extremely elastomeric composite material with high conductivities that is also super-repellent to water can be of

great use in adaptable electronics technology; or any application where a foldable, light-weight, electro-conductive material is required. The primary component forming the polymer matrix, ParafilmTM (PF), is produced in large quantities for commercial production and ubiquitous laboratories world-wide. Additionally, carbon nanofibers (CNF) form excellent charge-conducting pathways with the dual role in the composite of imparting reentrant nanoscale roughness. The synthesis of these composite is substrate-independent and can be applied on large-scales for high throughput processing; making them not only highly efficient, but also inexpensive.

8.3 PVDF Nonwovens

PVDF-blend nonwovens have been produced by NC State. Work began in summer 2013 on adding functionalities and characterizing the PVDF blend substrates in their as-received state, with the PVDF-PLA blend nonwovens received in winter of the same year. Results have shown great potential for filter applications, as well as for added functionality via conformal surface treatments assisted by the inherent fiber morphology ($\sim 1\ \mu\text{m}$) and high surface areas (10–15 m^2/g).

In regards to adding functionalized coatings to the PVDF nonwovens, we have demonstrated the existence of β -phase crystallinity in the as-received fabrics, and enhanced fluid repellency with tunable porosity for oil-water emulsion separation. Highly conductive conformal coatings are being investigated for their potential in flexible energy storage and wearable electronics applications. Ongoing work on current and new functionalities is a continuous component of this work.

A large degree of this work involves extensive investigation into the β -phase of PVDF, whether through modifying (if necessary) the existing PVDF fibers, or methods of fabrication, which can enhance this during production. Additionally, electrical poling of the PVDF fibers is currently underway.

8.4 Research contribution

The research contributions from each of the previous research topics is discussed below:

8.4.1 Water-based Superhydrophobic Coatings

- One of the first *water-based* dispersions for superhydrophobic surface treatments was presented; consisting of hydrophobic water-based fluoropolymer and hydrophilic nanoclay particles to eliminate the use of *volatile organic compounds*;
- The polymer and particle ratios were optimized along with deposition amount such that durable high-performance superhydrophobic coatings were formed with the least expenditure of materials;
- Tunable properties on nonwoven media such as fiber diameter and porosity were demonstrated, with fine control over pore size directly influenced by deposition amount;
- Characterized the lack of correlation between high contact angles (repellency) and increased water intrusion pressures (resistance) for relevant disposable nonwoven fabrics.

8.4.2 The Fluid Diode

- A novel fluid gating device analogous to the electronic diode has been developed, where fluid flow (*i.e.*, current) can be unidirectionally rectified;

- The performance of this device was characterized in terms of coating weight (in gsm) to verify the tunability of the operational ranges;
- The selective separation of multi-component fluid mixtures (*e.g.*, oil-water) based upon surface energy differences has been demonstrated;
- The device is not dependent upon our choice in repellent composite, nor substrate, but can be tuned for fluid function using any similarly *thin fluid barrier on any porous medium*.

8.4.3 Fluorine-free & Water-based Superhydrophobic Compositions

- The first *translucent-white, water-based, and fluorine-free* dispersion for superhydrophobic surface treatments has been developed consisting of hydrophobic water-based polyethylene co-polymers and titanium dioxide particles eliminating the need for *volatile organic or fluorinated compounds*;
- The polymer and particle ratios, along with particle size and phase, were optimized to form a durable high-performance superhydrophobic coating;
- The effect of particle size and phase on crystallinity of the polymer were determined;
- Particle aggregation and surface adsorption kinetics as determined by particle phase, dimensions, and dispersion pH were examined.

8.4.4 Graphene Composites for Conductive Paper Applications

- A novel composite from combining multilayer graphene (MLG) in an artists' acrylic paint has been presented;

- The durability, conductivity, and flexible of the composite for applications in conductive paper has been characterized and found suitable for a wide range of applications, namely, that of conductive paper or any similarly-flexible porous media;
- The composite was found to be suitable for THz radiation shielding.
- The composite demonstrates the ability to make similar conductive materials at low-cost with high performance due to the multi-layer graphene filler particles and our choice in low-cost binder.
- A simple circuit was designed to assess efficacy in paper-based electronics;

8.4.5 Elastomeric & Conductive Superhydrophobic Composites

- A highly-elastic composite comprising carbon nanofibers in a paraffinic and polyolefin polymer medium (ParafilmTM) is characterized;
- The electronic performance and recovery of the composite through extreme strain cycles was characterized, far exceeding previous performance benchmarks for similar materials;
- Water repellency performance and recovery of the composite through extreme strain cycles was characterized, adding additional functionality;
- The efficacy of the material for smart fabric applications (*i.e.*, wearable electronics) was ascertained on nonwoven media where flexibility and durability is paramount.

8.4.6 PVDF Nonwovens

- Novel PVDF-blend nonwovens fabricated using bicomponent spunlaid processing, “islands-in-the-sea” cross-sections have been produced by NCSU and characterized at UIC for specific applications and added functionality;
- Fiber fibrillation (1 μm fiber dia.) and nonwoven porosity for filtration applications is shown to be tunable;
- Fiber crystallinity and presence of β -phase PVDF has been determined, making feasible piezoelectric energy-harvesting fabrics;
- The fabrics are to be electrically poled to determine piezo-responsiveness for energy-harvesting and self-defouling filter applications.
- Flux rates and filtrate purity to be assessed for demonstrable potential in emulsion separation of water from relevant oils in the petrochemical industry.

8.5 Recommendations for future research

8.5.1 Water-based Superhydrophobic Coatings

This work has opened the door for other water-based and environmentally-friendly superhydrophobic coatings, namely, the advance of fluorine-free coatings which are covered in the next section. The characterization of coating deposition amount on nonwoven media has aided in the development of a novel fluid logic device covered in a later section. In terms of durability and cost-effectiveness, the coating formulation and tunability on porous nonwovens has great applications in commercial disposables and filtration.

8.5.2 The Fluid Diode

A novel device for fluid flow rectification has been presented, with applications from consumer clothing, disposable hygienic products, and filtration. The fluid barrier chosen was our water-based dispersion on paper towel substrates. These were chosen to display a low environmental impact approach on ubiquitous materials, although the core of what is presented, that of the mechanism itself, does not rely on these components. It can be duplicated with any similarly-thin fluid barrier on any porous material. The mechanism can be extended to oils, where an oil-diode is possible if the fluid barrier is made to be oleophobic. For an oleophobic barrier, lower surface energy fluids (< 40 mN/m) can be separated. Additionally, this technology has applications in garments, both disposable and otherwise. For instance, a jogging jacket with a similar coating could wick sweat away, and keep the wearer dry in wet weather; Or, a diaper could pass bodily fluids without leak-back, also maintaining dryness of contacted skin.

8.5.3 Fluorine-free & Water-based Superhydrophobic Compositions

As stated, the previous work on water-based superhydrophobic treatments has led to the development of this formulation. The characterization of particle size and phase on polymer crystallinity and aggregate size is useful for further development of similarly water-based and fluorine-free composites for fluid repellency. Although generating repellency to lower surface energy fluids nominally requires fluorine bonds, there may exist avenues for enhancing hydrophobic functionality through similar means to be oleophobic as well.

8.5.4 Graphene Composites for Conductive Paper Applications

By incorporating multi-layer graphene in a highly durable and adhesive polymer matrix, a method for conductive porous materials has been achieved with a low-cost and large-area approach. The addition of pigment nanoparticles in the acrylic paint matrix has made possible n-type doping functionality for cathodic energy storage applications. This work opens the door for “off-the-shelf” materials which may be otherwise overlooked; as is often the case, novel techniques can be used to transform commonplace materials into new devices. Current work in this field involves the investigation of graphene for its advantageous properties, but is currently hindered by high costs associated with its synthesis. These problems are overcome by the use of a much cheaper alternative, that of MLG.

8.5.5 Elastomeric & Conductive Superhydrophobic Composites

Similar to the previous section, a novel composite capable of high performance under extreme strain is presented that is formed from commonplace laboratory materials. The performance of this composite far exceeds benchmarks from the literature, for both water repellency and conductivity under high strain. Limitations on current technology designed for such robustness would be lifted, as this composite has demonstrated applicability on flexible fabric material for wearable electronics. In addition to wearable electronics, this composite has shown promise in energy storage applications such as battery and supercapacitor technology.

8.5.6 PVDF Nonwovens

Nonwoven production has a dominant foothold in filtration technologies, among many other industries such as automotive and household furniture. These materials are prized for their ho-

mogeneity, high throughput, and low cost. PVDF nonwovens have posed problems in the past due to their low melt strength limiting their production speed and thus, their viability. These difficulties have been overcome through spunlaid processing with ‘islands-in-the-sea’ cross-sections, making possible for the first time, PVDF nonwovens with 1 μm fiber diameters. These highly degradation-resistant textiles have applications in all types of filtration, especially that of emulsion separation. Additionally, by virtue of their β -phase crystallinity, they are capable of piezoelectric actuation, making self-defouling filters and energy harvesting fabrics a potential reality.

APPENDICES

Appendix A

SUPPORTING INFORMATION: WATER-BASED SUPERHYDROPHOBIC COATINGS

A.1 Contact Angle Measurements

In determining contact angles (CA), the irregularities in surface topography of the substrates made it difficult to obtain accurate and consistent measurements. This is due to the surface features having nearly the same length scale as the test droplet size, as well as some of the substrates possessing fibers that extended through the surface treatment, thus obscuring the contact line between droplet and substrate See Table VII.

A.2 Pore Size

Pore sizes for the same substrate varied as a function of coating level and initial fiber spacing, as shown in Table VIII. The light coating (2.4 gsm, middle column) generates a thin conformal film around the surface fibers and leaves most of the larger pores intact. This coating level essentially has a sealing effect on those substrates that are hydrophilic initially without a noticeable reduction in pore size. For the smaller pores, the light coating is able to bridge these gaps and thus completely seal some of the finer pore sizes, such as those seen in the middle meltblown layer of SMS. The heaviest coating level (9.6 gsm, right column) is seen to eliminate much of the original surface features of the fibers and has smoothed out all but the largest pores. These large pores still remain in the sample and designate the hydrohead limit.

Appendix A (Continued)

The coating required to fully clog these pores (and raise the hydrohead even further) will affect coating breathability and cost, thus making such coating add-on levels undesirable for industrial applications.

A.3 Hydrohead Apparatus

Figure A1 shows the apparatus used to determine resistance to external water pressure, as based on ASTM standard F1670-08. A 1" diameter acrylic tube measuring 1.4 m in length was used as a graduated column of water for measuring hydrostatic pressure in centimeters (hydrohead). The water flow was driven by an aquarium pump (Lifegard Aquatics QuietOne 2200). For a given test, 1" circles of test material were cut and placed at the bottom of the tube, where a nitrile rubber gasket was screwed on top to ensure proper seal. Water was then pumped at a rate $< 1.5 \times 10^{-2}$ L/s to avoid inertial effects through flow disturbances introduced in the rising liquid column. An optical mirror on a swivel mount was placed directly beneath the column of water to enable a direct view of the sample (via a CCD camera) as hydrostatic pressure was gradually increased. Water breakthrough appeared as a bright spot of light at the point of first penetration, as shown in the inset on Figure A1. The height of the water column at breakthrough designated the maximum hydrohead that a sample could tolerate reliably. This process was repeated at least 5 times for a given test sample, and the pressures were then averaged to determine the final resistance pressure and the accompanying standard deviation.

Appendix A (Continued)

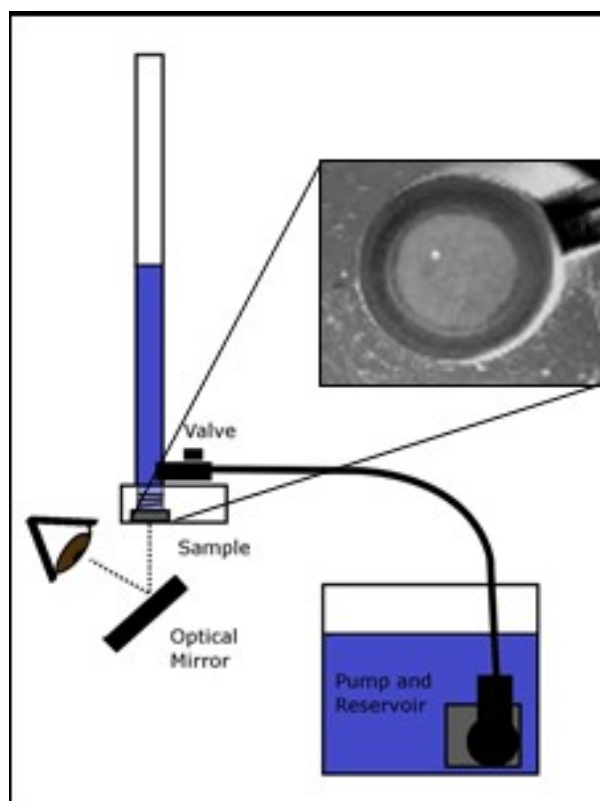
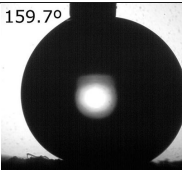
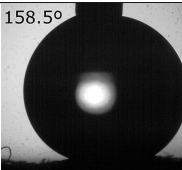
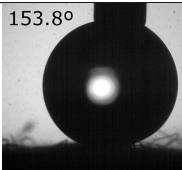
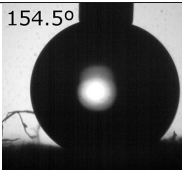
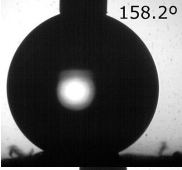
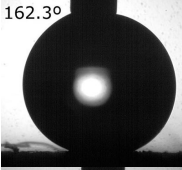
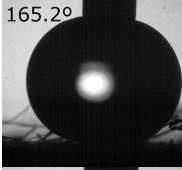
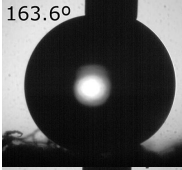
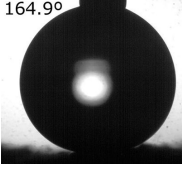
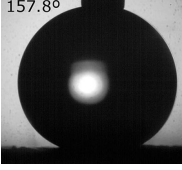
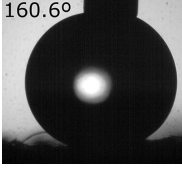
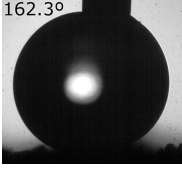


Figure A1. Schematic of hydrohead apparatus consisting of pump reservoir, viewing mirror and column. The water column is filled slowly until breakthrough is seen (shown as a white spot in the inset).

Appendix A (Continued)

TABLE VII

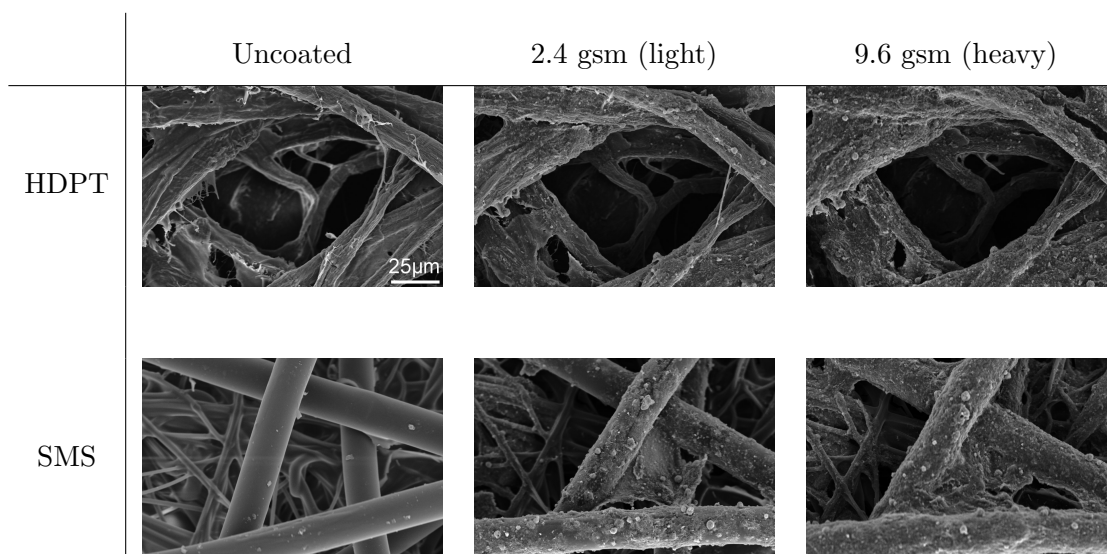
TYPICAL IMAGES CAPTURED DURING CA MEASUREMENTS FOR ALL FOUR SAMPLES AT THREE COATING ADD-ON LEVELS. THE ROUGH NATURE OF THE SURFACE TOPOGRAPHY MAKES IT DIFFICULT TO OBTAIN ACCURATE AND CONSISTENT CA MEASUREMENTS. ALL MEASUREMENTS WERE TAKEN USING A HORIZONTAL SIDE VIEW AND THE CORRESPONDING CA ARE LISTED ABOVE LEFT OF EACH DROPLET MEASURED. ALL OF THE SHOWN COATING LEVELS ACHIEVE SUPERHYDROPHOBICITY ($CA > 150^\circ$) ON ALL SUBSTRATES. CA MEASUREMENTS FOR SIMILAR COATING LEVELS WERE OBTAINED ON GLASS SLIDES FOR COMPARISON WITH THESE ROUGH SAMPLES. THE NEEDLE DIAMETER IN ALL IMAGES IS 1 MM, IMPLYING AN AVERAGE DROPLET DIAMETER BETWEEN 3 AND 4 MM.

	HDPT	SMS	Spunlace	Tissue
2.4 ± 0.2 gsm	159.7° 	158.5° 	153.8° 	154.5° 
4.7 ± 0.2 gsm	158.2° 	162.3° 	165.2° 	163.6° 
9.4 ± 0.2 gsm	164.9° 	157.8° 	160.6° 	162.3° 

Appendix A (Continued)

TABLE VIII

PORE SIZE AS A FUNCTION OF ADD-ON COATING LEVEL FOR TWO REPRESENTATIVE SUBSTRATES: HYDROPHILIC HDPT (TOP ROW), HYDROPHOBIC SMS (BOTTOM ROW). THE LEFT COLUMN DISPLAYS IMAGES OF UNCOATED PORES, THE MIDDLE COLUMN IS AT THE LIGHTEST COATING LEVEL OF 2.4 GSM, AND THE RIGHT COLUMN IS AT THE HEAVIEST COATING LEVEL OF 9.6 GSM. IT CAN BE CLEARLY SEEN FOR THE LARGER PORE SIZES ON HDPT, THE COATING HAS A NEGLIGIBLE EFFECT ON REDUCING PORE SIZE AS THE PORES ARE TOO LARGE FOR THE POLYMER TO BRIDGE AND SEAL. IN CONTRAST, THE MUCH SMALLER PORE SIZES OF SMS ARE GREATLY REDUCED BY THE COATING. THE SCALE BAR IN THE TOP LEFT SEM MICROGRAPH APPLIES TO ALL IMAGES.



Appendix B

SUPPORTING INFORMATION: THE FLUID DIODE

B.1 Dispersion/Application Parameters

The 50:50 polymer-to-nanoclay solids ratio was chosen based on preliminary qualitative results: increased polymer content significantly reduced coating surface roughness; and conversely, increased nanoclay content adversely impacted coating wettability, as the clay is hydrophilic and requires a significant fluoropolymer content to counteract the inherent tendency of the clay to absorb water. Likewise, increasing the overall solid content in the final spray dispersion also increased viscosity, in turn hindering the ability to spray; thus, the solids wt. % in the dispersion was deliberately maintained below 3% to avoid complications during spraying. An airbrush atomizer (Paasche, VL siphon feed, 0.55 mm spray nozzle) was used to spray the samples from a distance of 25 cm. Water-based spray dispersions pose several challenges as the surface roughness imparted by the particle filler, and needed for repellency, is inhibited by the slow evaporation from the wetted substrate surface after spraying. To this end, the specific spray nozzle was chosen because it offered the finest spray atomization achievable with the employed sprayer, in turn, enhancing water evaporation during spray application. The spray distance also greatly affects coating morphology and deposition rate, and was fixed at 25 cm to avoid excessive substrate wetting during spray (increased at shorter distances) and maximize coating deposition rate (decreased at longer distances).

Appendix B (Continued)

B.2 Coating Characterization

In determining contact angles (CA), the irregularities in surface topography of the porous substrates made it difficult to obtain accurate and consistent measurements. This is due to the surface features having nearly the same length scale as the test droplet size, as well as some of the substrates possessing fibers that extended through the surface treatment, thus obscuring the contact line between droplet and substrate. Representative CA data verifying superhydrophobicity were obtained from images of water droplets on coated glass slides (Figure 6) and paper substrates for comparison (Table IX). Sliding angles were also difficult to accurately measure on the textured surfaces of the paper towels, as water droplets could easily find a depression in the imprinted patterning of the material, thus hindering estimations of the true roll-off angle that would be observed on a relatively flat surface.

B.3 Hydrohead Apparatus

Figure A1 shows a schematic of the apparatus (41) used to determine penetration resistance to external water pressure, as based on ASTM standard F1670-08. A 2.5 cm diameter acrylic tube measuring 1.4 m in length was used as a graduated column of water for measuring hydrostatic pressure in centimeters head (hydrohead). The water flow was driven by an aquarium pump (Lifegard Aquatics QuietOne 2200). For a given test, 2.5 cm-dia. circles of test material were cut and secured in place at the bottom of the tube, where a nitrile rubber gasket was screwed on top to ensure proper seal. Water was then pumped in the column at a rate $< 1.5 \times 10^{-2}$ L/s to avoid inertial effects from flow disturbances introduced in the rising liquid. An optical mirror on a swivel mount was placed directly beneath the column of water to enable

Appendix B (Continued)

a direct view of the sample (via a CCD camera) while hydrostatic pressure was gradually increased. Water breakthrough appeared as a bright light spot at the point of first penetration, as shown in the inset of Figure A1. The height of the water column at breakthrough designated the maximum hydrohead that a sample could tolerate reliably. This process was repeated at least 5 times for a given test sample, and the pressures were then averaged to determine the final resistance pressure and the corresponding standard deviation.

B.4 Fluoropolymer (PMC) Surface Energy Calculation

The surface energy (γ_S) of a given solid can be determined via the contact angles of two probe liquids (80), in this case water and hexadecane oil. The Owens/Wendt equation relating the interfacial energies is given by:

$$\frac{\gamma_L(\cos \theta + 1)}{2\sqrt{\gamma_L^D}} = \frac{\sqrt{\gamma_S^P}\sqrt{\gamma_L^P}}{\sqrt{\gamma_L^D}} + \sqrt{\gamma_S^D}, \quad (C1)$$

where the surface energies are divided into two components: polar (P) and dispersive (D). The known surface energies of probe liquids (γ_L) and their measured contact angles (θ) are used to generate a line from two points in the above equation which is of the form $y = mx + b$, where

$$y = \frac{\gamma_L(\cos \theta + 1)}{2\sqrt{\gamma_L^D}}, m = \sqrt{\gamma_S^P}, \text{ and } b = \sqrt{\gamma_S^D} \quad (C2)$$

The resultant water contact angles (WCA) and oil contact angles (OCA) on the solid PMC film were $117^\circ \pm 1.5^\circ$ and $57^\circ \pm 3^\circ$, respectively. Using a surface energy of 72.8 mN/m (γ_L) for water, comprised of a dispersive component (γ_L^D) of 21.8 mN/m and a polar component

Appendix B (Continued)

(γ_L^P) of 51 mN/m, and a surface energy for oil of 27.5 mN/m, derived completely from the dispersive component due to lack of polarity ($\gamma_L^P = 0$), the square of both the slope (γ_S^P) and intercept (γ_S^D) can be calculated and summed for a total solid surface energy (γ_S) estimate for the fluoropolymer PMC:

$$\gamma_S = \gamma_S^P + \gamma_S^D = 0.01\text{mN/m} + 16.4\text{mN/m} \approx 16.4\text{mN/m} \quad (\text{C3})$$

B.5 Electron Microscopy Characterization

Appendix B (Continued)

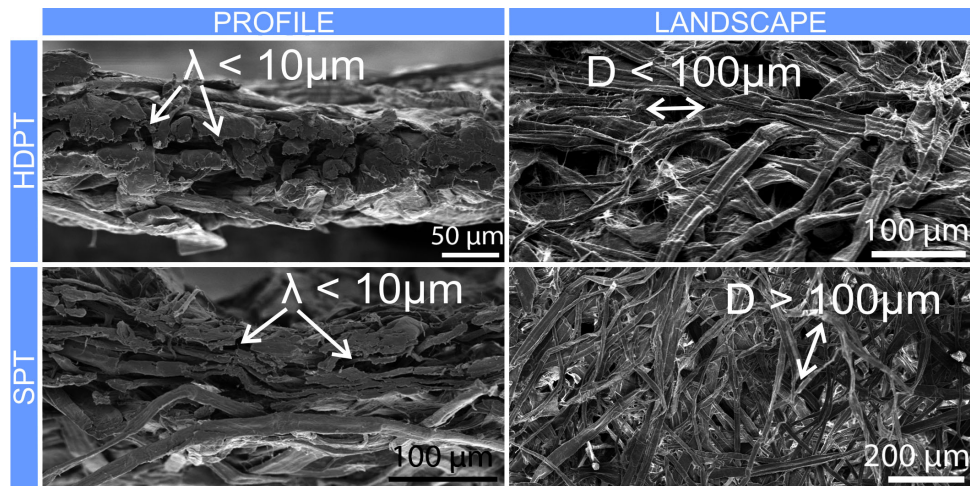


Figure C1. SEM images of uncoated HDPT and SPT for comparison of fiber spacing (effective pore radii) and fiber depth. Side-by-side comparison of substrates in profile show the fiber depths can be approximated to less than 10 μm , with clear evidence that it can be much smaller at intervals. Threshold pressures in the forward flow CU orientation will be limited by the fiber depth shown in profile, the weakest point will be the point where fiber depth is smallest. Further comparison of the two substrates in panoramic landscape “top-down” images reveals the much larger fiber spacing for SPT as opposed to HDPT, the Laplace pressure of the corresponding pores will determine the threshold pressure for the reverse-flow CD orientation. The weakest point in this orientation will be where the spacing is the largest.

Appendix B (Continued)

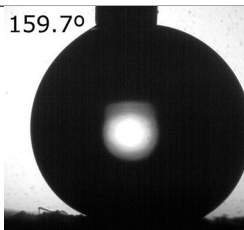
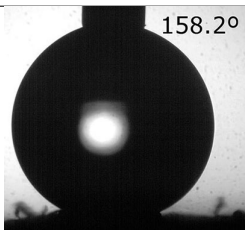
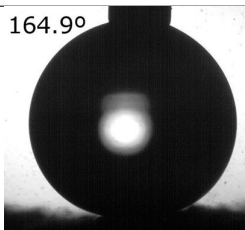
TABLE IX

TYPICAL IMAGES CAPTURED DURING WATER CA MEASUREMENTS FOR HDPT AT THREE PMC/NANOCLAY COATING ADD-ON LEVELS, WITH ACCOMPANYING CA MEASUREMENTS ON COATED GLASS SLIDES LISTED FOR COMPARISON. THE ROUGH NATURE OF THE PAPER SURFACE TOPOGRAPHY POSED CHALLENGES

IN OBTAINING ACCURATE AND CONSISTENT CA MEASUREMENTS. ALL MEASUREMENTS WERE TAKEN USING A HORIZONTAL SIDE VIEW AND THE CORRESPONDING CA FOR HDPT ARE LISTED WITHIN THE IMAGE OF EACH DROPLET MEASURED. ALL COATING LEVELS SHOWN ACHIEVED

SUPERHYDROPHOBICITY ($CA > 150^\circ$) ON ALL SUBSTRATES. THE NEEDLE DIAMETER (TOP) IN ALL IMAGES IS 1 MM, IMPLYING AN AVERAGE DROPLET

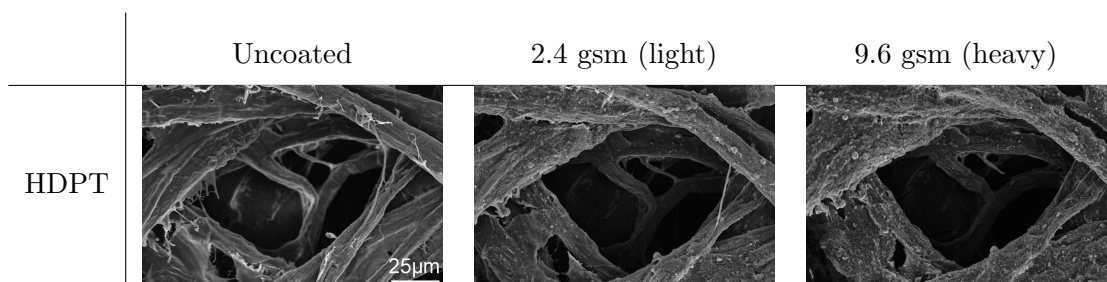
DIAMETER BETWEEN 3 AND 4 MM.

	2.5 gsm	5 gsm	10 gsm
HDPT	 159.7°	 158.2°	 164.9°
Glass Slides	$158.8^\circ \pm 4.5^\circ$	$166.2^\circ \pm 1.4^\circ$	$155.3^\circ \pm 7.5^\circ$

Appendix B (Continued)

TABLE X

SUBSTRATE PORE SIZE AS A FUNCTION OF ADD-ON COATING LEVEL ON HDPT: THE LEFT IMAGE DISPLAYS THE UNCOATED PORE; THE MIDDLE IMAGE SHOWS THE SAME PORE WITH A LIGHT COATING LEVEL OF ~2.5 GSM; THE RIGHT IMAGE IS OF THE SAME PORE WITH A HEAVIER COATING LEVEL OF ~10 GSM. FOR THE LARGER PORE SIZES, THE COATING HAS A NEGLIGIBLE EFFECT ON REDUCING PORE SIZE, AS PORES ARE TOO LARGE FOR THE POLYMER TO BRIDGE AND SEAL. THE SCALE BAR IN THE LEFTMOST SEM MICROGRAPH APPLIES TO ALL IMAGES.



Appendix C

SUPPORTING INFORMATION: WATER-BASED & NONFLUORINATED SUPERHYDROPHOBIC COATINGS

Appendix C (Continued)

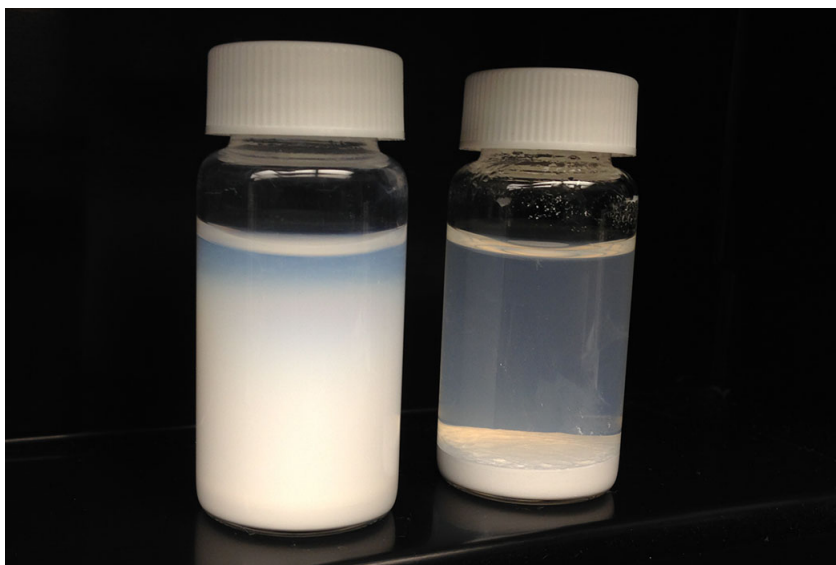


Figure B1. 20 ml vials of sonicated TiO_2 particles in water after one month. The left vial is the 21 nm mixed-phase nano TiO_2 , and maintained suspension in water indefinitely. A small amount of the larger particles or aggregates separated out, seen resting in the bottom of the vial. As compared to the anatase form on the right composed of much heavier particles which settled within the first hour.

Appendix D

SUPPORTING INFORMATION: DURABLE & FLEXIBLE GRAPHENE COMPOSITES BASED ON ARTISTS' PAINT FOR CONDUCTIVE PAPER APPLICATIONS

TABLE XI

ROUGHNESS AVERAGE (R_A , IN μM) VALUES FOR THE SMALLEST AND LARGEST
MLG SIZES TESTED FOR BOTH THE M- AND S-TYPE (XG SCIENCES AND STREM,
RESPECTIVELY).

MLG Type-Size	Unpolished	Polished
M-5	6.84 ± 0.4	2.15 ± 0.1
M-25	33.24 ± 4.1	3.88 ± 1.2
S-5	11.11 ± 2.1	1.60 ± 0.3
S-25	43.4 ± 9.0	3.16 ± 0.6

Appendix D (Continued)

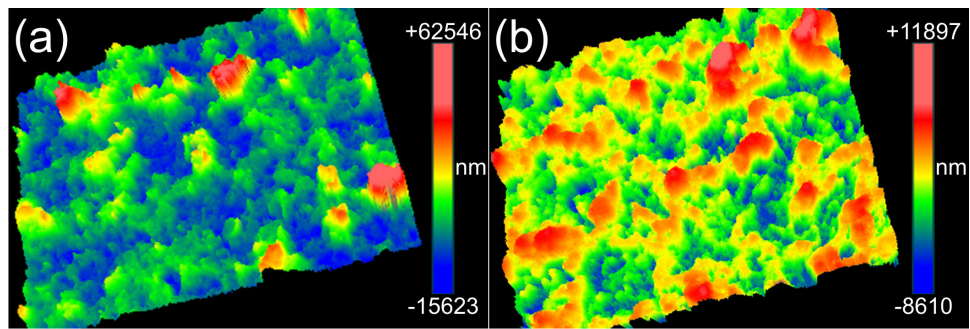


Figure D1. Profilometry images of an unpolished 50 wt. % M-5 composite (a), as compared to the same composite after polishing (b). The deep valleys shown in blue are in stark contrast to the several peaks of deep red shown in (a). For the polished surface in (b), there are many more peaks of red, but these are much more common and not nearly as sharply angled as that observed in the unpolished surface. The unpolished surface has a roughness average, R_a , of $6.84 \pm 0.4 \mu\text{m}$ as compared to the polished R_a of $1.60 \pm 0.3 \mu\text{m}$.

Appendix D (Continued)

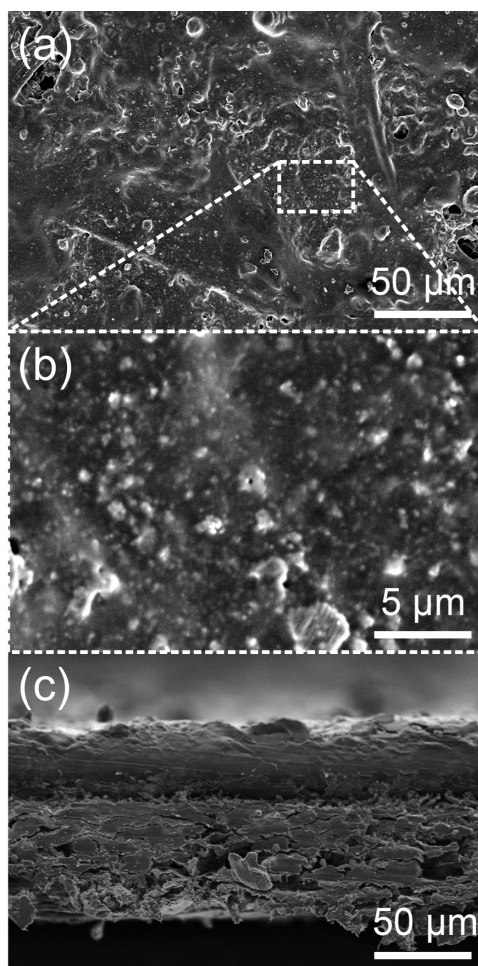


Figure D2. SEM images of an all-paint coating in low-magnification (a), to high magnification (b) where individual CuPc aggregates can be discerned. A cross-sectional profile image (c) was also included to estimate coating thickness in the absence of any MLG filler particles.

Appendix D (Continued)

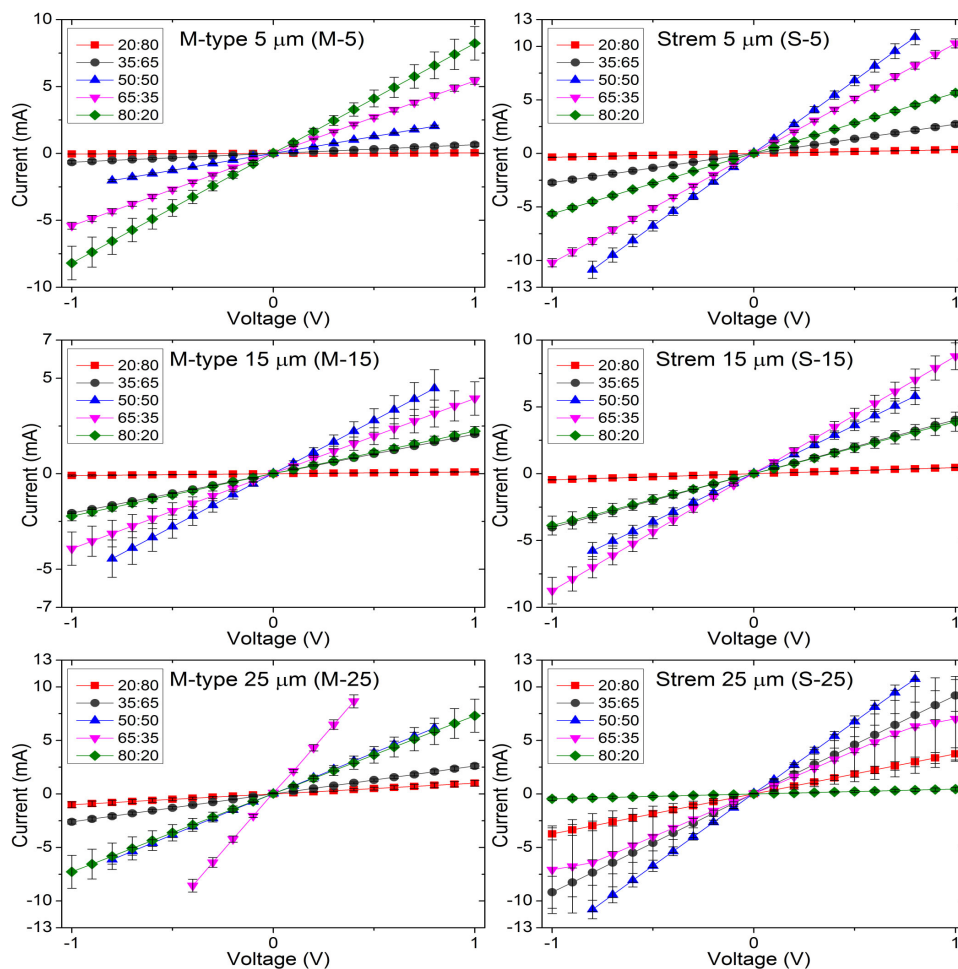


Figure D3. I-V plots for both types of MLG samples, Strem and xGNP, and all mass ratios tested. All 3 sizes (5, 15, and 25 μm) were tested in all 5 mass fractions of particle filler content in the final composite (20, 35, 50, 65 and 80 wt. %). All samples, sizes, and ratios demonstrate linear (Ohmic) behavior, and decreasing electrical resistance with increased particle filler content, until the point where decreased polymer content provides inadequate adhesion to retain the MLG within the composite during the polishing step.

Appendix D (Continued)

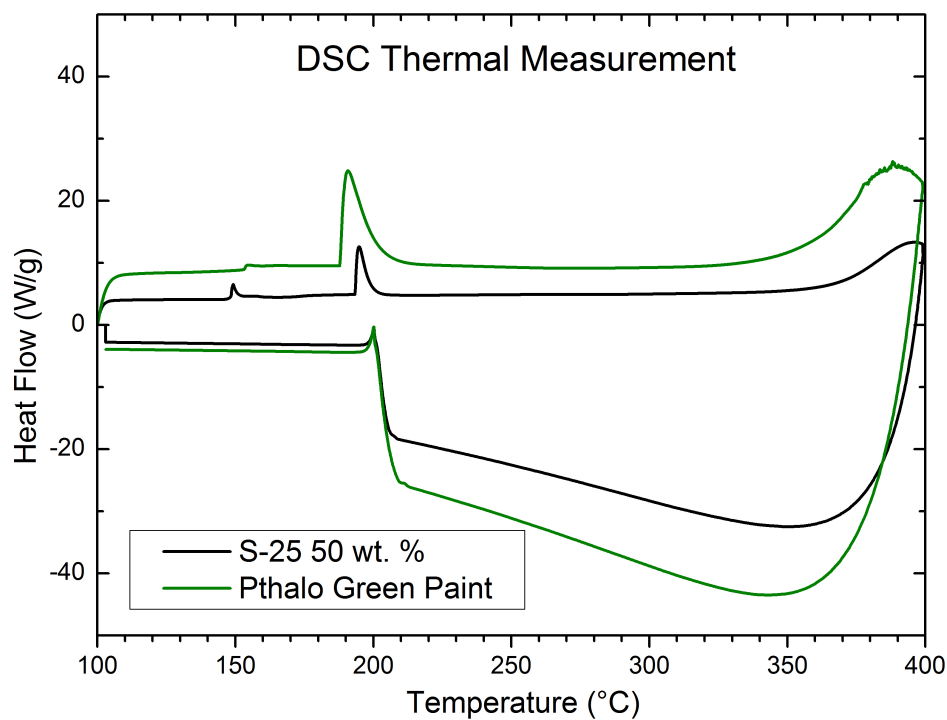


Figure D4. DSC thermal characterization for the dried paint (green) as compared to a representative sample of S-25 in a 50 wt. % composite (black). The glass transition temperature (T_g) is found to be approximately around 190 °C for both samples. The heat transfer of the composite is increased by the addition of MLG, as seen by the sharper transitions and less relative heat flow.

Appendix D (Continued)

Non-contact AFM measurements on the artists paint containing chlorinated copper phthalocyanine: Obtaining reproducible AFM data from the spray-cast films was not possible due to solvent-induced roughness formation during spray-casting. The AFM data were collected by dispersing 1% of the original paint emulsion in acetone. The solution was ultrasonic processed and allowed to rest for 24 hours. Afterwards, the acetone-thinned paint was drop-cast on a clean microscope glass slide. It was allowed to dry and cure for 16 hours before AFM measurements.

Appendix D (Continued)

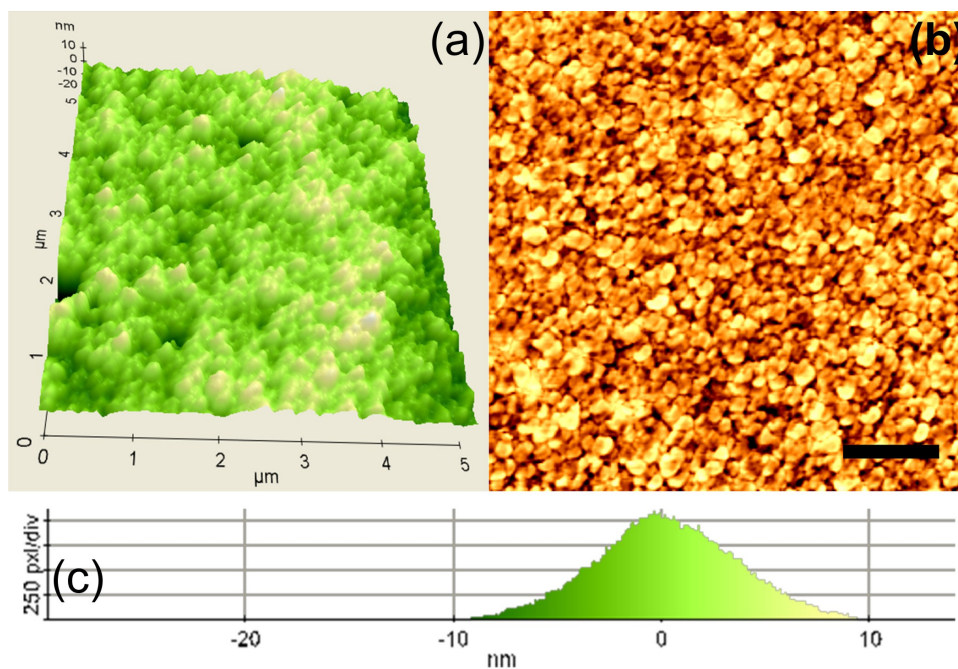


Figure D5. (a) Morphological characteristics of the original artist paint containing CuPc particles in $5 \times 5 \mu\text{m}^2$ surface topography image obtained from drop-casting from a dilute acetone solution. (b) AFM phase contrast image. The particle-like features are likely chlorinated CuPc aggregates. The scale-bar is $1 \mu\text{m}$. (c) Roughness histogram of the measured film.

Appendix D (Continued)



Figure D6. A simple circuit was fabricated to display the collaboration between the Italian Institute of Technology (IIT) and the University of Illinois at Chicago (UIC). The circuit was designed such that the three LED lights would bridge the circuit forming a connection at the three i's in the logos. The LED's were affixed with adhesive copper tape, with a spot of silver paint to ensure good contact. The paper was sprayed with Strem 25 μm (S-25) MLG particles in a 50 wt. % blend with the CuPC paint solids. The electrical circuit is closed once the battery is placed upside down on the two conductive paper leads, and the i's are "dotted" with a bright white light.

Appendix E

SUPPORTING INFORMATION: HIGHLY ELASTOMERIC & CONDUCTIVE SUPERHYDROPHOBIC COMPOSITES

Appendix E (Continued)

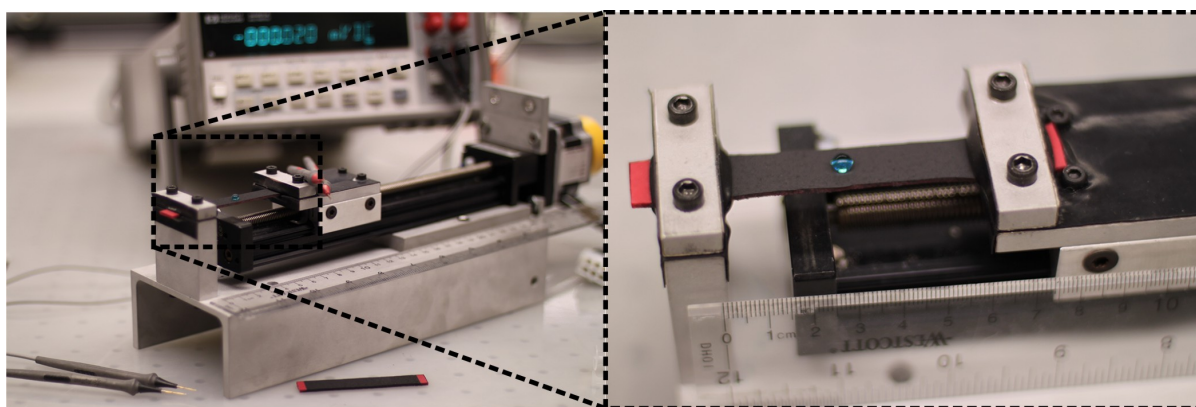


Figure E1. Images of the stretch apparatus used for deformation of the coated substrates through fixed stretch ratios. In the background on left, the 4-probe multimeter is included with two leads visible on the left with the other two resting on top of the machine. In the inset on left, a top-down view of the stretched composite with a beaded water droplet in center (dyed blue for visualization).

Appendix E (Continued)

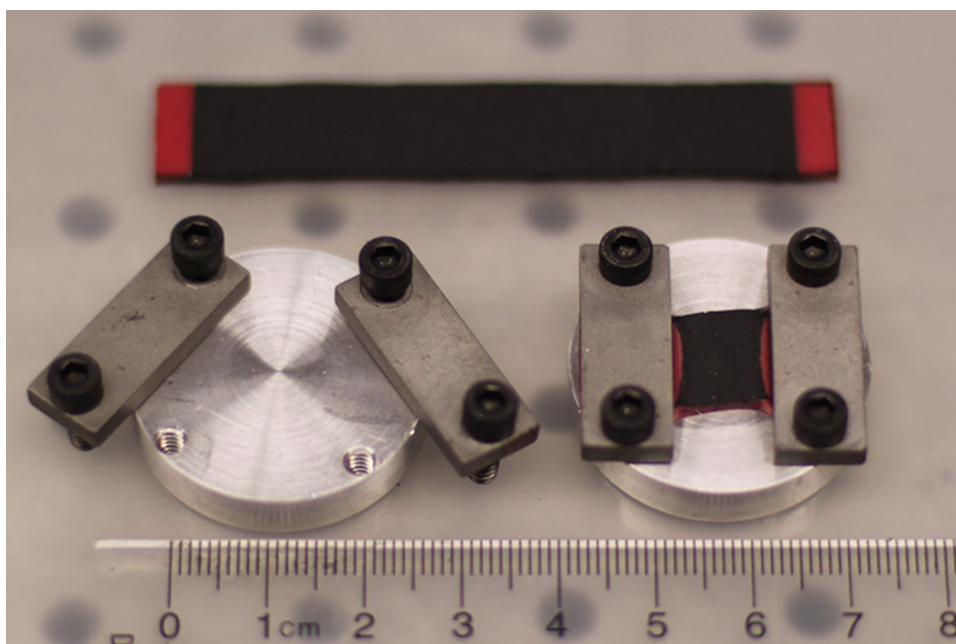


Figure E2. Special SEM stubs were prepared to maintain the stretch ratios from the stretch apparatus in order to image the morphological deformation of the composites. On top of the image is a coated rubber strip along with a cm ruler in the bottom for size. The stub on the left is empty to display how the clamps swivel for inserting substrates *in situ* from the stretch apparatus. Once inserted, as shown in the stub on the left containing a coated substrate in a stretch ratio of $\lambda = 2$, a razor is used to sever any unnecessary material.

Appendix E (Continued)

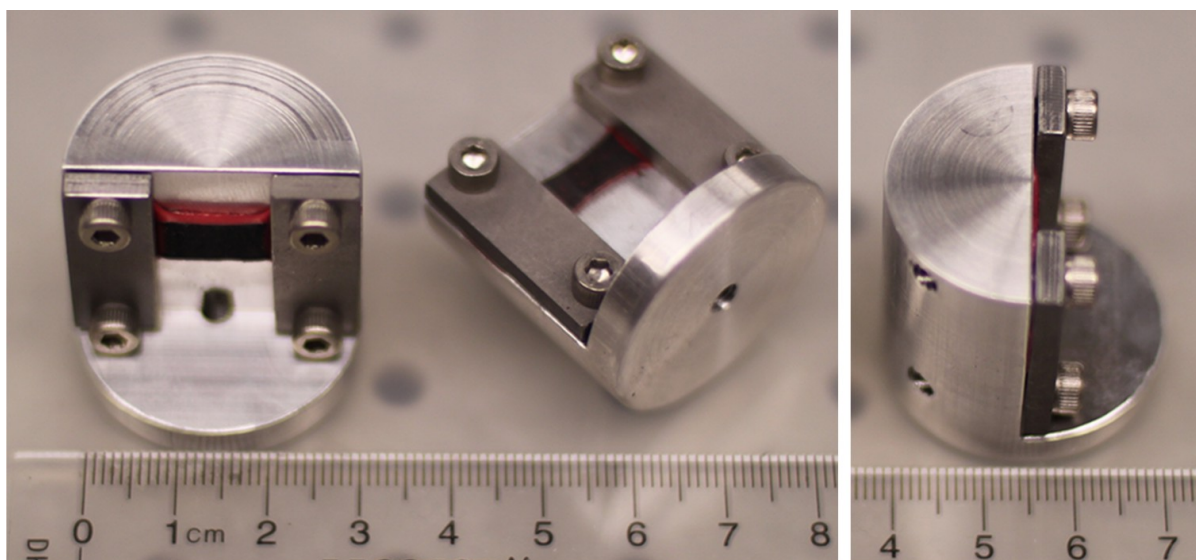


Figure E3. Similar SEM stubs as those shown in Figure E2 were prepared in order to image cross-sectional profiles of the composites through various stretch ratios; useful for determining volume of the conductive composite.

Appendix F

SUPPORTING INFORMATION: RIGHTS & PERMISSIONS

F.1 Copyright

Chapter 2 is subject to copyright. This chapter is reprinted (adapted) with permission from Industrial & Engineering Chemistry Research, 53, Joseph E. Mates, Thomas M. Schutzius, Ilker S. Bayer, Jian Qin, Don E. Walldroup, and Constantine M. Megaridis, 222–227, Copyright 2014, American Chemical Society (41). The permission to reprint (both print and electronically) was obtained on November 24th, 2014 for a one-time use in the author’s thesis (see Figure E1).

Chapter 3 is subject to copyright. This chapter is reprinted (adapted) with permission from ACS Applied Materials & Interfaces, 6, Joseph E. Mates, Thomas M. Schutzius, Jian Qin, Don E. Walldroup, and Constantine M. Megaridis, 12837–12843, Copyright 2014, American Chemical Society (63). The permission to reprint (both print and electronically) was obtained on November 24th, 2014 for a one-time use in the author’s thesis (see Figure E2).

F.2 Co-authorship

All co-authors approve of co-authored content being included in this thesis.

Appendix F (Continued)




[Home](#)
[Create Account](#)
[Help](#)
[Live Chat](#)


ACS Publications
Most Trusted. Most Cited. Most Read.

Title: Water-Based Superhydrophobic Coatings for Nonwoven and Cellulosic Substrates

Author: Joseph E. Mates, Thomas M. Schutzius, Ilker S. Bayer, et al

Publication: Industrial & Engineering Chemistry Research

Publisher: American Chemical Society

Date: Jan 1, 2014

Copyright © 2014, American Chemical Society

User ID

Passvord

☐ Enable Auto Login

LOGIN

[Forgot Password/User ID?](#)

If you're a copyright.com user, you can login to RightsLink using your copyright.com credentials. Already a RightsLink user or want to [learn more?](#)



PERMISSION/LICENSE IS GRANTED FOR YOUR ORDER AT NO CHARGE

This type of permission/license, instead of the standard Terms & Conditions, is sent to you because no fee is being charged for your order. Please note the following:


- Permission is granted for your request in both print and electronic formats, and translations.
- If figures and/or tables were requested, they may be adapted or used in part.
- Please print this page for your records and send a copy of it to your publisher/graduate school.
- Appropriate credit for the requested material should be given as follows: "Reprinted (adapted) with permission from (COMPLETE REFERENCE CITATION). Copyright (YEAR) American Chemical Society." Insert appropriate information in place of the capitalized words.
- One-time permission is granted only for the use specified in your request. No additional uses are granted (such as derivative works or other editions). For any other uses, please submit a new request.

Figure E1. Copy of the license allowing republication of copyright material for Chapter 2.

Appendix F (Continued)

[Home](#)
[Create Account](#)
[Help](#)
[Live Chat](#)


ACS Publications
Most Trusted. Most Cited. Most Read.

Title: The Fluid Diode: Tunable Unidirectional Flow through Porous Substrates

Author: Joseph E. Mates, Thomas M. Schutzius, Jian Qin, et al

Publication: Applied Materials

Publisher: American Chemical Society

Date: Aug 1, 2014

Copyright © 2014, American Chemical Society

User ID
Password
<input type="checkbox"/> Enable Auto Login
LOGIN
Forgot Password/User ID?

If you're a copyright.com user, you can login to RightsLink using your copyright.com credentials. Already a RightsLink user or want to [learn more?](#)

PERMISSION/LICENSE IS GRANTED FOR YOUR ORDER AT NO CHARGE

This type of permission/license, instead of the standard Terms & Conditions, is sent to you because no fee is being charged for your order. Please note the following:

- Permission is granted for your request in both print and electronic formats, and translations.
- If figures and/or tables were requested, they may be adapted or used in part.
- Please print this page for your records and send a copy of it to your publisher/graduate school.
- Appropriate credit for the requested material should be given as follows: "Reprinted (adapted) with permission from (COMPLETE REFERENCE CITATION). Copyright (YEAR) American Chemical Society." Insert appropriate information in place of the capitalized words.
- One-time permission is granted only for the use specified in your request. No additional uses are granted (such as derivative works or other editions). For any other uses, please submit a new request.

Figure E2. Copy of the license allowing republication of copyright material for Chapter 3.

CITED LITERATURE

1. Kelly, K. L., Coronado, E., Zhao, L. L., and Schatz, G. C.: The optical properties of metal nanoparticles: The influence of size, shape, and dielectric environment. Journal of Physical Chemistry B, 107(3):668–677, 2003.
2. Freestone, I., Meeks, N., Sax, M., and Higgitt, C.: The lycurgus cup - a roman nanotechnology. Gold Bulletin, 40(4):270–277, 2007.
3. Link, S. and El-Sayed, M. A.: Shape and size dependence of radiative, non-radiative and photothermal properties of gold nanocrystals. International Reviews in Physical Chemistry, 19(3):409–453, 2000.
4. Faraday, M.: The bakerian lecture: Experimental relations of gold (and other metals) to light. Philosophical Transactions of the Royal Society of London, 147:145–181, 1857.
5. Baker, G.: The early history of medicine, health & disease (1576). EEBO Editions, ProQuest, 2010.
6. Daniel, M. C. and Astruc, D.: Gold nanoparticles: Assembly, supramolecular chemistry, quantum-size-related properties, and applications toward biology, catalysis, and nanotechnology. Chemical Reviews, 104(1):293–346, 2004.
7. Feynman, R. P.: There's plenty of room at the bottom. Engineering and Science, 23(5):22–36, 1960.
8. Voice, E. H.: The history of the manufacture of pencils. Transactions of the Newcomen Society, 27(1):131–141, 1949.
9. Boardman, J., Edwards, I. E. S., Hammond, N. G. L., and Sollberger, E.: The Cambridge Ancient History Volume 3, Part 1. Cambridge University Press, 1982.
10. Anderson, K. J.: Leading up to the pencil. Materials Research Society, 19(6):69, 1994.

11. Takami, G., Ohba, T., Morito, S., and Das, A. K.: Microstructural observation on materials of the japanese sword under fold-forging process. Materials Science Forum, 654-656:134–137, 2010.
12. Wallace, P. R.: The band theory of graphite. Physical Review, 71(9):622–634, 1947.
13. Brodie, B. C.: On the atomic weight of graphite. Philosophical Transactions of the Royal Society of London, 149:249–259, 1859.
14. Kohlschütter, V. and Haenni, P.: Zur kenntnis des graphitischen kohlenstoffs und der graphitsäure. Zeitschrift für Anorganische und Allgemeine Chemie, 105(1):121–144, 1947.
15. Iijima, S.: Carbon nanotubes: past, present, and future. Physica B - Condensed Matter, 323(1-4):1–5, 2002.
16. Novoselov, K. S., Geim, A. K., Morozov, S. V., Jiang, D., Zhang, Y., Dubonos, S., Grigorieva, I. V., and Firsov, A. A.: Electric field effect in atomically thin carbon films. Science, 306(5696):666–669, 2004.
17. Guggenheim, S. and Martin, R. T.: Definition of clay and clay mineral: Joint report of the aipea nomenclature and cms nomenclature committees. Clays and Clay Minerals, 43(2):255–256, 1995.
18. Diebold, U.: The surface science of titanium dioxide. Surface Science Reports, 48(5-8):53–229, 2003.
19. Mulhaupt, R.: International historic chemical landmark: The foundation of polymer science by hermann staudinger (1881-1965). Macromolecular Chemistry and Physics, 200(8):U5–U8, 1999.
20. Baldi, P. and Hatfield, G. W.: DNA Microarrays and Gene Expression: From Experiments to Data Analysis and Modeling. Cambridge University Press, 2002.
21. Galli, P., Danesi, S., and Simonazzi, T.: Polypropylene based polymer blends: Fields of application and new trends. Polymer Engineering & Science, 24(8):544–554, 1984.
22. Young, T.: An essay on the cohesion of fluids. Philosophical Transactions of the Royal Society of London, 95:65–87, 1805.

23. Wenzel, R. N.: Resistance of solid surfaces to wetting by water. Industrial and Engineering Chemistry, 28(8):988–994, 1936.
24. Cassie, A. B. D. and Baxter, S.: Wettability of porous substrates. Transactions of the Faraday Society, 40:546–551, 1944.
25. Zhu, X. Y., Loo, H. E., and Bai, R. B.: A novel membrane showing both hydrophilic and oleophobic surface properties and its non-fouling performances for potential water treatment applications. Journal of Membrane Science, 436:47–56, 2013.
26. Furmidge, C. G. L.: Studies at phase interfaces. i. the sliding of liquid drops on solid surfaces and a theory for spray retention. Journal of Colloid Science, 17(4):309–324, 1962.
27. Extrand, C. W. and Gent, A. N.: Retention of liquid drops by solid surfaces. Journal of Colloid and Interface Science, 138(2):431–442, 1990.
28. Tuteja, A., Choi, W., Ma, M. L., Mabry, J. M., Mazzella, S. A., Rutledge, G. C., McKinley, G. H., and Cohen, R. E.: Designing superoleophobic surfaces. Science, 318(5856):1618–1622, 2007.
29. Rao, C. N. R., Sood, A. K., Subrahmanyam, K. S., and Govindaraj, A.: Graphene: The new two-dimensional nanomaterial. Angewandte Chemie-International Edition, 48(42):7752–7777, 2009.
30. Shante, V. K. S. and Kirkpatr, S.: Introduction to percolation theory. Advances in Physics, 20(85):325–357, 1971.
31. Das, D. and Pourdeyhimi, B.: Composite Nonwoven Materials: Structure, Properties and Applications. Woodhead Publishing, 2014.
32. Zhang, D., Sun, Q., Bhat, G., and Wadsworth, L.: Structure and property characterization of spunbonded filaments and webs using thermal analysis. Journal of Applied Polymer Science, 69(3):421–434, 1998.
33. Fedorova, N., Verenich, S., and Pourdeyhimi, B.: Strength optimization of thermally bonded spunbond nonwovens. Journal of Engineered Fibers and Fabrics, 2(1):38–48, 2007.

34. Anantharamaiah, N., Verenich, S., and Pourdeyhimi, B.: Durable nonwoven fabrics via fracturing bicomponent islands-in-the-sea filaments. Journal of Engineered Fibers and Fabrics, 3(3):1–9, 2008.
35. Hutten, I. M.: Handbook of Nonwoven Filter Media. Butterworth-Heinemann, 2007.
36. Kawai, H.: The piezoelectricity of poly (vinylidene fluoride). Japanese Journal of Applied Physics, 8:975–976, 1969.
37. Jafferis, N. T., Stone, H. A., and Sturm, J. C.: Traveling wave-induced aerodynamic propulsive forces using piezoelectrically deformed substrates. Applied Physics Letters, 99(11):3, 2011.
38. Sencadas, V., Lanceros-Mendez, S., and Mano, J. F.: Characterization of poled and non-poled beta-pvdf films using thermal analysis techniques. Thermochimica Acta, 424(1-2):201–207, 2004.
39. Hadimani, R. L., Bayramol, D. V., Sion, N., Shah, T., Qian, L. M., Shi, S. X., and Siores, E.: Continuous production of piezoelectric pvdf fibre for e-textile applications. Smart Materials and Structures, 22(7):6, 2013.
40. Soin, N., Shah, T. H., Anand, S. C., Geng, J. F., Pornwannachai, W., Mandal, P., Reid, D., Sharma, S., Hadimani, R. L., Bayramol, D. V., and Siores, E.: Novel "3-d spacer" all fibre piezoelectric textiles for energy harvesting applications. Energy & Environmental Science, 7(5):1670–1679, 2014.
41. Mates, J. E., Schutzius, T. M., Bayer, I. S., Qin, J., Waldroup, D. E., and Megaridis, C. M.: Water-based superhydrophobic coatings for nonwoven and cellulosic substrates. Industrial & Engineering Chemistry Research, 53(1):222–227, 2014.
42. Marmur, A.: The lotus effect: Superhydrophobicity and metastability. Langmuir, 20(9):3517–3519, 2004.
43. Miwa, M., Nakajima, A., Fujishima, A., Hashimoto, K., and Watanabe, T.: Effects of the surface roughness on sliding angles of water droplets on superhydrophobic surfaces. Langmuir, 16(13):5754–5760, 2000.
44. Roach, P., Shirtcliffe, N. J., and Newton, M. I.: Progress in superhydrophobic surface development. Soft Matter, 4(2):224–240, 2008.

45. Zhang, X., Shi, F., Niu, J., Jiang, Y. G., and Wang, Z. Q.: Superhydrophobic surfaces: from structural control to functional application. Journal of Materials Chemistry, 18(6):621–633, 2008.
46. Ogihara, H., Okagaki, J., and Saji, T.: Facile fabrication of colored superhydrophobic coatings by spraying a pigment nanoparticle suspension. Langmuir, 27(15):9069–9072, 2011.
47. Wu, W. C., Wang, X. L., Liu, X. J., and Zhou, F.: Spray-coated fluorine-free superhydrophobic coatings with easy repairability and applicability. ACS Applied Materials & Interfaces, 1(8):1656–1661, 2009.
48. Das, A., Hayvaci, H. T., Tiwari, M. K., Bayer, I. S., Erricolo, D., and Megaridis, C. M.: Superhydrophobic and conductive carbon nanofiber/ptfe composite coatings for emi shielding. Journal of Colloid and Interface Science, 353(1):311–315, 2011.
49. Manoudis, P. N., Karapanagiotis, I., Tsakalof, A., Zuburtikudis, I., and Panayiotou, C.: Superhydrophobic composite films produced on various substrates. Langmuir, 24(19):11225–11232, 2008.
50. Bayer, I. S., Tiwari, M. K., and Megaridis, C. M.: Biocompatible poly(vinylidene fluoride)/cyanoacrylate composite coatings with tunable hydrophobicity and bonding strength. Applied Physics Letters, 93(17):3, 2008.
51. Tiwari, M. K., Bayer, I. S., Jursich, G. M., Schutzius, T. M., and Megaridis, C. M.: Highly liquid-repellent, large-area, nanostructured poly(vinylidene fluoride)/poly(ethyl 2-cyanoacrylate) composite coatings: Particle filler effects. ACS Applied Materials & Interfaces, 2(4):1114–1119, 2010.
52. Das, A., Schutzius, T. M., Bayer, I. S., and Megaridis, C. M.: Superoleophobic and conductive carbon nanofiber/fluoropolymer composite films. Carbon, 50(3):1346–1354, 2012.
53. Xu, L., Zhuang, W., Xu, B., and Cai, Z.: Superhydrophobic cotton fabrics prepared by one-step water-based sol-gel coating. The Journal of The Textile Institute, 103:311, 2012.
54. Tiwari, M. K., Bayer, I. S., Jursich, G. M., Schutzius, T. M., and Megaridis, C. M.: Poly(vinylidene fluoride) and poly(ethyl 2-cyanoacrylate) blends through con-

- trolled polymerization of ethyl 2-cyanoacrylates. Macromolecular Materials and Engineering, 294(11):775–780, 2009.
55. Schutzius, T. M., Bayer, I. S., Tiwari, M. K., and Megaridis, C. M.: Novel fluoropolymer blends for the fabrication of sprayable multifunctional superhydrophobic nanostructured composites. Industrial & Engineering Chemistry Research, 50(19):11117–11123, 2011.
 56. Ma, M. L., Mao, Y., Gupta, M., Gleason, K. K., and Rutledge, G. C.: Superhydrophobic fabrics produced by electrospinning and chemical vapor deposition. Macromolecules, 38(23):97429748, 2005.
 57. Martin, J. W., Whittle, D. M., Muir, D. C. G., and Mabury, S. A.: Perfluoroalkyl contaminants in a food web from lake ontario. Environmental Science & Technology, 38(20):5379–5385, 2004.
 58. Xu, X. M. and Wang, X. P.: The modified cassie’s equation and contact angle hysteresis. Colloid and Polymer Science, 291(2):299–306, 2013.
 59. Wong, T. S., Kang, S. H., Tang, S. K. Y., Smythe, E. J., Hatton, B. D., Grinthal, A., and Aizenberg, J.: Bioinspired self-repairing slippery surfaces with pressure-stable omniphobicity. Nature, 477(7365):443–447, 2011.
 60. Feng, L., Zhang, Y. A., Xi, J. M., Zhu, Y., Wang, N., Xia, F., and Jiang, L.: Petal effect: A superhydrophobic state with high adhesive force. Langmuir, 24(8):4114–4119, 2008.
 61. Tuteja, A., Choi, W., Mabry, J. M., McKinley, G. H., and Cohen, R. E.: Robust omniphobic surfaces. Proceedings of the National Academy of Sciences of the United States of America, 105(47):18200–18205, 2008.
 62. Wendt, G. A., Chiu, K. F., Burazin, M. A., Farrington, T. E., and Heaton, D. A.: Method of making soft tissue product, 1997. US Patent 5,672,248.
 63. Mates, J. E., Schutzius, T. M., Qin, J., Waldroup, D. E., and Megaridis, C. M.: The fluid diode: Tunable unidirectional flow through porous substrates. ACS Applied Materials & Interfaces, 6(15):12837–12843, 2014.
 64. Franklin, K. J.: Valves in veins: An historical survey. Proceedings of the Royal Society of Medicine, 21(1):1–33, 1927.

65. Boreyko, J. B., Zhao, Y. J., and Chen, C. H.: Planar jumping-drop thermal diodes. Applied Physics Letters, 99(23), 2011.
66. Fadl, A., Zhang, Z. Q., Geller, S., Tolke, J., Krafczyk, M., and Meyer, D.: The effect of the microfluidic diodicity on the efficiency of valve-less rectification micropumps using lattice boltzmann method. Microsystem Technologies-Micro-and Nanosystems-Information Storage and Processing Systems, 15(9):1379–1387, 2009.
67. Lagubeau, G., Le Merrer, M., Clanet, C., and Quere, D.: Leidenfrost on a ratchet. Nature Physics, 7(5):395–398, 2011.
68. Chen, H., Cogswell, J., Anagnostopoulos, C., and Faghri, M.: A fluidic diode, valves, and a sequential-loading circuit fabricated on layered paper. Lab on a Chip, 12(16):2909–2913, 2012.
69. Megaridis, C. M., Schutzius, T. M., Bayer, I. S., and Qin, J.: Superhydrophobic compositions, 2013. US Patent 20130030098.
70. Schutzius, T. M., Bayer, I. S., Qin, J., Waldroup, D., and Megaridis, C. M.: Water-based, nonfluorinated dispersions for environmentally benign, large-area, superhydrophobic coatings. ACS Applied Materials & Interfaces, 5(24):13419–13425, 2013.
71. Song, H. J., Shen, X. Q., and Meng, X. F.: Superhydrophobic surfaces produced by carbon nanotube modified polystyrene composite coating. Journal of Dispersion Science and Technology, 31(11):1465–1468, 2010.
72. Ogihara, H., Xie, J., Okagaki, J., and Saji, T.: Simple method for preparing superhydrophobic paper: Spray-deposited hydrophobic silica nanoparticle coatings exhibit high water-repellency and transparency. Langmuir, 28(10):4605–4608, 2012.
73. Zhou, H., Wang, H. X., Niu, H. T., and Lin, T.: Superphobicity/philicity janus fabrics with switchable, spontaneous, directional transport ability to water and oil fluids. Scientific Reports, 3:6, 2013.
74. Lim, H. S., Baek, J. H., Park, K., Shin, H. S., Kim, J., and Cho, J. H.: Multifunctional hybrid fabrics with thermally stable superhydrophobicity. Advanced Materials, 22(19):2138–2141, 2010.

75. Schutzius, T. M., Elsharkawy, M., Tiwari, M. K., and Megaridis, C. M.: Surface tension confined (stc) tracks for capillary-driven transport of low surface tension liquids. Lab on a Chip, 12(24):5237–5242, 2012.
76. Schutzius, T. M., Bayer, I. S., Jursich, G. M., Das, A., and Megaridis, C. M.: Superhydrophobic-superhydrophilic binary micropatterns by localized thermal treatment of polyhedral oligomeric silsesquioxane (poss)-silica films. Nanoscale, 4(17):5378–5385, 2012.
77. Sun, T. L., Feng, L., Gao, X. F., and Jiang, L.: Bioinspired surfaces with special wettability. Accounts of Chemical Research, 38(8):644–652, 2005.
78. Calcagnile, P., Fragouli, D., Bayer, I. S., Anyfantis, G. C., Martiradonna, L., Cozzoli, P. D., Cingolani, R., and Athanassiou, A.: Magnetically driven floating foams for the removal of oil contaminants from water. ACS Nano, 6(6):5413–5419, 2012.
79. Lau, C., Butenhoff, J. L., and Rogers, J. M.: The developmental toxicity of perfluoroalkyl acids and their derivatives. Toxicology and Applied Pharmacology, 198(2):231–241, 2004.
80. Owens, D. and Wendt, R.: Estimation of the surface free energy of polymers. Journal of Applied Polymer Science, 13(8):1741–1747, 1969.
81. Wang, C. X., Yao, T. J., Wu, J., Ma, C., Fan, Z. X., Wang, Z. Y., Cheng, Y. R., Lin, Q., and Yang, B.: Facile approach in fabricating superhydrophobic and superoleophilic surface for water and oil mixture separation. ACS Applied Materials & Interfaces, 1(11):2613–2617, 2009.
82. Lee, C. H., Johnson, N., Drelich, J., and Yap, Y. K.: The performance of superhydrophobic and superoleophilic carbon nanotube meshes in water-oil filtration. Carbon, 49(2):669–676, 2011.
83. Zhu, Q., Pan, Q. M., and Liu, F. T.: Facile removal and collection of oils from water surfaces through superhydrophobic and superoleophilic sponges. Journal of Physical Chemistry C, 115(35):17464–17470, 2011.
84. Kota, A. K., Kwon, G., Choi, W., Mabry, J. M., and Tuteja, A.: Hygro-responsive membranes for effective oil-water separation. Nature Communications, 3:8, 2012.

85. Kang, Y. K., Wang, J. Y., Yang, G. B., Xiong, X. J., Chen, X. H., Yu, L. G., and Zhang, P. Y.: Preparation of porous super-hydrophobic and super-oleophilic polyvinyl chloride surface with corrosion resistance property. Applied Surface Science, 258(3):1008–1013, 2011.
86. Wang, C. F. and Lin, S. J.: Robust superhydrophobic/superoleophilic sponge for effective continuous absorption and expulsion of oil pollutants from water. ACS Applied Materials & Interfaces, 5(18):8861–8864, 2013.
87. Gao, L. and He, J.: Surface hydrophobic co-modification of hollow silica nanoparticles toward large-area transparent superhydrophobic coatings. Journal of Colloid and Interface Science, 396:152–9, 2013.
88. Nakajima, A., Fujishima, A., Hashimoto, K., and Watanabe, T.: Preparation of transparent superhydrophobic boehmite and silica films by sublimation of aluminum acetylacetonate. Advanced Materials, 11(16):1365–1368, 1999.
89. Xing, S. Y., Jiang, J., and Pan, T. R.: Interfacial microfluidic transport on micropatterned superhydrophobic textile. Lab on a Chip, 13(10):1937–1947, 2013.
90. Lang, F. J., Clough, P. H., Dyer, T. J., Goulet, M. T., Liu, K. C., Lostocco, M. R., Nickel, D. J., Rekoske, M. J., Runge, T. M., Seabaugh, M. L., Timm, J. J., and Zwick, K. J.: Tissue products containing non-fibrous polymeric surface structures and a topically-applied softening composition, 2009. US Patent 7,588,662.
91. FDA: Inventory of effective food contact substance notifications, 2004. FCS Notifications, FCN No. 424, The Dow Chemical Company.
92. FDA: Food and drugs chapter 1–food and drug administration department of health and human services subchapter a–general. Code of Federal Regulations, 1(21):73, 2014.
93. Chen, X., Wu, J., Ma, R., Hua, M., Koratkar, N., Yao, S., and Wang, Z.: Nanograsped micropyramidal architectures for continuous dropwise condensation. Advanced Functional Materials, 21(24):4617–4623, 2011.
94. Miljkovic, N., Enright, R., and Wang, E. N.: Effect of droplet morphology on growth dynamics and heat transfer during condensation on superhydrophobic nanostructured surfaces. ACS Nano, 6(2):1776–1785, 2012.

95. Li, M., Zhai, J., Liu, H., Song, Y. L., Jiang, L., and Zhu, D. B.: Electrochemical deposition of conductive superhydrophobic zinc oxide thin films. Journal of Physical Chemistry B, 107(37):9954–9957, 2003.
96. Han, J. T., Kim, S. Y., Woo, J. S., and Lee, G. W.: Transparent, conductive, and superhydrophobic films from stabilized carbon nanotube/silane sol mixture solution. Advanced Materials, 20(19):3724–3727, 2008.
97. Chen, Y. J., Li, Y., Yip, M. C., and Tai, N.: Electromagnetic interference shielding efficiency of polyaniline composites filled with graphene decorated with metallic nanoparticles. Composites Science and Technology, 80:80–86, 2013.
98. Lafuma, A. and Quere, D.: Superhydrophobic states. Nature Materials, 2(7):457–460, 2003.
99. Joanny, J. F. and Degennes, P. G.: A model for contact-angle hysteresis. Journal of Chemical Physics, 81(1):552–562, 1984.
100. Tadanaga, K., Morinaga, J., Matsuda, A., and Minami, T.: Superhydrophobic-superhydrophilic micropatterning on flowerlike alumina coating film by the sol-gel method. Chemistry of Materials, 12(3):590–592, 2000.
101. Wang, R., Hashimoto, K., Fujishima, A., Chikuni, M., Kojima, E., Kitamura, A., Shimohigoshi, M., and Watanabe, T.: Light-induced amphiphilic surfaces. Nature, 388(6641):431–432, 1997.
102. Preliminary risk assessment of the developmental toxicity associated with exposure to perfluorooctanoic acid and its salts. Report, E.P.A., Office of Pollution Prevention & Toxics and Risk Assessment Division, 2003.
103. Quéré, D.: Non-sticking drops. Reports on Progress in Physics, 68(11):2495–2532, 2005.
104. Weir, A., Westerhoff, P., Fabricius, L., Hristovski, K., and von Goetz, N.: Titanium dioxide nanoparticles in food and personal care products. Environmental Science & Technology, 46(4):2242–2250, 2012.
105. Cromer, D. T. and Herrington, K.: The structures of anatase and rutile. Journal of the American Chemical Society, 77(18):4708–4709, 1955.

106. Reyes-Coronado, D., Rodriguez-Gattorno, G., Espinosa-Pesqueira, M. E., Cab, C., de Coss, R., and Oskam, G.: Phase-pure tio_2 nanoparticles: anatase, brookite and rutile. Nanotechnology, 19(14):145605, 2008.
107. Pettibone, J. M., Cwiertny, D. M., Scherer, M., and Grassian, V. H.: Adsorption of organic acids on tio_2 nanoparticles: Effects of ph, nanoparticle size, and nanoparticle aggregation. Langmuir, 24(13):6659–6667, 2008.
108. Salameh, S., Schneider, J., Laube, J. and; Alessandrini, A., Facci, P., Seo, J. W., Ciacchi, L. C., and Madler, L.: Adhesion mechanisms of the contact interface of tio_2 nanoparticles in films and aggregates. Langmuir, 28(31):11457–11464, 2012.
109. Zhang, H., Penn, R. L., Hamers, R. J., and Banfield, J. F.: Enhanced adsorption of molecules on surfaces of nanocrystalline particles. Journal of Physical Chem. B, 103(22):46564662, 1999.
110. Wang, C. Y., Groenzin, H., and Shultz, M. J.: Comparative study of acetic acid, methanol, and water adsorbed on anatase tio_2 probed by sum frequency generation spectroscopy. Journal of the American Chemical Society, 127(27):97369744, 2005.
111. Gao, Y., Wahi, R., Kan, A. T., Falkner, J. C., Colvin, V. L., and Tomson, M. B.: Adsorption of cadmium on anatase nanoparticles—effect of crystal size and ph. Langmuir, 20(22):95859593, 2004.
112. Barnard, A. S. and Curtiss, L. A.: Prediction of tio_2 nanoparticle phase and shape transitions controlled by surface chemistry. Nano Letters, 5(7):1261–1266, 2005.
113. Barnard, A. S., Zapol, P., and Curtiss, L. A.: Modeling the morphology and phase stability of tio_2 nanocrystals in water. Journal of Chemical Theory and Computation, 1(1):107–116, 2005.
114. Henderson, M. A.: The interaction of water with solid surfaces: fundamental aspects revisited. Surface Science Reports, 46(1-8):1308, 2002.
115. Panaitescu, D. M., Radovici, C., Ghiurea, M., Paven, H., and Iorga, M. D.: Influence of rutile and anatase tio_2 nanoparticles on polyethylene properties. Polymer-Plastics Technology and Engineering, 50(2):196–202, 2011.

116. Jongsomjit, B., Ngamposri, S., and Praserttham, P.: Role of titania in tio_2tio_2 mixed oxides-supported metallocene catalyst during ethylene/1-octene copolymerization. Catalysis Letters, 100(3-4):139–146, 2005.
117. Wevers, R. and Vyorykka, J.: Polyolefin dispersions, an aqueous moisture barrier. Tech report, The DOW Chemical Company, 2009.
118. Xi, J. and Jiang, L.: Biomimic superhydrophobic surface with high adhesive forces. Industrial & Engineering Chemistry Research, 47(17):6354–6357, 2008.
119. Chen, H., Muller, M. B., Gilmore, K. J., Wallace, G. G., and Li, D.: Mechanically strong, electrically conductive, and biocompatible graphene paper. Advanced Materials, 20(18):3557–3561, 2008.
120. Hu, L. B., Choi, J. W., Yang, Y., Jeong, S., La Mantia, F., Cui, L. F., and Cui, Y.: Highly conductive paper for energy-storage devices. Proceedings of the National Academy of Sciences of the United States of America, 106(51):21490–21494, 2009.
121. Nystrom, G., Razaq, A., Stromme, M., Nyholm, L., and Mihranyan, A.: Ultrafast all-polymer paper-based batteries. Nano Letters, 9(10):3635–3639, 2009.
122. Tobjork, D. and Osterbacka, R.: Paper electronics. Advanced Materials, 23(17):1935–1961, 2011.
123. Hyun, W. J., Park, O. O., and Chin, B. D.: Foldable graphene electronic circuits based on paper substrates. Advanced Materials, 25(34):4729–4734, 2013.
124. Gao, T., Huang, K., Qi, X., Li, H. X., Yang, L. W., and Zhong, J. X.: Free-standing snO_2 nanoparticles graphene hybrid paper for advanced lithium-ion batteries. Ceramics International, 40(5):6891–6897, 2014.
125. Boon, J. J. and Learner, T.: Analytical mass spectrometry of artists' acrylic emulsion paints by direct temperature resolved mass spectrometry and laser desorption ionisation mass spectrometry. Journal of Analytical and Applied Pyrolysis, 64(2):327–344, 2002.
126. Scalarone, D. and Chiantore, O.: Separation techniques for the analysis of artists' acrylic emulsion paints. Journal of Separation Science, 27(4):263–274, 2004.

127. Jones, F. N., Mao, W. J., Ziemer, P. D., Xiao, F., Hayes, J., and Golden, M.: Artist paints - an overview and preliminary studies of durability. Progress in Organic Coatings, 52(1):9–20, 2005.
128. Winnik, M. A. and Feng, J. R.: Latex blends: An approach to zero voc coatings. Journal of Coatings Technology, 68(852):39–50, 1996.
129. Russell, J., Singer, B. W., Perry, J. J., and Bacon, A.: The identification of synthetic organic pigments in modern paints and modern paintings using pyrolysis-gas chromatography-mass spectrometry. Analytical and Bioanalytical Chemistry, 400(5):1473–1491, 2011.
130. Warner, M., Din, S., Tupitsyn, I. S., Morley, G. W., Stoneham, A. M., Gardener, J. A., Wu, Z. L., Fisher, A. J., Heutz, S., Kay, C. W. M., and Aepli, G.: Potential for spin-based information processing in a thin-film molecular semiconductor. Nature, 503(7477):504–508, 2013.
131. Ng, T. W., Lo, M. F., Zhou, Y. C., Liu, Z. T., Lee, C. S., Kwon, O., and Lee, S. T.: Ambient effects on fullerene/copper phthalocyanine photovoltaic interface. Applied Physics Letters, 94(19):3, 2009.
132. Boehm, H. P., Clauss, A., Fischer, G. O., and Hofmann, U.: Das adsorptionsverhalten sehr dünner kohlenstoff-folien. Zeitschrift für anorganische und allgemeine Chemie, 316(3-4):119–127, 1962.
133. Lee, C., Wei, X. D., Kysar, J. W., and Hone, J.: Measurement of the elastic properties and intrinsic strength of monolayer graphene. Science, 321(5887):385–388, 2008.
134. Siegel, A. C., Phillips, S. T., Dickey, M. D., Lu, N. S., Suo, Z. G., and Whitesides, G. M.: Foldable printed circuit boards on paper substrates. Advanced Functional Materials, 20(1):28–35, 2010.
135. Compton, O. C., Dikin, D. A., Putz, K. W., Brinson, L. C., and Nguyen, S. T.: Electrically conductive “alkylated” graphene paper via chemical reduction of amine-functionalized graphene oxide paper. Advanced Materials, 22(8):892–896, 2010.
136. Yang, G., Jung, Y., Cuervo, C. V., Ren, F., Pearton, S. J., and Kim, J.: GaN-based light-emitting diodes on graphene-coated flexible substrates. Optics Express, 22(9):A812–A817, 2014.

137. Huang, Q. J., Shen, W. F., Xu, Q. S., Tan, R. Q., and Song, W. J.: Room-temperature sintering of conductive ag films on paper. Materials Letters, 123:124–127, 2014.
138. Li, W., Li, W. J., Wei, J., Tan, J. J., and Chen, M. F.: Preparation of conductive cu patterns by directly writing using nano-cu ink. Materials Chemistry and Physics, 146(1-2):82–87, 2014.
139. Singh, N., Galande, C., Miranda, A., Mathkar, A., Gao, W., Reddy, A. L. M., Vlad, A., and Ajayan, P. M.: Paintable battery. Scientific Reports, 2:5, 2012.
140. Al-Saleh, M. H., Saadeh, W. H., and Sundararaj, U.: EMI shielding effectiveness of carbon based nanostructured polymeric materials: A comparative study. Carbon, 60:146–156, 2013.
141. Liu, L., Das, A., and Megaridis, C. M.: Terahertz shielding of carbon nanomaterials and their composites - a review and applications. Carbon, 69:1–16, 2014.
142. Liang, J. J., Wang, Y., Huang, Y., Ma, Y. F., Liu, Z. F., Cai, F. M., Zhang, C. D., Gao, H. J., and Chen, Y. S.: Electromagnetic interference shielding of graphene/epoxy composites. Carbon, 47(3):922–925, 2009.
143. Zhang, H. B., Yan, Q., Zheng, W. G., He, Z. X., and Yu, Z. Z.: Tough graphene-polymer microcellular foams for electromagnetic interference shielding. ACS Applied Materials & Interfaces, 3(3):918–924, 2011.
144. Eswaraiah, V., Sankaranarayanan, V., and Ramaprabhu, S.: Functionalized graphene-pvdf foam composites for EMI shielding. Macromolecular Materials and Engineering, 296(10):894–898, 2011.
145. Kim, M. S., Yan, J., Joo, K. H., Pandey, J. K., Kang, Y. J., and Ahn, S. H.: Synergistic effects of carbon nanotubes and exfoliated graphite nanoplatelets for electromagnetic interference shielding and soundproofing. Journal of Applied Polymer Science, 130(6):3947–3951, 2013.
146. Lorenzoni, M., Giugni, A., and Torre, B.: Oxidative and carbonaceous patterning of Si surface in an organic media by scanning probe lithography. Nanoscale Research Letters, 8(75):1–9, 2013.

147. Celebi, K., Jadhav, P. J., Milaninia, K. M., Bora, M., and Baldo, M. A.: The density of states in thin film copper phthalocyanine measured by kelvin probe force microscopy. Applied Physics Letters, 93(083308):1–3, 2008.
148. Shams, M. I. B., Jiang, Z., Rahman, S., Qayyum, J., Cheng, L. J., Xing, H. G., Fay, P., and Liu, L.: Approaching real-time terahertz imaging with photo-induced coded apertures and compressed sensing. Electronics Letters, 50(11):801–802, 2014.
149. Iqbal, M. W., Singh, A. K., Iqbal, M. Z., and Eom, J.: Raman fingerprint of doping due to metal adsorbates on graphene. Journal of Physics-Condensed Matter, 24(33), 2012.
150. Wu, W., Yu, Q., Peng, P., Liu, Z., Bao, J., and Pei, S.-S.: Control of thickness uniformity and grain size in graphene films for transparent conductive electrodes. Nanotechnology, 23(3), 2012.
151. Fernandez-Garcia, M., Cuervo-Rodriguez, R., and Madruga, E. L.: Glass transition temperatures of butyl acrylate-methyl methacrylate copolymers. Journal of Polymer Science Part B-Polymer Physics, 37(17):2512–2520, 1999.
152. Sommerhalter, C., Matthes, T. W., Glatzel, T., Jager-Waldau, A., and Lux-Steiner, M. C.: High-sensitivity quantitative kelvin probe microscopy by noncontact ultra-high-vacuum atomic force microscopy. Applied Physics Letters, 75(2):286–288, 1999.
153. Ago, H., Kugler, T., Cacialli, F., Salaneck, W. R., Shaffer, M. S. P., Windle, A. H., and Friend, R. H.: Work functions and surface functional groups of multiwall carbon nanotubes. Journal of Physical Chemistry B, 103(38):8116–8121, 1999.
154. Zerweck, U., Loppacher, C., Otto, T., Grafstroem, S., and Eng, L. M.: Kelvin probe force microscopy of c-60 on metal substrates: towards molecular resolution. Nanotechnology, 18(8), 2007.
155. Su, W. S., Leung, T. C., and Chan, C. T.: Work function of single-walled and multiwalled carbon nanotubes: First-principles study. Physical Review B, 76(23), 2007.
156. Das, A., Megaridis, C. M., Liu, L., Wang, T., and Biswas, A.: Design and synthesis of superhydrophobic carbon nanofiber composite coatings for terahertz frequency shielding and attenuation. Applied Physics Letters, 98(17):3, 2011.

157. Woo, S. J., Kong, J. H., Kim, D. G., and Kim, J. M.: A thin all-elastomeric capacitive pressure sensor array based on micro-contact printed elastic conductors. Journal of Materials Chemistry C, 2(22):4415–4422, 2014.
158. Kim, K. S., Jung, K. H., and Jung, S. B.: Design and fabrication of screen-printed silver circuits for stretchable electronics. Microelectronic Engineering, 120:216–220, 2014.
159. Brook, I., Mechrez, G., Suckeveriene, R. Y., Tchoudakov, R., and Narkis, M.: A novel approach for preparation of conductive hybrid elastomeric nano-composites. Polymers for Advanced Technologies, 24(8):758–763, 2013.
160. Chun, K. Y., Oh, Y., Rho, J., Ahn, J. H., Kim, Y. J., Choi, H. R., and Baik, S.: Highly conductive, printable and stretchable composite films of carbon nanotubes and silver. Nature Nanotechnology, 5(12):853–857, 2010.
161. Shin, M. K., Oh, J., Lima, M., Kozlov, M. E., Kim, S. J., and Baughman, R. H.: Elastomeric conductive composites based on carbon nanotube forests. Advanced Materials, 22(24):2663–2667, 2010.
162. Dalmas, F., Cavaille, J. Y., Gauthier, C., Chazeau, L., and Dendievel, R.: Viscoelastic behavior and electrical properties of flexible nanofiber filled polymer nanocomposites. influence of processing conditions. Composites Science and Technology, 67(5):829–839, 2007.
163. Yan, C., Wang, X., Cui, M., Wang, J., Kang, W., Foo, C. Y., and Lee, P. S.: Stretchable silver-zinc batteries based on embedded nanowire elastic conductors. Advanced Energy Materials, 4(5), 2014.
164. Xu, S., Zhang, Y., Cho, J., Lee, J., Huang, X., Jia, L., Fan, J. A., Su, Y., Su, J., Zhang, H., Cheng, H., Lu, B., Yu, C., Chuang, C., Kim, T. I., Song, T., Shigeta, K., Kang, S., Dagdeviren, C., Petrov, I., Braun, P. V., Huang, Y., Paik, U., and Rogers, J. A.: Stretchable batteries with self-similar serpentine interconnects and integrated wireless recharging systems. Nature Communications, 4, 2013.
165. Gaikwad, A. M., Zamarayeva, A. M., Rousseau, J., Chu, H., Derin, I., and Steingart, D. A.: Highly stretchable alkaline batteries based on an embedded conductive fabric. Advanced Materials, 24(37):5071–5076, 2012.

166. Bayer, I. S., Caramia, V., Fragouli, D., Spano, F., Cingolani, R., and Athanassiou, A.: Electrically conductive and high temperature resistant superhydrophobic composite films from colloidal graphite. Journal of Materials Chemistry, 22(5):2057–2062, 2012.
167. Qu, M., Zhao, G., Cao, X., and Zhang, J.: Biomimetic fabrication of lotus-leaf-like structured polyaniline film with stable superhydrophobic and conductive properties. Langmuir, 24(8):4185–4189, 2008.
168. Zhu, Y., Zhang, J. C., Zheng, Y. M., Huang, Z. B., Feng, L., and Jiang, L.: Stable, superhydrophobic, and conductive polyaniline/polystyrene films for corrosive environments. Advanced Functional Materials, 16(4):568–574, 2006.
169. Sethi, S. and Dhinojwala, A.: Superhydrophobic conductive carbon nanotube coatings for steel. Langmuir, 25(8):4311–4313, 2009.
170. Park, E. J., Kim, K. D., Yoon, H. S., Jeong, M. G., Kim, D. H., Lim, D. C., Kim, Y. H., and Kim, Y. D.: Fabrication of conductive, transparent and superhydrophobic thin films consisting of multi-walled carbon nanotubes. RSC Advances, 4(57):30368–30374, 2014.
171. Schutzius, T. M., Tiwari, M. K., Bayer, I. S., and Megaridis, C. M.: High strain sustaining, nitrile rubber based, large-area, superhydrophobic, nanostructured composite coatings. Composites Part A-Applied Science and Manufacturing, 42(8):979–985, 2011.
172. Vosgueritchian, M., Lipomi, D. J., and Bao, Z.: Highly conductive and transparent pedot:pss films with a fluorosurfactant for stretchable and flexible transparent electrodes. Advanced Functional Materials, 22(2):421–428, 2012.
173. Yang, Y., Ruan, G., Xiang, C., Wang, G., and Tour, J. M.: Flexible 3-dimensional nanoporous metal-based energy devices. Journal of the American Chemical Society, 136(17):61876190, 2014.
174. Cho, S. J., Nam, H., Ryu, H., and Lim, G.: A rubberlike stretchable fibrous membrane with anti-wettability and gas breathability. Advanced Functional Materials, 23(45):55775584, 2013.
175. Grobert, N.: Carbon nanotubes - becoming clean. Materials Today, 10(1-2):28–35, 2007.

176. Molnar, K., Szebenyi, G., Szolnoki, B., Marosi, G., Vas, L. M., and Toldy, A.: Enhanced conductivity composites for aircraft applications: carbon nanotube inclusion both in epoxy matrix and in carbonized electrospun nanofibers. Polymers for Advanced Technologies, 25(9):981–988, 2014.
177. Kim, C. and Zhang, S.: Mechanical and bending properties of a conductive thin single layer composite consisting of carbon nanofibers and polypyrrole. Journal of Mechanical Science and Technology, 28(7):2581–2585, 2014.
178. Wiggins-Camacho, J. D. and Stevenson, K. J.: Effect of nitrogen concentration on capacitance, density of states, electronic conductivity, and morphology of n-doped carbon nanotube electrodes. Journal of Physical Chemistry C, 113(44):19082–19090, 2009.
179. Al-Saleh, M. H. and Sundararaj, U.: A review of vapor grown carbon nanofiber/polymer conductive composites. Carbon, 47(1):2–22, 2009.
180. Cipriano, B. H., Kota, A. K., Gershon, A. L., Laskowski, C. J., Kashiwagi, T., Bruck, H. A., and Raghavan, S. R.: Conductivity enhancement of carbon nanotube and nanofiber-based polymer nanocomposites by melt annealing. Polymer, 49(22):4846–4851, 2008.
181. Luo, X. and Mather, P. T.: Conductive shape memory nanocomposites for high speed electrical actuation. Soft Matter, 6(10):2146–2149, 2010.
182. Chatterjee, A. and Deopura, B. L.: Thermal stability of polypropylene/carbon nanofiber composite. Journal of Applied Polymer Science, 100(5):3574–3578, 2006.
183. Elgafy, A. and Lafdi, K.: Effect of carbon nanofiber additives on thermal behavior of phase change materials. Carbon, 43(15):3067–3074, 2005.
184. Khattab, A., Liu, C., Chirdon, W., and Hebert, C.: Mechanical and thermal characterization of carbon nanofiber reinforced low-density polyethylene composites. Journal of Thermoplastic Composite Materials, 26(7):954–967, 2013.
185. Yu, C. H., Saha, S., Zhou, J. H., Shi, L., Cassell, A. M., Cruden, B. A., Ngo, Q., and Li, J.: Thermal contact resistance and thermal conductivity of a carbon nanofiber. Journal of Heat Transfer-Transactions of the ASME, 128(3):234–239, 2006.

186. Kim, H. M., Kim, K., Lee, C. Y., Joo, J., Cho, S. J., Yoon, H. S., Pejakovic, D. A., Yoo, J. W., and Epstein, A. J.: Electrical conductivity and electromagnetic interference shielding of multiwalled carbon nanotube composites containing fe catalyst. Applied Physics Letters, 84(4):589–591, 2004.
187. Tsai, P., Pacheco, S., Pirat, C., Lefferts, L., and Lohse, D.: Drop impact upon micro- and nanostructured superhydrophobic surfaces. Langmuir, 25(20):12293–12298, 2009.
188. Hsieh, C. T. and Fan, W. S.: Superhydrophobic behavior of fluorinated carbon nanofiber arrays. Applied Physics Letters, 88(24), 2006.
189. Zhu, J., Wei, S., Ryu, J., Budhathoki, M., Liang, G., and Guo, Z.: In situ stabilized carbon nanofiber (cnf) reinforced epoxy nanocomposites. Journal of Materials Chemistry, 20(23):4937–4948, 2010.
190. McCullen, S. D., Stevens, D. R., Roberts, W. A., Ojha, S. S., Clarke, L. I., and Gorga, R. E.: Morphological, electrical, and mechanical characterization of electrospun nanofiber mats containing multiwalled carbon nanotubes. Macromolecules, 40(4):997–1003, 2007.
191. Yang, Y. L., Gupta, M. C., Dudley, K. L., and Lawrence, R. W.: Conductive carbon nanoriber-polymer foam structures. Advanced Materials, 17(16):1999–2003, 2005.
192. Zhang, K., Han, B., and Yu, X.: Electrically conductive carbon nanofiber/paraffin wax composites for electric thermal storage. Energy Conversion and Management, 64:62–67, 2012.
193. Sanusi, O., Warzoha, R., and Fleischer, A. S.: Energy storage and solidification of paraffin phase change material embedded with graphite nanofibers. International Journal of Heat and Mass Transfer, 54(19-20):4429–4436, 2011.
194. Beineke, W. F.: Parafilm - new way to wrap grafts. Hortscience, 13(3):284–284, 1978.
195. Ewens, M. and Felker, P.: The potential of mini-grafting for large-scale production of *prosopis alba* clones. Journal of Arid Environments, 55(2):379–387, 2003.
196. Gaskin, P., Macmillan, J., Firn, R. D., and Pryce, R. J.: Parafilm - convenient source of n-alkane standards for determination of gas chromatographic retention indices. Phytochemistry, 10(5):1155–1157, 1971.

197. Higham, S. M. and Edgar, W. M.: Effects of parafilm and cheese chewing on human dental plaque ph and metabolism. Caries Research, 23(1):42–48, 1989.
198. Salamzadeh, J., Dadashzadeh, S., Habibi, M., and Estifaie, S.: Serum and saliva theophylline levels in adult outpatients with asthma and chronic obstructive pulmonary disease (copd): A cross-sectional study. Iranian Journal of Pharmaceutical Research, 7(1):83–87, 2008.
199. Javaherian, S., O'Donnell, K. A., and McGuigan, A. P.: A fast and accessible methodology for micro-patterning cells on standard culture substrates using parafilmTM inserts. PLOS One, 6(6), 2011.
200. Steele, A., Bayer, I., and Loth, E.: Inherently superoleophobic nanocomposite coatings by spray atomization. Nano Letters, 9(1):501–505, 2009.
201. Arkema: Kynar[®] polyvinylidene fluoride chemical resistance chart. <http://www.plastomatic.com/789.pdf>, 2014.
202. Liu, Q. F., Wang, Q., and Yan, S. H.: Modification of pvdf membranes by alkaline treatment. Applied Mechanics and Materials, 1033:316–317, 2013.
203. Feng, L., Zhang, Z. Y., Mai, Z. H., Ma, Y. M., Liu, B. Q., Jiang, L., and Zhu, D. B.: A super-hydrophobic and super-oleophilic coating mesh film for the separation of oil and water. Angewandte Chemie-International Edition, 43(15):2012–2014, 2004.
204. Yang, J., Zhang, Z. Z., Xu, X. H., Zhu, X. T., Men, X. H., and Zhou, X. Y.: Superhydrophilic-superoleophobic coatings. Journal of Materials Chemistry, 22(7):2834–2837, 2012.
205. Lee, Y. M., Kim, J. W., Choi, N. S., Lee, J. A., Seol, W. H., and Park, J. K.: Novel porous separator based on pvdf and pe non-woven matrix for rechargeable lithium batteries. Journal of Power Sources, 139(1-2):235–241, 2005.

VITA

NAME

Joseph E. Mates

EDUCATION

Ph.D., Mechanical Engineering, University of Illinois at Chicago, Expected 2014

B.S., Physics, University of Florida, 2006

TEACHING EXPERIENCE

Teaching Assistant (TA), Introduction to Thermodynamics (ME 255), University of Illinois at Chicago

Teaching Assistant (TA), Experimental Methods in Mechanical Engineering (ME 341), University of Illinois at Chicago

Teaching Assistant (TA), Introduction to Heat Transfer (ME 321), University of Illinois at Chicago

PUBLICATIONS

J.E. Mates, T.M. Schutzius, I.S. Bayer, J. Qin, D.E. Waldrup, C.M. Megaridis, "Water-Based Superhydrophobic Coatings for Nonwoven and Cellulosic Substrates," Industrial & Engineering Chemistry Research, 2013, 53, 222-227

J.E. Mates, T.M. Schutzius, J. Qin, D.E. Waldrup, C.M. Megaridis, "The Fluid

Diode: Tunable Unidirectional Flow through Porous Substrates,” ACS Applied Materials & Interfaces, 2014, 6, 12837-12843

J. Song, S. Huang, Y. Lu, X. Bu, J.E. Mates, A. Ghosh, R. Ganguly, C.J. Carmalt, I. Parkin, W. Xu, C.M. Megaridis, “Self-Driven One-Step Oil Removal from Oil Spill on Water via Selective-Wettability Steel Mesh,” ACS Applied Materials & Interfaces, 2014, 10.1021/am505254j

J.E. Mates, I.S. Bayer, M. Salerno, P.J. Carroll, Z. Jiang, L. Liu, C.M. Megaridis, “Durable & Flexible Graphene Composites for Conductive Paper Applications,” *Submitted for publication in Carbon.*

S. Gart, J. Mull, J.E. Mates, C.M. Megaridis, S. Jung, “Droplet impacting on a cantilever: a leaf-raindrop system,” *Submitted for publication in Physical Review Letters.*

J.E. Mates, I.S. Bayer, J. Palumbo, P.J. Carroll, C.M. Megaridis, “Elastomeric Conductive Composites for Flexible Power Storage and Wearable Electronics Applications,” *In preparation for Nature Nanotechnology.*

J.E. Mates, R. Ibrahim, A. Vera, J. Qin, D.E. Walldrop, S. Guggenheim, C.M. Megaridis, “Translucent Water-based & Nonfluorinated Superhydrophobic Compositions for Large-area Applications,” *In preparation for Advanced Functional Materials.*

J.E. Mates, B. Pourdeyhimi, C.M. Megaridis, “Large-area Fabrics for High-flux Oil-water Emulsion Separation,” *In preparation for Nature Communications.*

J.E. Mates, B. Pourdeyhi, S. Guggenheim, C.M. Megaridis, “Piezoelectric Composites for Energy Harvesting and Self-defouling Filtration,” *In preparation for Advanced Materials*.

PATENTS & DISCLOSURES

J. Qin, D.E. Waldroup, C.M. Megaridis, J.E. Mates and T.M. Schutzius. *One-Way Valve Nonwoven Material*. US Non-provisional Patent Application 61/898126 (10-31-2013).

CONFERENCES

J. E. Mates, C. M. Megaridis. Selective Multicomponent Fluid Separation: Effects of Surface Energy, Morphology, and Fluid Density In: *American Filtration and Separation Society Annual Conference*, Oct. 14 - 15, 2015, Chicago, IL.

J. E. Mates, T. M. Schutzius, C. M. Megaridis. One-way Water Permeable Valve via Water-based Superhydrophobic Coatings. In: *American Physical Society Division of Fluid Dynamics*. Nov. 24 - 26, 2013, Pittsburgh, PA.

J. E. Mates, T. M. Schutzius, C. M. Megaridis. One-way Water Permeable Valve from Superhydrophobic Coatings on Hydrophilic Cellulosic Substrates. In: *ASME 4th Joint US-European Fluids Engineering Summer Meeting*. Aug. 3 - 7, 2014, Chicago, IL.